Université de Lille

Faculté des Sciences et Technologies

Laboratoire d'Optique Atmosphérique

Manuscrit de thèse

Présentée pour l'obtention du grade de : Docteur en physique de l'Université de Lille
spécialité Terre, enveloppes fluides

Inferring aerosol particles inhomogeneity from remote sensing observations

Détermination de l'inhomogénéité des particules d'aérosol à partir d'observations par télédétection

Soutenue publiquement le 29 Avril 2026 par

Philippe Lesueur

devant le jury composé de :

Rapportrice:	Claudia Di Biagio	CR/ HDR	LISA
Rapporteur:	Aliaksandr Siniuk	Senior Scientist	GSFC
Examinateur:	Jean-Claude Roger	PR	LaMP
Examinateur:	Yinon Rudich	PR	Weizmann Institute
Directeur de thèse:	Yevgeny Derimian	CR/ HDR	LOA
Co-directeur de thèse:	Oleg Dubovik	DR	LOA
Co-encadrante de thèse:	Marie Boichu	CR	LOA

Président du jury : Jean-Claude Roger

Graduate School

Sciences de la Matière, du Rayonnement et de l'Environnement

Sciences de la Matière, du Rayonnement et de l'Environnement

Candidate: Philippe Lesueur, No. 11600895,
philippe.lesueur@univ-lille.fr

Publically defended April 29th 2026 by **Philippe Lesueur** in front of a jury composed of :

Referee: Claudia Di Biagio, Laboratoire Interuniversitaire des Systèmes Atmosphériques, CNRS/Université Paris Cité, CR/HDR, claudia.dibiagio@lisa.ipsl.fr

Referee: Aliaksandr Siniuk, Goddard Space Flight Center, NASA, Senior Scientist, aliaksandr.sinyuk-1@nasa.gov

Examiner: Jean-Claude Roger, Laboratoire de Météorologie Physique, Université Clermont Auvergne, PR, j-claude.roger@uca.fr

Examiner: Yinon Rudich, Department of Earth and Planetary Sciences, Weizmann Institute of Science, PR, yinon.rudich@weizmann.ac.il

Thesis Director: Yevgeny Derimian, Laboratoire d'Optique Atmospherique, CNRS/Université de Lille, CR/HDR, yevgeny.derimian@univ-lille.fr

Co-director: Oleg Dubovik, Laboratoire d'Optique Atmospherique, CNRS/Université de Lille, DR, oleg.dubovik@univ-lille.fr

Co-supervisor: Marie Boichu, Laboratoire d'Optique Atmospherique, CNRS/Université de Lille, CR, marie.boichu@univ-lille.fr

Département de Physique
Faculté des Sciences et Technologies
Campus Cité Scientifique, Bât. P5, 59655 Villeneuve-d'Ascq

I dedicate this thesis to my parents.

Acknowledgements

I would first like to express my sincere gratitude to my supervisor and co-supervisor, Dr. Yevgeny Derimian and Dr. Oleg Dubovik, for the opportunity they gave me to undertake a PhD on such a stimulating and meaningful topic. I am deeply thankful for the trust they placed in me, particularly given my background in computer science, and for the constant support and guidance they provided throughout these years. Their mentorship not only enabled me to complete this work but also introduced me to the field of atmospheric science and to scientific research more broadly.

I am especially grateful for the exceptional opportunities they offered me to present my work internationally. Participating in conferences such as EGU in Vienna, APOLO in Japan, and AGU in the United States has been an invaluable experience, both scientifically and personally, and these moments will remain among the highlights of my doctoral journey.

I would also like to thank the members of my scientific committee, Dr. Juan Cuesta, Dr. Marc Tommasi, and Dr. Bénédicte Baqué, for their time, their thoughtful feedback, and the care with which they followed my progress over the past three years. Their insights have greatly contributed to strengthening this work. I want to also express my gratitude to the jury for the time, interest invested in my work and for the intellectually stimulating questioning.

My sincere thanks go to the teams of GRASP and LOA for their support, collegiality, and the stimulating work environment they fostered. I am particularly grateful to Anne Priem and Marie-Lyse Liévin for their invaluable administrative assistance, responsiveness, efficiency, and kindness, which allowed me to focus fully on my research. I would also like to thank François Thulieux, Fabrice Ducos, Christian Matar, and Tatsiana Lapyonok for their precious technical support, for introducing me to the internal processes of LOA and GRASP, for their help with algorithm compilation on the servers and preparation for code modifications, and for the many interresting discussions we shared. I am grateful to Professor Viktor Tishkovets for generously sharing his calculation code for layered spheres. Finally, I warmly thank Anton Lopatin, Pavel Litvinov, Benjamin Torres, Masahiro Momoi, and Elise Devigne for their valuable discussions

on scientific concepts and various aspects of algorithm tuning.

I gratefully acknowledge the financial support and sustained interest of the Agence de l'Innovation de la Défense and Labex CaPPA, without which this research would not have been possible.

My heartfelt appreciation goes to my girlfriend for her unwavering encouragement, unconditional support, and patience, especially during times of doubt and fatigue. Her love has been a constant source of strength throughout this journey.

Finally, and most importantly, I wish to express my deepest gratitude to my parents. They have supported me throughout my education, always encouraging me to give my best, to seek deep understanding rather than superficial knowledge, and to persevere in the face of challenges. I would not have come this far if it weren't for them.

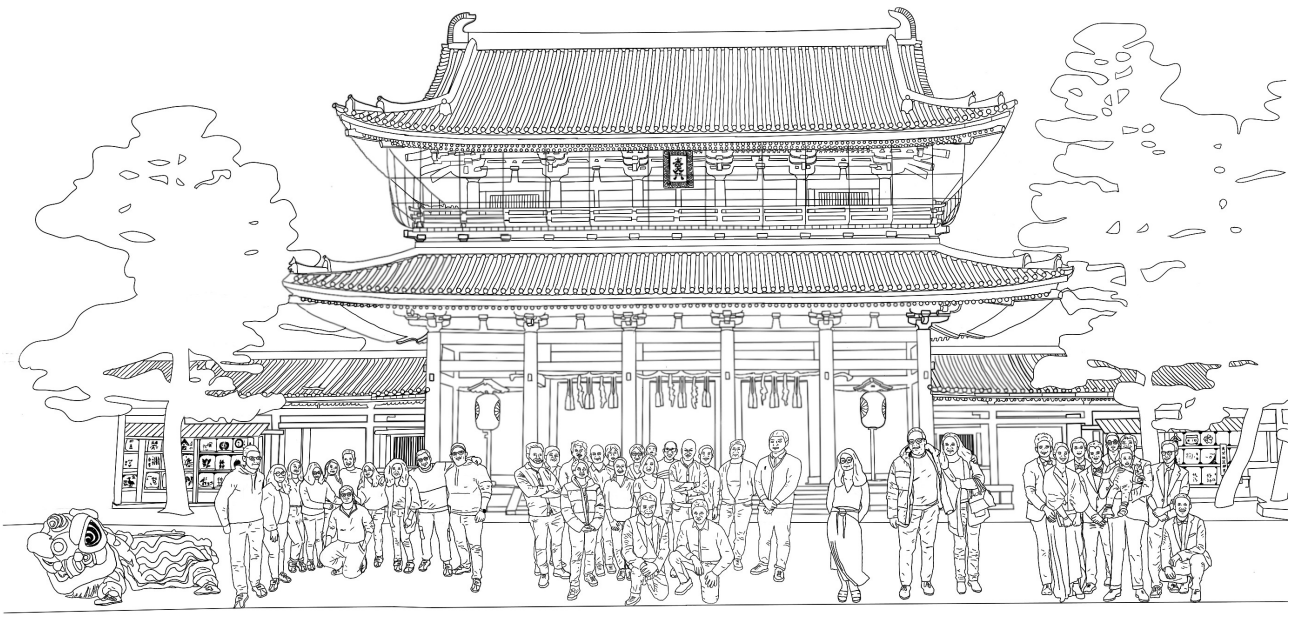

Abstract

Atmospheric aerosols influence the Earth's radiative budget in the surface-atmosphere system, affect the cloud formation and microphysics, air quality and visibility, hence have an important impact on climate, environment and even socio-economical processes. Remote sensing methods of aerosol observations can provide information on optical and microphysical properties on a wide scale in near real-time, but also on global, regional or local climatology.

Composition and mixing state of aerosol is crucial for understanding and evaluation of aerosol interactions with climate and environment. However, such characterisation by remote sensing is an extremely challenging task. In addition, aerosol can suffer from rapid and important structural modifications during their lifetime in the atmosphere, for which monitoring can be difficult. One of those modifications is water uptake and the creation of coating on particles. This aerosol coating can significantly change their radiative impact, but also their ability to interact with other substances in the atmosphere and serve as cloud condensation nuclei.

This thesis work is focused on the problematic of the aerosol coating by a liquid material and is dedicated to : (i) study the impact of particles coating on scattering properties using numerical simulation of a core/shell model by the Mie theory for layered spheres; (ii) calculation and implementation of pre-computed tables of a core/shell model for an inversion algorithm (GRASP); (iii) tuning and testing the sensitivity to core/shell aerosol retrieval using synthetic measurements; (iv) numerical inversion of ground-based sunphotometric measurements by the AERONET global network using the newly suggested aerosol model; and (v) studying its impact on aerosol retrievals and coherence of the retrieved core/shell aerosol fraction with the on-site conditions.

This work thus presents results of theoretical influence of aerosol coating on light scattering properties, a newly suggested parametrisation of a remote sensing algorithm, analysis of the regime of the algorithm applicably and illustration for the performance using several measurement sites that represent urban, desert or mixed aerosol types.

Keywords: : Aerosol, aerosol water uptake, aerosol inhomogeneity, remote sensing, photometer, AERONET network

Résumé

Les aérosols atmosphériques influencent le bilan radiatif du système surface-atmosphère de la terre, affectent la formation et la microphysique des nuages, ainsi que la qualité de l'air et la visibilité ; ils exercent ainsi un impact majeur sur le climat, l'environnement et, plus largement, sur certains processus socio-économiques. Les méthodes de télédétection dédiées à l'observation des aérosols permettent d'obtenir, à large échelle et en quasi temps réel, des informations sur leurs propriétés optiques et microphysiques, ainsi que sur leur climatologie aux échelles globale, régionale ou locale.

La composition et l'état de mélange des aérosols constituent des paramètres essentiels pour comprendre et évaluer leurs interactions avec le climat et l'environnement. Toutefois, une telle caractérisation par télédétection demeure particulièrement complexe. En outre, les aérosols peuvent subir, au cours de leur temps de résidence atmosphérique, des modifications structurales rapides et significatives, dont la surveillance s'avère délicate. Parmi celles-ci figurent l'adsorption d'eau et la formation d'une pellicule à la surface des particules. Cette pellicule peut modifier de manière substantielle l'impact radiatif, mais aussi la capacité des aérosols à interagir avec d'autres constituants atmosphériques et à agir en tant que noyaux de condensation des nuages.

Le présent travail de thèse porte sur la problématique de l'enrobage des particules d'aérosol par un matériau liquide et s'articule autour des objectifs suivants : (i) étudier l'impact de l'enrobage des particules sur leurs propriétés de diffusion du rayonnement à l'aide de simulations numériques basés sur un modèle core/shell et calculé par la théorie de Mie appliquée aux sphères stratifiées ; (ii) calculer et implémenter des tables de pré-calculs associées au modèle core/shell au sein d'un algorithme d'inversion (GRASP) ; (iii) ajuster et tester la sensibilité de la restitution des fractions core/shell des aérosols à l'aide de mesures synthétiques ; (iv) réaliser l'inversion numérique de mesures photométriques solaires acquises au sol par le réseau mondial AERONET en utilisant le nouveau modèle d'aérosol proposé dans cette étude; (v) analyser l'impact de ce modèle sur les restitutions d'aérosols et évaluer la cohérence de la fraction core/shell restituée au regard des conditions environnementales locales d'observation.

Ce travail présente ainsi des résultats relatifs à l'influence théorique de l'enrobage des aérosols sur les propriétés de diffusion de la lumière, propose une nouvelle paramétrisation d'un algorithme de télédétection, analyse son domaine d'applicabilité et illustre ses performances à partir de mesure sur plusieurs sites représentants d'aérosols urbains, désertiques ou mixtes.

Mots-clés:Aérosol, adsorption d'eau par aérosol, inhomogénéité des aérosols, télédétection, photométrie solaire, réseau AERONET

Table of contents

Chapter 1: Introduction **1**

1.1 Background . . . 1

1.1.1 Aerosol sources and composition . . . 3

1.1.2 Ageing processes . . . 6

1.2 Remote sensing of aerosol composition for climate, environmental and air quality studies . . . 9

1.2.1 Aerosols impacts . . . 10

1.2.2 Dry fraction for PM . . . 11

1.2.3 Modelisation of aerosol properties . . . 12

1.3 Relevant principles of light scattering and remote sensing . . . 13

1.3.1 Light scattering by spherical particles . . . 14

1.3.2 Remote sensing and inversion principles . . . 16

1.4 Aerosol inhomogeneity . . . 18

1.4.1 Insights from previous studies . . . 18

1.4.2 Reports on implications for remote sensing . . . 19

1.5 Thesis objectives . . . 21

1.5.1 Scientific question . . . 21

1.5.2 Specific goals . . . 22

1.5.3 Thesis structure . . . 23

Chapter 2: Algorithmic framework and Working basis **25**

2.1 Core/Shell Model . . . 25

2.2 Introduction of inhomogeneity in the GRASP algorithm . . . 26

2.2.1 GRASP algorithm . . . 26

2.2.2 Implementation . . . 29

2.2.3 Settings preparation . . . 32

2.3 Data selection . . . 33

2.3.1 AERONET and its data . . . 33
2.3.2 Selection of sites of interest . . . 35
2.4 Data preparation . . . 36
2.4.1 Creation of GRASP input files for AERONET measurements . . . 36
2.4.2 Implementation of AERONET degree of polarisation measurements treatment for sdata preparation . . . 37

Chapter 3: Optical properties of core/shell particles under single scattering approximation 41
3.1 Algorithm and Input . . . 41
3.2 Protocol . . . 43
3.3 Analysis . . . 46
3.3.1 Particularity of scattering and polarisation for core/shells particles . . . 46
3.3.2 Absolute and angular difference due to change in size vs. structure . . . 50
3.4 Conclusion . . . 54

Chapter 4: Synthetic tests with GRASP/ARIA 55
4.1 Definition of the initial guess and constrains . . . 57
4.2 Approach and results analysis . . . 58
4.3 Inversion of inhomogeneous aerosol signal with a homogeneous model . . . 60
4.4 Effects of Core/Shell refractive index contrast . . . 73
4.5 Effects of aerosol concentration on GRASP/ARIA retrievals . . . 92
4.6 Conclusion . . . 103

Chapter 5: GRASP/ARIA application to real AERONET measurements 105
5.1 Selected sites and their description . . . 105
5.2 Inversion quality assessment . . . 106
5.3 Evaluation of consistency between retrieved core/shell fraction and other aerosol characteristics . . . 126
5.4 Conclusion . . . 142

Chapter 6: Summary and perspectives 145
6.1 Summary and Conclusions . . . 145
6.2 Perspectives . . . 148

References 152

Appendix A **167**
A.1 In depth description of GRASP algorithm settings file 167
A.2 Optical properties of core/shell particles under single scattering approximation . 177
A.3 Synthetic tests with GRASP/ARIA 184
A.3.1 Inversion of inhomogeneous aerosol signal with a homogeneous model . . 184
A.3.2 Scope of applicability 205
A.3.3 Complementary figures 208
A.4 GRASP/ARIA application to real AERONET measurements 233
A.4.1 Relative humidities 233
A.4.2 Complementary figures 234
A.4.3 Grouped by AOD 255
A.5 TACO database ER diagramm 257

List of Figures

1.1 Components of climate radiative forcing and their radiative impact according to the IPCC Assessment Report [AR5]. 4
1.2 Schematic multi-modal particle size distribution with typical transformations and example particle types within each mode. Courtesy of [Deutscher Wetterdienst, Research, Observing the atmosphere, Atmospheric composition, Aerosols, Particle Size-Distribution, Figure 1]. 7
1.3 Health effects associated with airborne particulate matter pollution. 12
1.4 General structure of the thesis. 24

2.1 Representation of the spherical Core/Shell structure as a particle divided in two parts. The Core part is made of a solid spherical aerosol of any origin. The Shell part is considered as an evenly distributed solution of ammonium sulphate/nitrate on the surface of the core. 25
2.2 Representation of different, non-exhaustive, models of inhomogeneity, e.g.: a) Cluster model; b) Inclusion model; c) Spheroidal Core/Shell model; d) Spherical eccentric Core/Shell model; e) Spherical Core/Shell model. 26
2.3 General structure of GRASP inversion algorithm. 27
2.4 Representation of kernel structure top part is the description of the different kernel files, with the particle type and corresponding element of the scattering matrix. The bottom part describes the content of a file except for "00" which does not contain the angular dimensionality. 29
2.5 Example of scattering properties calculations during inversion. If the loaded kernels are [0.9,0.8,0.7,0.6,0.5] and the core ratio value is 0.963, then the function will select the scattering properties' values according to the refractive index, bin radius and scattering angle from the homogeneous spherical kernel (as it is the equivalent to 1.0 core ratio) and the 0.9 kernel and return the interpolated values. 31
2.6 Worldwide distribution of AERONET sites. 33

2.7 Representation of AERONET measurement scenarios. Direct measurements are single measurements, whereas almucantar and hybrid are composed of a series of measurements. 34
2.8 Mapping of the selected AERONET sites. 35

3.1 Screenshots of a python interface created for the input parameters selection for fast analysis of the calculation results. This interface also generates an input file (.txt) following the format required by the GRASP code. 42
3.2 Size Distributions for each type of aerosols. Ordinates are the concentrations : $\frac{dV(r)}{dln(r)}$ and abscissas are the radii r (μm). Re is the refractive index real part of the homogeneous aerosol and the core. The radii r_f and r_c are the mean radii of the lognormal distribution of the dominant mode. 45
3.3 Phase function (P_{11}) with refractive indices corresponding to urban and biomass burning aerosol models with a fine mode dominated size distribution as common trait. Wavelength of 440 nm corresponds to the closest available wavelength to particle size and 1020 nm is the opposite, being closer to coarse size distributions. 47
3.4 Phase function (P_{11}) with refractive indices corresponding to desert dust aerosol models with a coarse dominated size distribution as common trait. Wavelength of 1020 nm corresponds to the closest available wavelength to particle size and 440 nm is the opposite, being closer to fine size distributions. 48
3.5 DoLP ($\frac{-P_{12}}{P_{11}}$) with refractive indices corresponding to each used aerosol models. The chosen wavelengths are the closest available to the size distribution of the particles. 49
3.6 Impacts of changes in size and structure on the phase function ($\mid P_{11^{homog.}}(rm) - P_{11^{homog.}}(0.7rm) \mid \Rightarrow \Delta r$ and $\mid P_{11^{inhomog.}}(rm) - P_{11^{homog.}}(rm) \mid \Rightarrow \Delta shell$) at 440 nm and 1020nm. Fine mode dominated size distribution. 50
3.7 Impacts of changes in size and structure on the phase function ($\mid P_{11^{homog.}}(rm) - P_{11^{homog.}}(0.7rm) \mid \Rightarrow \Delta r$ and $\mid P_{11^{inhomog.}}(rm) - P_{11^{homog.}}(rm) \mid \Rightarrow \Delta shell$) at 440 nm and 1020nm. Coarse dominated size distribution. 51
3.8 Impacts of changes in size and structure on the phase function ($\mid P_{12^{homog.}}(rm) - P_{12^{homog.}}(0.7rm) \mid \Rightarrow \Delta r$ and $\mid P_{12^{inhomog.}}(rm) - P_{12^{homog.}}(rm) \mid \Rightarrow \Delta shell$) at 440 nm and 1020nm. 52

3.9 Angular variation of impacts of changes in size and structure on the phase function for urban aerosol model represented by fine mode dominated size distribution and desert aerosol model represented by coarse dominated aerosol model. 53

4.1 Collection of plots of aerosol optical and microphysical characteristics derived by inversion of synthetic AERONET measurements. The case of fine mode dominated aerosol size distribution. The radiances, are generated using GRASP/ARIA (with inhomogeneous aerosol model)and inverted using GRASP/Standard (with homogeneous aerosol only). In panels a) and b) are results where only radiance intensity (no polarisation) is used, the refractive indices are a) n=1.41, k=0.003 and b) n=1.50 and k=0.003. Panels c) and d) are the same, but polarisation is used. 64
4.2 Same as Figure 4.1, but for a coarse mode size distribution. 68
4.3 Same as Figure 4.1, but for a bimodal size distribution. 72
4.4 R^2 scores for retrieved vs. assumed core and sphere fractions as function of real refractive index (spectrally invariant) of core, for fine and coarse mode dominated size distributions. Sub-graph in the bottom left corner shows negative R^2 values, which produces when the real refractive index of core is close or below that of shell. 74
4.5 Collection of plots of aerosol optical and microphysical characteristics derived by inversion of synthetic AERONET measurements. The case of fine mode dominated aerosol size distribution. The radiances, are generated and inverted using GRASP/ARIA (with inhomogeneous aerosol model).In panels a) and b) are results without measurements noise, the refractive indices are a) n=1.41, k=0.003 and b) n=1.50 and k=0.003. Panels c) and d) are the same, but simulation of measurements noise is included. 77
4.6 Collection of plots of aerosol optical and microphysical characteristics derived by inversion of synthetic AERONET measurements. The case of fine mode dominated aerosol size distribution. The radiances, including polarisation, are generated and inverted using GRASP/ARIA (with inhomogeneous aerosol model). In panels a) and b) are results with measurements noise, the refractive indices are a) n=1.41, k=0.003 and b) n=1.50 and k=0.003. 80
4.7 Same as Figure 4.5, but for coarse mode dominated size distribution. 84
4.8 Same as Figure 4.6, but for coarse mode dominated size distribution. 86

4.9 Same as Figure 4.5, but for bimodal size distribution. 89
4.10 Same as Figure 4.6, but for coarse mode dominated size distribution. 91
4.11 Collection of plots of aerosol optical and microphysical characteristics derived by inversion of synthetic AERONET measurements. The case of fine mode dominated aerosol size distribution and of refractive index n=1.50 and k=0.003. The radiances, are generated and inverted using GRASP/ARIA (with inhomogeneous aerosol model). In panels a) and b) are results without measurements noise and no polarisation, the AOD at 440 nm are a) 0.1 and b) 1.5. Panels c) and d) are the same, but simulation of measurements noise and polarisation are included. . 95
4.12 Same as 4.11, but for coarse mode dominated size distribution. 99
4.13 Same as 4.11, but for bimodal size distribution. 102

5.1 Collection of plots of aerosol optical and microphysical characteristics retrieved by GRAS/ARIA and GRASP/Standard using real AERONET measurements for the period from 2008 to 2025, for the sites representing urban aerosol. 110
5.2 Same as Figure 5.1, but for AERONET sites representing mixed aerosol type. . 114
5.3 Same as Figure 5.1, but for AERONET site dominated by desert dust aerosol. . 117
5.4 Collection of plots of aerosol optical and microphysical characteristics derived using GRASP/ARIA (parameterisation of inhomogeneity included) of all available inversible observations for AERONET sites representing domination of urban aerosol (Lille and GSFC sites). The data covers the perid of 2008 to 2025. . . . 120
5.5 Same as 5.1 for AERONET sites with mixed aerosols. 123
5.6 Comparison of retrieved core fraction from inversions of measurements with and without information on polarisation for the sites of GSFC and Barcelona. 124
5.7 Collection of plots illustrating the interpretation of core fraction retrievals in the context of residual improvement, seasonality, dominant particle size (represented by the Ångström exponent), composition (represented by the real refractive index), and shifts in the particle size distribution. The plots show results of GRASP/ARIA retrievals for real AERONET measurements from the period 2008 to 2025, which do not include information on light polarisation. The data are filtered by quality of radiance fit. The AERONET sites GSFC, Kanpur, Tamanrasset INM and Dakar represent a variety of urban, industrial, desert, and mixed aerosol types. 133

5.8 Same as Figure 5.7, but for AERONET sites representing urban aerosol and for measurements that include information on light polarization. The time period is, however, much more limited. 138
5.9 Same as Figure 5.8 (information on polarisation is included), but for AERONET sites representing mixed aerosol type. 140

List of Acronyms

ACTRIS *Aerosols, Clouds, and Trace gases Research InfraStructure*

AERONET *AErosol RObotic NETwork*

AOD *Aerosol Optical Depth*

API *Application Programming Interface*

ARIA *Augmented Retrieval for Inhomogeneous Aerosols*

CCN *Cloud Condensation Nuclei*

DoLP *Degree of Linear Polarization*

GRASP *Generalized Retrieval of Aerosol and Surface Properties*

GSFC *Goddard Space Flight Center*

LDR *LIDAR Depolarization Ratio*

LIDAR *Laser Imaging Detection And Ranging*

LSM *Least Square Method*

OP *Oxidative potential*

OPAC *Optical Properties of Aerosols and Clouds*

PM *Particulate Matter*

SD *Size Distribution*

SSA *Single Scattering Albedo*

TACO *Table of Aerosol and Cloud Optics*

TAO *Table of Aerosol Optics*

TOD *Total Optical Depth*

Chapter 1

Introduction

1.1 Background

Atmospheric aerosols are microscopic particles and are abundantly present in Earth's atmosphere. They vary in size, shape and chemical composition and exist in solid or liquid state, with sizes ranging from a few nanometres to several tens of micrometers. The size scale of aerosols is comparable to the wavelength of solar radiation spectrum, which makes them particularly interesting in terms of their interaction with sunlight. Atmospheric aerosol can be naturally emitted or be emitted as a result of human activities, so-called anthropogenic aerosols. The aerosol particles can originate from direct emission and are called primary aerosols, or be formed by chemical reactions in the atmosphere involving gaseous precursors and are defined as secondary aerosol (Boucher, 2015; Grandey et al., 2018; Kroll and Seinfeld, 2008).

The main emitters of natural aerosols are global ocean with sea salt and organic matter being released by the bursting of air bubbles. The deserts are known as second contributor with mineral dust being lifted by heavy wind blows. Massive, but more sporadic, aerosol emissions can be caused by volcanoes injecting ash and sulphates. Another type of natural aerosol is biogenic; these particles can be primarily emitted from biosphere, e.g. pollen, or formed by reactions of chemical compounds, e.g., volatile organics. Wildfires generate emissions of carbonaceous aerosol that can contain so-called Black Carbon (BC) and Organic Carbon (OC)

created during partial combustion (Bond et al., 2013). At the same time, the wildfires often have anthropogenic origin and most of the emitted aerosols are thus not natural. The anthropogenic aerosol sources lie in urban, industrial and rural areas. They are related to partial combustion like exhaust, power plants, cooking or biomass burning, particle displacement due to surface abrasion, resuspension, mining and farming.

The size of these aerosols ranges from a few nanometres to a few micrometers and are separated into two or three size modes. When divided in three, there are the nucleation mode, the accumulation mode and the coarse mode (Morawska et al., 1999). Nucleation mode is composed of the smallest particles in the atmosphere (diameter < 10 nm). The nucleation mode has the highest number concentration of aerosols in the atmosphere, but is almost negligible in terms of volume. Because interaction of light with small particles depends on particles cross-section or volume, the sensitivity to the nucleation mode is very limited. This is why the two modes model is the most used in remote sensing, where the nucleation mode and the accumulation mode are gathered into a single "fine mode" (diameter below about 1 μm) (Dubovik et al., 2002). Accumulation mode particles can be emitted directly or come from ageing processes of nucleation mode particles. The coarse mode particles (diameter $>$ about 1 μm) are usually those that directly emitted and originate in arid regions, volcanic ash eruptions and sea spray.

Aerosol ageing is a process of particles evolution that undergoes during its lifetime in the atmosphere. The lifetime of particles ranges from hours to years depending on the size of the particle and the altitude (Textor et al., 2006; Boichu et al., 2023). Smaller particles remain longer in the atmosphere, while most of the large aerosol particles have a short lifetime and are not transported far from their emission site. There are however common exceptions like the transport of Saharan dust over the Atlantic and the transport of volcanic plumes injected into upper troposphere or even stratosphere. Some wildfire emissions were also recently reported as reaching the stratosphere, e.g., (Peterson et al., 2018; Khaykin et al., 2020, 2025). During this transport, the great variety of compounds and the energy provided by sunlight create an ideal environment for chemical transformations and interactions.

The interaction of solar and terrestrial (thermal infrared) radiation with the aerosol particles is, thus, varying according to aerosol origin, physico-chemical proprieties and transformation during the lifetime in the atmosphere. These interactions are impacting climate by radiative cooling or warming, but also enables the detection and evaluation of aerosol properties and

radiative impacts by remote sensing techniques. This is why understanding of aerosol origins, microphysics, chemical composition and radiative properties by means of remote sensing is highly useful and important for climate studies. One aspect of such interactions is addressed in this thesis work, with a detailed description and analysis provided below.

1.1.1 Aerosol sources and composition

Natural and anthropogenic emissions define either aerosol impact on climate is of natural or human made origin. Figure 1.1, courtesy of the IPCC Assessment Report [AR5] lists anthropogenic components of climate radiative forcing by their origins and summarises forcing evaluation due to interactions with incoming and outgoing solar and terrestrial radiation. In addition to gases, land use and solar radiation, one can distinguish the effects of aerosol and precursors. Namely, distinguished are the next anthropogenic aerosol types : nitrate/sulphate; carbonaceous aerosols from fossil or biofuel or biomass burning; and anthropogenic part of mineral dust. In addition to the anthropogenic origin, practically all these aerosol classes and species can be emitted from natural sources, while marine aerosol are considered as of natural origin only, e.g., (Stocker et al., 2013).

Natural emissions

Marine aerosols represent the largest fraction of atmospheric aerosols, they can not only be found over water bodies and in coastal areas, but also transported far over land on altitude. The presence of marine aerosols is correlated to wind speed as aerosols are released by air bubbles exploding when reaching the surface with coarse particles reaching centimetres above the surface and fine particle being able to reach high altitudes by convection. The chemical composition of marine aerosols is mainly made of sea salt but also from an organic material. The sea salt itself is composed of sodium and chloride with part of the chloride reacting in the atmosphere to produce sulphuric and nitric acid. Marine aerosols are also a great contributor to organic carbon with primary and secondary emissions like phytoplankton that emits organic compounds like dimethyl-sulphide contributing to the production of sulphates. The marine particles are the greatest contributors to coarse aerosols in the atmosphere (De Leeuw et al., 2011; White, 2008).

Mineral dust aerosols are composed of different minerals lifted from the ground by the wind. They can potentially come from any type of soil but mainly from arid surfaces as their bond to

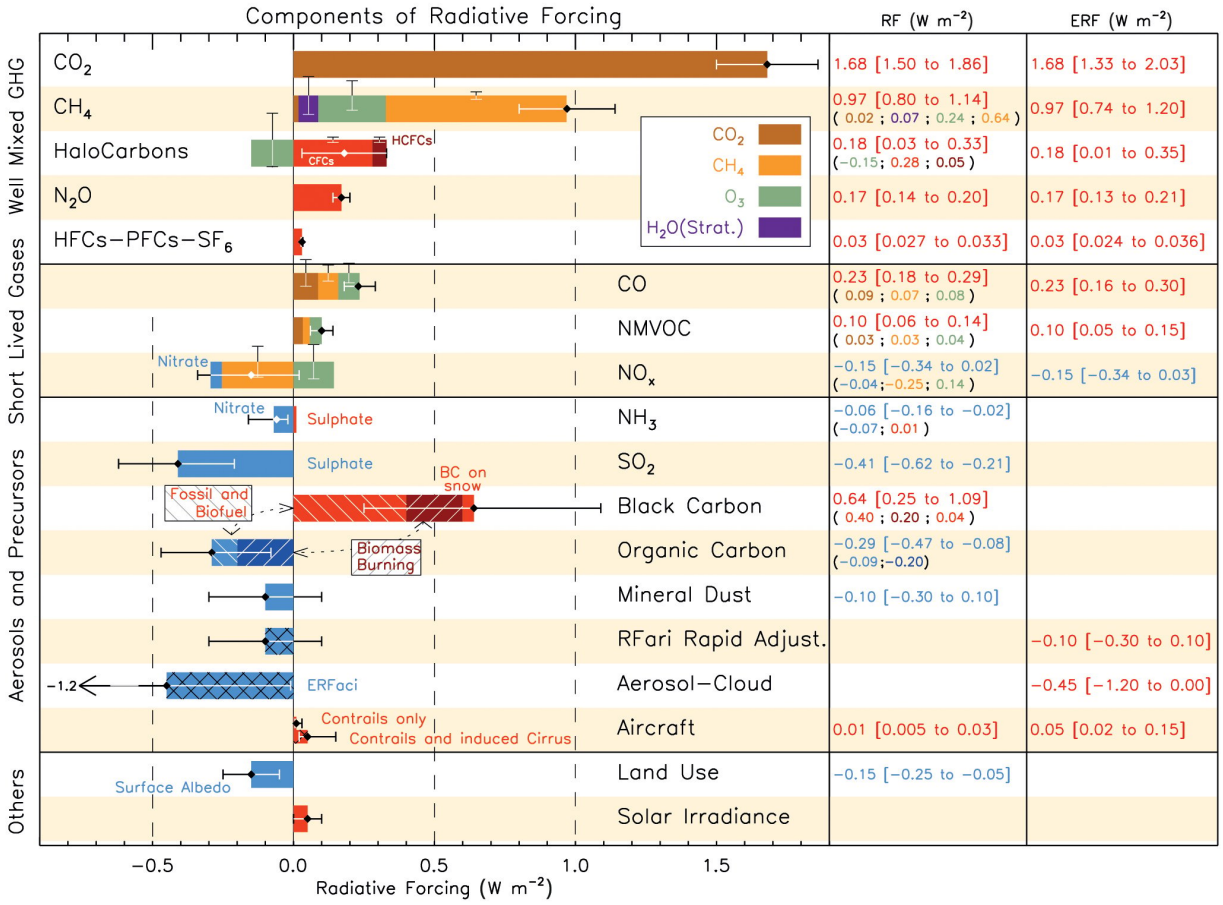

Figure 1.1: Components of climate radiative forcing and their radiative impact according to the IPCC Assessment Report [AR5].

other particles is weaker than humid ones and are easier to lift. The main sources of mineral dust are the deserts such as the Sahara in the North of Africa, the deserts in the Arabian Peninsula and Oman, Gobi and Taklamakan in China, that form the global dust belt. Other emitting regions lie outside this belt, including Lake Eyre and the Great Artesian Basin in Australia or desert areas in Patagonia and in Western Argentina (Formenti et al., 2011; LeGrand et al., 2019). Deserts can produce fine, coarse and even supercoarse particles in case of strong winds. Under certain conditions, vast amount of aerosols can be transported from deserts to other parts of the world like Saharan dust being transported to Europe or America (Prospero et al., 2020). Such transport can then be defined by an external mixing of minerals, which will define its interactions with sunlight and chemical reactions in the atmosphere. Due to their size and chemical composition, mineral dust has many different shapes, are rarely spherical and generally is believed to have a weak hygroscopicity. However, under certain condition and after

interaction with pollutants with ageing, the desert dust can present highly hygroscopic properties; for example, clays, calcium, magnesium and salt-containing mineral dust (Chen et al., 2020; Guo et al., 2019).

Volcanic aerosols are primarily emitted during explosive eruptions, which can be highly energetic events capable of releasing substantial quantities of both primary aerosols and precursors to secondary aerosols, but also during a passive volcanic degassing. In cases of high energy explosive eruptions, these aerosols can be injected into the stratosphere. The emitted type of aerosols depends on the type of eruption; however, the most predominant are the sulphates originating from the release and oxidation of SO_2 (Chin and Jacob, 1996). Explosive eruptions may also inject a wide range of additional chemical compounds into the atmosphere with the volcanic debris ranging from 1 to 10 μm. Tropospheric emissions have a lifetime of about one week, in contrast, stratospheric emission have a lifetime reaching a few years (Watanabe et al., 2004; Boichu et al., 2023). Due to limited vertical mixing between troposphere and stratosphere, volcanic aerosols that reach the stratosphere represent some of the aerosol particles with the longest lifetime in the atmosphere.

Biogenic aerosols are the particles emitted by the flora and fauna. They encompass both primary aerosols and precursors to secondary aerosols. Among the most widely recognised are pollen and spores; however, a wide variety of other types also exist, such as bacteria, viruses, fragments of organic material, etc. (Pöschl, 2005; Winiwarter et al., 2009). The range of precursor compounds contributing to secondary biogenic aerosols is even more diverse, primarily consisting of volatile organic compounds (VOCs) emitted by vegetation. Despite their diversity, they represent a small fraction of total atmospheric aerosol mass. The main impacts of these aerosols lie in their impact on health, but recent studies also report an impact on cloud formation by acting as *Cloud Condensation Nuclei* (CCN) (Sun and Ariya, 2006).

Biomass burning

Although human activities influence the natural emissions because of their impact on the ecosystem, they are usually not directly tempered with, except for the case of biomass burning. Wildfires can release vasts amounts of fine mode aerosols resulting from the partial combustion of vegetation. Those emissions are predominantly composed of particulate matter with diameters under 1 μm, primarily consisting of black carbon (soot) and organic carbon (carbonaceous

organic compound). The wildfires' phenomenon can also be caused by human activities, either accidentally or as part of agricultural activities, e.g. land preparation (Cook et al., 2007; Urbanski et al., 2011). Nonetheless, anthropogenic biomass burning extends to other activities, for instance, domestic biomass burning which consists in small scale repeated burnings for cooking and heating. Individually negligible, they become an important fraction of anthropogenic biomass burning on a societal scale (Calvo et al., 2013).

Anthropogenic emissions

Anthropogenic emissions primarily originate from the incomplete combustion of organic and inorganic materials (Bond et al., 2013). Among the most significant sources are exhaust emissions, which encompass not only road traffic but also maritime, aviation, and even space transportation, which role is getting an interest with increasing number of nowadays space launches and experiments. These emissions consist of greenhouse and other gases that may serve as precursors to secondary aerosols, as well as ultrafine black carbon particles. Said modes of transportation also produce non-exhaust aerosols from their points of friction like brake wear, tire wear and road surface abrasion, particles emitted then depend on the materials. These non-exhaust aerosols are generally coarse size particles.
Industrial activities are one of the biggest emitters of aerosols and precursors. For example, anthropogenic emissions reach up to 80% of total sulphur emissions in the atmosphere (Calvo et al., 2013). Industrial activities are comprised of several stages (e.g., raw material gathering, transformation, production, transport, energy, etc.) each releasing aerosols or precursors. The industrial aerosol emissions are also believed to be amongst the most impactful in terms of health hazard.

1.1.2 Ageing processes

During their lifetime in the atmosphere, aerosols can undergo various changes called ageing that will influence their structure, composition or size. Figure 1.2 illustrates size regimes and several aerosol physico-chemical transformations. The size and morphology of aerosol can change during these transformations importantly impacting their optical properties. Detection and monitoring of these transformations is however highly challenging task, specially for remote sensing observations (Rudich et al., 2007; Liu et al., 2016; Konovalov et al., 2017; Chaboureau et al., 2022). For instance, evaluation of hygroscopic growth and modification of internal aerosol

structure is practically not addressed in present-day remote sensing algorithms (Si et al., 2021).

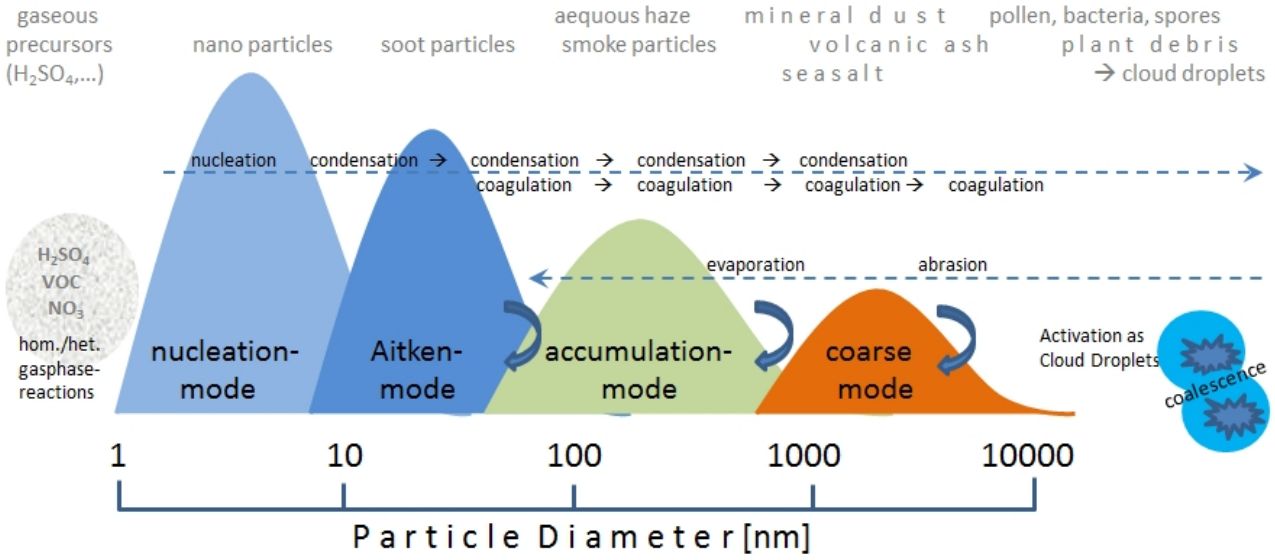

Figure 1.2: Schematic multi-modal particle size distribution with typical transformations and example particle types within each mode. Courtesy of [Deutscher Wetterdienst, Research, Observing the atmosphere, Atmospheric composition, Aerosols, Particle Size-Distribution, Figure 1].

Hygroscopic Growth and Evaporation

Aerosols can serve as condensation nuclei for water vapour, and the condensation process is influenced by both external atmospheric conditions and the intrinsic properties of the particles themselves. External conditions of temperature, pressure and water vapour (relative humidity) must be sufficient to reach the dew point. Dew point is met when relative humidity (RH) is reaching 100%. Mathematically, relative humidity is expressed as : $RH = \frac{P_w}{P_s}$ where P_w is the partial pressure of water and P_s is the saturation pressure of water.Conversely, when RH is below 100%, water tends to evaporate from the particle surface. Internally, the chemical composition and size of aerosol particles are critical determinants of their hygroscopic behaviour. In respect to size, for example, the Ostwald–Freundlich equation describes the P_s over a curved surface (i.e., a droplet or particle of radius R) as:

$$P_s = P_{s0} \cdot \exp\left(\frac{2 \cdot \gamma \cdot V_{atom}}{k_B \cdot T \cdot R}\right) \tag{1.1}$$

where

- P_{s0} is the saturation pressure on a flat surface $(N \cdot m^{-2})$

- γ is the surface tension ($J \cdot m^{-2}$)
- V_{atom} is the atomic volume (m^3)
- k_B is the Boltzmann constant ($J \cdot K^{-1}$)
- T is the absolute temperature (K)

The hygroscopicity of an aerosol is also largely determined by its chemical composition. Highly hygroscopic particles, like solubles, can facilitate condensation and start the process while RH is well below 100%. Marine (e.g., sea-salt), volcanic and industrial sulphate aerosol are soluble and, therefore, more prone to hygroscopic growth. Biomass burning and traffic aerosols are fine particles that can also present a strong hygroscopicity. Dust minerals are, however, coarse particles with generally low hygroscopic properties, e.g., (Petters and Kreidenweis, 2007).

Coagulation and Fragmentation

Aerosols can collide with other particles or compounds which can either break them into smaller fragments - fragmentation, or bind them into a bigger one - coagulation. It should be mentioned here however that for collisions to happen, the aerosol concentration in atmosphere must be sufficiently high. Coagulation of two particles in a defined environment, as described by the Brownian kernel (Jacobson et al., 1994), depends on their diameter, their mean thermal speed (mean speed of particles inside the system), their mass, their mean free path (average length before changing direction because of collision), their Brownian diffusivity (strength of random wiggling of particles due to constant bombardment by gas particles), the temperature and the viscosity of the air. Coagulation appends at a faster rate for pairs of small and large particles because the small particle has a higher velocity while the larger is easier to collide with and to bond with. Marine, volcanic sulphate, industrial, traffic and biomass burning have a higher tendency to coagulate as it is helped by their size and hygroscopicity (Friedlander and Friedlander, 2000; Seinfeld and Pandis, 2016).

Chemical reaction

A chemical reaction can be defined as "a process that results in the interconversion of chemical species", hence, a process in which one or more substances, the reactants, are converted to one or more different substances, the products (Muller, 1994). Gases can undergo chemical transformations that generate aerosols but, also, compounds can react on the surface of aerosols

to alter their properties. One of the main requirements for a chemical reaction, is energy to be able to break and rearrange or create bonds. The atmosphere constitutes a complex system comprised of elements with diverse chemical compositions, into which substantial amounts of energy are continuously introduced, primarily as a result of solar radiation. There are 3 main types of chemical transformation in the atmosphere :

- Photolysis : the decomposition or separation of molecules by the action of the light;
- Homogeneous reaction : reaction in which the reactants are in the same phase;
- Heterogeneous reaction : reaction in which the reactants are in different phases (two or more) or reaction that take place on a catalyst of a different phase (JACOB, 1999).

Homogeneous reactions are primarily happening for gas phase particles with precursors generating aerosols in the accumulation mode. The generated aerosol continues to interact with gas particles, now creating heterogeneous reactions. Other heterogeneous reactions happen on bigger aerosol particles like mineral dust and modify their structure, potentially influencing their hygroscopicity (Laskin et al., 2005). Inside inhomogeneous particles, chemical reactions can happen and modify the internal structure like phase separation and replacement reactions (Cappa et al., 2008).

1.2 Remote sensing of aerosol composition for climate, environmental and air quality studies

Characterisation of the atmospheric aerosol climatic, environmental and health impacts requires the knowledge of aerosol spatio-temporal distribution and composition. Atmospheric chemical transport models can provide this information, however, the models rely on many assumptions and thus the accuracy of evaluations, particularly quantitative, is limited, e.g. (Kinne et al., 2003; Gliß et al., 2021). Remote sensing from satellites and ground networks can provide the observational-based information about aerosol concentrations and properties on global scale, however, is primary sensitive to optical quantities. At the same time, atmospheric aerosol composition, shape, morphology and mixing state affects the light scattering and absorption in a complex way and attribution of specific physico-chemical feature to observed remote sensing signal is a challenging task. In fact, only since recently, the remote sensing instruments and algorithms provide some information about aerosol composition and no one about the aerosol

mixing state or morphology. Therefore, the data from remote sensing do not offer all details required for direct validation of chemical transport models (Eck et al., 2018; Li et al., 2019). Moreover, derivation of the information about aerosol complex refractive index and size distribution from remote sensing sensors is a prerogative of only advanced instruments or complex synergy. In addition, relation of optical quantities to aerosol chemistry and morphology is ambiguous and conversion of aerosol optical characteristics to their chemical components concentration is one of the major sources of uncertainties in models. The same challenge persists for deriving physico-chemical information from remote sensing. The advantage of remote sensing from satellites or ground networks is however in providing the observations of atmospheric properties' dynamics at global scale. At the same time, remote sensing of aerosols relies primarily on detectable aerosol optical properties.The challenge is, thus, in defining these detectable aerosol components and features, which are at the same time close to what is used in models and can be useful for assimilation or tuning of the model.

1.2.1 Aerosols impacts

Atmospheric aerosols strongly affect Earth's radiation balance because they scatter and absorb incoming solar and outgoing terrestrial (thermal) radiation. They also influence cloud formation and precipitation because serve as CCN, can uptake atmospheric water and impact radiation in vicinity of clouds (Twomey, 1977; Rosenfeld et al., 2014). Aerosol can also influence marine ecosystem through deposition of nutrition minerals, and finally air quality and human health because the dry fraction of aerosol settle in human lungs.

The term radiative forcing is employed in respect to the radiative effect due to human intervention, e.g., due to anthropogenic aerosol. The positive aerosol radiative forcing means that the amount of energy contained in the surface-atmosphere system is increasing due to aerosol presence, which is similar to the greenhouse gases effect. The negative aerosol forcing means that aerosol presence increases the Earth's albedo and thus cool the climate.

For several decades, radiative forcing has been studied to estimate the influence of the different atmospheric components on climate. Some gases' influence is known with small margins of uncertainty like carbon dioxide, however, the variety, scarceness and lifetime of aerosols makes it much more challenging to study and, therefore, aerosols remain the major source of uncertainty.

Besides the aforementioned climatic impacts, aerosol are also of height importance for the air quality. For example, in 2015, it was estimated that exposition to $PM_{2.5}$ (Particulate Matter with a diameter of 2.5 µm or smaller) caused nearly 4 million deaths, ranking $PM_{2.5}$ as the fifth-highest mortality risk factor that year. This production of $PM_{2.5}$ in populated areas highly coincides with industrial activities (along with fossil fuel combustion) as heavily industrialised countries like India, Bangladesh and China show increased concentrations while others less industrialised countries show a slight decrease or stabilisation (Cohen et al., 2017).

Aerosol chemical composition can be itself toxic and have impacts on health. For instance, acidic particles (i.e., highly sulphated particles) favorise the dissolution of water-soluble transition metals (e.g., manganese and copper), which, in turns, increases its *Oxidative potential* (OP). For example, as reported by (Fang et al., 2017), "Epidemiological studies have found associations of water-soluble transition metals with health endpoints, such as reductions in birth weight and preterm birth". It worth mentioning in this context that sulphate aerosols, responsible for health hasards, potentially leading to death.

1.2.2 Dry fraction for PM

Particulate Matter (PM) refers to the amount of atmospheric aerosols of a certain diameter and smaller. For instance $PM_{2.5}$ refers to particulate matter smaller or equal to $2.5\mu m$, it is mostly used as an air quality estimation as small pollution particles contribute to health issues. The smaller the particles, the higher the risks; for instance, PM_{10} can penetrate in the lungs and PM_1 are extremely dangerous as they can pass through lung tissue and enter the blood stream, potentially damaging arteries and propagating to different organs (Figure 1.3). Remote sensing plays a role in air quality monitoring with *Size Distribution* (SD) retrieval, providing the volume concentration for different radius sizes. However, this retrieval lacks precision as PM calculations require the dry radius of the aerosols and inhomogeneity is not part of retrieval models, potentially inducing an underestimation in PM estimation. The main reason is that aerosol toxicity is bound to the dry matter interactions with internal tissues and, since particles are considered homogeneous in retrieval algorithm models, they are considered either entirely liquid or entirely solid (Fuzzi et al., 2015; Grant-Jacob and Mills, 2022).

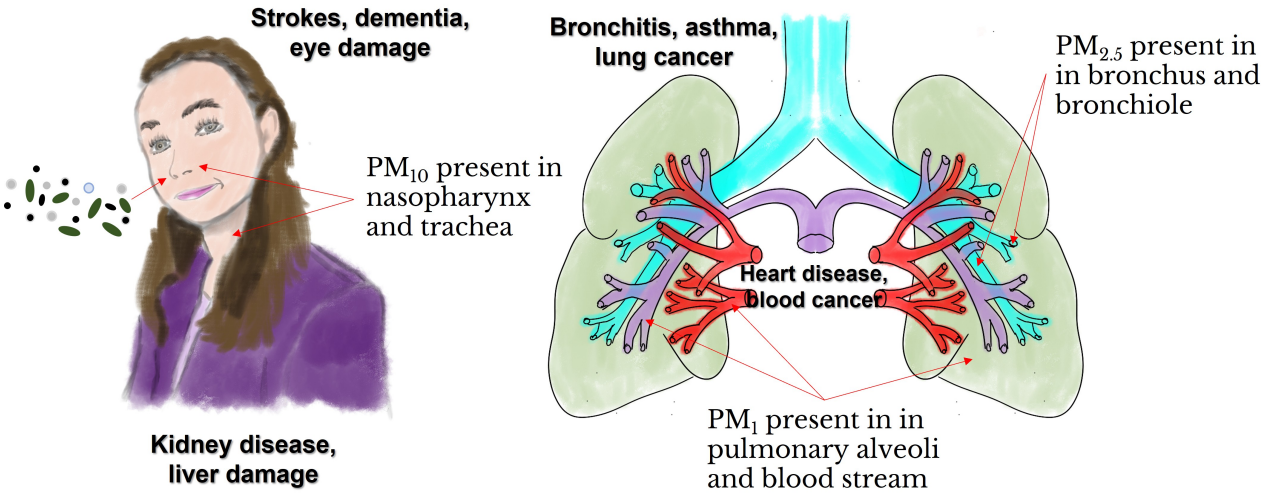

Figure 1.3: Health effects associated with airborne particulate matter pollution.

1.2.3 Modelisation of aerosol properties

Inferring aerosol properties on a global scale is mainly performed by remote sensing, the examples are the network of sunphotometers AERONET, or satellite measurements. The retrieval of aerosol properties from the measured radiances are however requiring parameterisation of aerosol characteristics and assuming a set of aerosol models supposed to represent the real aerosol and reproduce the measured radiation. The inversion procedure, thus, should reconstruct aerosol properties related to aerosol light scattering and absorption from the measured radiances. Aerosol, in the atmosphere, exist in a variety of species, sizes, shapes and mixing states, which need to be accounted for in modelling because it can heavily impact the output, if the measurements have sensitivity to these characteristics.

The selection of aerosol properties parameterisation and models has, therefore, a tradeoff of advantages and inconveniences with factors to be taken into account such as: uniqueness of the solution, accuracy of the radiance representation and the required computational resources. The different aerosol models respond to these criteria by focusing the quality enhancement of a specific part. Hence, different aerosol models account for different degree of details of aerosol properties to better reproduce the reality. Modal size distribution models can represent aerosol size by modes (e.g., coarse, fine or subdivision of coarse and fine) using generally log-normal distributions. Each mode then can have its characteristic like a modal, mean or effective radius, but also a mean composition. The size distribution can be discretised as fine as e.g., 22 bins, the case of *AErosol RObotic NETwork* (AERONET) operational algorithm, or represented by

only a few log-normal bins as in satellite retrievals. The former is due to limited sensitivity of the satellite measurements geometry to aerosol size information. The aerosol complex refractive index can be assumed as the same for all sizes or be resolved by fine and coarse modes. Particle sphericity can also be parameterised by a distribution of spheroid axis ratio, e.g., (Dubovik et al., 2006). Size and composition resolved models are more demanding in terms of measurements sensitivity and computational time, which makes for a challenging application on a global scale.

The detailed information about aerosol composition, size, shape and morphology is however of high importance for aerosol modelling by global chemical transport models. These models employ numerous assumptions on aerosol emission and transport features and need to be adjusted based on measurements. Assimilation of information from measurements can be required not only about concentrations, but also about aerosol composition and morphology. The aerosol properties are highly variable on spacial and temporal scales and may need to be refined because of the complexity associated with initial conditions and the physical processes that take place, like transport, aging and mixing. Harmonisation with observations and the measured data assimilation then becomes necessary to adjust those processes. For example, under some conditions, a coated black carbon particle can absorb more radiation than its uncoated counterpart; a coated dust surface can accelerate its wet removal; coagulated sulfate-organic carbon particles can provide number concentrations for cloud condensation nucleus activation different from those counted separately (Bauer et al., 2013). The worldwide observation networks, like AERONET and satellite measurements are thus supposed to provide such information to improve global aerosol transport modelling, e.g., (Angela Benedetti, 2008).

1.3 Relevant principles of light scattering and remote sensing

This thesis work focuses on introducing the spherical aerosol core/shell model into a remote sensing retrieval algorithm. This section is therefore revising the principles of light scattering by small spherical particles and importance of accounting for aerosol morphology in remote sensing.

1.3.1 Light scattering by spherical particles

The fundamentals of the light scattering by small spherically shaped particle is described by the Mie theory that provides exact solutions for interactions of an electromagnetic wave and a particle, when wavelength and particle radius are of comparable magnitude. Developed by Mie (1908), it provides an analytical solution to Maxwell's equations for the scattering of electromagnetic radiation by homogeneous and isotropic spheres. This theory enables the precise modelling of particle optical properties, such as scattering, absorption, and extinction efficiencies, which constitute fundamental components in remote sensing applications.

The scattering coefficients correspond to the amplitudes of the electric (a_n) and magnetic (b_n) multipole contributions to the scattered field for each order n in the spherical harmonic expansion (Eq. 1.3). By determining these coefficients, one can derive key optical properties such as the scattering, extinction, and absorption cross-sections denoted respectively by C_{sca}, C_{ext} (Eq. 1.2), and $C_{abs} = C_{ext} - C_{sca}$.

$$\begin{aligned} C_{sca} &= \frac{2\pi}{k^2} \sum_{n=1}^{\infty} (2n+1)(\mid a_n \mid^2 + \mid b_n \mid^2), \\ C_{ext} &= \frac{2\pi}{k^2} \sum_{n=1}^{\infty} (2n+1) Re\{a_n + b_n\} \end{aligned} \tag{1.2}$$

$$\begin{aligned} a_n &= \frac{m\psi_n(mx)\psi_n'(x) - \psi_n(x)\psi_n'(mx)}{m\psi_n(mx)\xi_n'(x) - \xi_n(x)\psi_n'(mx)}, \\ b_n &= \frac{\psi_n(mx)\psi_n'(x) - m\psi_n(x)\psi_n'(mx)}{\psi_n(mx)\xi_n'(x) - m\xi_n(x)\psi_n'(mx)} \end{aligned} \tag{1.3}$$

where :

- k^2 is the wave number of the incident electromagnetic wave ($k = \frac{2\pi N}{\lambda}$ with N the refractive index of the medium and λ the wavelength)
- x is the size parameter (kr with r the sphere radius)
- m is the complex refractive index ratio between the particle and the medium
- ψ_n and ξ_n are Riccati-Bessel functions

In order to solve these equations, the required information includes the wavelength of the incident radiation, the complex refractive indices of the medium and the particle and the radius of the particle. Furthermore, from a_n and b_n can be derived the entire scattering matrix (eq. 1.4):

$$\begin{pmatrix} I_s \\ Q_s \\ U_s \\ V_s \end{pmatrix} = \frac{1}{k^2 r^2} \begin{pmatrix} S_{11} & S_{12} & 0 & 0 \\ S_{12} & S_{22} & 0 & 0 \\ 0 & 0 & S_{33} & S_{34} \\ 0 & 0 & -S_{34} & S_{44} \end{pmatrix} \begin{pmatrix} I_i \\ Q_i \\ U_i \\ V_i \end{pmatrix}, \tag{1.4}$$

$$\begin{aligned} S_{11} &= \frac{1}{2}(\mid S_2 \mid^2 + \mid S_1 \mid^2), \qquad S_{12} = \frac{1}{2}(\mid S_2 \mid^2 - \mid S_1 \mid^2), \\ S_{33} &= \frac{1}{2}(S_2^* S_1 + S_2 S_1^*), \qquad S_{34} = \frac{i}{2}(S_1 S_2^* - S_2 S_1^*), \\ S_{22} &= S_{11}, \qquad S_{44} = S_{33}, \end{aligned} \tag{1.5}$$

$$S_1 = \sum_n \frac{2n+1}{n(n+1)}(a_n \pi_n + b_n \tau_n), \qquad S_2 = \sum_n \frac{2n+1}{n(n+1)}(a_n \tau_n + b_n \pi_n), \tag{1.6}$$

$$\begin{aligned} \pi_n &= \frac{2n-1}{n-1}\mu\pi_{n-1} - \frac{n}{n-1}\pi_{n-2}, \\ \tau_n &= n\mu\pi_n - (n+1)\pi_{n-1}, \end{aligned} \tag{1.7}$$

where π_n and τ_n are the functions of angle dependence, $\mu = \cos\theta$, $\pi_0 = 0$ and $\pi_1 = 1$. The purpose of the scattering matrix is to describe the angular behaviour of the scattering properties like the scattering phase function, polarisation, depolarisation, etc. (Craig F. Bohren, 1998a).

Mie theory for layered spheres extends the classical formulation to composite spherical particles composed of two or more concentric layers of different materials. In the specific case of two layers, this configuration corresponds to the Core/Shell model. This adaptation of Mie theory involves a redefinition of the scattering coefficients a_n and b_n to account for the additional

layer structure (Eq. 1.8) (Craig F. Bohren, 1998b):

$$a_n = \frac{\psi_n(y)[\psi'_n(m_2y) - A_n\chi'_n(m_2y)] - m_2\psi'_n(y)[\psi_n(m_2y) - A_n\chi_n(m_2y)]}{\xi_n(y)[\psi'_n(m_2y) - A_n\chi'_n(m_2y)] - m_2\xi'_n(y)[\psi_n(m_2y) - A_n\chi_n(m_2y)]},$$
$$b_n = \frac{m_2\psi_n(y)[\psi'_n(m_2y) - B_n\chi'_n(m_2y)] - \psi'_n(y)[\psi_n(m_2y) - B_n\chi_n(m_2y)]}{m_2\xi_n(y)[\psi'_n(m_2y) - B_n\chi'_n(m_2y)] - \xi'_n(y)[\psi_n(m_2y) - B_n\chi_n(m_2y)]}, \tag{1.8}$$

$$A_n = \frac{m_2\psi_n(m_2x)\psi'_n(m_1x) - m_1\psi'_n(m_2x)\psi_n(m_1x)}{m_2\chi_n(m_2x)\psi'_n(m_1x) - m_1\chi'_n(m_2x)\psi_n(m_1x)},$$
$$B_n = \frac{m_2\psi_n(m_1x)\psi'_n(m_2x) - m_1\psi'_n(m_2x)\psi'_n(m_1x)}{m_2\chi'_n(m_2x)\psi_n(m_1x) - m_1\psi'_n(m_1x)\chi_n(m_2x)}, \tag{1.9}$$

where :

- x is the size parameter of the inner sphere (kr_{inner});
- y is the size parameter of the outer sphere (total sphere; kr_{outer});
- m_1 is the complex refractive index ratio between the core and the coating;
- m_2 is the complex refractive index ratio between the coating and the medium;
- χ_n is another Riccati-Bessel function.

The relative simplicity of these equations is permitted by the sphericity of the particles, however, for non-spherical particles, the scattering properties are much more complex to calculate because of the lack of available simplifications to the resolution of Maxwell's equations. They, then, require more complex numerical tools like the Transition Matrix Method (T-Matrix).

1.3.2 Remote sensing and inversion principles

Atmospheric remote sensing consists in using optical instruments to detect the influence of atmospheric components on light. Remote sensing thus enables to study some of the atmospheric components properties, e.g., particulate matter concentration, particles physical properties, vertical profiling and chemical speciation. Observing systems can be ground-based or satellite-borne with each their advantages and inconveniences. These ground-based instruments can be federated in a network (e.g., AERONET) and networks can, be integrated to a structure

(e.g., *Aerosols, Clouds, and Trace gases Research InfraStructure* (ACTRIS)) that centralises documented data and defines norms of data quality control.

Retrieval algorithms estimate aerosol properties using theoretical models by inferring aerosol parameters to reproduce observed radiation field. The ability to retrieve aerosol parameters depend on numerous factors related to the observations, e.g., number of observations, angles and wavelengths.

Inversion procedures and aerosol parametrisation were modified throughout the years to produce a more accurate depiction of real atmospheric conditions. One of the examples of aerosol model modification, is the addition of aerosol shape representation, which is an expression of aerosol morphological feature. Prior to accounting for non-sphericity, all aerosol particles were considered spherical in remote sensing algorithms; it was deemed as a sufficient approximation of reality given the available measurement configurations and sensitivity. Nevertheless, since non-spherical particles scatter light differently to spherical particles, it generated discrepancies in the directional distribution of radiance and inversion algorithms had to compensate the differences in light scattering with something else in the retrieved parameters. Alternatively, it would increase residual noise in fitting the radiances - a marker for measurement reproduction inaccuracies. For instance, early AERONET inversions could compensate the absence of non-spherical aerosol model by adding an artificial peak in the fine mode of the retrieved SD (Dubovik et al., 2000). Differences in backward scattering between spherical and non-spherical particles could lead to discrepancies during inversion of satellite measurements Mishchenko and Travis (1997) and, especially of *Laser Imaging Detection And Ranging* (LIDAR) which observe aerosol scattered light in backward direction. LIDAR observes its own light emission backscattered to the telescope, extremely close to 180°. By definition, the geometrical configuration of satellite observations locates the light source (sun) behind or to the side of the sensor, meaning observed scattering angles mostly range from about 60° to 180°. Ground-based sun-photometers, are also affected, since they observe from 3.5° up to 160°.

In the case of aerosol non-sphericity, the tradeoff between aerosol model complexity, computational time and effectiveness for the retrievals, was found by introducing a model of randomly oriented spheroids. Indeed, non-spherical particles are highly diverse yet, the integrated nature of the signal and limited sensitivity of the measurements, including due to level of measurements noise, smoothes their scattering properties' details and a simplified model can be sufficient to

effectively reproduce the radiance.

1.4 Aerosol inhomogeneity

For sake of clarity, it should be mentioned here that the term aerosol inhomogeneity can get different meanings in communities of atmospheric chemistry, modelling or remote sensing. In this study, inhomogeneity denotes non-uniform internal structure of atmospheric aerosol particles. Furthermore, it is represented by a simplified model of spherical particles coated by a liquid shell.

1.4.1 Insights from previous studies

Numerous studies have investigated the presence and characterisation of inhomogeneous particles in the atmosphere. The internal structure of aerosol particles has been shown to significantly influence their optical properties (Fuller, 1995). The absorption and scattering characteristics of aerosols are known as depending on the assumed particle mixing state, either external or internal, e.g. (Bond and Bergstrom, 2006). In some aerosol property modelling approaches, internally mixed particles are represented as mixtures of different chemical species, where the complex refractive index of the particle results from the combination of the refractive indices of the individual species. The refractive index of such mixed particles is typically computed using effective medium approximation rules, such as the Maxwell–Garnett or Bruggeman theories, or using simple volume-weighted averaging. Another commonly used representation of particle internal structure is the concentric multilayered particle model, e.g. (Stamnes et al., 1988). Changes in the optical properties of aerosol particles can be investigated using numerical simulations e.g. (Kahnert, 2015; Mishchenko et al., 2014), but the influence of particle microstructure and heterogeneity has also been studied in laboratory experiments, e.g. (Lang-Yona et al., 2010). The radiative impact of particle inhomogeneity has also been assessed using remote sensing observations (Derimian et al., 2017; Li et al., 2013; Schuster et al., 2009). This thesis builds upon the work of Unga et al. (2018), who examined inhomogeneity of in situ sampled particles through two representative case studies: a pollution event in March 2014 in Lille, and a measurement campaign conducted from March to April 2015 and from December 2015 to January 2016 in Mbour (80 km south of Dakar), Senegal. These cases represent two aerosol types: desert dust aerosols and urban aerosols. Electron microscope images of particles sampled during these campaigns show the presence of residual deposits, indicating the presence

on the particles' surface of a liquid film dried during the microscopic observation process. The study provided several important insights. First, 60% of the observed urban particles were inhomogeneous with a liquid shell, compared to 20% for desert particles. This suggests that inhomogeneous aerosols can represent a significant fraction of atmospheric aerosols, even for desert dust in some cases. Furthermore, the dimension of the shell appeared to account for 30% to 50% of the total aerosol radius on average. Observations also showed dependences between the size of the particle core and the fraction of shell, they behaved differently for urban and dust aerosols.

This work underlines that aerosols coated by a liquid shell represent a notable proportion of inhomogeneous particles in the atmosphere and, therefore, worth of attention. The sphericity of the coated cores was also studied, as it is an important factor in the pertinence of the use of Mie theory for layered spheres' employment for the scattering calculations of inhomogeneous particles. Axis ratio, derived from microscopic image analysis, was used as the metric for non-sphericity. The results show that the axis ratio of particles coated by a liquid was persistently shifting towards unit, indicating more spherical shapes relative to uncoated ones. The axis ratio of cores was 1.37±0.30 (± standard deviation) for urban particles and practically the same values (1.31±0.23) for desert dust. This result suggests an overall applicability of sphericity assumption for coated particles and the pertinence of Mie theory. More complex representations, such as coated spheroids, should also be considered in the future, although they will require a substantial increase in computation time.

1.4.2 Reports on implications for remote sensing

The impact of aerosol inhomogeneity on retrievals of aerosol properties from remote sensing were examined in early studies of the sunphotometric measurements inversion by Dubovik et al. (2000). It was done together with the test on impact of aerosol non-sphericity. The non-sphericity was found as producing artificially high concentrations of fine mode aerosols in the employed inversion procedure and, thus, accounted for. Non-spherical aerosol model was realised as of high importance. While the particles' inhomogeneity, represented by core/shell model, was found as substituted by an equivalent complex refractive index. That is, a sort of averaged value between the refractive indices of core and shell was found as good enough to reproduce the measured radiation field. However, the context of (Dubovik et al., 2000) study was limited to a specific core/shell materials and to only fine mode dominated particles because

coarse particles were considered hydrophobic. The size of the shell was fixed, and the shell composition was supposed to be pure water and core was the black carbon. Furthermore, the study of Mishchenko et al. (2016) showed a significant influence of inhomogeneity on remote sensing. Another study, of a case of a smoke plume observations with the NASA Langley High Spectral Resolution Lidar-2 (HSRL-2) (Burton et al., 2015), revealed highly unusual Linear Depolarisation Ratio (LDR) values reaching 0.2 at the 355 nm lidar wavelength. The results that were possible to reproduce by several models of particles inhomogeneity.

The objective of Mishchenko et al. (2016) was to confirm that the observed spectral dependence can be attributed to smoke particles and therefore the ability of *LIDAR Depolarization Ratio* (LDR) to measure and characterise them using T-matrix method to solve the macroscopic Maxwell equations. Calculated LDRs from the measurements at 355 nm, 532 nm and 1064 nm, respectively were 0.203±0.053, 0.093±0.026 and 0.018±0.009, which is highly unusual for a smoke plume and doesn't correspond to dust aerosols either. Pure black-carbon monomers in the atmosphere are present in small quantity and can't be the origin of the measured spectral dependencies. Which means, other morphologies with significant amounts of non-absorbing or weakly absorbing materials had to be examined. Four morphologies were, then, selected and studied. The main outcome of this study was that, to reproduce the observed LDRs, the smoke particles need to contain substantial amounts of non-absorbing, or weakly-absorbing, refractory materials (e.g., water diluted sulphate). The conclusion stated that, although, a range of morphologies was found able to reproduce the observations, they shared specificities essential to the quality of the reproduction; demonstrating the importance of accounting for particles' morphology.

The study of Derimian et al. (2017), the microscopic observations of the core/shell aerosol particles sampled in the Negev desert of Israel were interpreted in terms of variabilities of the phase function and degree of linear polarisation. It was also illustrated that inversion of these properties under single scattering assumption, using homogeneous aerosol model only, could not produce physically acceptable effective refractive indices and even could modify the initially assumed size distribution. The consequent study of Unga et al. (2018) showed that inhomogeneity and aerosol liquid coating is quite common in the atmosphere. The study was based on microscopic observations of particles sampled in urban and desert environments during field campaigns in north of France (urban environment), Senegal and Israel (desert environments) in years 2012 - 2015. Microscopic observations showed that for urban aerosol particles

the mean fraction of shell represented 44%, while for desert dust it represented 32% of the total particle radius.

1.5 Thesis objectives

1.5.1 Scientific question

Aerosol aging during the lifetime in the atmosphere and aerosol water uptake are highly variable in space and time processes . In addition, cloud formation is a complex phenomenon and despite its fundamentals are well documented, gaps are still present, namely in respect to aerosol-cloud interactions. These processes and interactions are largely influenced by aerosol composition and morphology. Aerosol inhomogeneity, as defined in this work, reflects the aerosol water uptake and presumably the aerosol-cloud interactions. Aerosol might prevent or delay cloud formation monopolising water vapour, hence, diminishing relative humidity, or might have radiative effects affecting atmospheric dynamic. Accurate modelling and prediction of these processes require measurement-based information for the models adjusting. In this context, the remote sensing technologies are best suitable for providing solution for global-scale, near-real-time assessments. However, the characteristics related to the aerosol ageing and water uptake are only indirectly deductible from the remote sensing observations.

Systematic monitoring of PM is crucial for the air quality evaluation and human health. The PM categories describe the mass concentration of the particulate matter, while hasardousness of aerosol is related to their size because they can infiltrate living organisms. For instance, PM1 can infiltrate lungs and supposedly trigger illnesses like cancer, or just obstruct cavities. Worth noting that PM considers mostly the dry mass of aerosol and thus detection of the liquid aerosol fraction is important for the PM evaluation by non-conventional techniques such as remote sensing. Viruses and bacteria may need a wet environment to survive. Hence, the transport of inhomogeneous aerosols might play a significant role in virus' and bacteria's airborne transportation, which is another source of health hazard.

Aerosol retrieval revolves around mathematical model algorithms that want to maximise a score based on measurement reproduction (Herrera et al., 2022). The retrieved properties are based on the result of the reproduction. If the model lacks a property, present in reality and absent in the model, the algorithm might compensate this absence with other properties in

the model or the reproduction of the measurement might lack reliability. As inhomogeneity is widely present in the atmosphere, adding this property in the model might help improve others or improve the fidelity to measurements.

Finally, particles structure is expected to change the polarisation state of light (e.g., Mishchenko et al. (2000)), which means differences in degree of linear polarisation for homogeneous versus inhomogeneous particles. These differences might greatly improve sensitivity in the retrieval algorithm for instruments that measure polarisation. Unfortunately, instruments that measure polarisation aren't that common because cost and maintenance purposes. This is why, one of the objectives of this work is to discuss on the cost/benefice of polarisation data for the retrieval of inhomogeneity.

1.5.2 Specific goals

The specific objectives of this research work are :

- to provide solution for detection and monitoring of inhomogeneity based on ground-based sunphotometric measurements of AERONET and to prepare basis for space-borne applications;
- to parameterise aerosol inhomogeneity by core/shell particles structure based on a series of sensitivity studies;
- to integrate new parameterisation into the GRASP remote sensing algorithm, including additional calculations of new kernels;
- to achieve a general improvement of the retrievals by accounting for aerosol microphysics that was not parameterised previously;
- to identify case studies and analyse real conditions where aerosol water uptake and core/shell structure play an important role;
- to create a climatology based on real data processing and document the created datasets;
- finally, because the newly calculated kernels and the obtained climatology present an interest for the community, efforts should be dedicated to an effective way of the data sets communication to the community

1.5.3 Thesis structure

This thesis is structured in 5 parts, as summarised in Figure 1.4. The first one is a sensitivity study under single scattering approximation aiming to determine if a change in particle structure, from homogeneous to inhomogeneous, is differentiable from a change in other properties. This part insures that the future inversions of atmospheric radiances has potential for stable retrievals. The second part is a study of retrievals limitations that could be explained by the presence of inhomogeneous particles and could be improved using the new aerosol model. The third part is the implementation of the model inside the algorithm and the sensitivity test using synthetically created measurements to assess its efficacy. The fourth part is the inversion and analysis of real data; first with problematic data then with global data from multiple locations characterised by various environmental conditions. The final part focuses on possible applications, and discusses the perspectives of the inhomogeneity implementation in remote sensing.

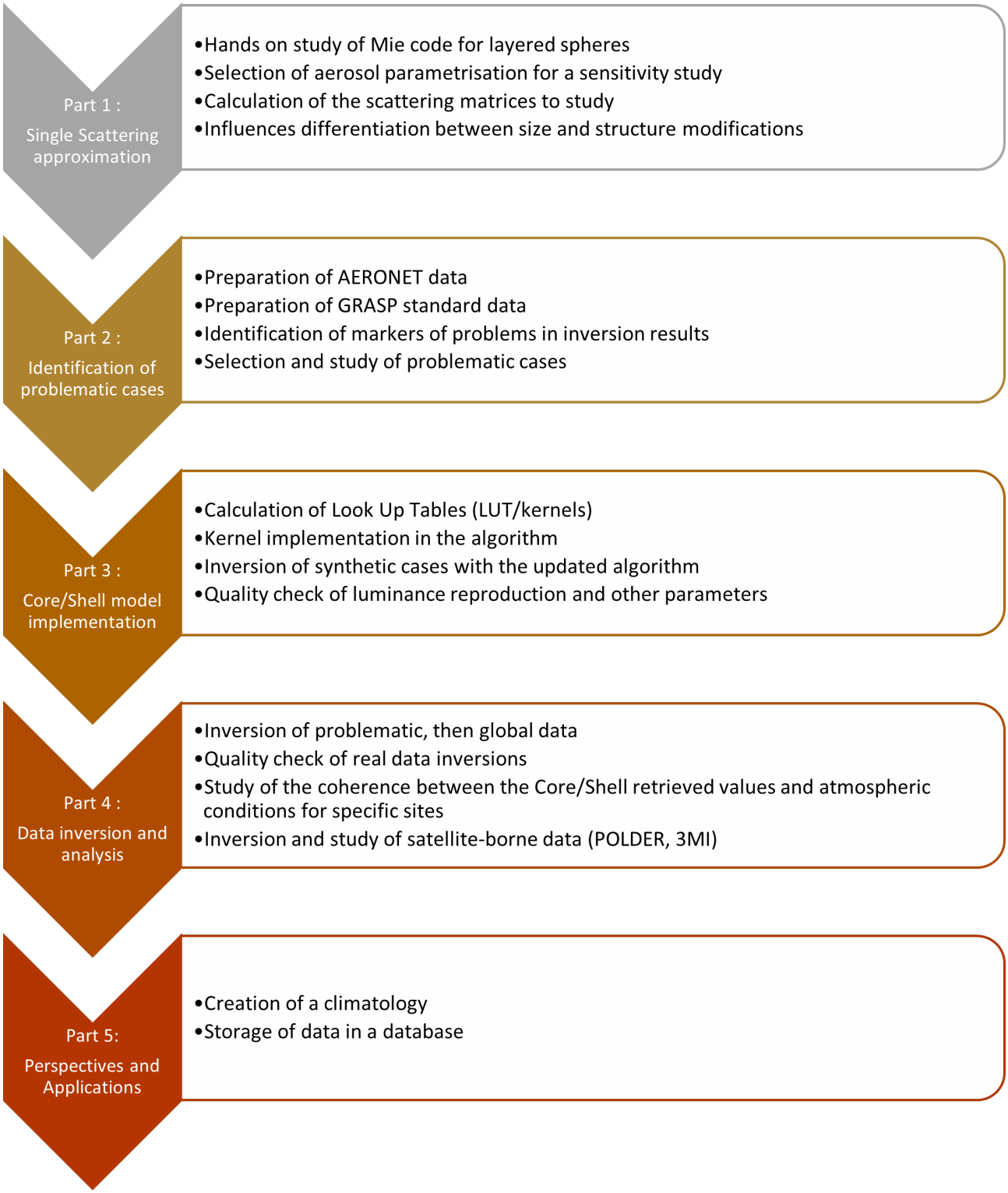

Figure 1.4: General structure of the thesis.

Chapter 2

Algorithmic framework and Working basis

2.1 Core/Shell Model

The chosen model for inhomogeneity is the Core/Shell model with a spherical shaped core surrounded by a liquid shell (Figure 2.1). As discussed in 1.4.2, there can be several models to describe inhomogeneous particles, but, for our purpose, the Core/Shell model was selected as the most appropriate for the first study of the approach feasibility, also considering reasonable computational time. For instance, a simplification also exists for modelling of particles non-sphericity. Indeed, most of the current algorithms model atmospheric aerosol by spherical particles or randomly oriented spheroids to describe the measured radiation field whereas atmospheric aerosol shapes are much more complex. The assumption is that this modelling could, indeed, be improved using, other, more complete models but the reliability and computational cost tradeoff is expected to be

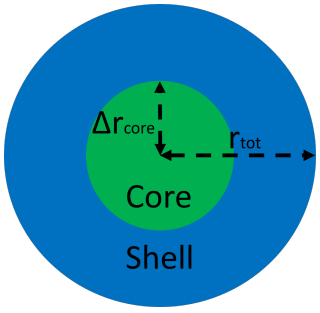

Figure 2.1: Representation of the spherical Core/Shell structure as a particle divided in two parts. The Core part is made of a solid spherical aerosol of any origin. The Shell part is considered as an evenly distributed solution of ammonium sulphate/nitrate on the surface of the core.

sufficiently reasonable for current needs. Moreover, one has
to keep in mind that remote sensing relies on radiation interactions integrated over the entire atmospheric columns or layers containing great amounts of particles whose scattering properties are smoothed out with the integration. The liquid shell has been selected following the scenario of aerosol water uptakes. The work of Unga et al. (2018), for instance, estimated the average liquid shell to correspond to ammonium nitrate/sulphate at 90% humidity with a refractive index of $1.37 + 2.084 \times 10^{-8}i$.

The diversity of particle inhomogeneity (e.g., Figure 2.2) is assumed, in the same fashion

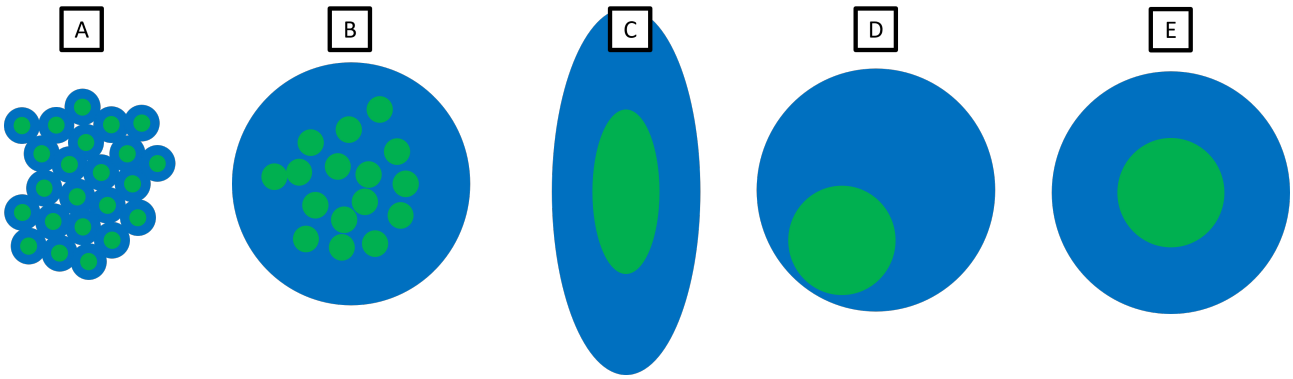

Figure 2.2: Representation of different, non-exhaustive, models of inhomogeneity, e.g.: a) Cluster model; b) Inclusion model; c) Spheroidal Core/Shell model; d) Spherical eccentric Core/Shell model; e) Spherical Core/Shell model.

as particle shape, as averaged out and to be sufficiently well represented by the Core/Shell model. This model is also convenient because, if it is constrained to spheres, it can be described by the Mie theory for layered sphere which allows for fast calculations of the stokes matrix elements. In this theory, scattering coefficients can be calculated with particle total radius, the radius of the core (or its fraction of the total radius), the refractive index of the core and the refractive index of the shell.

2.2 Introduction of inhomogeneity in the GRASP algorithm

2.2.1 GRASP algorithm

Generalized Retrieval of Aerosol and Surface Properties (GRASP) algorithm uses a generalist approach for the retrieval of aerosol properties and land-surface-reflectance from remote sensing.

It allows, with the same algorithm, to process multiple types of remote sensing measurements like sun-photometer, lidar, satellite and their combination. Depending on the measurement configuration, around 50 parameters describing aerosol and surface properties can be inferred as result of optimal estimation. For instance, provided are aerosol size distribution, spectral index of refraction, degree of sphericity and deduced parameters such as *Single Scattering Albedo* (SSA), absorption coefficient, optical thickness etc. The structure of the algorithm is designed to facilitate the addition of other parameters or modules (see Figure 2.3).

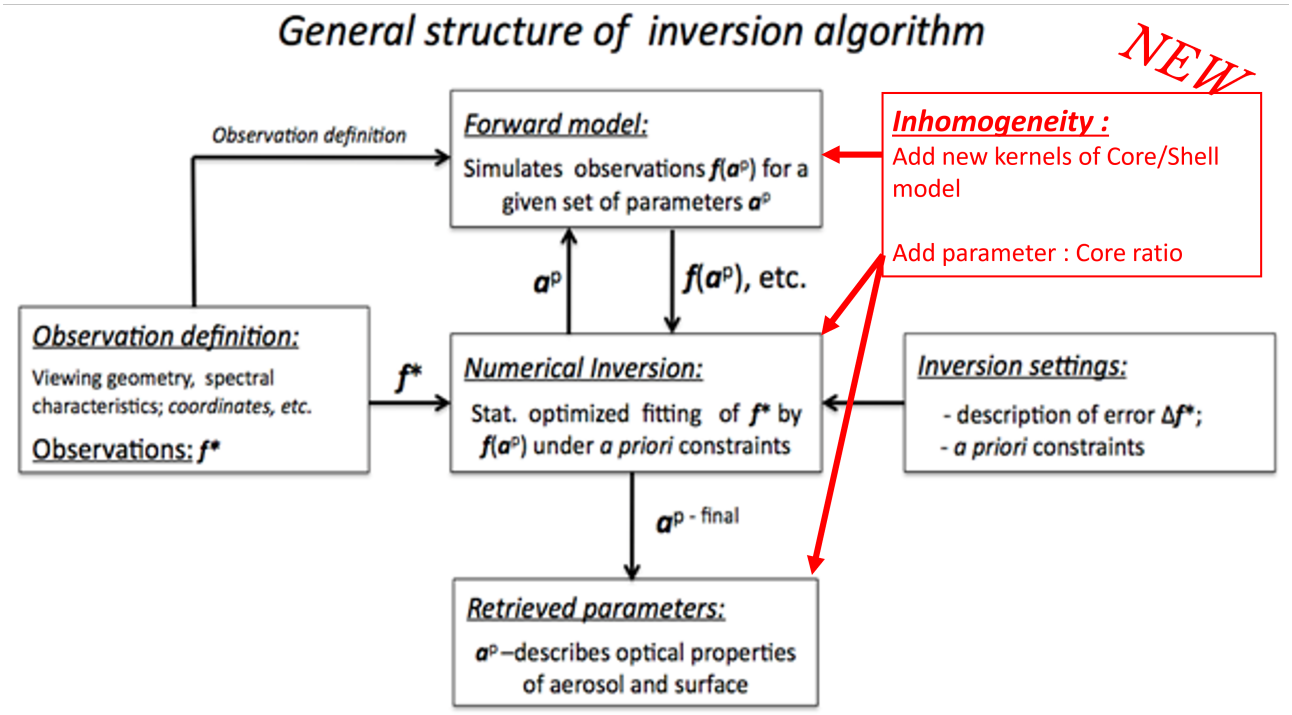

Figure 2.3: General structure of GRASP inversion algorithm.

GRASP is split into two main independent modules. The first module is the numerical inversion based on the Multi-Term *Least Square Method* (LSM). LSM is a mathematical approach used to estimate the parameters of a model by minimizing the sum of the squared differences between observed data and model predictions. The formula is the next: $f^* = f(a) + \Delta f^*$ where f^* is the vector composed by the measurements of physical characteristics, $f(a)$ is the result of the second module (forward model), a is the vector of unknowns representing the parameters to be retrieved and Δf^* is the vector of measurement errors. Because Δf^* is only estimated, the model cannot be a perfect reflection of reality. It will result in having Δa - the vector of errors

of the retrieved parameters. Δa is the term that needs to be minimized. With a non-linear function, the solution can be found iteratively through the process of linearisation following the principles of Taylor expansion, with $a^{P+1} = a^P - \Delta a^P$. As previously mentioned, the inversion uses a purely mathematical approach, which has to be constrained based on previous experimental or physical knowledge. In its basic configuration, inversion techniques apply a single prior covariance matrix, on the contrary, GRASP allows the inclusion of multiple independent constraints as separate terms in the cost function. These constraints influence the algorithm's behaviour aiming for the derivation of physically expected results. For a more precise description of the mathematical theory behind the algorithm, cf. Dubovik et al. (2021).

The second module is a forward model, simulating observations (e.g., radiance, polarisation) using the aerosol parameters given by the first module to compare with the input observation data. It is composed of several semi-independent submodules corresponding to different types of interactions like multiple scattering, aerosol single scattering columnar/volume properties, aerosol vertical profile, surface reflectance and gas absorption calculations. Submodules will interact with one another to simulate the observation, but each module can be changed without affecting the others, meaning that the forward model can evolve with the ever-improving theoretical understanding and techniques of those physical phenomena. Input measurement type will require different submodules: aerosol single scattering columnar/volume properties for Nephelometer, aerosol single scattering columnar/volume properties and aerosol vertical profile for LIDAR , or every module in the case of photometers. Radiative transfer calculation, which also accounts for the effects of multiple scattering, is based on the method described by Lenoble et al. (2007). It allows for the calculation of the radiative transfer from a 1-D vector (the vector "a"), solving it fast and with small errors. Another technique was implemented for the radiative transfer called truncation (Waquet and Herman, 2019); the objective is to separate the forward peak of the phase function from the rest to allow for faster calculation without affecting the accuracy. This truncation can start loosing some accuracy for *Aerosol Optical Depth* (AOD)s exceeding 2.0. This and other approximations can be fiddled with in the settings file to balance computation time and accuracy (described in 2.2.3). A recent addition to the module is the possibility to retrieve the fraction of some of the chemical components of aerosols (Li et al., 2019).

To account for inhomogeneity, changes in both modules need to be implemented, the numerical module was prepared beforehand to focus on the Core/Shell model for the forward model.

2.2.2 Implementation

Implementation of inhomogeneity in GRASP algorithm is made by modifying slightly both modules. For the numerical inversion part, the only modification will be the addition of a new parameter named "SphereCore" referring to Spherical Core Fraction, the fraction of the total particle radius occupied by the Core. This value needs to be added to the first module as a supplementary variable, added as a new value to the vector "a". Then it has to be added as an input variable to the settings so that it can be initialised and constrained (cf. appendix A.1).

Once this value added to the algorithm, change needed to be brought to the forward model part of the algorithm. The idea is that inhomogeneity influences light scattering properties such as scattering, absorption cross-section and elements of the scattering matrix; which are, in the GRASP algorithm, stored in pre-calculated tables named kernels. There are two groups of kernels in the standard version of the GRASP algorithm, one for spherical particles and one for spheroids. The goal is to add new kernels for inhomogeneity to be used in addition to the two previous kernels (Figure 2.4). These new kernels were calculated with a code following Mie theory for layered spheres. The calculations are done for 41 radii (fixed step on a logarithmic scale), which corresponds to triangle bins. Each one is an integration of a spectrum between two points over calculations for 1001 radii.

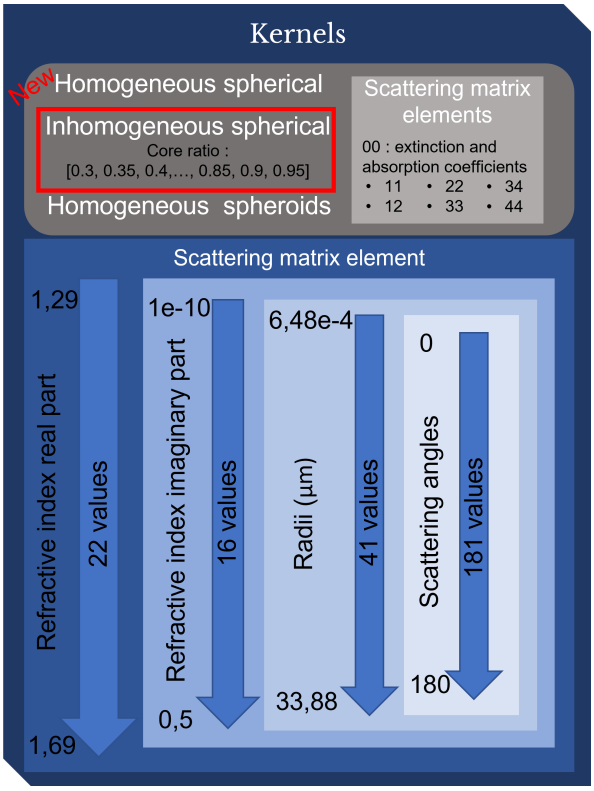

Figure 2.4: Representation of kernel structure top part is the description of the different kernel files, with the particle type and corresponding element of the scattering matrix. The bottom part describes the content of a file except for "00" which does not contain the angular dimensionality.

Primarily, the used code originated from an adaptation of Toon O. B. (1981). Yet, as the

kernels are created through a wide range of refractive indices and radii, calculation was particularly time-consuming not only because of the computational time, but also because, for some parameter combinations, code-based approximations lead to inexplicable scattering values exceeding extinction. In order to overcome this problem, a collaboration was established with the Department of Space Radio Physics, Institute of Radio Astronomy of the Academy of Sciences of Ukraine (Prof. Viktor Tishkovets). The code of prof. V. Tishkovets (link opened in January 2026) was specially revised so that providing the computations in all size and refractive indices' regime. The algorithm was, then, adapted to run this code.

The first step to include kernels inside the algorithm was to read and store them inside a structure holding every kernel. This part was implemented based on the same structure as the original ones. The reading function does not change, yet, one had to be operated in the reading sequence to add a choice in reading the inhomogeneous kernels. This choice is made through the settings file with an optional parameter asking for a list of ratios corresponding to the present kernels (illustrated below).

```
aerosol:
    sphere_core:
        kernels_folder: kernels_sphere_core/
        value:
            mode[1]: [0.9, 0.8, 0.7, 0.65, 0.6, 0.55, 0.5, 0.45, 0.4,
            ↪  0.35]
        use_layered_spheres: true
```

Those kernels are organised in a dedicated folder where file names are composed of four parts with the nomenclature as follows. First, they all begin with "kernels", followed by 1.0000, stating their axis ratio equals 1, which designates spherical particles. The third part of the file name is the ratio of core radius compared to total particle radius, going from 0.2 to 0.95 with a 0.05 step. All the calculated kernels are not used at once during computational process because their complex structure (see Figure 2.4) would require extensive memory usage (each file weighing 35.2 Mo). Note that each kernel is composed of 6 files of the scattering and absorption coefficients and the scattering matrix element, denoted in the last part of the file name as 00, 11, 12, etc. To limit a systematic loading of all the kernels in memory, while running the algorithm, the structure containing the kernels is limited to 10 inhomogeneous and 2 homogeneous ones. In the same optic, when the sphere_core option is not mentioned in the

settings file or when the list of values is empty, inhomogeneous kernels aren't read. When the list of Core/Shell values is provided, the values are compared to the third part of the file names and corresponding kernels are read and loaded.

Once loaded, they are used in the forward model calculations. Original kernels already had a function that, according to the state of the vector "a", would output the corresponding scattering values. The concept was to get the values from the spherical kernel, the ones from the spheroid kernel and, then, weigh each with the sphere fraction. If the option "use_layered_spheres" is set to "true", the function used for the spherical particles changes because, now, the properties are also bound to the core ratio of the vector "a". It should also be clarified that the kernels are calculated for discrete values of the core fraction. In order to ensure the continuity of the solutions and find the value that will fit best the optimal solution, a linear interpolation is performed between the two closest available kernels to the core value.

If an interpolation is needed between core/shell fraction and a case of homogeneous parti-

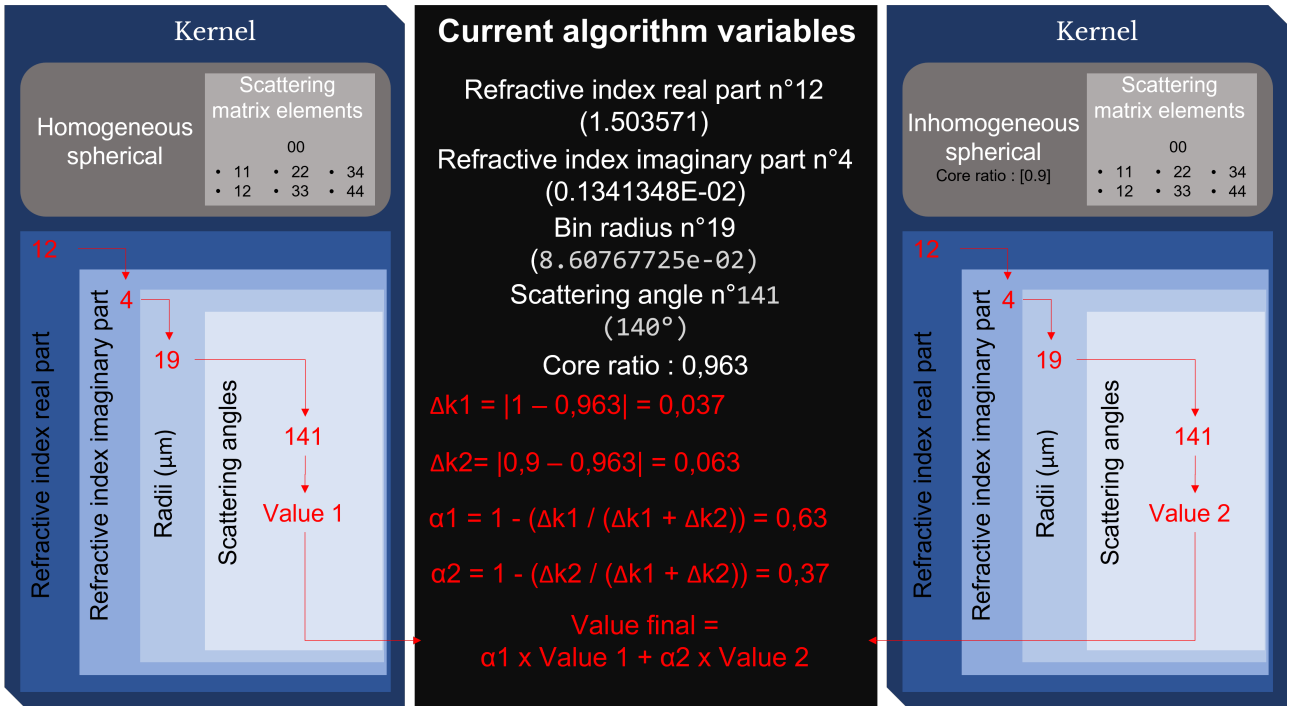

Figure 2.5: Example of scattering properties calculations during inversion. If the loaded kernels are [0.9,0.8,0.7,0.6,0.5] and the core ratio value is 0.963, then the function will select the scattering properties' values according to the refractive index, bin radius and scattering angle from the homogeneous spherical kernel (as it is the equivalent to 1.0 core ratio) and the 0.9 kernel and return the interpolated values.

cle, e.g., core fraction equal 0.99, then the optical characteristics will be interpolated between the highest available inhomogeneous kernel and the homogeneous one. An example of this logistics is illustrated in the Figure 2.5. Available kernels and limits to the core fraction value are set up in the settings file, the likes of which are important constraints to apply to the algorithm as they will, ultimately, influence its behaviour. It is also important to say that this Core/Shell model's implementation is designed to exist as an independent version of the GRASP algorithm and can be combined with other versions of the algorithm. Note that different versions of the algorithm are distinguished by names. For instance, the version of the algorithm called GRASP/Standard, does not involve particular conceptual changes relative to the aerosol model formalisation in the operational retrievals of AERONET. The new version, that incorporates the Core/Shell parametrisation, is named "GRASP/ARIA", standing for "Augmented Retrieval for Inhomogeneous Aerosols".

2.2.3 Settings preparation

The so-called "settings file" contains the formulation of the aerosol model, definition of the inversion parameters, e.g., prior information, initial guess, as well as definition of the measurements noise and other settings defining the use of radiative transfer calculations, and input and output characteristics. Formulation of the aerosol model and inversion constraints have to be properly balanced to ensure that the measured sky radiances and *Total Optical Depth* (TOD) are reproduced more accurately, but also with an optimal quality of the derived aerosol properties. Adding of a new variable, e.g., a parameter describing inhomogeneity requires a special attention because it can destabilise the algorithm. That is, a new parameter can create overfitting or compensate other parameters, the solution can become nonunique, and the initial guess can gain too much importance for the end result and retrieved aerosol properties.

The objective is, thus, to prepare a settings file, while making the tests batches of data, in a way to find a balance between the number of parameters to be retrieved, the constraints applied and the quality of the measurements fit. The description of the elements composing the settings files is available in the appendix A.1.

2.3 Data selection

2.3.1 AERONET and its data

AERONET is a federation of ground-based photometers in a network for atmospheric observation. This network offers extensive global coverage (Figure 2.6) and is well suited for large-scale studies of various aerosol types under different environmental conditions.

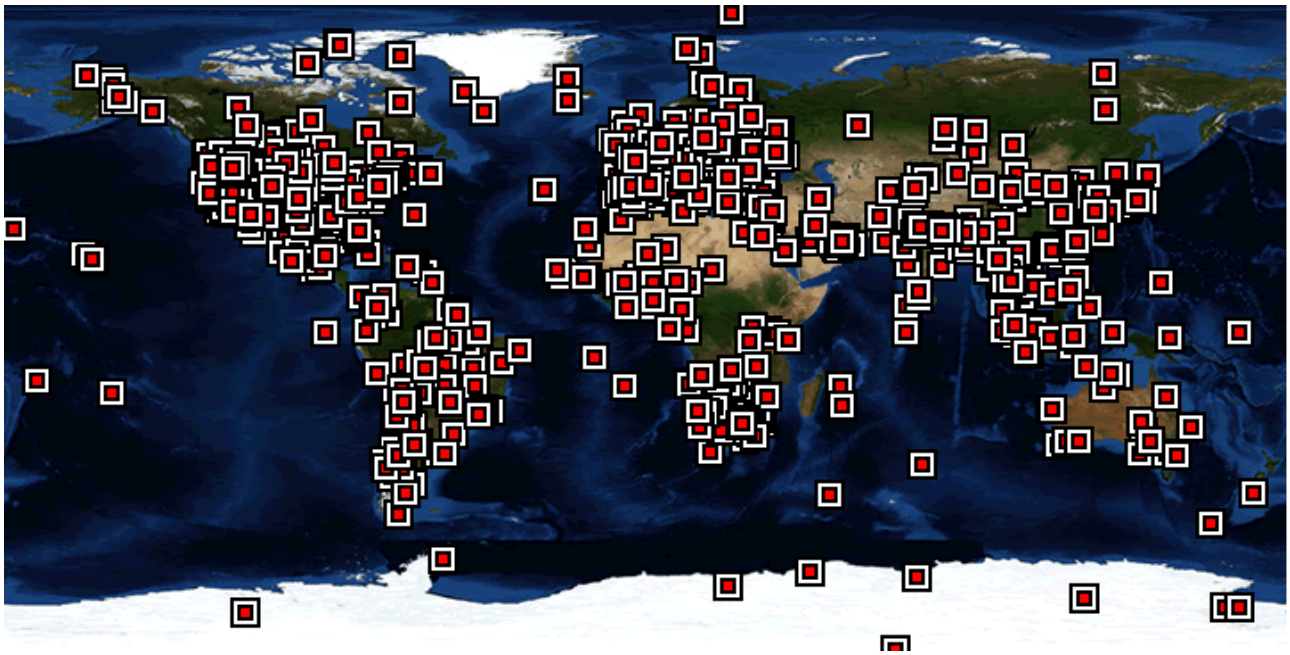

Figure 2.6: Worldwide distribution of AERONET sites.

AERONET photometers observe the transmitted or scattered solar radiance through an atmospheric column at multiple wavelengths and perform three complementary types of measurements. The first type is direct solar measurements; the second, known as the almucantar scan, consists of a series of sky radiance measurements at varying azimuthal angles relative to the sun (26 measurements per wavelength: 13 between 3.5° and 30° and 13 between 35° and 160° taken on the same plane, parallel to the ground); and the third is known as hybrid measurements and is similar to an almucantar except for the fact that the 13 first measurements are taken on an inclined plane intersecting the sun and the addition of a measurement at 180° (Figure 2.7). These multi-angular and multi-spectral observations enable the retrieval of key aerosol properties such as SD, complex refractive index, fraction of spherical particles and calculation of SSA, phase function and other aerosol parameters through the application of an inversion algorithm. Almucantar measurements, are however not sensitive to the vertical variation of the

aerosol concentration profile (Dubovik et al., 2006).

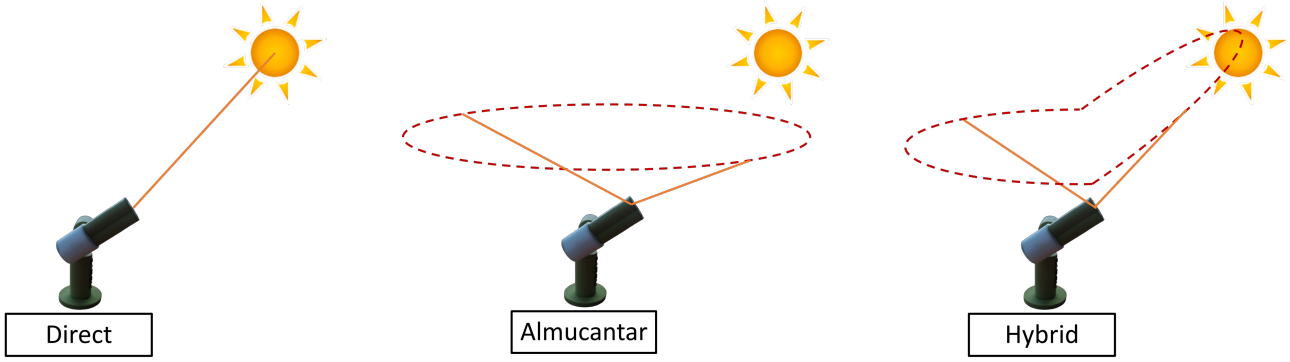

Figure 2.7: Representation of AERONET measurement scenarios. Direct measurements are single measurements, whereas almucantar and hybrid are composed of a series of measurements.

A few sunphotometers with polarimetric measurement capability were recently also deployed within the AERONET network and their measurements have now been added to the pool of available data. There are several levels of data products. Level 1.0 corresponds to raw data, while Level 1.5 indicates that the data have undergone preprocessing steps, primarily involving the filtering of cloud-contaminated or otherwise disturbed measurements. These are the best data available in near-real time. Level 2.0 includes quality-assured data; however, these require the instrument to be returned for calibration and final quality checks, a process that takes additional time (up to several months). In this thesis, the preferred data will be of Level 1.5 because it enables to inverse all available measurements, before some of the data are removed due to high residual of fit or other quality criteria applied to the final product.

The studies in this thesis are conducted using the AERONET real or simulated measurements offering high sensitivity of measurements to aerosol properties. As a ground-based upward looking instrument that avoids strong influence of surface reflectance, it also increases measurement sensitivity to aerosols. Whereas measurements from satellite-borne instruments have the Earth's surface in background and thus require accurate surface reflectance characterisation to be able to effectively distinguish the aerosol signal.

2.3.2 Selection of sites of interest

The first step was to define a group of AERONET sites (Figure 2.8) characterised by different aerosol types, environmental conditions and some preliminary knowledge about aerosol seasonality. As the work of this thesis follows the thesis of Unga et al. (2018) who performed a series of field observations, the sites of Lille, Dakar and Sede Boker were particularly interesting to study and compare the algorithm performance to the results learned during the field campaigns. The other sites are also selected following the category of aerosols encountered most of the time through observations.



Figure 2.8: Mapping of the selected AERONET sites.

The first site is AgiaMarina_Xyliatou, Cyprus, in the eastern Mediterranean area. The typical aerosol composition expected for this site is a mixture of marine, transported (aged) industrial and desert dust aerosols. This site is particularly prone to aerosol liquid coating surrounded by the sea. Similar characteristics are expected on the Barcelona (Spain) site; it has been added to the pool of sites also because it is one of the rare AERONET sites equipped with a photometer with polarimetric measurements. Then, there are Beijing (China), Kanpur (India) and Sede Boker (Israel) with a mix of urban and dust aerosol. These sites are interesting because, of the type of events that may occur. In Beijing, there can be heavy plumes of pollution; in Kanpur, there are seasonal biomass burning events; in Sede Boker, the conditions are ever-changing throughout the year between dust events in spring and mixtures of urban/industrial aerosol under high humidity conditions in summer. After, there are Dunkerque, Lille and Paris which are urban areas with occasional influence of industrial particles. These three sites are at various

distances from the sea, potentially modifying the influence of the sea on aerosol composition and inhomogeneity. The *Goddard Space Flight Center* (GSFC) (USA) site can be added to this group of urban aerosol dominated sites, it is also one of the oldest AERONET reference sites that is now equipped with polar sunphotometers. Finally, Banizoumbou, Dakar and Tamanrasset_IMN are desert aerosol sites where the Dakar site is periodically affected by transport of biomass burning aerosols. Volcanic aerosols are also of particular interest for aerosol inhomogeneity study as they are highly hygroscopic. They are, however, not tied to specific site nor seasonally predictable.

2.4 Data preparation

2.4.1 Creation of GRASP input files for AERONET measurements

GRASP algorithm utilises its own format of data file (.sdata) that needs to be constructed from the original measurements. The, so-called, "sdata" files that are used for AERONET require merging at least 2 or 3 types of measurement. The first one is the optical depth, it can either be TOD or AOD depending on available data. Nonetheless, TOD was the preferred measurement type in this case as GRASP uses its own method to account for gas optical influences. The second type of measurements is the sky radiance which is measured during so-called almucantar measurements; they are a series of measurements at different scattering angles going from 3.5° to 160° on each side of the plane of intersection with the sun. In order to inverse these measurements, the sky radiances must respect quality standards for which the limits of acceptability slightly vary depending on data quality policy. GRASP's data quality policy is generally similar to the one used by AERONET, however the differences may lead disparities in the accepted or rejected data. In order to ensure the data quality, all measurements required for an inversion should be acquired within 15 minutes, arguing that otherwise temporal sky radiance fluctuation can be too strong to consider measurements to occur in the same sky conditions. The policy also states that a certain symmetry in the sky radiance measurements must be respected to consider that the observed atmosphere is representative; the relative difference between measurements of pairs of angles must be smaller than 20% of the mean of the values : $\frac{2\times(|\alpha_{k-}-\alpha_{k+}|)}{\alpha_{k-}+\alpha_{k+}} \leq 0.2$ where α is the measurement value, k is the angle with k- and k+ corresponding to both sides of the plane of intersection with the sun. Subsequent to this condition, the last one is the number of angles remaining; there must remain at least two measurements between 3° and 6°, five between 6° and 25°, four between 30° and 80° and three between 90°

and 180°. Most AERONET measurements are also archived on GRASP servers, and scripts and functions were built to load mersurement files and combine them to generate "sdata" files.

As previously mentioned, the third type of AERONET measurements, that can be added to "sdata" files, corresponding to almucantar measurements of *Degree of Linear Polarization* (DoLP) at scattering angles ranging from 25° to 160° (14th last angles of original almucantar measurements). However, this type of measurements is rare for AERONET, moreover, polarimetric AERONET measurements integration into GRASP input data format required development of a new data preparation process. This is why, for the purpose of the thesis, the treatment of this type of data had to be implemented along with the policy of data quality filtering, for the first time.

2.4.2 Implementation of AERONET degree of polarisation measurements treatment for sdata preparation

This part has been realised using the GRASP's functions developed for AERONET file treatment and with the aim to integrate the implemented functions and quality filtering as part of GRASP's data creation processes. The first task was to understand the file's content to be able to extract the desired information. The structure of both almucantar and polarisation measurements files are sufficiently structurally similar to be able to read polarisation files with the GRASP function "load_aeronet_site", which allowed for a fast understanding of said structure and what parts of the processing chain to adapt. For both files, the first columns describe the conditions of measurements: the AERONET site name, date, time, device number, nominal wavelength, exact wavelength, solar zenith angle, type of measurement, latitude, longitude and elevation. Then come the measurements, which are referenced by their attached scattering angle. The angular radiance measurement of the almucantar corresponds to a single measurement, whereas, for polarised almucantar, it is composed of three measurements corresponding to the orientation of the polariser axis inside the instrument (three polarisers shifted by 60°, i.e. -60°, 0°, 60°). From these three measurements, the DoLP can be calculated using : $DoLP = \frac{2\sqrt{P_1^2+P_2^2+P_3^2-P_1P_2-P_1P_3-P_2P_3}}{P_1+P_2+P_3}$ where P_1, P_2 and P_3 correspond to the measurements at each axis orientation angle (Fedarenka et al., 2016). Basically, the already calculated value of the DoLP is also present in the polarisation data file, and it is this value that will be used for "sdata" file creation.

Two main function utilising almucantar files ("_load_radiances" and "_calculate_angle_averages") needed to be adapted, with a couple of other smaller functions. _load_radiances is meant to gather required elements of the data file in a structure and had to be changed to adapt to the new angle set, and a further modification was made as some of the data collection sites had multiple locations. The choice was made to only keep the data from the location with the most measurements and throw a warning to inform that part of the data will be discarded. This is done because further code does not allow to have multiple locations inside one data file as the information of the location is important when interpreting data (proximity to the sea, elevation, etc.), and usually files are created for single locations. Instead of radiances, it is the DoLP that is kept, however, there is still the need for $\frac{2*(P_1+P_2+P_3)}{3}$ because it is required for measurement symmetry calculations, that also had to be added to the structure. Indeed, Fedarenka et al. (2016) describes that the reconstitution of total sky radiance can be made through the latter formulated equation to allow for the application the same symmetry criterion as the sky radiances one, i.e., the difference in symmetry of the reconstituted radiance should not exceed 20%. The _calculate_angle_averages function then assembles pairs of angles and, therefore, calculates the symmetry between measurements to be able to assess data quality. It should be mentioned that by the time of the work of this thesis, there were no existing, documented, quality criteria for AERONET polarised almucantar measurements. After private communications with the AERONET team, the next considerations were taken into account. The radiance measurements are highly variable which prevents to define a singular absolute value as criteria, whereas the polarisation variability is smaller in absolute but can be considerably high in relative values, as also can be close to zero, rendering the almucantar symmetry criteria selection quite difficult. The solution was, thus, to reconstruct the radiance from the polar measurements as the best option to assess symmetry. As for the number of required angles to inverse, it is considered to be the same as for intensity almucantars for side and backwards scattering, four between 30° and 80° and three between 90° and 180. After all the useful information being gathered, the measurements are filtered and put in a more standardised structure (xarray) to prepare them to b merged with the other measurement types, that would constitute the entirety of the GRASP input (sdata) information.

The last developed function reunites the different measurement types together. There is one last filter here; the different measurement must not be separated for more than a defined amount of time which is set at 15 minutes for regular almucantar plus TOD. However, it can't be the same if adding polarisation measurements as their collection takes around 12 minutes, elevating

it to 17 minutes for both radiance and polarisation almucantars. It was, therefore, decided to set the time constraint to 20 minutes to allow a small operational variability margin without risking the assimilation of the next measurement or a strong change in the sky condition. A function to select matching time periods, comparing two measurement types at a time had to be adapted to handle the third type (polarised almucantar). The devised solution was to use it on exhaustive combinations of measurement type pairs. This function returns the data structure of each measurement type reduced to the parts that respect the collection time constraint.

Chapter 3

Optical properties of core/shell particles under single scattering approximation

The influence of particles structure on optical characteristics should be first studied under single scattering approximation. The rational is that if the optical characteristics related to particles structure are indistinguishable from variability in other properties, like refractive index or change in size, the differences on the level of atmospheric radiances will be even less pronounced due to multiple scattering. The goal of the current study is to determine influence of aerosol coating by a liquid on directional scattering and polarisation properties. Two things are happening when a particle is getting a coating, change of structure, but also of size. Both scenarios are thus analysed in this chapter. These computations are also preparing the creation of lookup tables that may serve retrieval an inhomogeneity parameter using inversion of remote sensing observations.

3.1 Algorithm and Input

The calculations under single scattering approximations were conducted using a GRASP code module allowing to calculate aerosol scattering, absorption coefficients and the elements of full

scattering matrix. The same module is also used for computations of full tables of aerosol characteristics for creation of the kernels. There is a main structure handling input and output, i.e., the characteristics calculation code is connected to the algorithm with bridge functions formatting the data structures to adapt to the chosen calculation code while keeping standardised inputs and outputs (input main ⇒ input bridge ⇒ model ⇒ output bridge ⇒ output main). As referenced earlier, the calculation code used to calculate Core/Shell particle characteristics corresponds to Mie theory for layered spheres, it was written as computer program described in (Toon and Ackerman, 1981), which was integrated in the general GRASP code prior to the work of this thesis. The input files are text files containing information about the characteristics of the aerosols such as SD, scattering angles, wavelengths and refractive indices. In the framework of the thesis, an interface enabling fast modifications of the characteristics and examination of the results was created. Illustration of the interface is in Figure 3.1

First, for the SD, there are the limits' definition with the number of bins and the limits

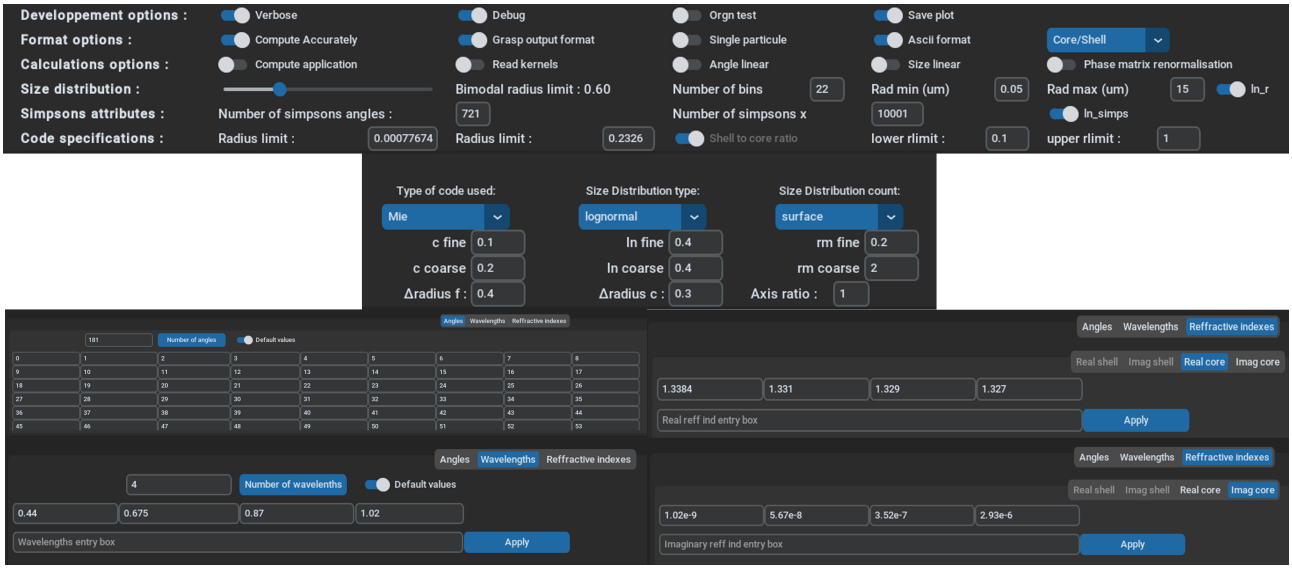

Figure 3.1: Screenshots of a python interface created for the input parameters selection for fast analysis of the calculation results. This interface also generates an input file (.txt) following the format required by the GRASP code.

of radius. "ln_r" defines if the step between each bin is logarithmic. Here, as the purpose is to see if the model is fit for inversion (especially for AERONET data), those specifications are used; meaning there are 22 bins going from 0.05 μm to 15.0 μm with a logarithmic step. Then, there is the description of the SD characteristics of the studied aerosols. In order to put this new study in context of already known aerosol models, the characteristics of the aerosols are

chosen from Table 1. of Dubovik et al. (2002), meaning the SD characteristics correspond to a lognormal distribution defined by a surface concentration c (or C), a standard deviation ln (or σ), and a mean radius rm (or r); each characteristic is defined for both fine and coarse modes.

The scattering angles, as well as the wavelengths, can be precisely defined to perform the calculations. Following the specification for AERONET inversion, there are 181 angles from 0 to 180 with a step of one degree, and four wavelengths : 440 nm, 675 nm, 870 nm and 1020 nm. Furthermore, refractive indices, both real and imaginary part, are considered possibly spectral dependent, hence, are defined for each wavelength. The triangle bins of size distribution are then sub-partitioned (simpsons attributes) to produce calculations at high particle size resolution, the results are then integrated to reconstitute the original bins. During testing, the number of simpsons triangle bins varied between 10001 and 1001. The tests showed that decreasing the resolution would not significantly affect the results but significantly reduce calculation time, which is important for massive computations of kernels.

Finally, there are the characteristics for the Core/Shell model to set. The model allows two ways to define the shell size, either as an absolute value or as a ratio of core to total radius. As previously mentioned, the core to total radius limits can be selected, based on the work of Unga et al. (2018), which describes tendencies derived from microscopic observations of sampled particles. Based on the same work, the size of the shell radius for the current test study was fixed to 30% of total radius.

The code doesn't allow the direct computations for bimodal size distributions, but each mode can be calculated individually and the outputs combined. The combination of the phase matrix elements is made by weighing with the scattering coefficient, i.e., $P_{xx(\theta)} = \frac{P_{xx^f}(\theta) \times C_{sca^f} + P_{xx^c}(\theta) \times C_{sca^c}}{C_{sca^f} + C_{sca^c}}$; while the SSA weighted by the extinction coefficient, i.e., $SSA = \frac{SSA_f \times C_{ext^f} + SSA_c \times C_{ext^c}}{C_{ext^f} + C_{ext^c}}$; the total scattering, absorption and extinction coefficients are the sums of each mode.

3.2 Protocol

The main objective of this study is to define if a change in structure, relative to a change in size, is differentiable through phase function and DoLP behaviours. The absence of differentiation would imply a lack of sensitivity to inhomogeneity in inversion algorithms as inhomogeneity and a change in size could compensate one another. The goal of the analysis presented below

is therefore to perform calculations of phase functions and DoLP for cases in which the aerosol changes only in size, consistent with the appearance of a liquid shell, or in which a change in the internal structure also occurs (core/shell contrast in refractive index).

In this analysis, the shell radius was fixed to 30% of total particle size, while the refractive indices of core and the aerosol size distribution were selected to represent models of urban, biomass burning and desert dust particles, as reported in the AERONET climatology study of Dubovik et al. (2002), see Table 1. Specifically, the urban aerosol parameters correspond to Crete–Paris, France, biomass burning to the Amazonian Forest, Brazil, and desert dust to Cape Verde and Saudi Arabia. The shell refractive index was fixed as described in 2.1.

The distinction between aerosol types is primarily characterised by two factors: the refractive index real part and the dominant mode of the size distribution. Another objective of this analysis is to examine how the refractive index contrast between core and shell influences the ability to differentiate the structural effects from the effects of size. The shell refractive index real part was fixed at 1.37 for all cases. The real refractive index of core was set to 1.40 for urban, to 1.47 for the biomass burning, and to 1.48 and 1.56 for the two desert dust aerosol models. Different values of the imaginary part of the refractive index were tested, all representing relatively weak absorption. However, regardless of whether the values corresponded to the climatological aerosol model or to completely non-absorbing particles, no significant impact on the results was observed. The dominant size modes were therefore the fine and coarse modes, and the aerosol composition was defined by the real part of the refractive index. This design was intended to evaluate the effect of single variations of the aerosol, i.e., size variation or refractive index variation.

For each aerosol type, five computations were conducted, i) two cases of homogeneous particles with a refractive index corresponding to the core; ii) two other cases of homogeneous with a refractive index corresponding to the shell; iii) one corresponding to inhomogeneous particles (Core/Shell model). The case of homogeneous particles with the refractive index of the shell was found to present conclusions similar to the case of the homogeneous particles with refractive index of core, thus those results are not shown in the figures here. For inhomogeneous aerosols, the size distribution is defined by a mean radius "rm", hence, core mean radius is defined as $rm - 0.3rm = 0.7rm$. For the homogeneous aerosols cases, the particle radii corresponded either to the size of the total Core/Shell particle radius (rm), or to the radius of the core (0.7rm),

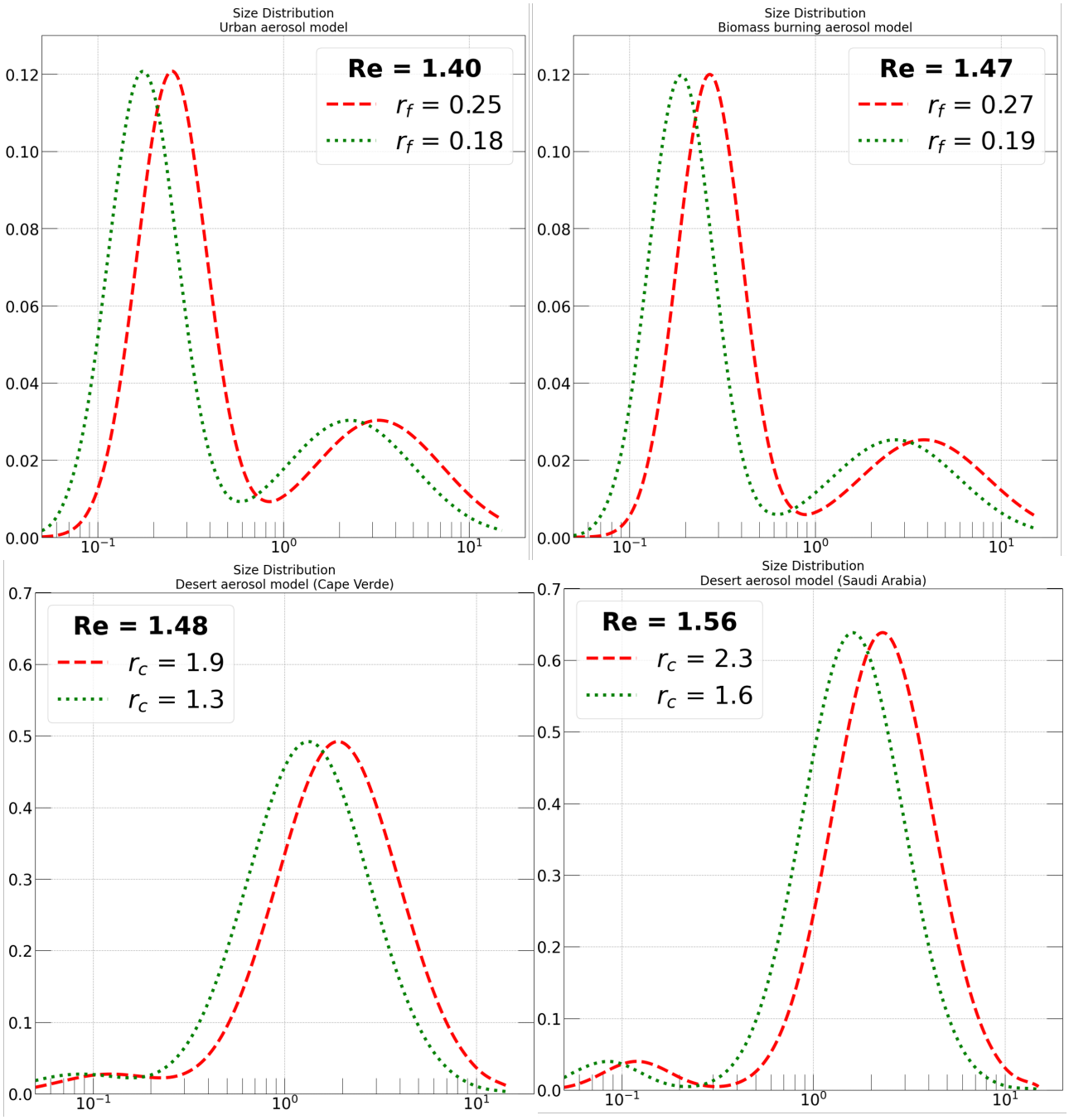

Figure 3.2: Size Distributions for each type of aerosols. Ordinates are the concentrations : $\frac{dV(r)}{dln(r)}$ and abscissas are the radii r (μm). Re is the refractive index real part of the homogeneous aerosol and the core. The radii r_f and r_c are the mean radii of the lognormal distribution of the dominant mode.

as illustrated in Figure 3.2

Once the calculations were completed, the analysis focused on the phase function and DoLP at 440 nm and 1020 nm, corresponding to the two extremes of the AERONET inversion spectral

range. Note also that these wavelengths are comparable to the mean radii of fine and coarse modes of the aerosol size distributions. Finally, three types of figures were made to study the differences.First is the plot of the phase functions and DoLP, that provide an appreciation of the general behaviours. Second, the plot of the change in size : $\mid P_{1x^{homog.}}(rm) - P_{1x^{homog.}}(0.7rm) \mid$ with the change in structure : $\mid P_{1x^{inhomog.}}(rm) - P_{1x^{homog.}}(rm) \mid$, to study directly their difference. Finally, the plot of the angular behaviour of the change in size and structure : $\frac{dP_{1x}}{d\Theta}$.

3.3 Analysis

3.3.1 Particularity of scattering and polarisation for core/shells particles

Information about directional scattering (phase function) and DoLP are used by inversion algorithms to deduce aerosol properties. In the presented analysis, the aerosol properties are predefined and the variability in phase functions and DoLP are calculated and analysed to understand the directional scattering and polarisation behaviour of the core/shell aerosol model in comparison to homogeneous particles. Mie theory for layered spheres is used for the calculations, which was verified to be identical to Mie theory for the homogeneous particle case. It is known that forward scattering (from 0° to 10° - 40° scattering angles) is quite insensitive to aerosol complex refractive index (i.e., chemical composition), however it is sensitive to the particles size, e.g., (Kaufman et al., 1994).

In Figure 3.3 and Figure 3.4, presenting the calculated phase function, it is noticeable that even with two distinct refractive indices, the core/shell and homogeneous particles of the same size exhibit quite a similar behaviour for the forward scattering. It can, therefore, be deduced that the retrieved size distribution should not be affected too much if the inhomogeneity is absent in the aerosol models and, thus, if the measurements are sensitive to inhomogeneity, the size distribution should still be well reproduced.

For fine mode dominated size distributions (Figure 3.3), identically sized core/shell and homogeneous particles are hardly differentiable from one another in terms of phase function in forward scattering angles, except for back and side scattering angles (150° - 180°); for core real refractive index of 1.47. From this information, it can be inferred that the differentiation between inhomogeneous and homogeneous particles is difficult for the shell radius of about 30% in the measurement configuration like the one of AERONET, capturing few measurement angles

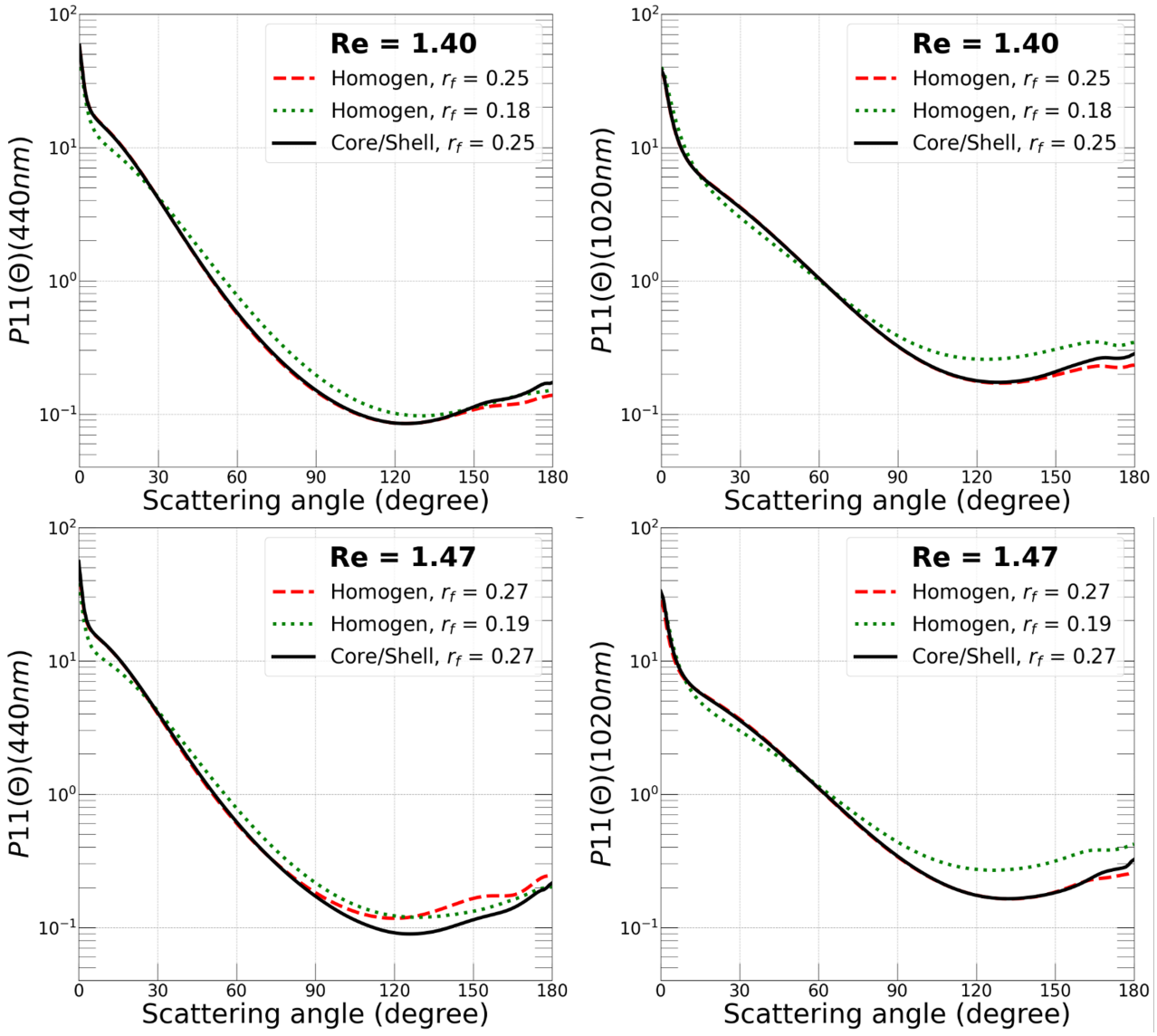

Figure 3.3: Phase function (P_{11}) with refractive indices corresponding to urban and biomass burning aerosol models with a fine mode dominated size distribution as common trait. Wavelength of 440 nm corresponds to the closest available wavelength to particle size and 1020 nm is the opposite, being closer to coarse size distributions.

receiving light scattered at an angle above 150°. However, an interesting observation is that increasing contrast in refractive index between core and shell allows a better differentiation, e.g., at 440 nm. This differentiation weakens with increasing wavelengths, i.e., smaller at 675 nm and almost negligible for 870 and 1020 nm, in this particular case.

For coarse mode dominated size distributions (Figure 3.4), the differentiation is more pronounced at side and back scattering angles. However, at this stage, it is difficult to conclude

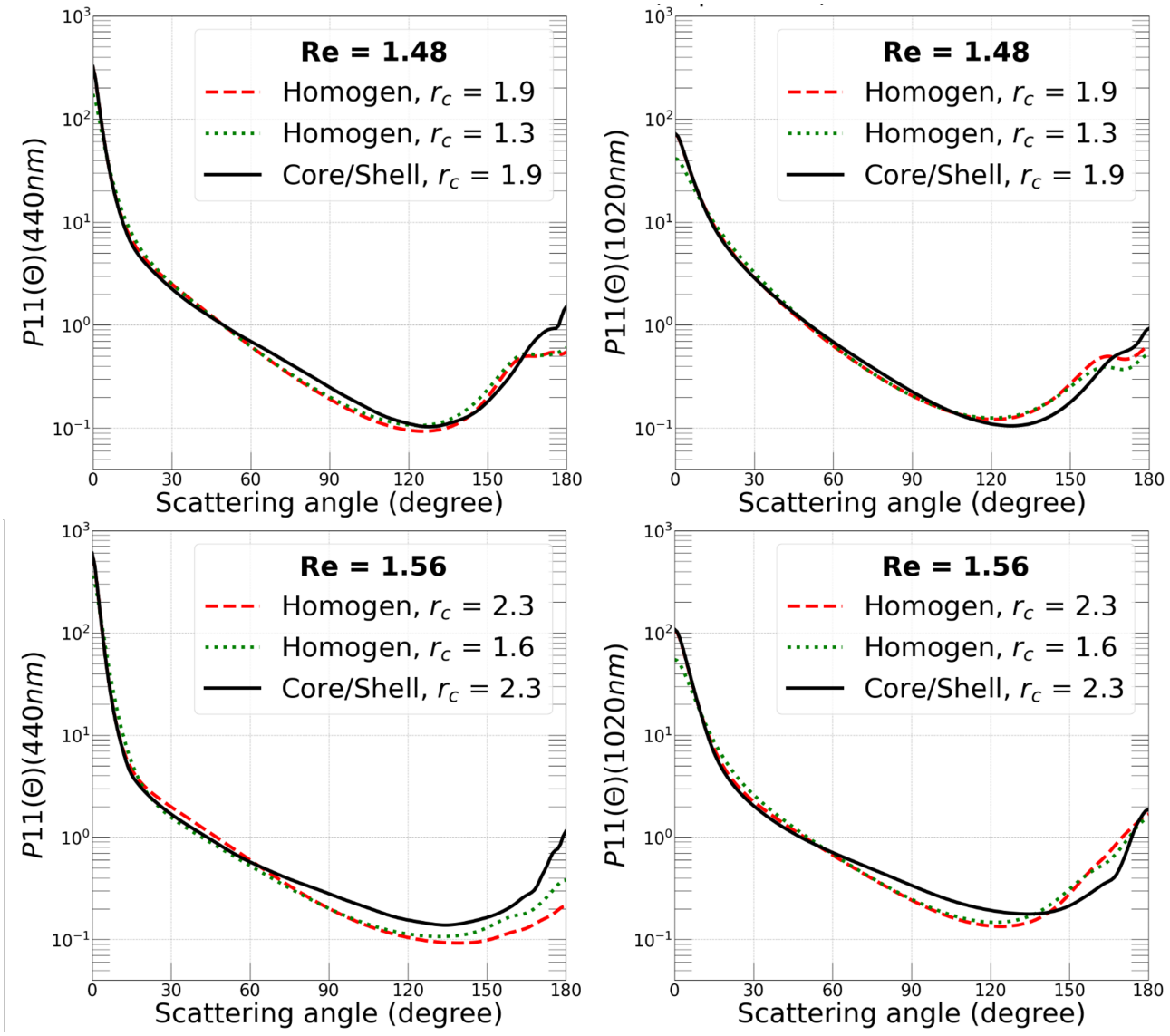

Figure 3.4: Phase function (P_{11}) with refractive indices corresponding to desert dust aerosol models with a coarse dominated size distribution as common trait. Wavelength of 1020 nm corresponds to the closest available wavelength to particle size and 440 nm is the opposite, being closer to fine size distributions.

if the absolute differences are sufficient to have sensitivity to core/shell in remote sensing retrievals. The advantage of having spectral observations is however seen already because the importance of the shell contribution is depending on wavelength. The earlier observation regarding contrast in refractive index is confirmed here, i.e., the case of core real refractive index of 1.56; the difference related to the core/shell model is substantially more pronounced in this case.

Figure 3.5 illustrates the variabilities in the DoLP. The differences between core/shell and homogeneous particles of every size is well seen in practically all cases, except for refractive

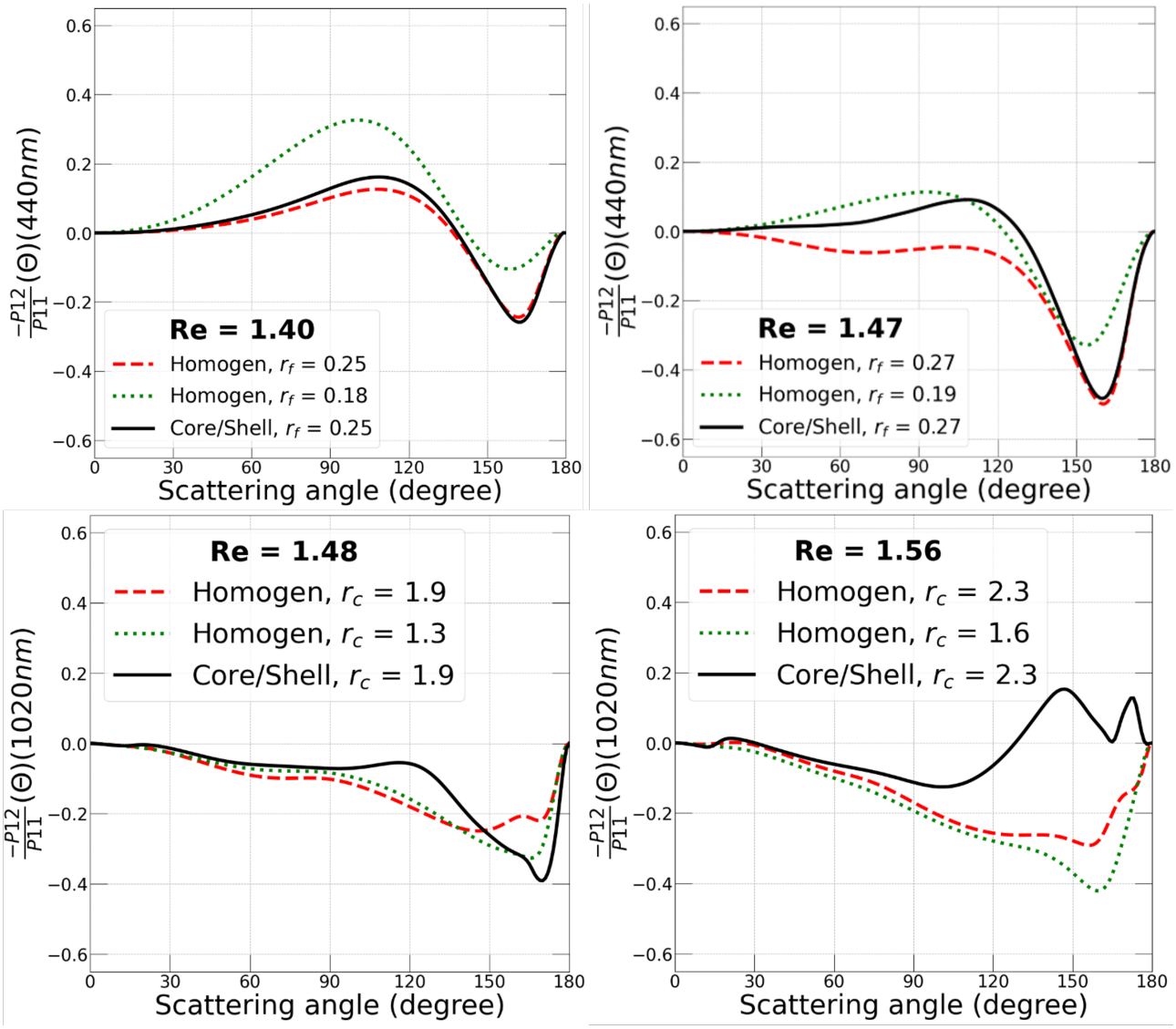

Figure 3.5: DoLP ($\frac{-P_{12}}{P_{11}}$) with refractive indices corresponding to each used aerosol models. The chosen wavelengths are the closest available to the size distribution of the particles.

index of core equal 1.40 (value close to the refractive index of the shell). It can be deduced that the increase in optical contrast between the core and the shell leads to a global increase in differentiability, both in the phase function and in the polarisation. In contrast to the phase function case, the differences in DoLP appear in a very wide range of scattering angles. Additionally, the shift in particle size does not result in any compensation.

The general behaviours of the phase function and DoLP show that the distinction between inhomogeneous and homogeneous particles increases with the contrast, furthermore, particle size also plays a role for the phase function as fine particles are less differentiated than coarse

ones. The better differentiation for the coarse particles is most likely related to the fact that, in relative values, the shell dimension is also more important which play a role for optical properties.

3.3.2 Absolute and angular difference due to change in size vs. structure

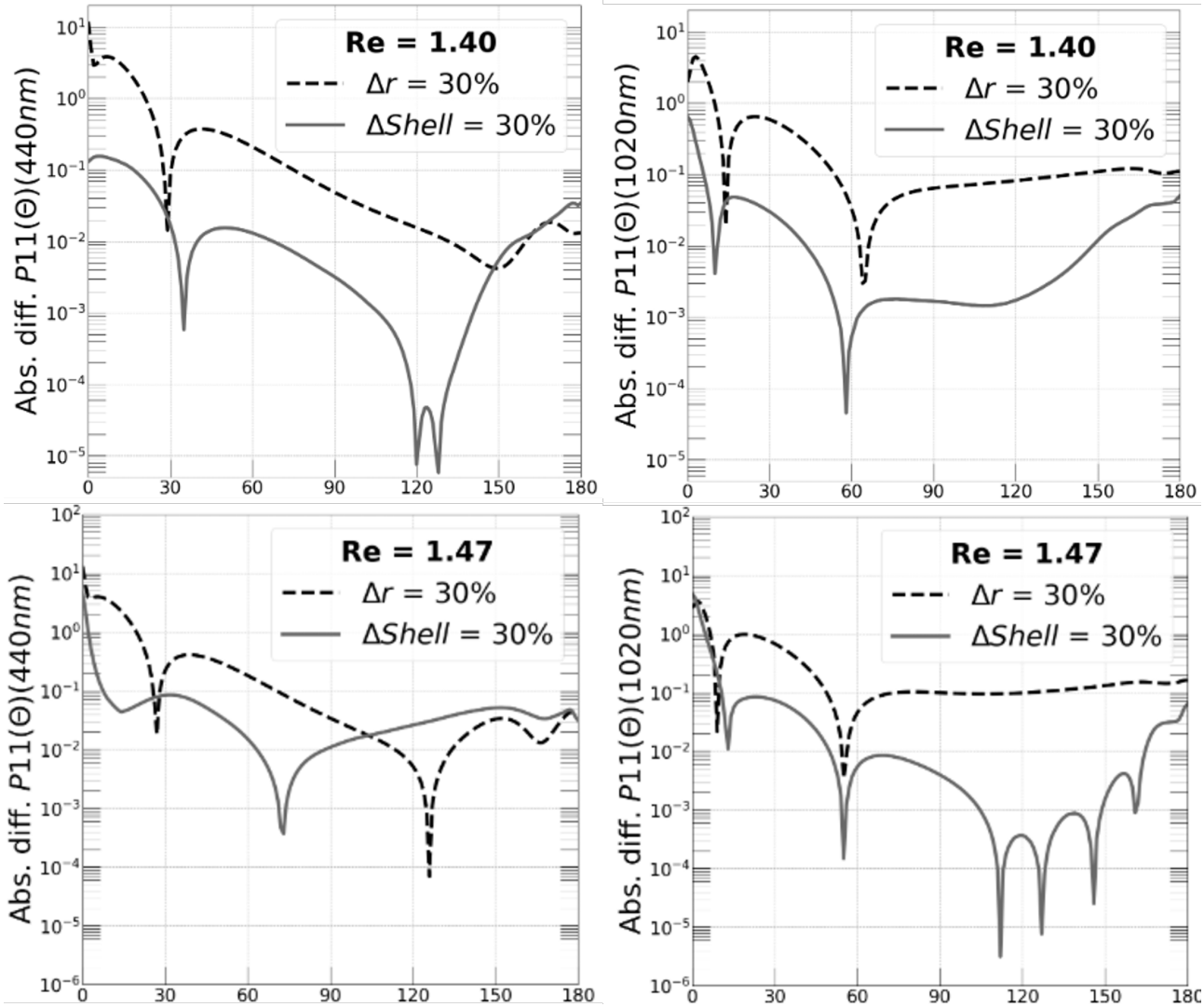

Figure 3.6: Impacts of changes in size and structure on the phase function ($\mid P_{11^{homog.}}(rm) - P_{11^{homog.}}(0.7rm) \mid \Rightarrow \Delta r$ and $\mid P_{11^{inhomog.}}(rm) - P_{11^{homog.}}(rm) \mid \Rightarrow \Delta shell$) at 440 nm and 1020nm. Fine mode dominated size distribution.

This section provides more detailed analysis of the absolute and angular changes attributed to the core/shell particle structure. Figures 3.6 - 3.9 show the differences resulting from adding

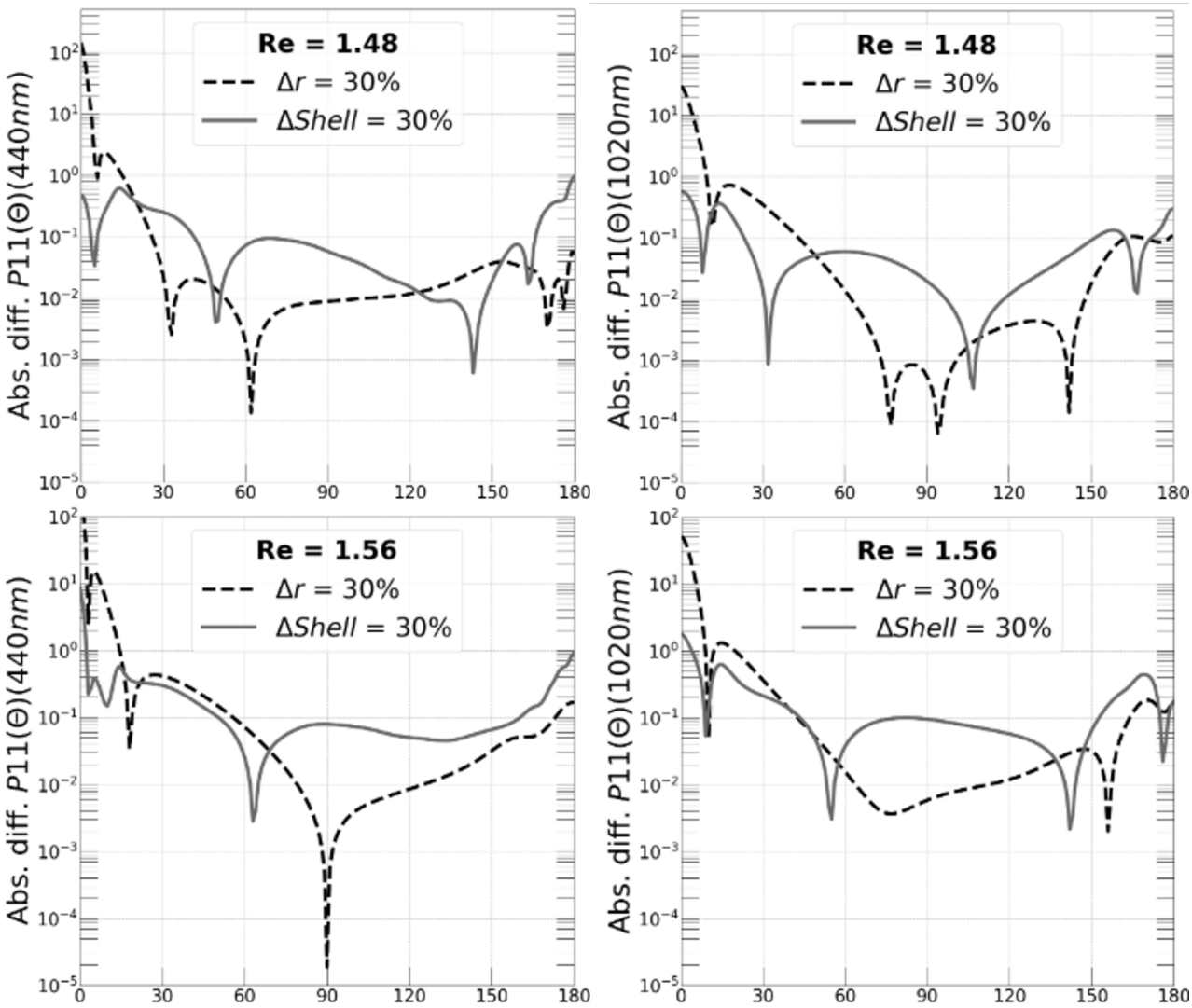

Figure 3.7: Impacts of changes in size and structure on the phase function ($\mid P_{11^{homog.}}(rm) - P_{11^{homog.}}(0.7rm) \mid \Rightarrow \Delta r$ and $\mid P_{11^{inhomog.}}(rm) - P_{11^{homog.}}(rm) \mid \Rightarrow \Delta shell$) at 440 nm and 1020nm. Coarse dominated size distribution.

a liquid shell or from an equivalent increase in particle size. The analysis enables to determine if a simple change in size can mimic particle growth due to appearance of a liquid shell. The angles where the most pronounced changes appear are also of importance given the available instrumentation and the observational geometry. For example, in case the of AERONET, the azimuthal angle of above 150° can be discarded as not achievable in the measurements; the range of possible scattering angles, then, reduced to 3.5°-140°.

Some information can be deducted by intuition from Figures 3.6 and 3.7. First, the presence of peaks in the case of the core/shell structure, which are absent with a simple shift in size. For

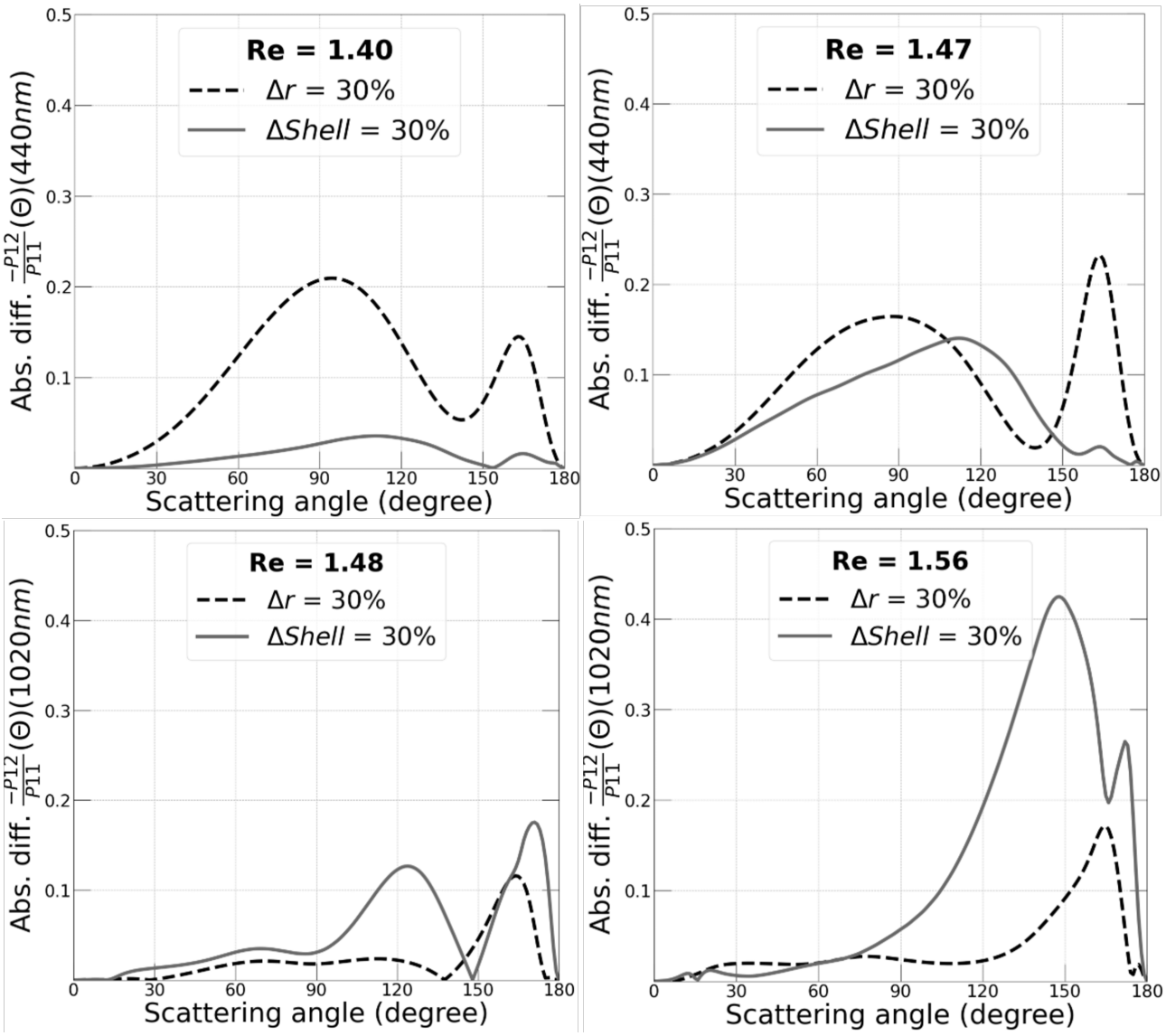

Figure 3.8: Impacts of changes in size and structure on the phase function ($\mid P_{12^{homog.}}(rm) - P_{12^{homog.}}(0.7rm) \mid \Rightarrow \Delta r$ and $\mid P_{12^{inhomog.}}(rm) - P_{12^{homog.}}(rm) \mid \Rightarrow \Delta shell$) at 440 nm and 1020nm.

instance, the peaks around 120° at 440 nm for refractive indices attributed to urban aerosol model particles, or the peaks at the back scattering, attributed to a biomass burning aerosol model at 1020 nm. This could mean that at some specific angles, or set of angles, the interaction of the light with the coated particles can produce quite unique features. Moreover, it can be seen that the shapes of the curbs describing the differences are quite distinguishable. Even if the absolute differences may not appear significant in some cases, the angular dependence is changing, meaning that the uniqueness of the core/shell can still be depicted in the angular measurements of the radiation field. As for the degree of linear polarisation, presented in Figure 3.8, the different behaviours are substantial in absolute value and in angular dependence for

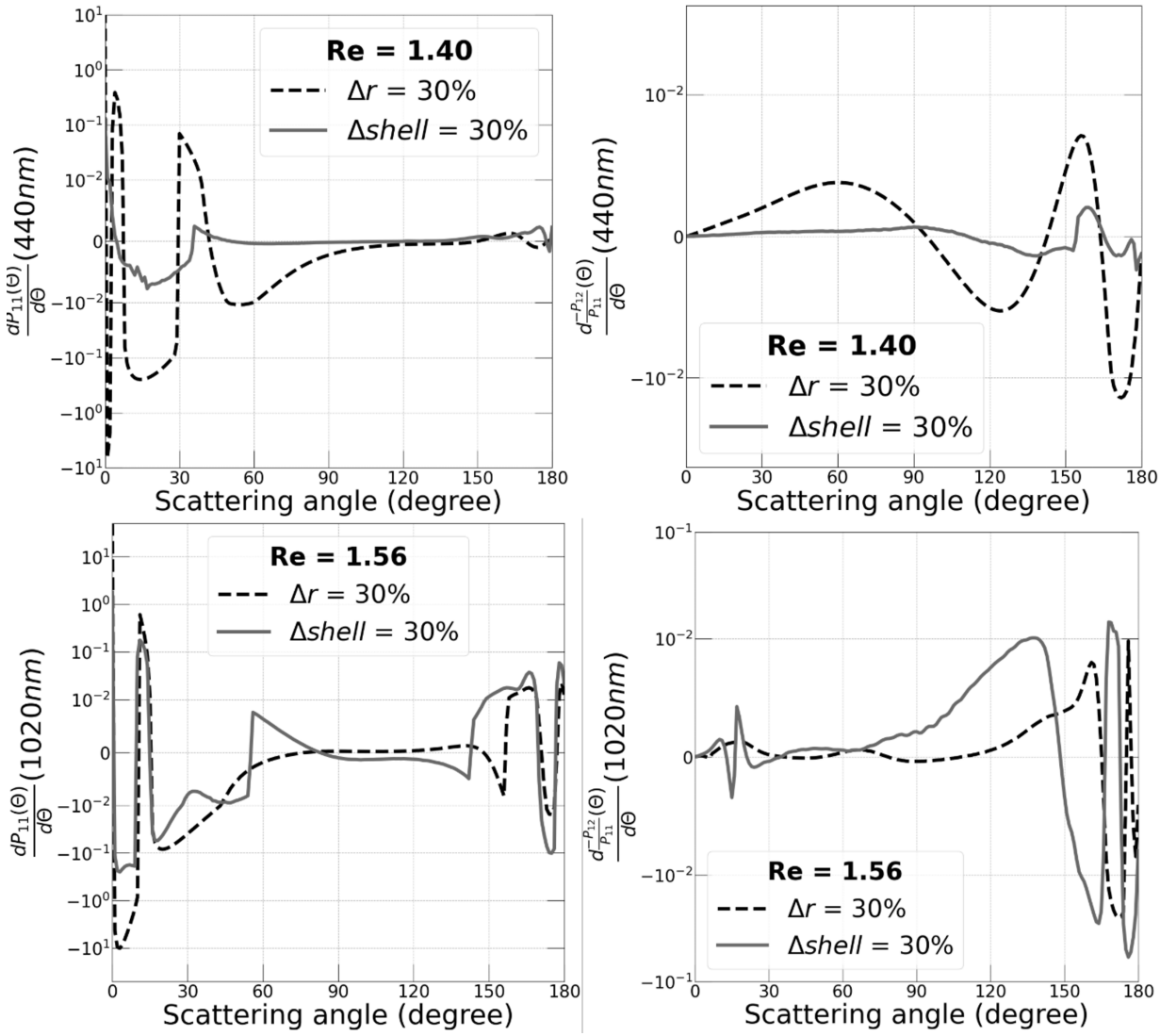

Figure 3.9: Angular variation of impacts of changes in size and structure on the phase function for urban aerosol model represented by fine mode dominated size distribution and desert aerosol model represented by coarse dominated aerosol model.

fine and coarse particles; the peaks appear as even more pronounced.

An emphasis on the angular behaviour is also given by presenting the angular derivatives of the phase function and DoLP, i.e. $\frac{dP_{1x}}{d\Theta}$ (Figure 3.9). The main information that can be extracted from this analysis is that changes in size are smoother than changes in structure. This could complete the earlier remark that the layered nature of the particles would produce further internal interactions with light, which would be reverberated on scattering and be hardly reproducible with changes in size.

The complete set of figures available in the appendix A.2.

3.4 Conclusion

The presented calculations, under the single scattering approximation, show that despite the core/shell particles and homogeneous ones share a similar forward scattering feature, the differences emerge for side and back scattering. These differences dependent on the size of the particles, relative to wavelength, and on the contrast between the refractive indices of the core and the shell. Namely, when the refractive index of core and shell are close and fine mode dominates in the size distribution, the differentiation in scattering and DoLP is small. However, for a core with contrasting refractive index (of 1.56) and a coarse mode dominating the size distribution, the differentiation is more prominent, especially for the DoLP. Therefore, adding a layer of coating changes the size of the particle the same way it would for a homogeneous one, but it changes the structure and can modify side and back scattering in quite a unique way. Even if, the change in structure, in some cases, has effects on scattering that can be similar to the change in size at some scattering angles, the whole angular dependence is still different. The similarity thus may not induce the possibility of a complete equivalence or compensation between inhomogeneity and size. The angular behaviour of scattering and polarisation due to particle structural changes presents rough changes at some angles, while those of size changes are much smoother, adding to the potential of particles structural changes detection by remote sensing. Finally, it should be clarified that for the sake of time and effort saving, this study was reduced to a single size of shell. Consequently, even though no definitive conclusion can be drawn, the results of this study supports further exploration of the topic. Indeed, it is not possible to exclude the possibility of compensations by different aerosol characteristics without conducting the inversion tests that include numerous parameters simultaneously, as well as noise of real measurements. The further efforts are thus dedicated to creation of kernels and their implementation into the GRASP retrieval algorithm that can operate atmospheric radiances measured by different instruments (cf. 2.2.2). The study also enlightened that DoLP seems much more efficient for distinguishing the inhomogeneous particles signal. On that account, an effort will be dedicated to including the polarimetric measurements in further studies.

Chapter 4

Synthetic tests with GRASP/ARIA

Inversion of synthetic measurements is an important step for testing the newly developed algorithm. It consists in simulation of radiances that can be measured by an instrument, assuming an aerosol model and concentration. These simulated (synthetic) radiances are then inverted, with the goal to find the initially assumed aerosol characteristics. Comparison of the obtained and the initially assumed aerosol characteristics serves as a validation and enables tuning of the algorithm. Any non-convergence, overfitting or instability of the results as function of changes in aerosol parameterisation, the initial guess or inversion constrains, will indicate mismatch between the aerosol properties parameterisation and the measurements' sensitivity. The tests also enable to define the regimes of the algorithm applicability. These tests are essential for defining the inversion settings because a new parameterisation of aerosol properties will also change the inversion behaviour. In this study, it adds an extra level of freedom that potentially can disturb the retrieval of all other characteristics. Some constrains might need to be tightened or released that may complicate the convergence of the inversion. This procedure enables studying the new aerosol model applicability, understanding its strengths, weaknesses, overall quality of retrievals and limitations. It is a crucial step to be able to interpret the results of the real data inversions.

The general protocol is to build the tests for a few representative cases by keeping a reasonable amount of computations. In the new configuration, the retrieved parameters are the size distribution, complex refractive index (real and imaginary parts), sphericity fraction and fraction of core radius in total radius of the particle. Defining each of these parameters is

also necessary for synthetic data generation. The size distributions were chosen to have fine and coarse mode dominated cases. The size distributions were chosen to have fine and coarse mode dominated cases. The selected SDs correspond to climatological values obtained for the AERONET sites in GSFC (Greenbelt , easy cost of USA) and Saudi Arabia, taken from Table 1. of Dubovik et al. (2002). Real part of refractive indices is taken to have two different contrasts, the first is the one of GSFC (equal to 1.41) - to keep a low contrast and the second is 1.5 - to have a high contrast. These pairs of elements are the basis for the creation of data files (fine mode, real refractive index of 1.41 and 1.5 and coarse mode, real refractive index of 1.41 and 1.5). The imaginary part of refractive index was left either as minimal or of 0.003, to keep the focus on scattering properties. Each generated data point corresponded to a pair of sphericity fraction and core fraction values. Sphericity fraction values varied from 0.05, which is the algorithmic minimum, to 1 for spherical particles; the variation is linear and, depending on the desired resolution, counted 11 to 41 values. Core fraction values started with a variation from 0.5 to 1 and a step of 0.05. The lower limit of the core fraction was however extended from 0.5 to 0.35 because the retrieval showed sufficient sensitivity to such thickness of shell and further tests on real AERONET measurements showed numerous cases of core fractions reaching the algorithmic limit.

Several tests are realised following the same general protocol for simulated only intensities and for intensities plus polarisation. The test are also conducted under ideal conditions (no measurements noise) and with an added random noise (cf. 2.2.3), i.e. by randomly modifying the input measurements to get a chosen amount of residual with the objective to mimic possible real conditions. When no noise is added, the expected residual of the radiance fit is around 0.25% or 0.5% as a high but still acceptable value, which indicates a good convergence of the gradient descent. The residual of fit above 2%, in case of synthetic data, indicates that the algorithm is actually not able to reproduce sufficiently well the radiances and do not converge properly. These results should not be used to draw any further conclusions. If the added random noise is, e.g. 3%, then the expected residual should be at about the same level of around 3%, while if getting to 5% is considered as high and the fitting above 10% basically indicates no proper convergence and should not be used to draw further conclusions.

4.1 Definition of the initial guess and constrains

The definition and tuning of the inversion settings is the most crucial and time-consuming step. It is the foundation of all inversions as it defines the properties of the settings file that will be used as a unique basis for all measurements during the inversion procedure, whether synthetic or real, and for both aerosol model formulations - "Standard" homoheneous or inhomogeneous. Approach that includes inhomogeneous aerosol model is named here as *Augmented Retrieval for Inhomogeneous Aerosols* (ARIA). Its goal is to set up the constraints to have the best balance between a sensible retrieval of aerosol properties and the best reproduction possible of the input measurement data. The settings file also defines some general properties of the aerosol model such as the definition of the kernels to load and the range of parameters that can be used, for instance, the minimal and maximal values of core fraction, as well as the starting default values (initial guess). The purpose is not to have a settings file that is optimal for all cases, but to have a general working basis for settings files that can later be tweaked when studying specific cases with this model, if needed.

This part is really dependent on the inner specificities of the algorithm, which are extremely complicated to predict and won't return a linear improvement of the retrieval. Furthermore, the time of computation is too long to test a wide variety of parameters through approaches like grid-search. Hence, the chosen approach is the empirical one, focusing on a few cases to inverse then, with a satisfying result, widening to other cases, then testing on real data. This needs to be done for several configurations to settle for the deemed best compromise. To begin the research, the constraints are initialised like in GRASP/standard settings files, as they are already optimised. For the kernels, the work of Unga et al. (2018) defined the minimal observed mean core fraction of 0.5 so, to minimise the number of kernels (and computation time), the loaded kernels were initially defined as [0.5, 0.6, 0.7, 0.8, 0.9] and the range minimum to maximum was set from 0.5 to 1 with an initial guess of 0.5.

After conclusive tests on synthetic measurements, the first results from tests on real measurements indicated that the minimal limit of core fraction should be extended, hence, new kernels were calculated and added. The kernels were calculated up to core fraction of 0.2, but tests revealed sensitivity only up to 0.35. Furthermore, the parameter "scale_for_finite_difference", defining the modification of the variables from vector "a" between each Q iteration, is not big enough to allow the core fraction to skim through the full range of available core fractions.

Hence, to guarantee the possibility of the algorithm to attain the value of smallest residual noise, the data is inverted two times, one for initial guess of 0.5 (covering range 0.35-0.75) and 0.9 (covering range 0.65-1).
Then, constraints on size distribution were slightly tightened with raising the Lagrange multiplier from 0.01 to 0.05 with the addition of a priori estimates constraining bins individually. It was also accompanied by a tuning of initial guesses in the same fashion as for operational AERONET inversions : $Conc_{bin} = \frac{AOD(440nm)}{200}$ divided once more by 100 for bin 1 and 22.One of the encountered problems was that, in about 2.5% of cases, the extremities of the size distribution (bins 1 and 22) showed artificial peaks. Though, even with those constraints, peaks continue to happen at a lesser rate. The problem originates from the lack of information given by the measurements for those two bins, allowing to compensate other optical properties. It is usually fixed through constraints put on the edges, however, GRASP/ARIA manifests major difficulties to converge toward a solution if the constraints are too harsh and the applied constraints could only fix the problem partially. The final decision was to simply discard from the final product the remaining problematic data points exhibiting this behaviour.
A bimodal (fine and coarse) size distribution corresponding to the climatology from the Lanai AERONET site has been added because of an overwhelming presence of bimodal distributions in real measurements.

4.2 Approach and results analysis

Results of the synthetic data tests are summarised in this chapter by a series of figures (cf. figures 4.1 to 4.13) with the structure described below. The figures are composed of panels corresponding to ensembles of graphs describing the assumed and retrieved microphysical and optical characteristics. The data from a panel is generated with two variables (core fraction and sphere fraction) simulating exhaustive combinations from selected values. The calculation of radiances is based on the precomputed kernels, which are covering spherical and spheroidal shapes, and, the homogeneous and inhomogeneous structures, which is the new element introduced by this work. As it was illustrated in the previous section, the inhomogeneity can produce differences in backward and side scattering, which can mimic the effect of non-sphericity. In this context, it is therefore, important to vary the sphere fraction along with the core fraction to be able to test the sensitivity of the algorithm. The analysis presented in the figure thus focuses on the interplay between the inhomogeneity and non-sphericity, in addition to the retrievals of complex refractive index, size distribution and single scattering albedo.

- The first two graphs of the panels describe the quality of the core fraction and sphericity retrievals. The diagonal line in these figures is the one-to-one line marking of a perfect match between the assumed and retrieved values, the further away from the line the dots are, the worst the quality of the retrieval is for this characteristic. R^2 is the coefficient of determination, relating the proportion of variation between retrieved and assumed data, that indicates overall quality of the retrieval. Values closer to 1 indicate a good agreement between assumed and retrieved. Negative values, including values exceeding unity, indicate that retrieved data give a worse agreement with assumed data than fixing the value to the mean of possible results.

- The third graph is the difference between the retrieved and assumed core fraction as function of the retrieved sphere fraction. The purpose of this graph is to study the dependency of the core fraction retrieval on the retrieved fraction of sphericity. Note also that the analysis and interpretations should take into account the relative proportion of spherical and nonspherical particles because only spherical particles can be inhomogeneous in the presented formulation of the retrieval. The main concern is a decreasing sensitivity along with the sphericity.

- The fourth graph is the residual in fitting the radiances as function of core fraction. The rational of this graph is to check the quality of the radiances reproducing over a range of the core fraction values, which is the new parameter. It is of importance because quality of reconstruction of the radiation field is a principal marker of the retrieval quality. In synthetic data, the appropriate residual depends on the added noise; if there is no added noise the optimal residual is around 0.2%, if 3% noise is added, then, residuals should be between 2% and 5%.

- The fifth and sixth graphs describe, respectively, the spectral real part and imaginary part of the refractive index. The assumed values are invariant, while the retrieved are described by their mean and standard deviation. The figure provides intercomparison of absolute values, but also of the spectral dependence; both are expected to be similar.

- The seventh graph is the size distribution, presenting volume concentrations per radius bin. Similarly to refractive indices, the assumed value is invariant, while the retrieved values are presented by a mean and standard deviation. The shape of the size distribution curb and the peaks are in the focus of the analysis in this case.

- The eighth graph is the spectral SSA, which is a ratio of scattering to total optical thickness calculated with the retrieved refractive index and size distribution (cf. equation 1.2). The figure indicates how the effectiveness of scattering (or absorption) in total extinction can fluctuate due to the retrieval uncertainty in case of introducing inhomogeneity. For instance, in the operational AERONET retrievals, the SSA error is evaluated as ± 0.3.

4.3 Inversion of inhomogeneous aerosol signal with a homogeneous model

Objective and protocol

The objective of this part is to understand the impact aerosol inhomogeneity might have on inversions performed with an only homogeneous aerosol model. The logic is to simulate radiances with the inhomogeneous aerosol model, but to invert them with a "standard" approach, i.e., an only homogeneous model. The term "standard" is used here in the sense of applying the same aerosol model formulation as done in operational AERONET retrievals. GRASP/Standard is the closest version of GRASP to the AERONET operational algorithm in terms of aerosol model formulation and all the retrieved parameters are identical. This step helps to understand the state of the current AERONET retrievals in case of inhomogeneous aerosol and identify if shortcomings exist, and if improvement can be done using a new model. The methodology is, thus, to generate synthetic measurements (the "sdata" files) using the GRASP/ARIA formulation of aerosol inhomogeneity with the purpose to inverse these synthetic radiances with GRASP/Standard approach. Then, to compare the input to output aerosol optical characteristic and observe emerging patterns, if any. The results of this study are illustrated in Figures 4.1, 4.2 and 4.3, each corresponds to a different type of size distribution : fine, coarse and bimodal, respectively. All the figures present inversion of the synthetic data with added random noise, mimicking real measurements.

Analysis

It should be said from the beginning that the figures that involve the assumed and retrieved fraction of particle core are not for the purpose of the core fractions intercomparison, because the core fraction is not retrieved with GRASP/Standard, but to get an idea about the influence of absence of inhomogeneity on fit residuals and other parameters. It is also important to recall

that the results of GRASP/ARIA add inhomogeneity only for the fraction of spherical particles.

Figure 4.1 in general shows that in case of fine mode dominated size distribution, the retrieved sphericity fraction is strongly dispersed and overestimated, no matter the fraction of the core or the refractive index. It indeed indicates generally known lack of sensitivity to non-sphericity in case of small particles, but also that presence of particles inhomogeneity signal perturbs the retrieval. The measurements simulated in this case do not contain information about polarisation (see upper panels of the figure). More specifically, the second graph in panels a), b) suggest an overestimation of the retrieved sphericity fraction, with an increasing tendency as the contrast between refractive index of core and shell increases; that is, the inhomogeneity signal becomes stronger. The third graph in the panels basically show how different the core fraction is from the homogeneous particle case and what is the most frequent retrieved sphericity fraction (see density of points). To understand this figure, it should be mentioned that originally, during simulation of input radiances, the number of points is equal for all sphericities and core fractions. Thus, any tendency in point density indicates a bias in retrieved sphericity as function of deviation from aerosol homogeneity. The figure shows that large non-sphericity is generally omitted.

The residual of radiance fit, however, does not seem to depend on the core fraction (fourth graph). That basically can mean that the inhomogeneity can be compensated by putting more spherical particles. Indeed, this regime of fine mode dominated particles is generally less favourable for retrieval of non-sphericity. At the same time, the residual demonstrates a slight increase when the refractive index of core evolves from 1.41 to 1.50, suggesting that some sensitivity exists even in this regime of small particles and without measured polarisation. The SSA and imaginary refractive index are generally well reproduced, while real part seems to be underestimated. There is however one aspect to consider, that is, the assumed refractive index is of the particle core, while the retrieved one is an effective refractive index, as the shell is absent. It means that, by default, the retrieved effective refractive index should be lower than one of particles core (recall that shell is liquid ammonium nitrate/sulphate).Taking the example of a refractive index of n=1.5 and k=0.003 and since the shell has n=1.37 and k=$2.048e^{-8}$, it is, therefore, expected for an effective refractive index to be between those two values. Even so, the mean retrieved real part is below 1.37, hence, is too low even for an effective refractive index in case of low contrast between the core and shell (first group of graphs). The values however look better when the contrast increases. In addition, slight discrepancies appear in SD, i.e. an increase in fine particles concentration and a shift in coarse mode.

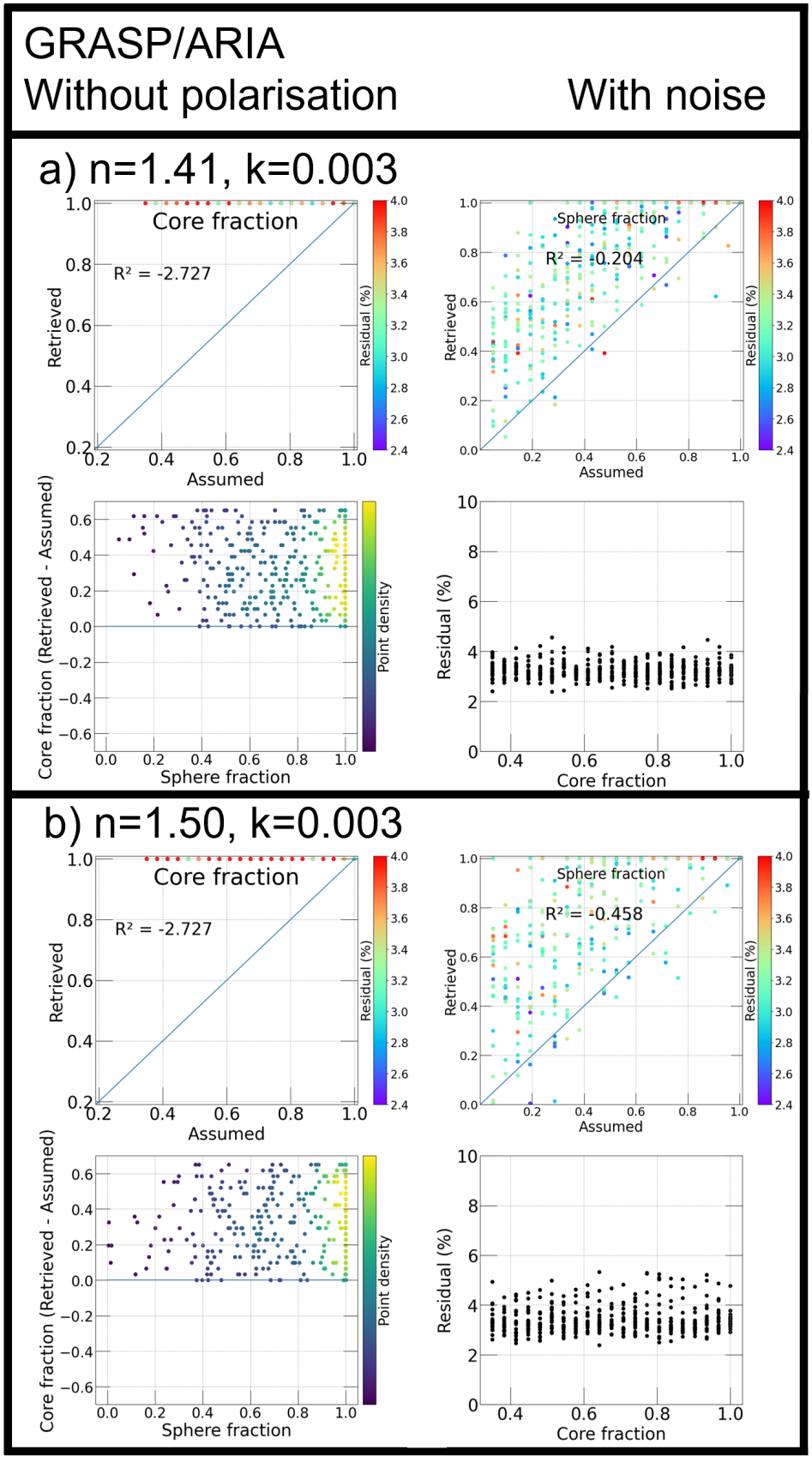

(4.1.1) Core and sphericity fractions, radiance residual. a) and b)

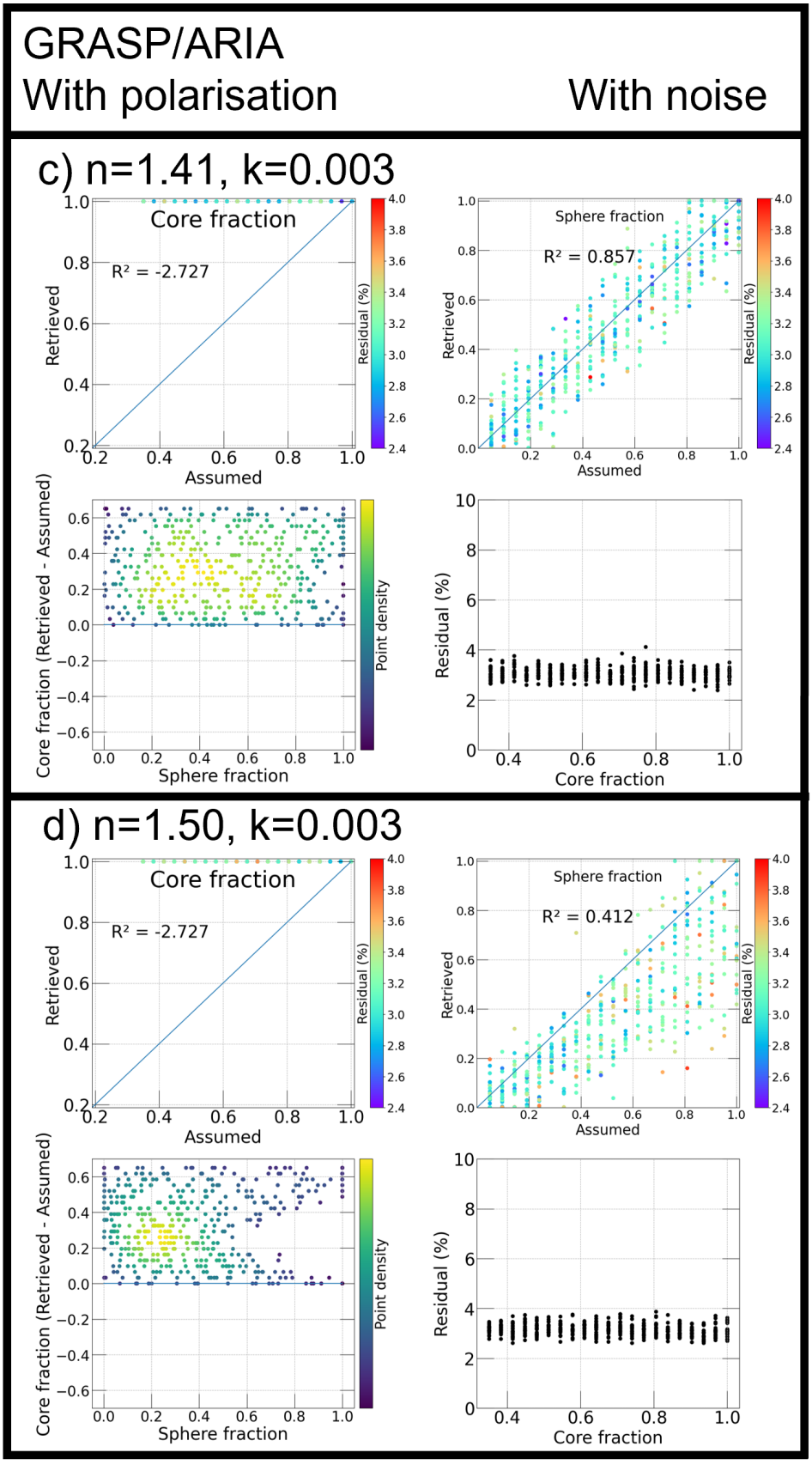

(4.1.2) Core and sphericity fractions, radiance residual. c) and d)

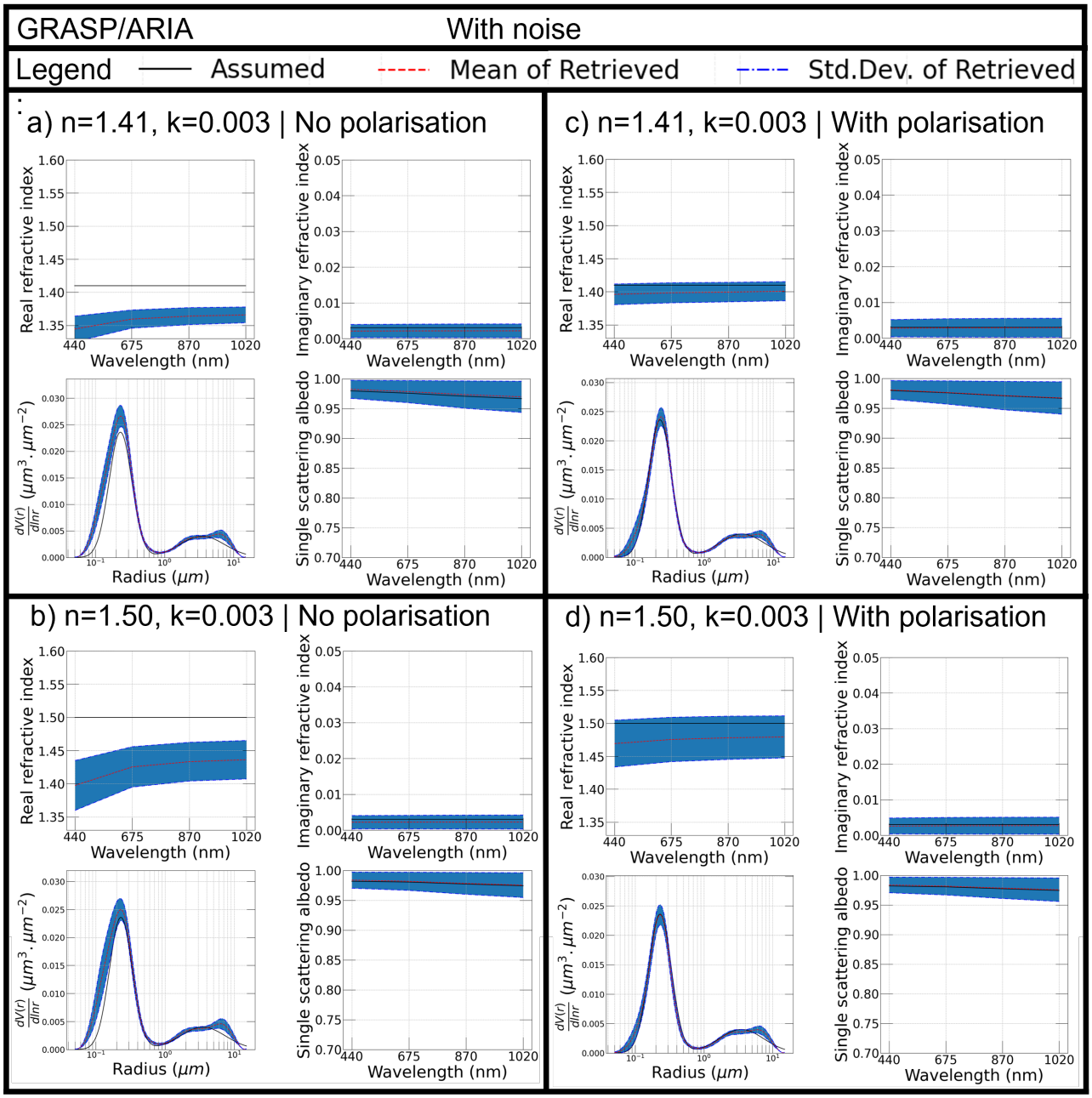

(4.1.3) Refractive index, Size distribution, SSA

Figure 4.1: Collection of plots of aerosol optical and microphysical characteristics derived by inversion of synthetic AERONET measurements. The case of fine mode dominated aerosol size distribution. The radiances, are generated using GRASP/ARIA (with inhomogeneous aerosol model)and inverted using GRASP/Standard (with homogeneous aerosol only). In panels a) and b) are results where only radiance intensity (no polarisation) is used, the refractive indices are a) n=1.41, k=0.003 and b) n=1.50 and k=0.003. Panels c) and d) are the same, but polarisation is used.

However, once polarisation is included, the results become quite different. The retrieval of the sphericity fraction is significantly improved in case of low contrasts of the core/shell real refractive index, no significant impact of inhomogeneity on the retrievals is notable. The differences however reappear at high contrast in the core/shell real refractive index and are more evidently imputable to the change in the aerosol model. Sphericity fraction in graph 2 is biased and underestimated, in contrast to overestimation in case of no polarisation; the R^2 is also degraded. The density of points in third graph is shifted and indicates that the core fraction of 0.2 has the major impact. The remaining parameters seem to be well retrieved, except for the coarse part of SD where, similarly to the no polarisation case, an increase of concentration appears. Retrieved refractive index looks to be within the range of expected for the effective values range. The main impact is thus on retrieval of sphericity fraction.

Figure 4.2 shows now the results for the coarse mode dominated size distribution. Overall, the impact of inhomogeneity on retrieval of sphericity is less pronounced in this case. But more importantly, the inversion now does not always achieve small residual of fit. There is a clear trend of non-convergence when the fraction of core is decreasing – stronger inhomogeneity. Overestimation of the sphere fraction seem to be related to smaller core fractions, which can be seen with the point densities of the third graphs (cf. A.3.1). Most of the overestimation comes from core fractions inferior to 0.7%, and they stir away from correct sphere fraction retrieval with the difference of 0.1 to 0.5 between the retrieved and assumed values. In addition, this difference in sphericity is accompanied by an increase of the residual fit, possibly exceeding 10%. The effects are increased with core/shell contrast in real refractive index and with involving polarisation. These results imply that a significant part of coarse mode dominated aerosol retrieval with high residual can be the consequence of the absence of a model taking inhomogeneity into account.

The SDs in Figure 4.2 displays similar shapes in all four cases. That is, the shape of fine mode is accurately reproduced with only slight changes in concentration. The coarse mode is however reproduced with an increased concentration of a large size bin, creating a bump in the distribution shape, which is not consequent enough to be considered as a third mode. The derived SSAs do not seem to be significantly affected by the introduced infomogeneity, the standard deviation is however higher than for the fine mode dominated case, yet the mean retrieved SSA strongly corresponds to the assumed one. The imaginary refractive index has the same quality of reproduction as for fine mode case. Results for the real refractive index

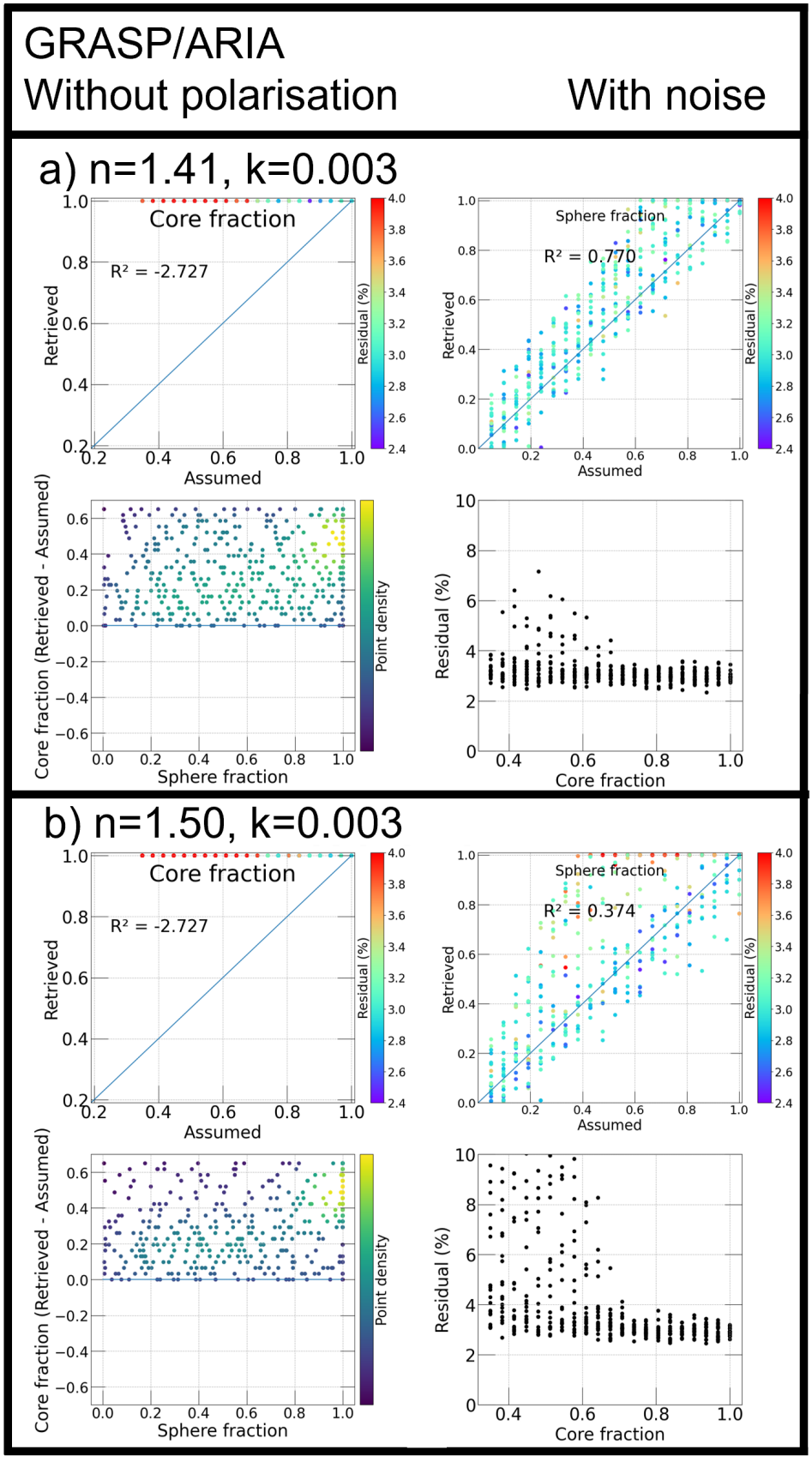

(4.2.1) Core and sphericity fractions, radiance residual. a) and b)

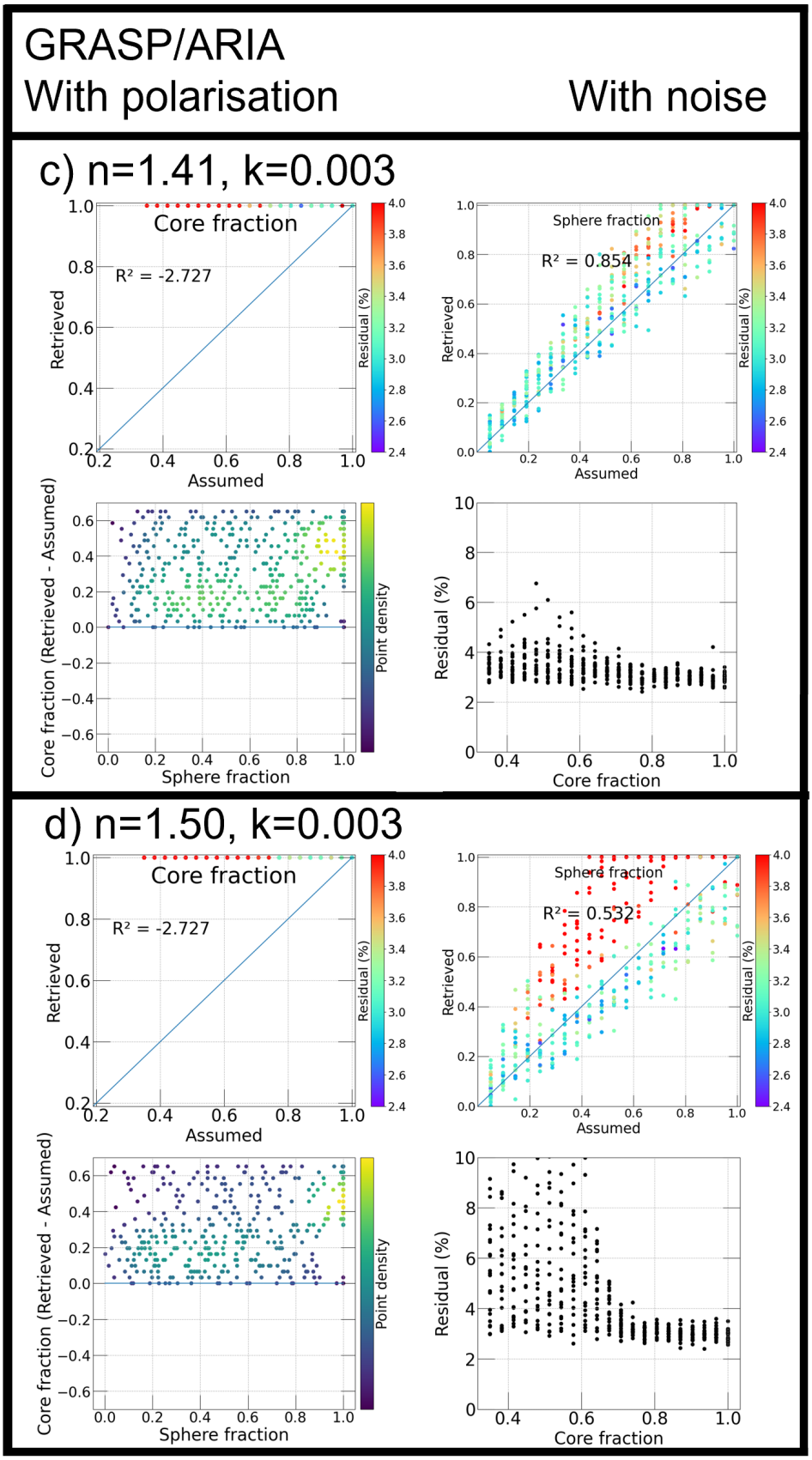

(4.2.2) Core and sphericity fractions, radiance residual. c) and d)

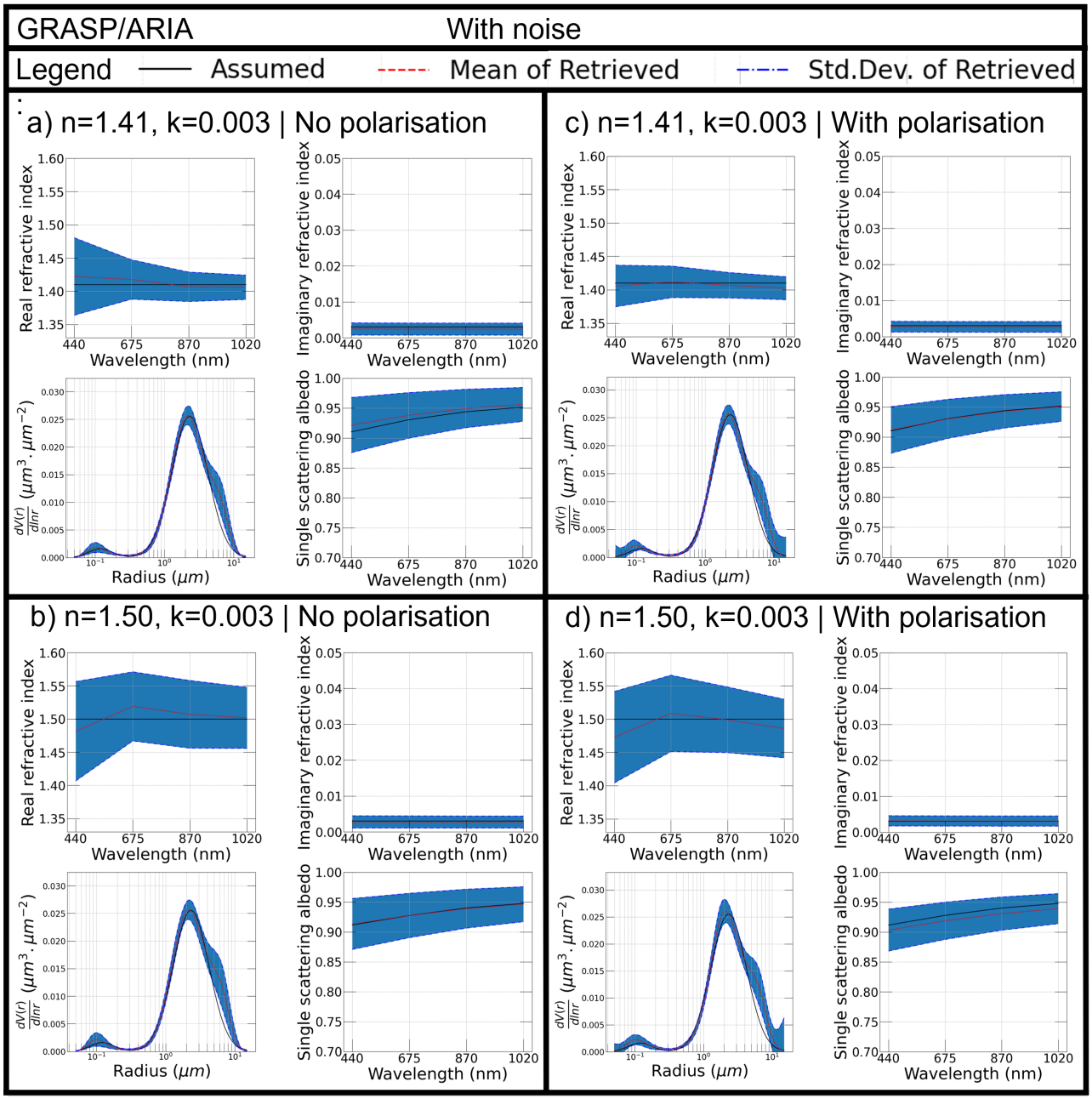

(4.2.3) Refractive index, Size distribution, SSA

Figure 4.2: Same as Figure 4.1, but for a coarse mode size distribution.

are, however, more complex. It is more stable for lower core/shell contrasts, but, there is a tendency of spectral dependance with lower values at 440 nm, strongly increasing for 675 nm then decreasing for the other wavelengths. As the input data generation and retrieval are performed with two different aerosol models, the difference are expected as discussed above, but the assumed refractive index in forward calculation should be always higher, which is not the case. There are, thus, also consequences of inhomogeneity for the real refractive index retrieval and its spectral dependence.

Figure 4.3 shows results for the case of bimodal size distribution. As can be expected, the results are somewhere a compromise between the fine and coarse mode dominated cases. This scenario is of interest because pronounced bimodality is quite frequent in many real cases. Again, the information on polarisation induces an overall improvement of sensitivity (cf A.3.1). The main difference is probably in a somewhat better retrieved refractive index, as the mean retrieved refractive index (real and imaginary) seems to be between the values for core and shell. In the case when n=1.50 for core, and the core fraction >= 0.7, the retrieved $n_{mean} \approx 1.49$; core fraction < 0.7, the retrieved $n_{mean} \approx 1.44$ with a small spectral dependency. The observed tendency is, indeed, logical. Also, when information on polarisation is included, there are some non-converging points (residual > 30%). These cases show no clear sphere fraction / core fraction dependence pattern and represent a consequential part of the inversions. These detailed look on these cases also revealed problem with reproduction of SD. Overall, it indicates a high sensitivity to the signal of inhomogeneity in this specific combination of parameters.

The same tests, but without noise have also been realised. Because the obtained results lead to the same conclusions and because noise inclusion is closer to reality, the corresponding figures are presented only in appendix A.3.1.

Intermediate conclusions

The purpose of this test was to identify if introducing of aerosol inhomogeneity can perturb AERONET standard retrieval, i.e. when inhomogeneous aerosol model is not taken into account during the inversion. The results showed that there is no effect only in the case of fine mode dominating particles and when the core/shell contrast in real refractive index is small. Although, the retried sphericity fraction appears as overestimated in this case, attribution to specifically inhomogeneity is difficult. The sensitivity to non-sphericity is low in general and

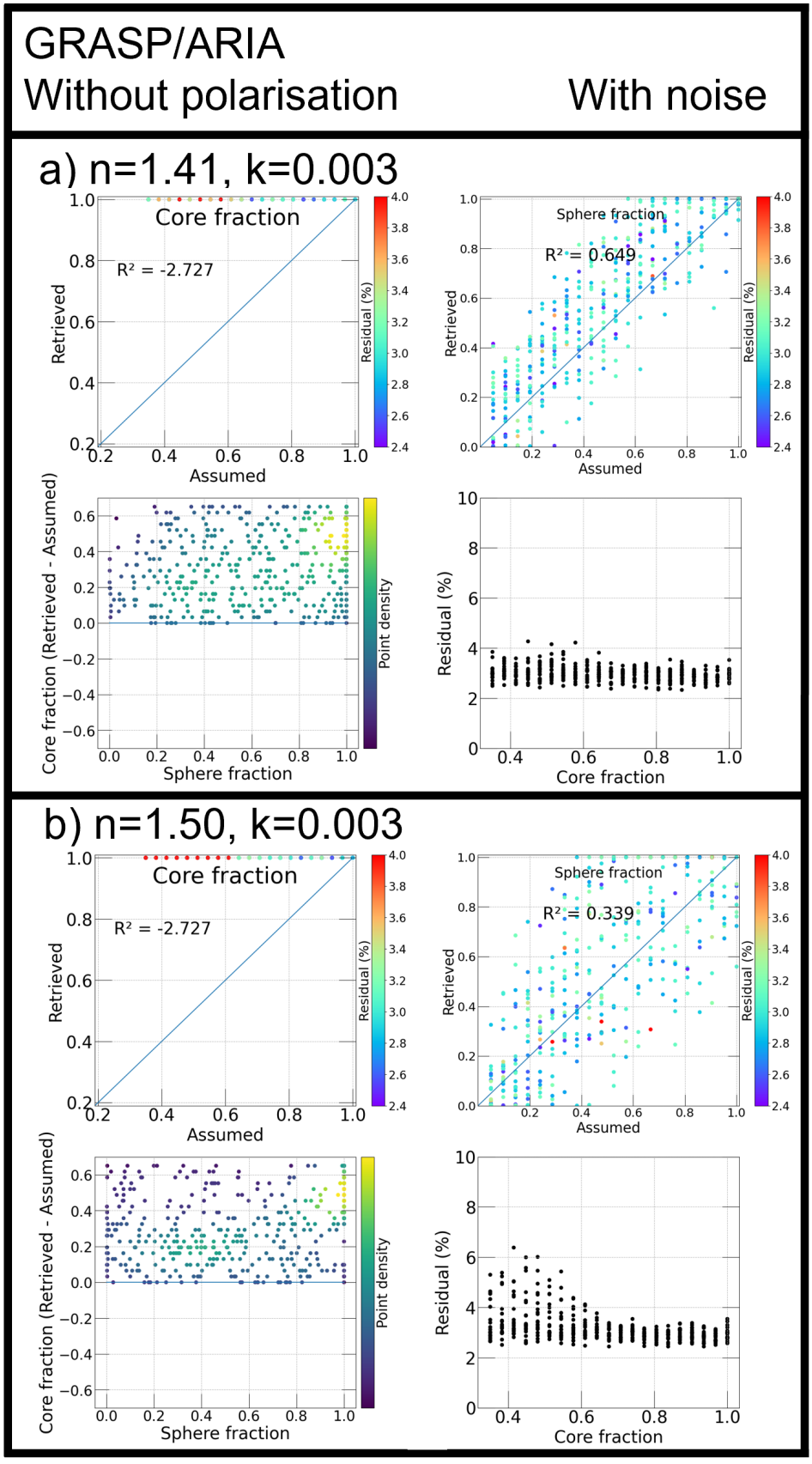

(4.3.1) Core and sphericity fractions, radiance residual. a) and b)

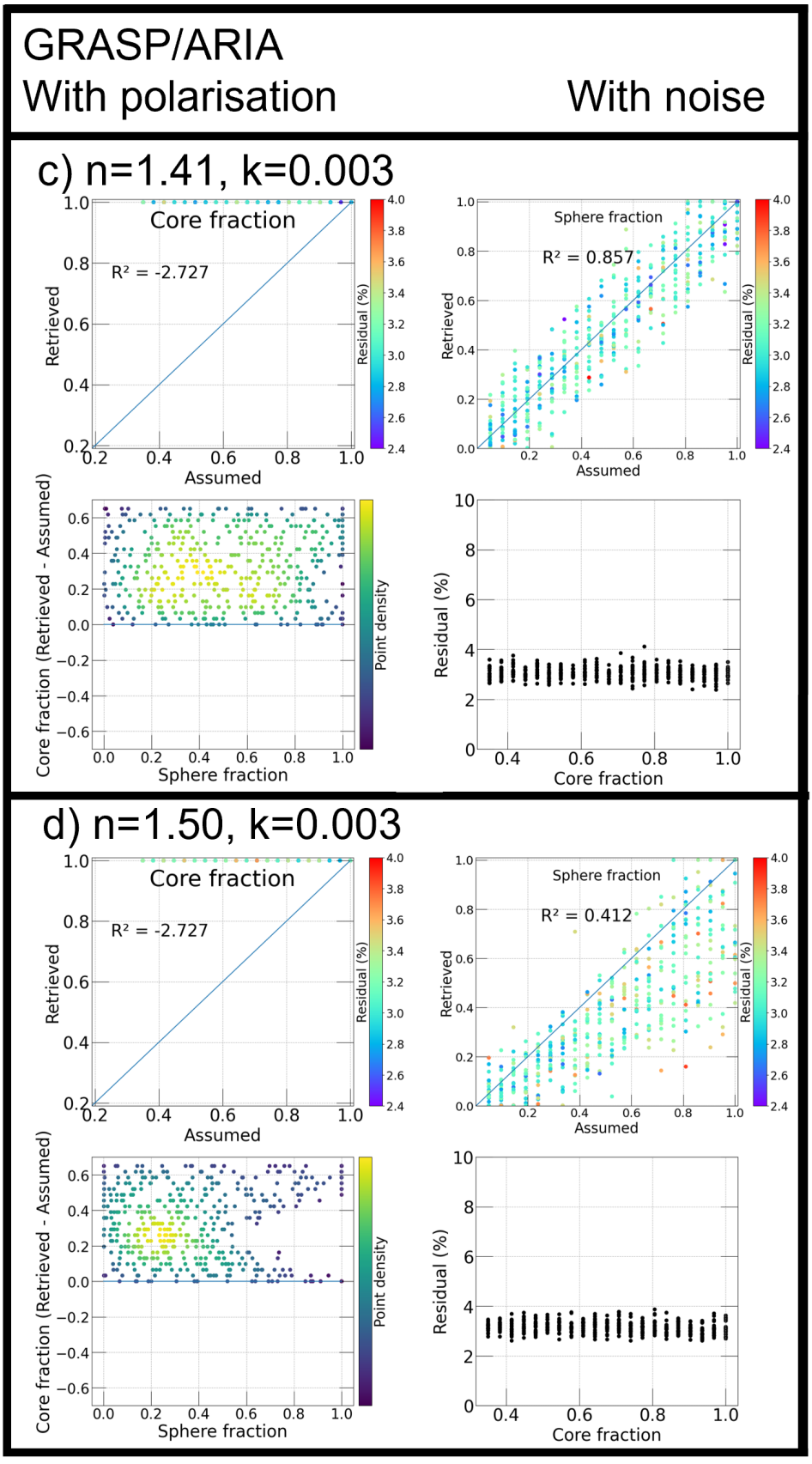

(4.3.2) Core and sphericity fractions, radiance residual. c) and d)

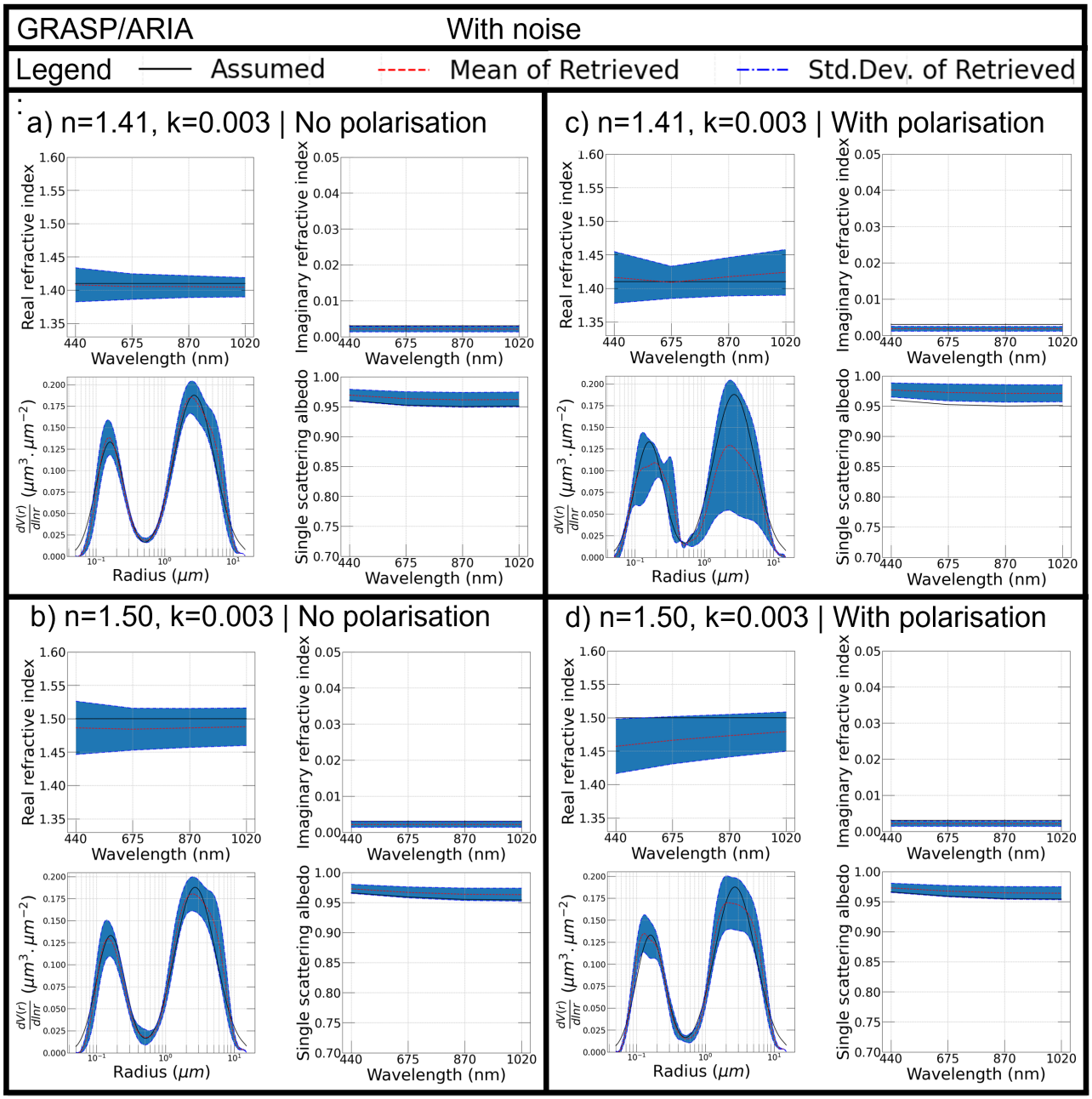

(4.3.3) Refractive index, Size distribution, SSA.

Figure 4.3: Same as Figure 4.1, but for a bimodal size distribution.

whatever perturbation can cause discrepancies in the reproduction of non-sphericity; the residual of the radiance fit remained low anyway. Still, for the case of fine mode dominating aerosol, when the core/shell contrast in refractive index was increased, the residual already started to increase. This is in addition to mismatch of the retrieved non-sphericity. Involvement of polarisation had significantly increased the sensitivity. The importance of the inhomogeneity signal has been increased for bimodal and coarse mode dominated cases. The great majority of the inversions have a slight increase ("a bump") in coarse mode aerosol concentration around the same range of radii. However, as will be seen in following figures, this "bump" seems to be present in most of the retrievals with noise included, hence, it might be caused by the addition of noise. Another systematic pattern is an underestimation of the sphericity fraction when core fractions are high and overestimation when core fractions become lower, which seems to be direct effects of the absence of inhomogeneous model during the inversion procedure. An impact on the retrieved real refractive index is also notable, sometime in form of apparent spectral dependence.

4.4 Effects of Core/Shell refractive index contrast

Objective and protocol

The main goal of this part of the study is to evaluate the influence of the contrast between refractive index of core and shell on the retrievals. The effect of contrast, under single scattering approximation, was reported above, illustrating increasing differentiation between homogeneous and inhomogeneous particles. The discussed differences are now evaluated considering multiple factors playing a role during inversion of measured radiances, e.g., presence of measurements noise, multiple scattering, simultaneous retrieval of particles shape, etc. The change of contrast (from n=1.41 to n=1.50 for real refractive index of core) has been realised for every synthetic data generated, however, only one case (AOD(440 nm) = 0.4) is reported here as a representative example. The retrievals were performed for multiple real refractive indices at a fine step (x-axis in Figure 4.4). The presented R^2 scores in Figure 4.4 are for correlations between the assumed and the retrieved fractions of core and of sphericity, indicates the quality of the retrieval. The figure shows that discrimination is possible starting from real refractive index of core of about 1.4. However, more important observation is rather weak dependence of R^2 on real refractive index.

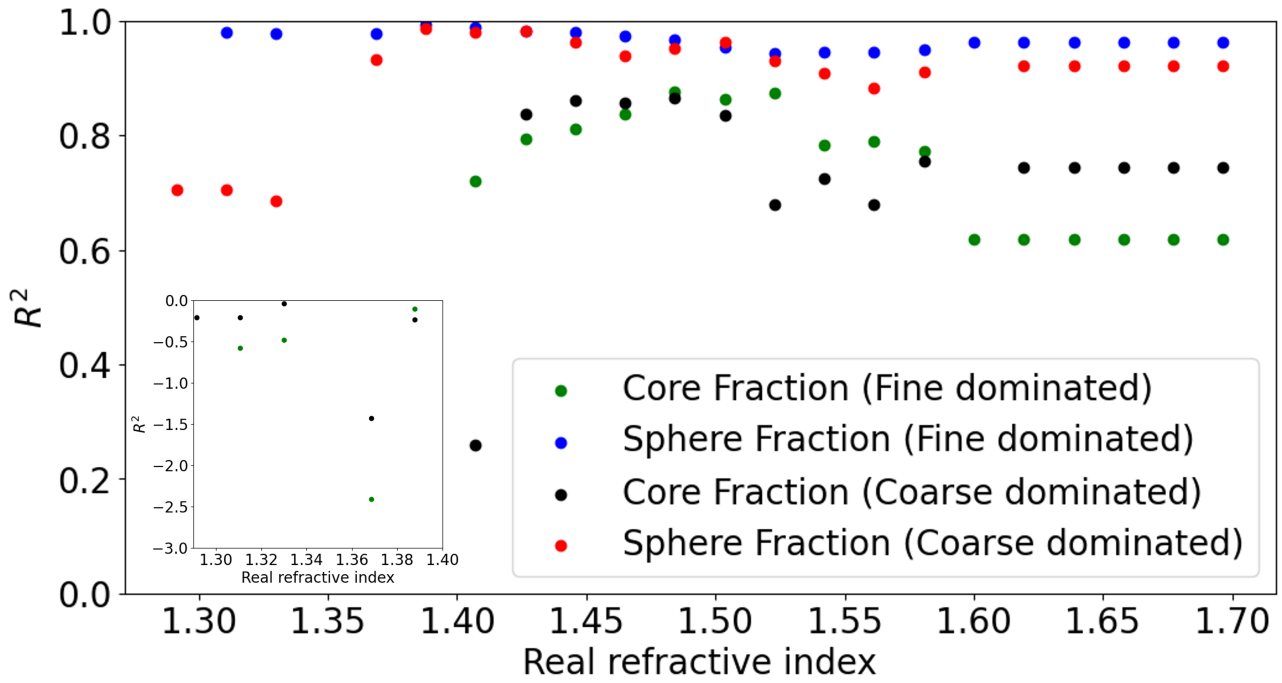

Figure 4.4: R^2 scores for retrieved vs. assumed core and sphere fractions as function of real refractive index (spectrally invariant) of core, for fine and coarse mode dominated size distributions. Sub-graph in the bottom left corner shows negative R^2 values, which produces when the real refractive index of core is close or below that of shell.

Figures 4.5 – 4.13 then present a detailed analysis of the retrieved characteristics in scenarios without/with noise, with/without polarisation and for two extreme refractive indices (1.41 and 1.5). The graphs without noise represent ideal conditions and the graphs with noise approximate real data retrievals.

Analysis

Contrary to the previous figures (inverted with GRASP/Standard), the both compared data sets in this section are realised with the same aerosol model (GRASP/ARIA), which means the retrieved and the assumed fractions of core are varying and ideally should correlate perfectly. The y-axis in the third graph of each panel represents now the difference between the retrieved and the assumed fraction of core as function of the retrieved fraction of sphericity, so we can learn about dependencies between the retrieved inhomogeneity and non-sphericity. In context of the retried refractive indices and the SSA, it should be remained that only spherical aerosol model has core/shell fraction, thus, when the fraction of spherical aerosol is low, the refractive indices and the SSA of non-spherical homogeneous aerosol will dominate.

Figure 4.5 presents the scenario of fine mode dominated size distribution and no use of

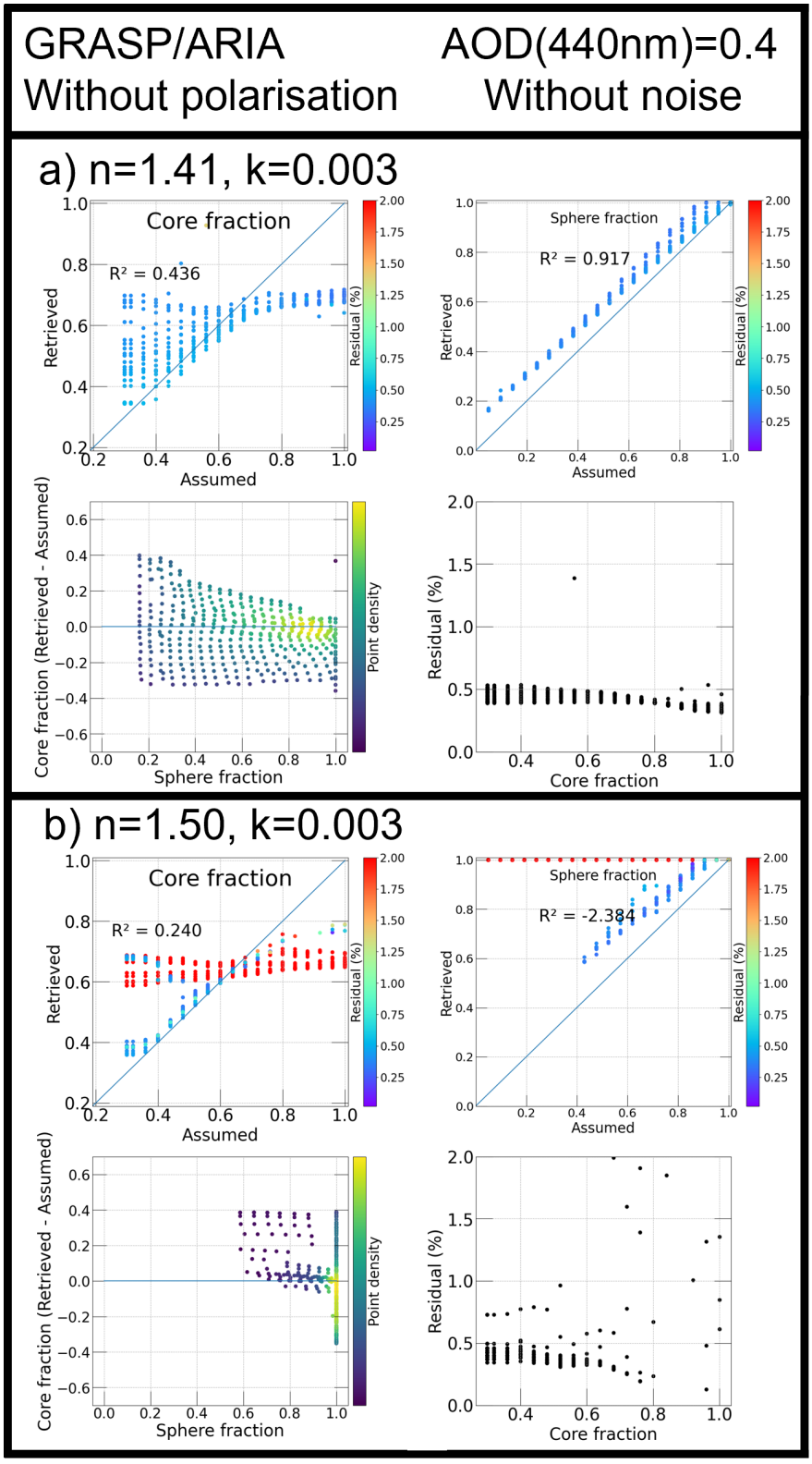

(4.5.1) Core and sphericity fractions, radiance residual. a) and b)

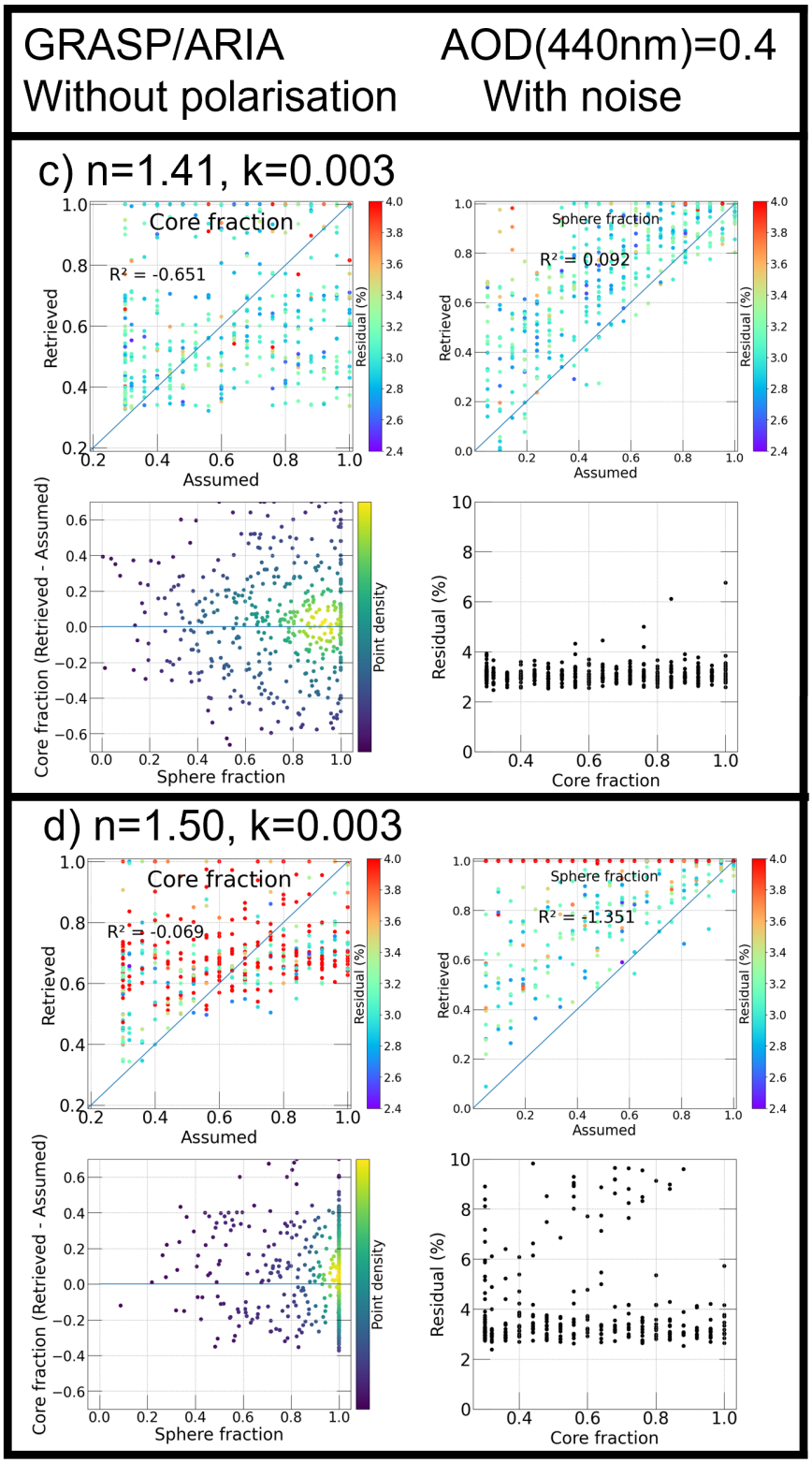

(4.5.2) Core and sphericity fractions, radiance residual. c) and d)

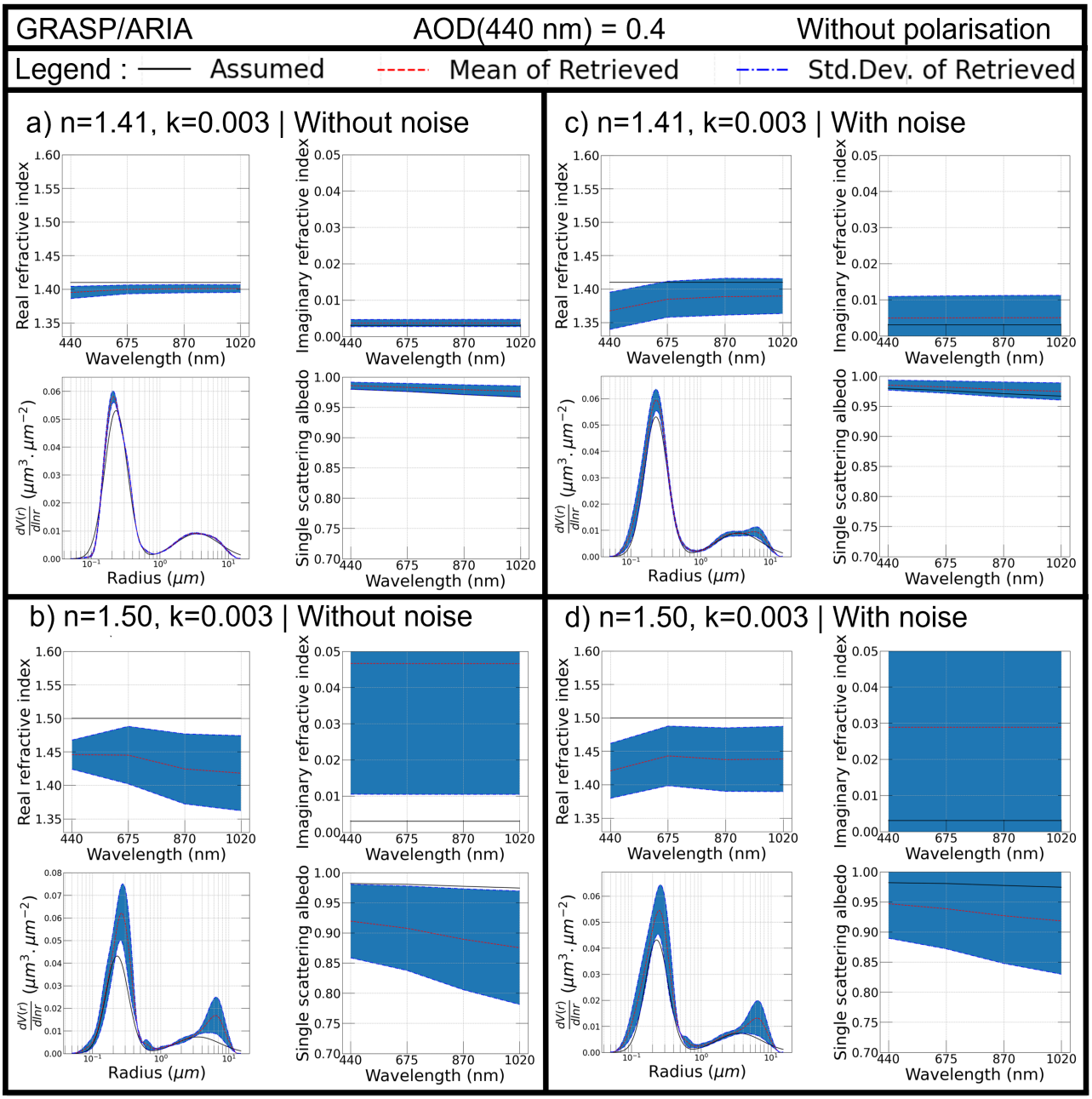

(4.5.3) Refractive index, Size distribution, SSA.

Figure 4.5: Collection of plots of aerosol optical and microphysical characteristics derived by inversion of synthetic AERONET measurements. The case of fine mode dominated aerosol size distribution. The radiances, are generated and inverted using GRASP/ARIA (with inhomogeneous aerosol model).In panels a) and b) are results without measurements noise, the refractive indices are a) n=1.41, k=0.003 and b) n=1.50 and k=0.003. Panels c) and d) are the same, but simulation of measurements noise is included.

polarised radiances. The figure shows quite interesting result, that is, when the contrast in the refractive index is low (weak effect of inhomogeneity) the quality of the core fraction retrieval is poor, and the sphericity fraction is overestimated. However, when the contrast in the refractive index is high, the sphericity fraction retrieval fails, same for the core fraction, and the residuals are high. This absence of convergence is an issue caused by a lack of score amelioration of the gradient descent in the available modifications of the vector of the retrieved parameters. The principal causes are the constraints defined in the settings that prevent the vector from taking values that have no physical meaning. The other cause can be the aerosol model being inadequate to describe correctly the radiation field. But, as the radiances are synthetically generated with the same aerosol model as the one used in the retrieval, the failure of the retrieval is most likely caused by the lack of sensitivity and score amelioration during the inversion.

In the case n = 1.41 and without noise, the retrieved sphericity fraction has only a little slight overestimation bias. The core fraction is divided in three parts. The first is the underestimation for fractions above 0.7, they are all considered being around 0.7, which enlightens a clear lack of sensitivity for thinner shells. The second part is the overestimation of the smaller core fractions, this is different from the previous one as they don't concentrate over the same value, but seem to degrade gradually reflecting a loss of sensitivity. The former is in line with the dependence in the third graph, showing a decrease of overestimation with the increase of sphericity. The third group of points of quite accurate retrievals correspond to the combination of sphericity fraction above 0.9 and the core fractions ranging from 0.7 to 0.35. Indeed, the density of points on the third graph is close to a correct estimation of the core fraction above 0.9. The exceptions are some heavy underestimation that is shown on first graph to be core fractions above 0.7. Including the random noise greatly affects the retrievals. The core and sphere fractions suffer an important loss of sensitivity. In addition, discrepancies in the retrieved real refractive index and SD are accentuated. It is important to note that for n = 1.50, for the assumed sphere fraction of 0.9, the retrieved core fraction is somewhat accurately evaluated ($\pm 15\%$, see appendix A.3.2), which is not the case for n = 1.41. However, since the sphere fraction is not accurately retrieved, this can't be applied to real data as the true sphericity is not known.

Figure 4.6 (fine mode dominated size distribution, with polarisation) only presents the results with random noise added, as a worst case. It is because the inversions without noise have shown a significant improvement in the quality of the retrieval, and it is very close to already

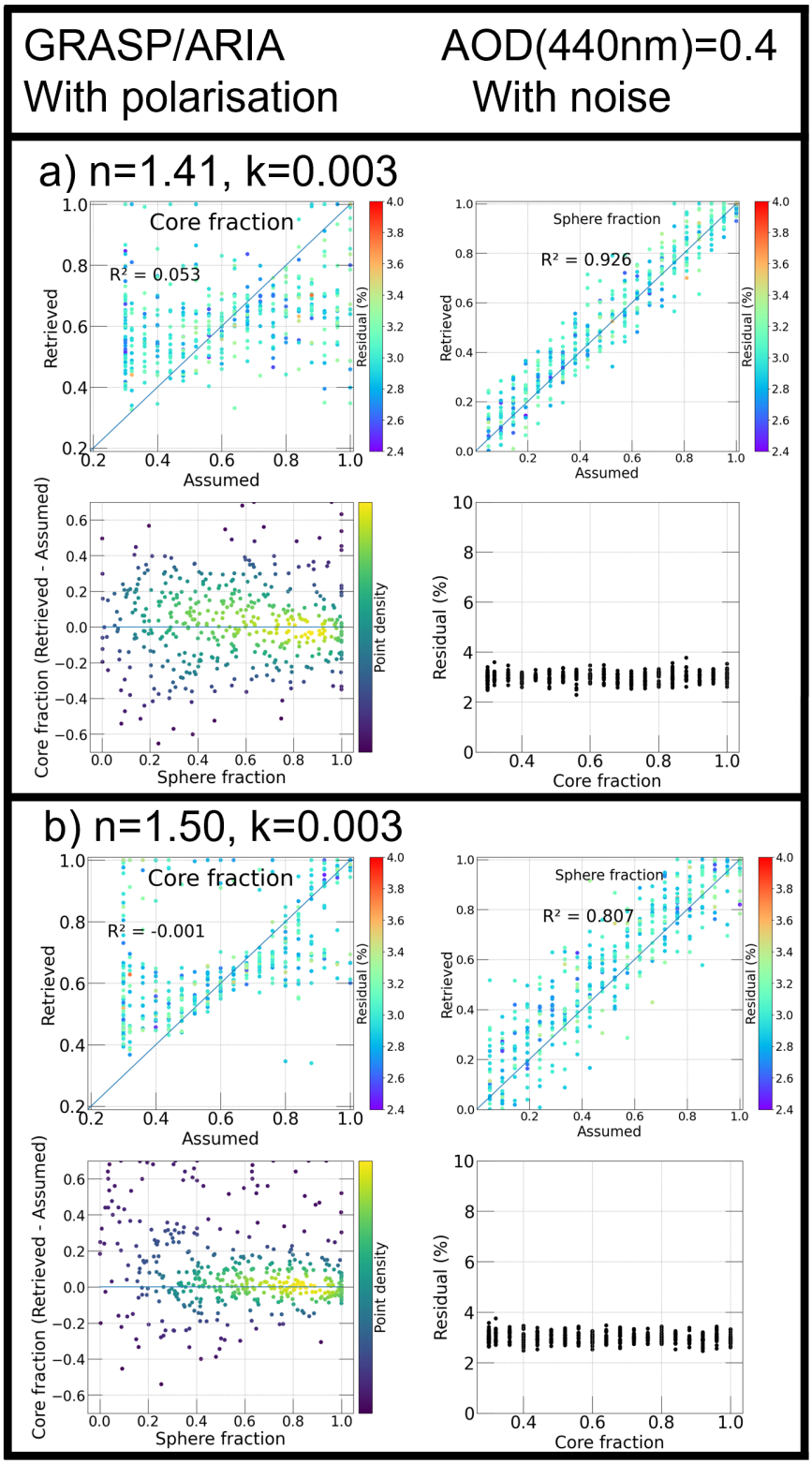

(4.6.1) Core and sphericity fractions, radiance residual.

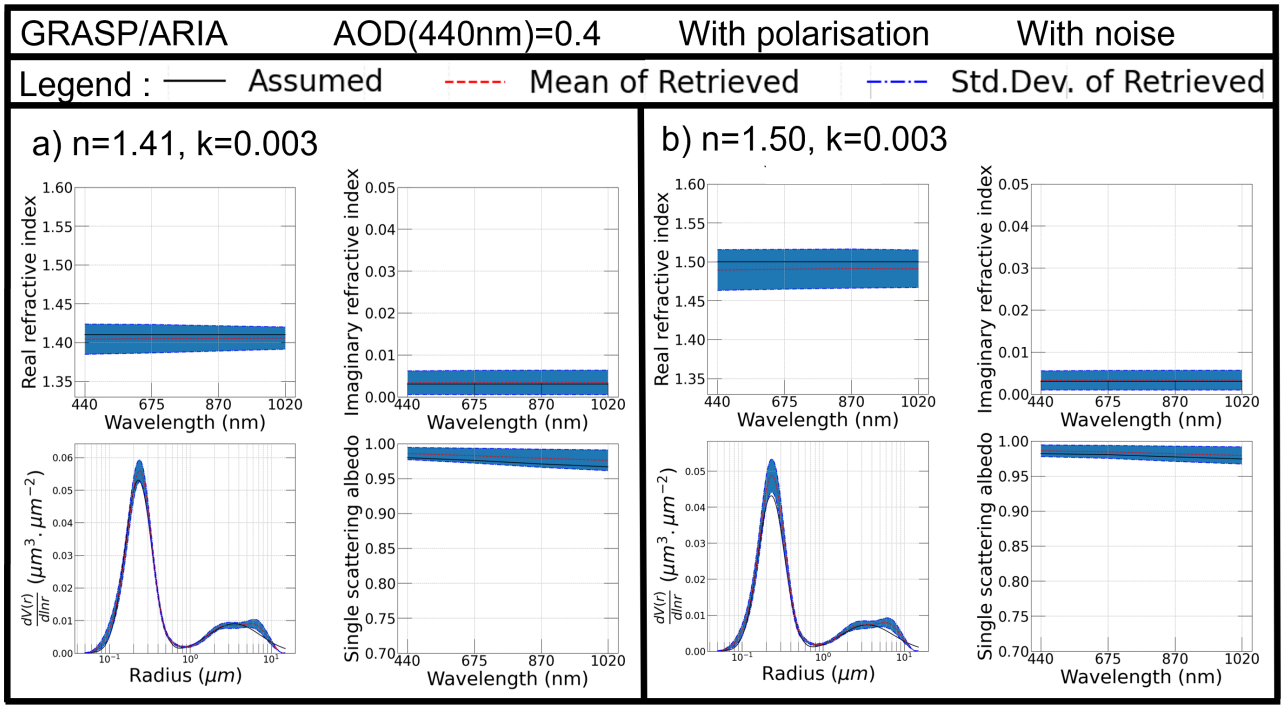

(4.6.2) Refractive index, Size distribution, SSA.

Figure 4.6: Collection of plots of aerosol optical and microphysical characteristics derived by inversion of synthetic AERONET measurements. The case of fine mode dominated aerosol size distribution. The radiances, including polarisation, are generated and inverted using GRASP/ARIA (with inhomogeneous aerosol model). In panels a) and b) are results with measurements noise, the refractive indices are a) n=1.41, k=0.003 and b) n=1.50 and k=0.003.

discussed ideal conditions (available in appendix A.3.3). The goal is, now, to see the advantage of including polarisation under the conditions of measurements noise for two contrasts in refractive indices. For n = 1.41, despite clear improvement in retrieval of all characteristics, the core fraction is still not accurately retrieved. The core fraction retrieval for n = 1.50 is, however, considerably improved. Sphere fraction, real refractive index and SD are slightly less accurate than for n = 1.41, but sphere fraction is far more accurate, except for assumed core fraction < 0.4. As can be seen in graph three, most of the retrieved core fractions are accurately retrieved with $\pm 5\%$ for sphere fractions from 1 to 0.7 except for assumed core fractions between 0.6 and 0.8 which have an uncertainty of -5 to 15%. We thus see again that once particles inhomogeneity is more pronounced, there is enough sensitivity to make its retrieval, but on the other hand some interference with non-sphericity appears.

Figure 4.7 (coarse mode dominated size distribution, without polarisation) reveals that without noise, for coarse particles, the retrievals have very high level of correspondence with the assumed characteristics. Surprisingly, the increase in contrast seem to create only a small confusion with non-sphericity, possibly associated with some data points with higher residuals than expected. With noise, n = 1.50 is better retrieved than n = 1.41, however, both cases lack sensitivity for small sphere fractions and most of coarse size distributions have sphere fraction under 0.1, which means that there would be a lack of sensitivity for most cases. The cases of sphericity fractions above 0.30 are well retrieved for n = 1.50, whereas it is above 0.50 for n = 1.41.

Figure 4.8 (coarse mode dominated size distribution, with polarisation) shows overall improved sensitivity to retrieval of all aerosol characteristics when polarisation measurements are included. For instance, core fractions above 0.20 are well retrieved for n = 1.50, whereas it is above 0.40 for n = 1.41.

Figure 4.9 (bimodal size distribution, without polarisation) displays good retrieval qualities for inversions without noise, except for SD and core fraction when the sphericity fraction is low. The convergence seems also more complicated to reach when inhomogeneity is important, i.e., smaller core fractions and real refractive index of core is 1.50. The main problem in the case of bimodal size distributions seems to be in retrieval of the fine mode, where a third mode appears. Many input settings have been tested with numerous constraints and this third mode appeared every time. An explanation would be a local minimum during gradient descent in the inversion, as it seems to disappear with addition of random noise that probably smooths

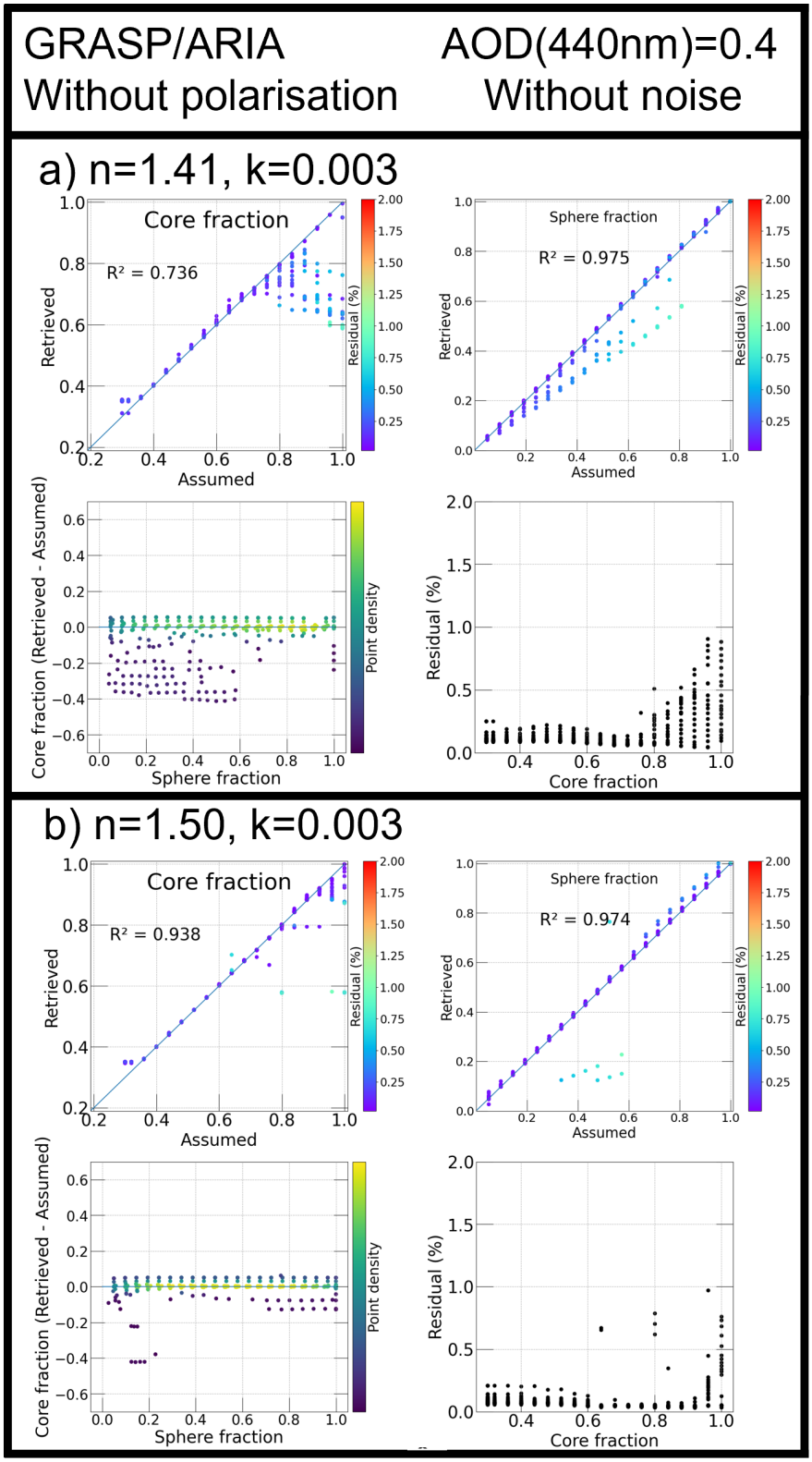

(4.7.1) Core and sphericity fractions, radiance residual. a) and b)

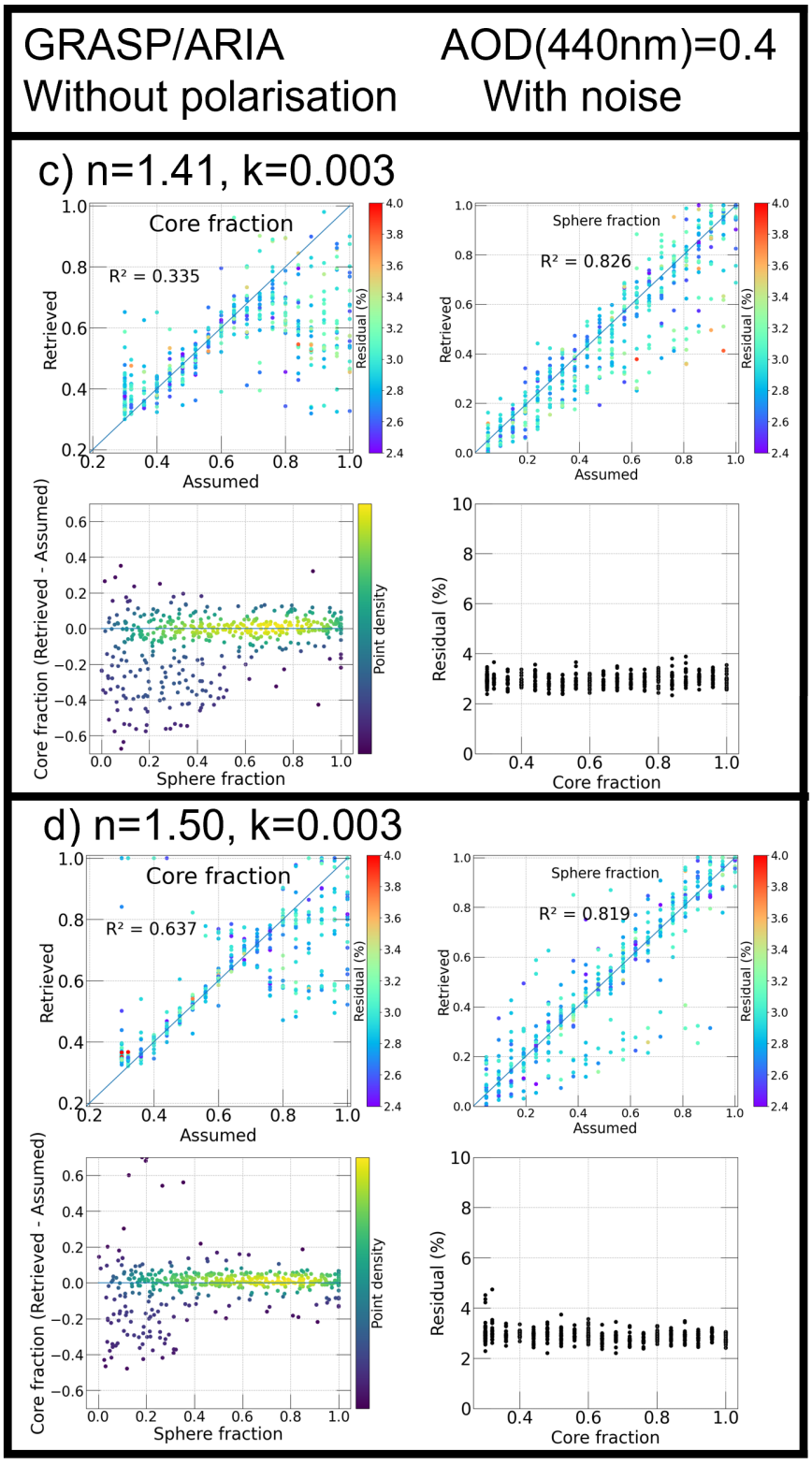

(4.7.2) Core and sphericity fractions, radiance residual. c) and d)

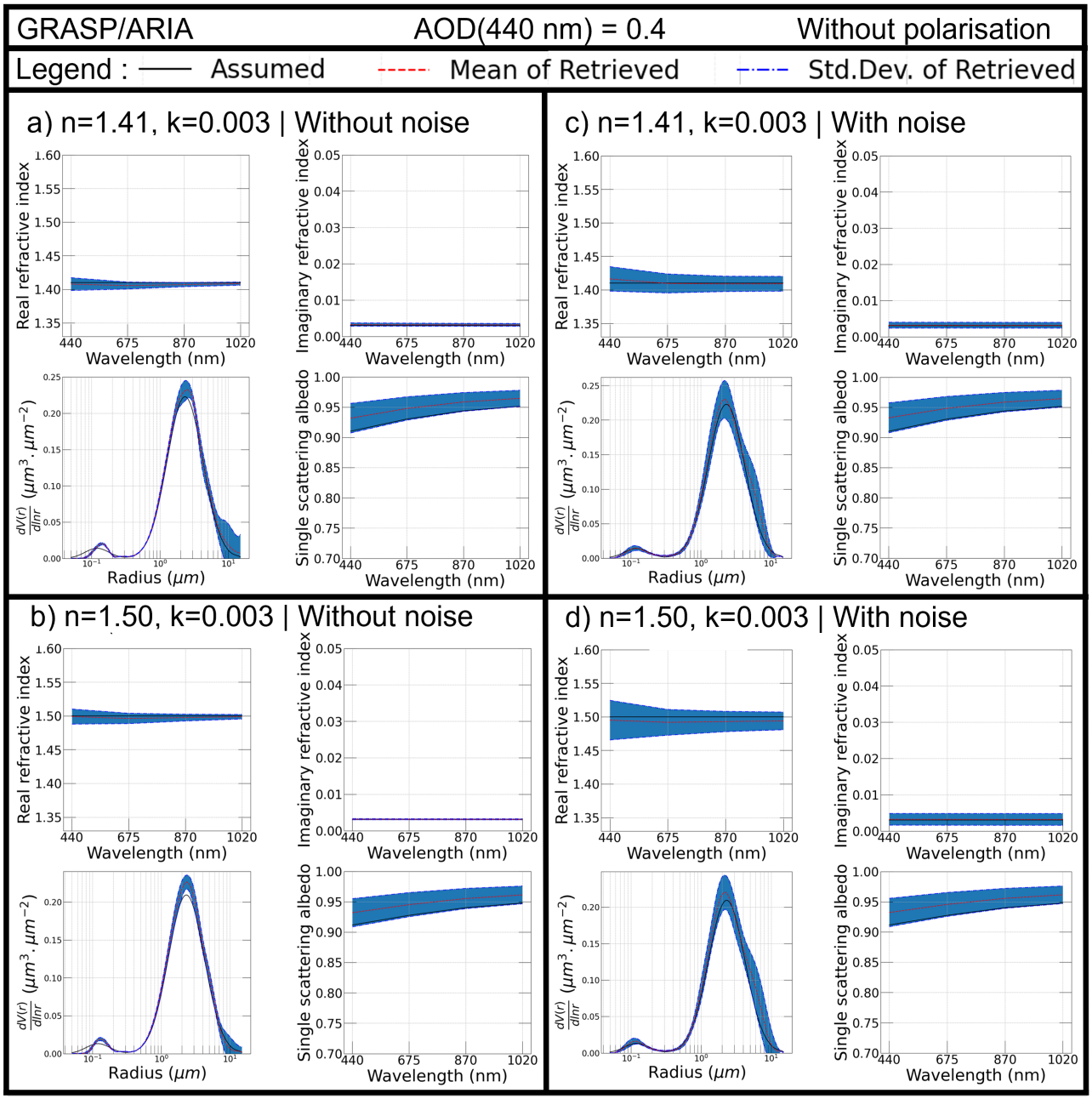

(4.7.3) Refractive index, Size distribution, SSA.

Figure 4.7: Same as Figure 4.5, but for coarse mode dominated size distribution.

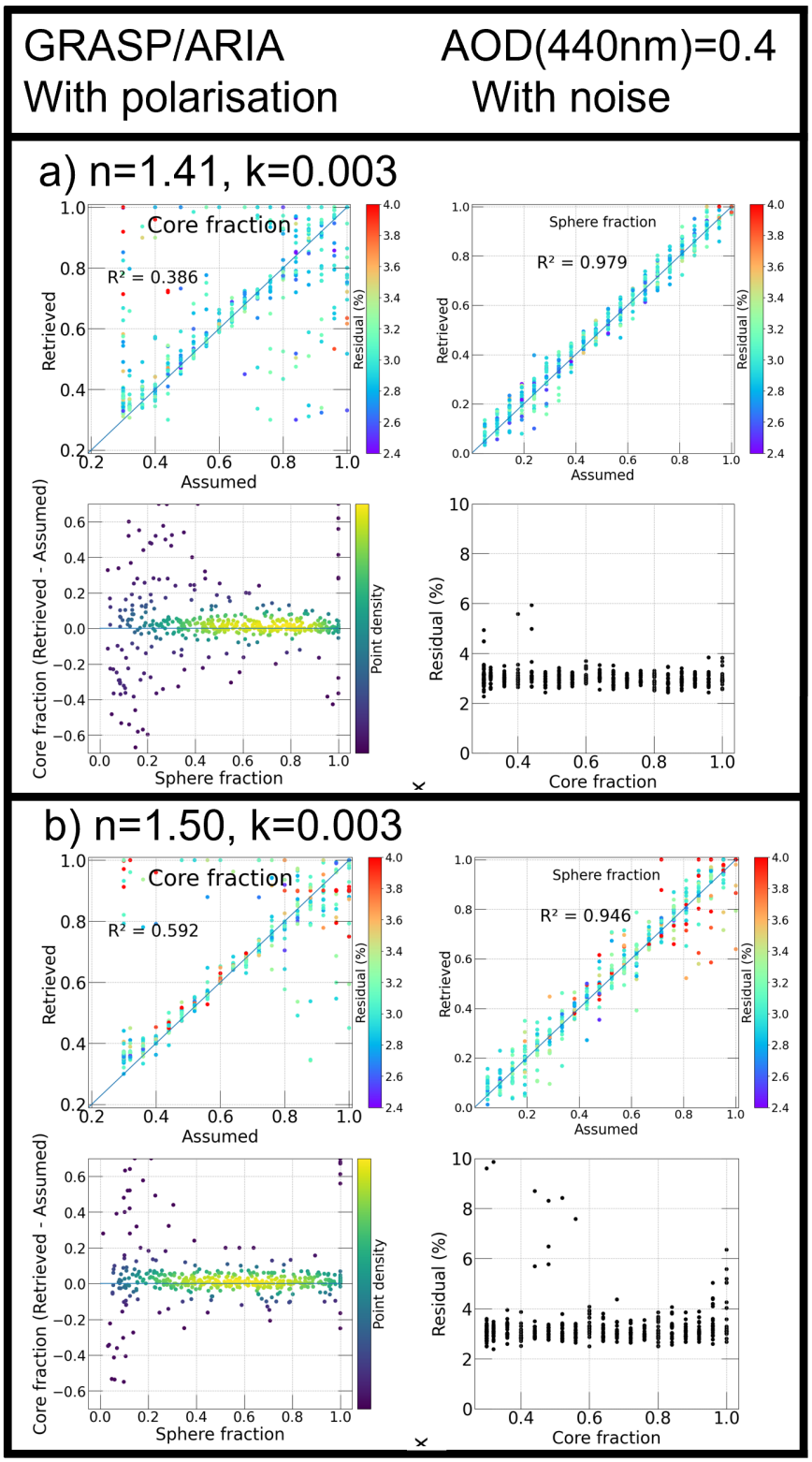

(4.8.1) Core and sphericity fractions, radiance residual.

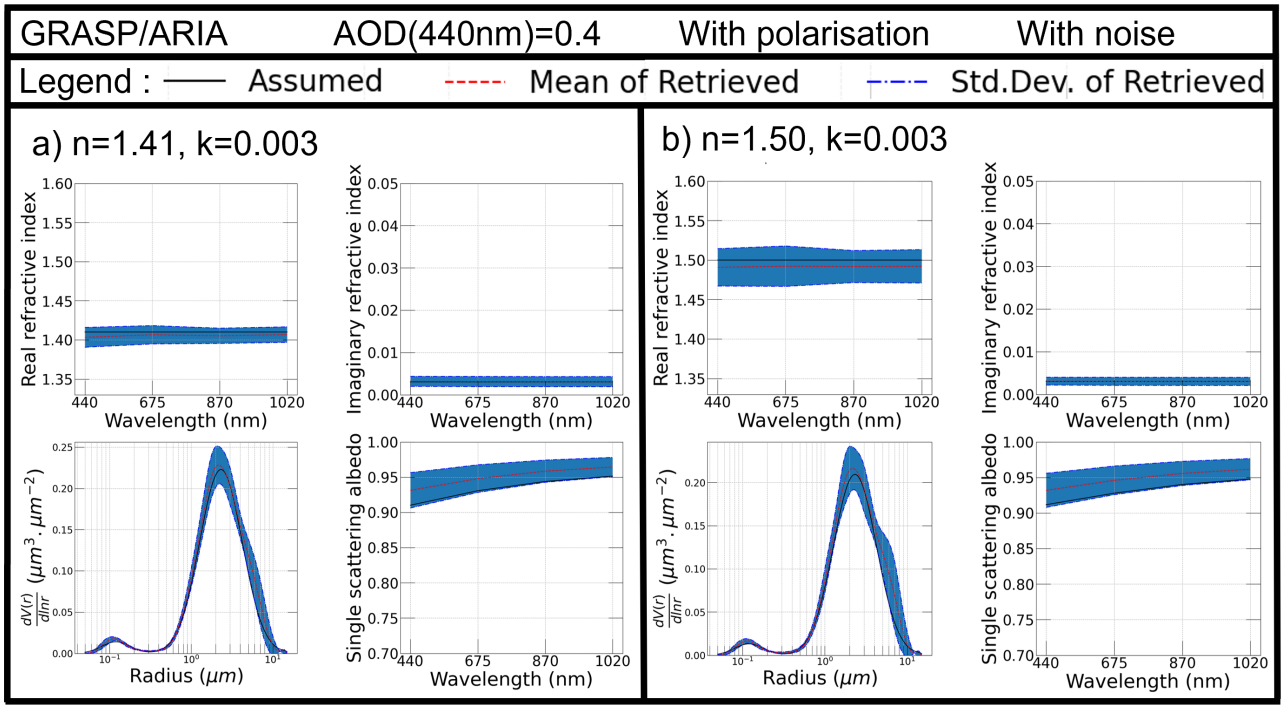

(4.8.2) Refractive index, Size distribution, SSA.

Figure 4.8: Same as Figure 4.6, but for coarse mode dominated size distribution.

some features. Overall, the analysis shows that when polarisation is not included, an increase in the inhomogeneity signal (increased contrast between real refractive index of core and shell) causes perturbation of the retrievals, specially of core and sphericity fractions. This problem is apparently related to the possibility that non-sphericity and inhomogeneity are mimicking each other.

Figure 4.10 (bimodal size distribution, with polarisation) demonstrates a global improvement of the retrievals, especially for sphere fraction, residual and SD. Polarisation clearly improved the quality of retrievals in all analysed scenarios. Analysis of the retrievals with involved polarisation measurements, therefore, enables defining the scopes of applicability with minimal a priori assumptions. This scope can be defined from both sphere and core fraction. To simplify, there is an overestimation of core fraction throughout the spectre of sphere fractions, which is contained between 0.8 and 1. Hence, uncertainty can be reduced by considering that every core fraction value can't be trusted above 0.8, allowing to have a wide range of accepted sphere fractions, yet with some level of sphericity, this range can be reduced and therefore, accept more core fractions. For n=1.41, the sphere fraction must be above 0.6 and for n=1.51, it must be above 0.4 (cf. appendix A.3.2)

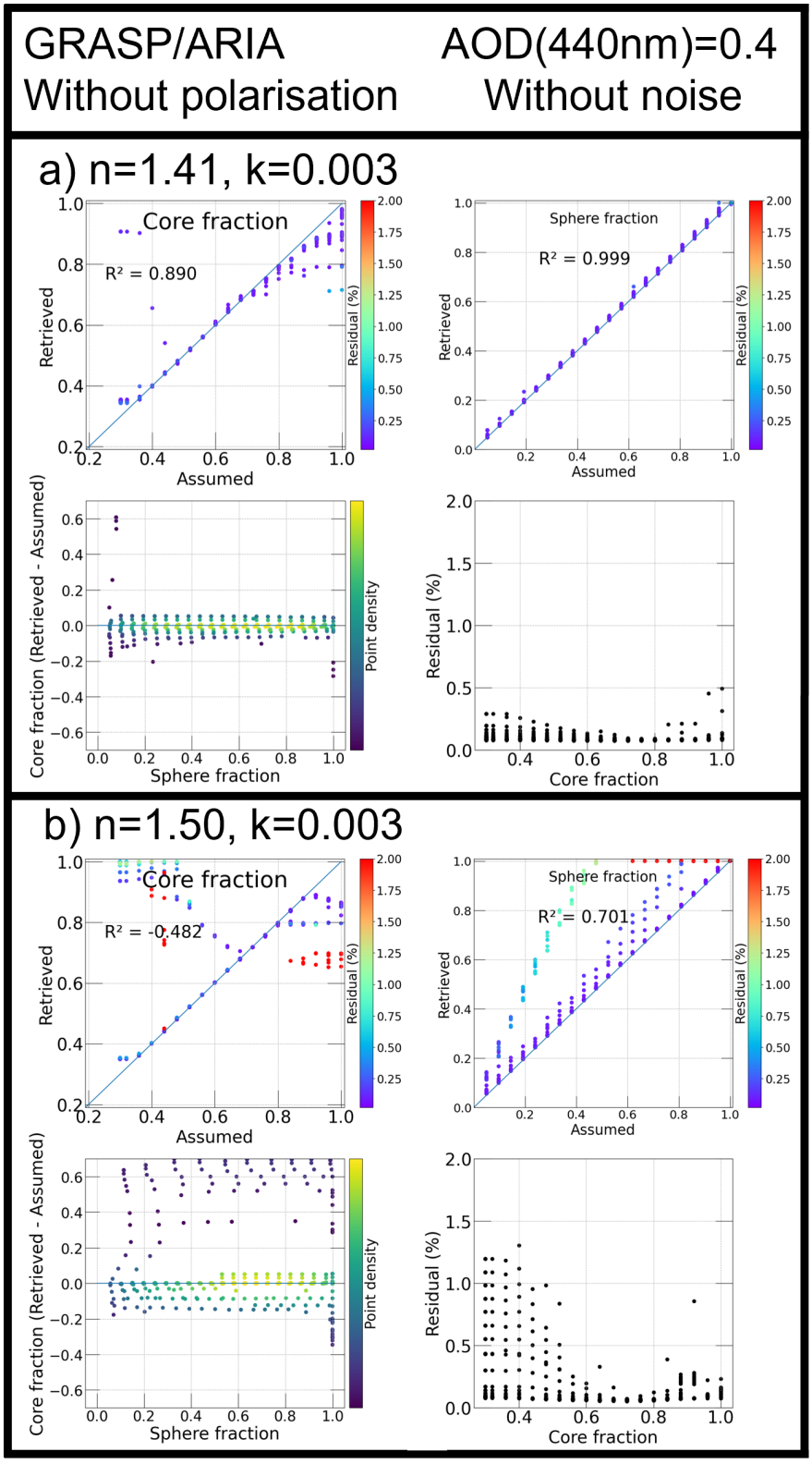

(4.9.1) Core and sphericity fractions, radiance residual. a) and b)

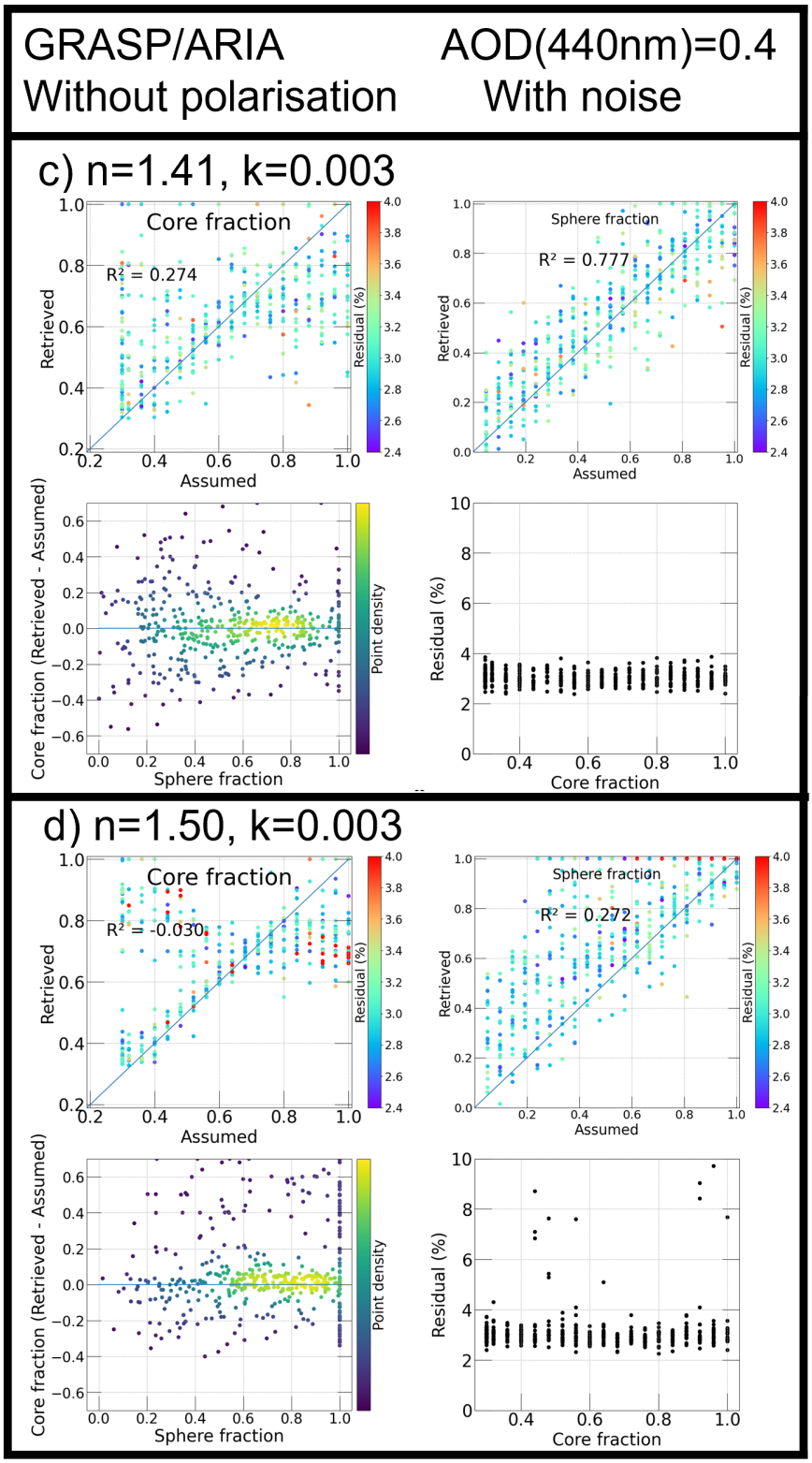

(4.9.2) Core and sphericity fractions, radiance residual. c) and d)

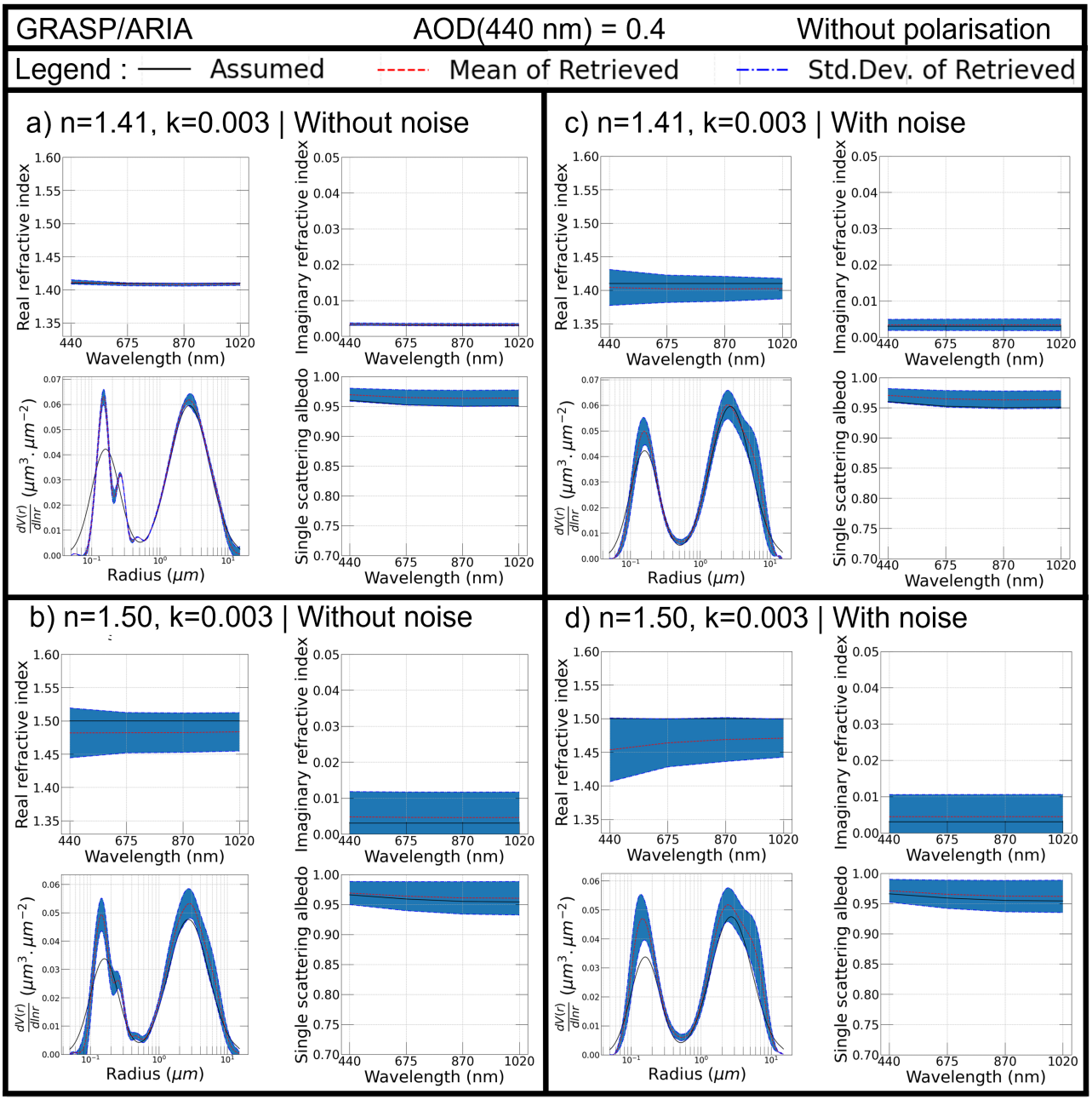

(4.9.3) Refractive index, Size distribution, SSA.

Figure 4.9: Same as Figure 4.5, but for bimodal size distribution.

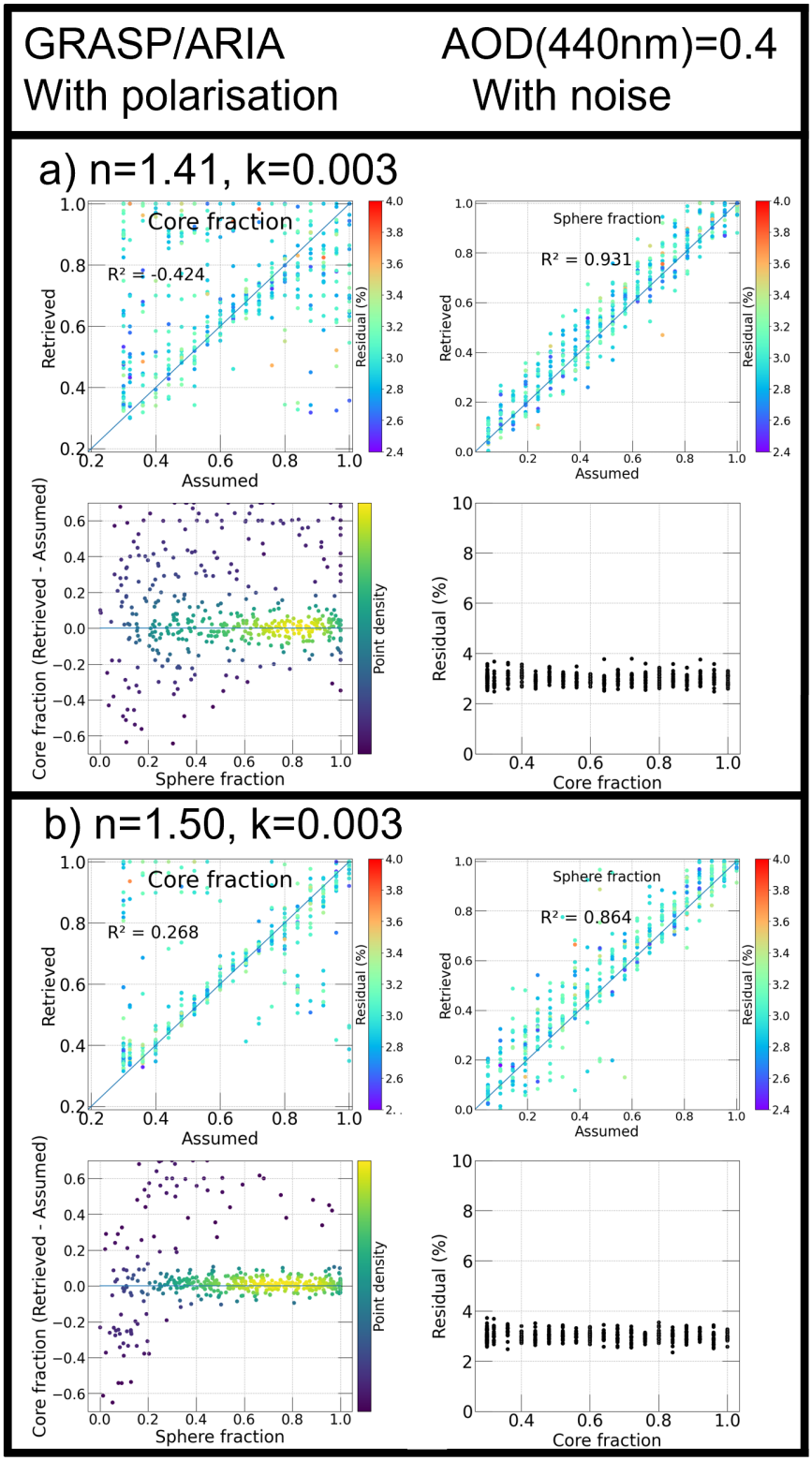

(4.10.1) Core and sphericity fractions, radiance residual.

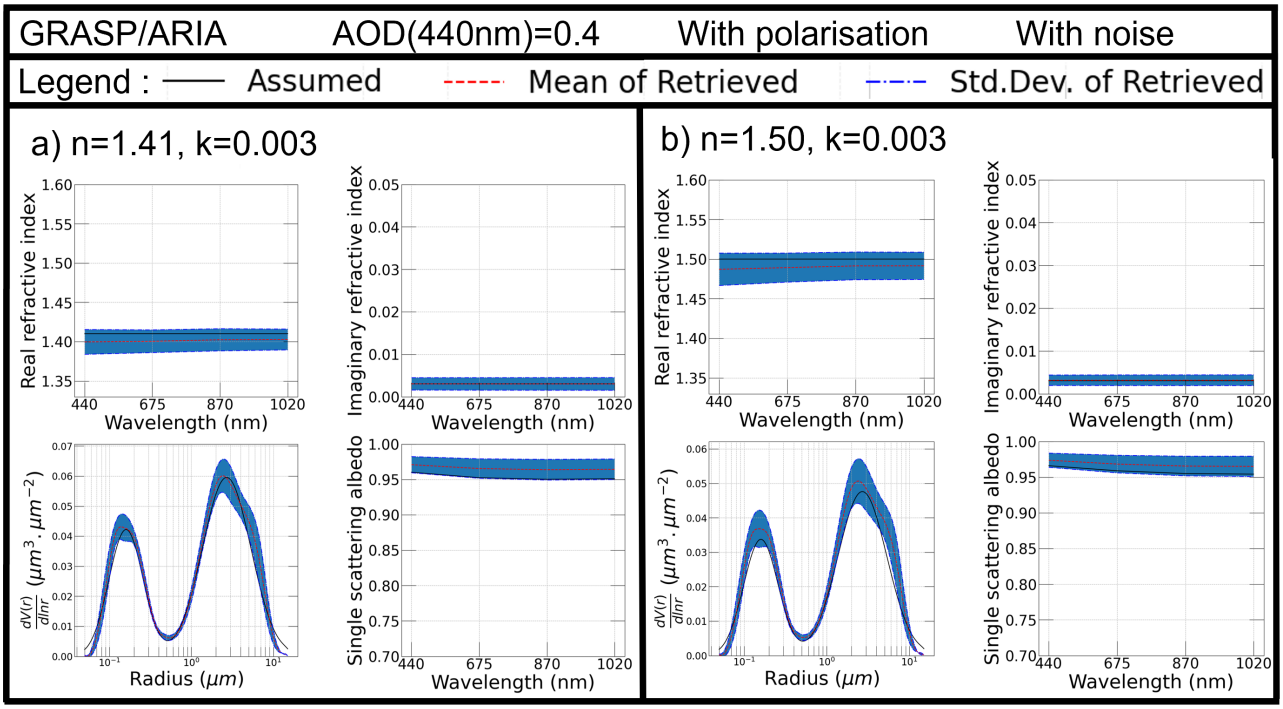

(4.10.2) Refractive index, Size distribution, SSA.

Figure 4.10: Same as Figure 4.6, but for coarse mode dominated size distribution.

Intermediate conclusions

One of the first things that can be learned from the study of the effect of contrast between real refractive index of core and shell is that more pronounced contrast can cause perturbation in retrievals of several aerosol characteristics, even if the contrast helps to improve the retrieval of the core fraction itself. Furthermore, it seems that it can make it harder for the algorithm to converge for highly inhomogeneous particles; additionally, the degradation of sphere fraction retrieval can lead to a globally worst core fraction retrieval. Inversions without polarisation and without noise globally show a good sensitivity to core fractions and, when converging properly, accurately reproduce assumed aerosol properties (except fine mode of the bimodal SDs). The radiances that include noise, greatly degrades the sensitivity and the retrieval of other properties leading, most of the time, to a shrinkage of regimes where retrieval of core fraction is reliable. Nevertheless, this issue can be partly resolved by using information on light polarisation, which has a great impact on the quality of the retrievals and enable defining scopes of applicability.

4.5 Effects of aerosol concentration on GRASP/ARIA retrievals

Objective and protocol

The main goal of this section is to observe the behaviour and quality of aerosol characteristic retrievals at different values of AOD. The idea is that with increase of AOD, multiple scattering interactions are increasing which can smooth the directional scattering features unique for core/shell particle structure. At the same time, low concentrations may present not enough signal for successful retrievals of aerosol characteristics. The concentration here is represented by its corresponding AOD value at 440 nm, e.g., the volume concentration expressed by 22 size distributions bins is adjusted to get a desirable value of AOD at 440 nm. The process thus consists in multiple running of forward radiative transfer calculations and renormalisation of the volume concentrations by obtained and desirable AOD. That is, dividing volume concentrations in all bins by an AOD from an initial run and multiplying them by the desired one. The chosen for the tests AODs are 0.05 (low), 0.1 (medium low), 0.4 (medium high) and 1.5 (high). As the effect was found to be linear and the previous section (4.4) displayed the results for AOD at 440 nm of 0.4, the finally presented results are only for the AODs of 0.1 and 1.5. The figures below display two types of scenarios chosen to illustrate the effects, but also not to multiply the figures, although more different scenarios were tested. The first scenario is retrievals without including the polarised radiances and without including the measurements noise in order to show the best theoretical sensitivity of measurements with minimised information content. The second scenario represents realistic measurements, that include the measurement noise but also improved information content by involving polarisation measurements. The figures illustrating other scenarios are available in the appendix (cf.

Analysis

Figure 4.11 (fine mode dominated size distribution) shows a global improvement of retrieval quality as aerosol concentration increases. The retrieval quality of imaginary refractive index and SSA are equivalent for both concentrations, however, the retrieval quality of other characteristics are improving as concentration is increasing. The sphericity fraction retrieval for AOD of 0.1 is moderately overestimated, while failures in the retrievals are associated with high residual. Retrievals for AOD of 1.5 are in a better agreement with the initially assumed values, except for cases of failures where residuals are also high. Recall that the residuals in synthetic

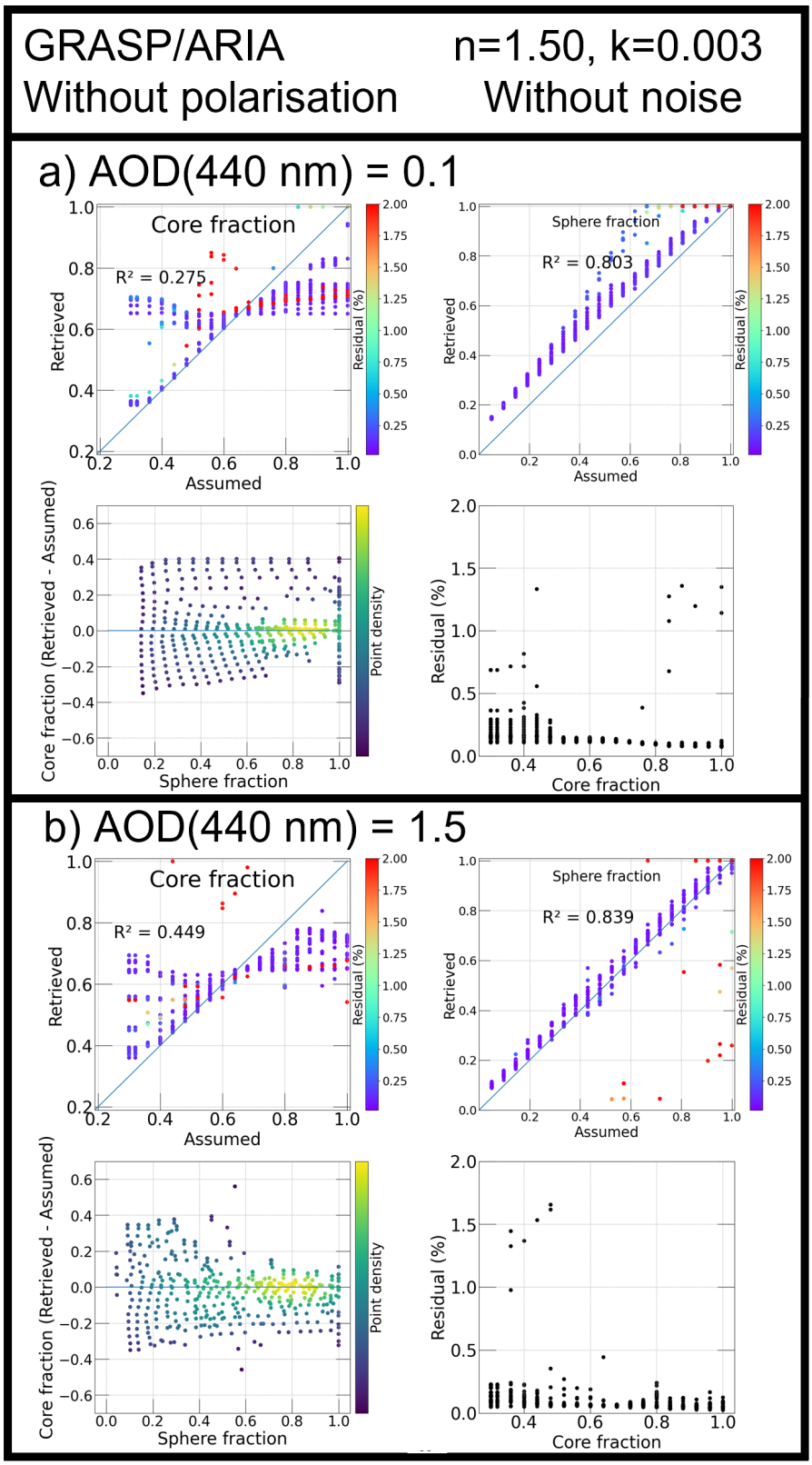

(4.11.1) Core and sphericity fractions, radiance residual. a) and b)

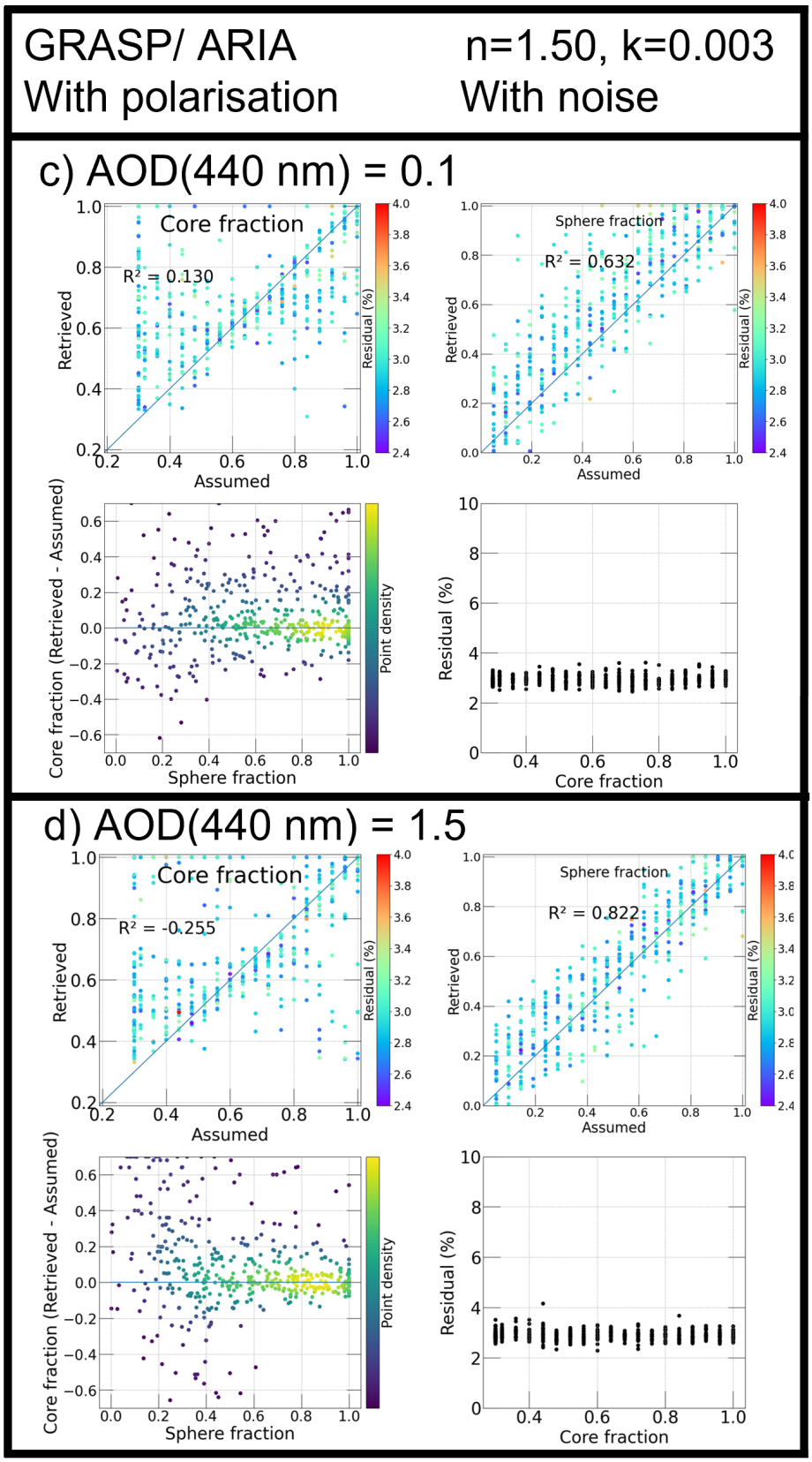

(4.11.2) Core and sphericity fractions, radiance residual. c) and d)

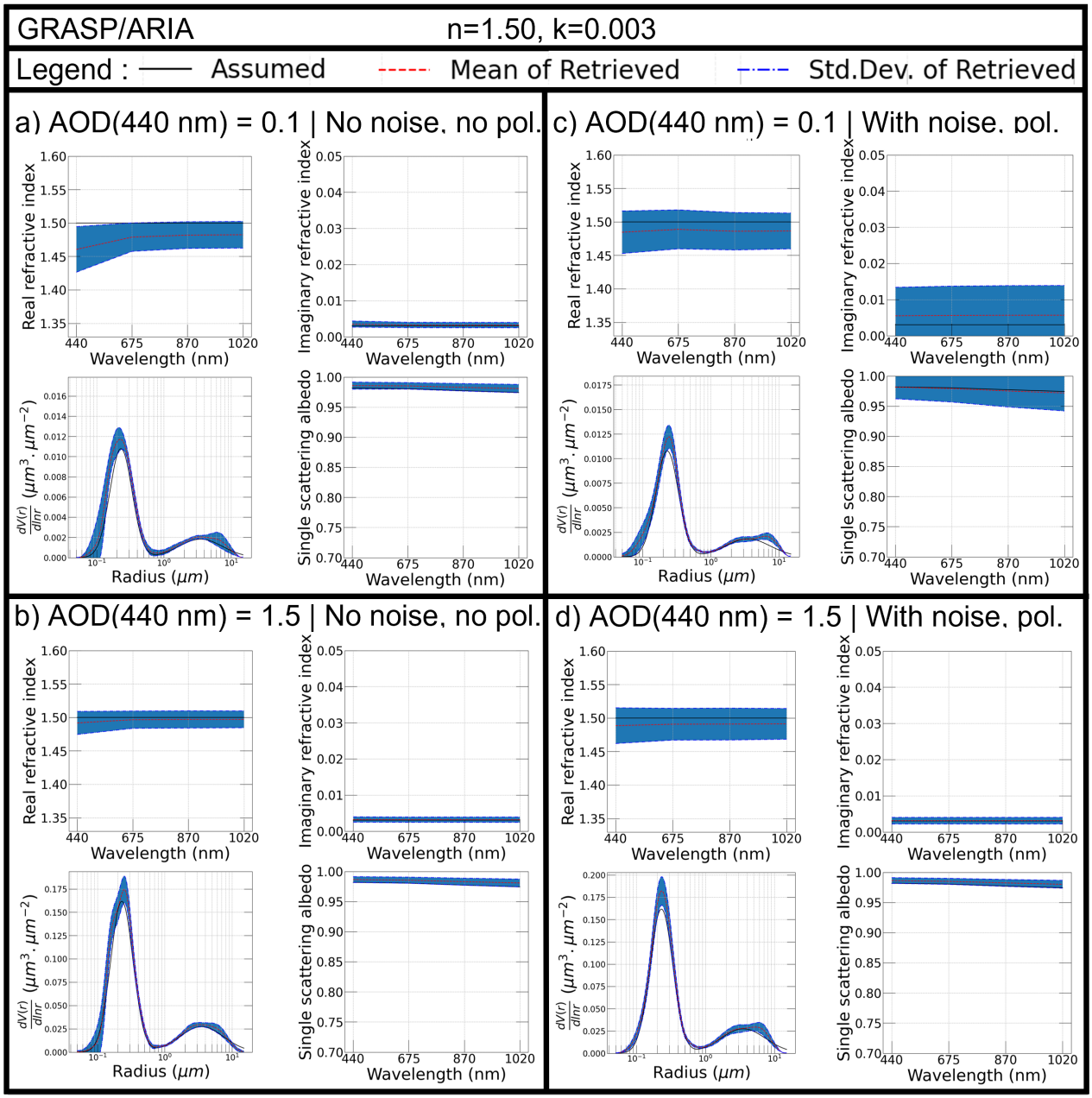

(4.11.3) Refractive index, Size distribution, SSA.

Figure 4.11: Collection of plots of aerosol optical and microphysical characteristics derived by inversion of synthetic AERONET measurements. The case of fine mode dominated aerosol size distribution and of refractive index n=1.50 and k=0.003. The radiances, are generated and inverted using GRASP/ARIA (with inhomogeneous aerosol model). In panels a) and b) are results without measurements noise and no polarisation, the AOD at 440 nm are a) 0.1 and b) 1.5. Panels c) and d) are the same, but simulation of measurements noise and polarisation are included.

test are expected to be very low as the measurements are created with the same aerosol models as retrieved. For the presented examples, for instance, there are 79 and 31 residuals, of 441 total number of retrievals, that are above 0.3% for AODs of 0.1 and 1.5, respectively. This tendency shows that as the AOD increases, the inversion algorithm generally converges better. However, at high AOD, some combination of aerosol characteristics also produces cases where the inversion does not converge well and the discrepancies in the initially assumed and retrieved core and sphere fraction are high. Retrievals of real refractive index show the most visible improvement as AOD increases, with a mean retrieved value is approaching the initially assumed, along with decreasing standard deviation. The size distributions for both cases, AOD of 0.1 and 1.5, are generally well reproduced, with the same tendencies as observed in the previous tests. Most of the presented conclusions are also true for tests that include the measurement noise and the polarisation information, except maybe for the real refractive index, for which the improvements can be more moderate. Retrievals of the core fraction show similar general improvements as AOD increases, except for situations where aerosol non-sphericity is important and the AOD is high. This situation has tendency to diminish the sensitivity to particles core/shell structure. The effect is expected as result of multiple scattering. It can be noted that there is no sensitivity to core fractions smaller than 0.35, which means that no matter the concentration, the effect of highly inhomogeneous fine particles can be compensated by other optical characteristics without increasing residual. Results suggest that the compensation is created by decrease of the real refractive index. It is because, when excluding assumed core fractions below 0.35, the retrieved mean values get closer to the assumed values and the standard deviation is also decreasing.

Figure 4.12 (coarse mode dominated size distribution) displays the opposite behaviour to fine mode dominated case. That is, the aerosol characteristics for coarse mode dominated size distribution are better retrieved for smaller concentrations. Figure 4.12 presents the results for AOD (440 nm) = 1.5, but it has to be noted that the results degraded even for AOD of 0.4, compared to 0.1 and 0.05. The effect of multiple scattering in the case of coarse mode dominated size distribution appears to be very important. The figures for AOD of 1.5 demonstrates the quality of the core and sphericity fractions retrieval when the inversion procedure does not converge.

Figure 4.13 illustrates, now, the results for bimodal size distribution, which in a way is combination of two previous cases. For measurements without noise and polarisation, it presents a

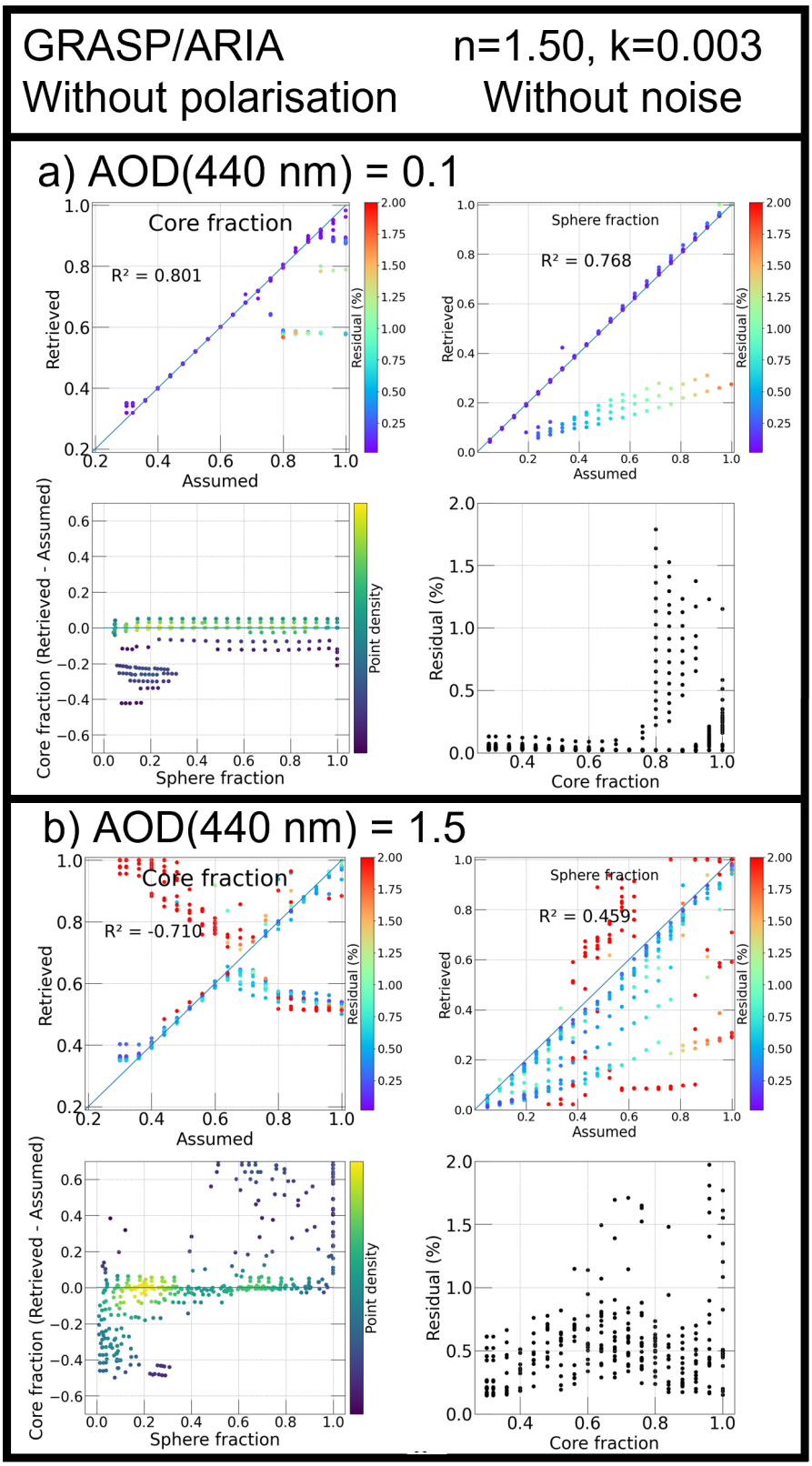

(4.12.1) Core and sphericity fractions, radiance residual. a) and b)

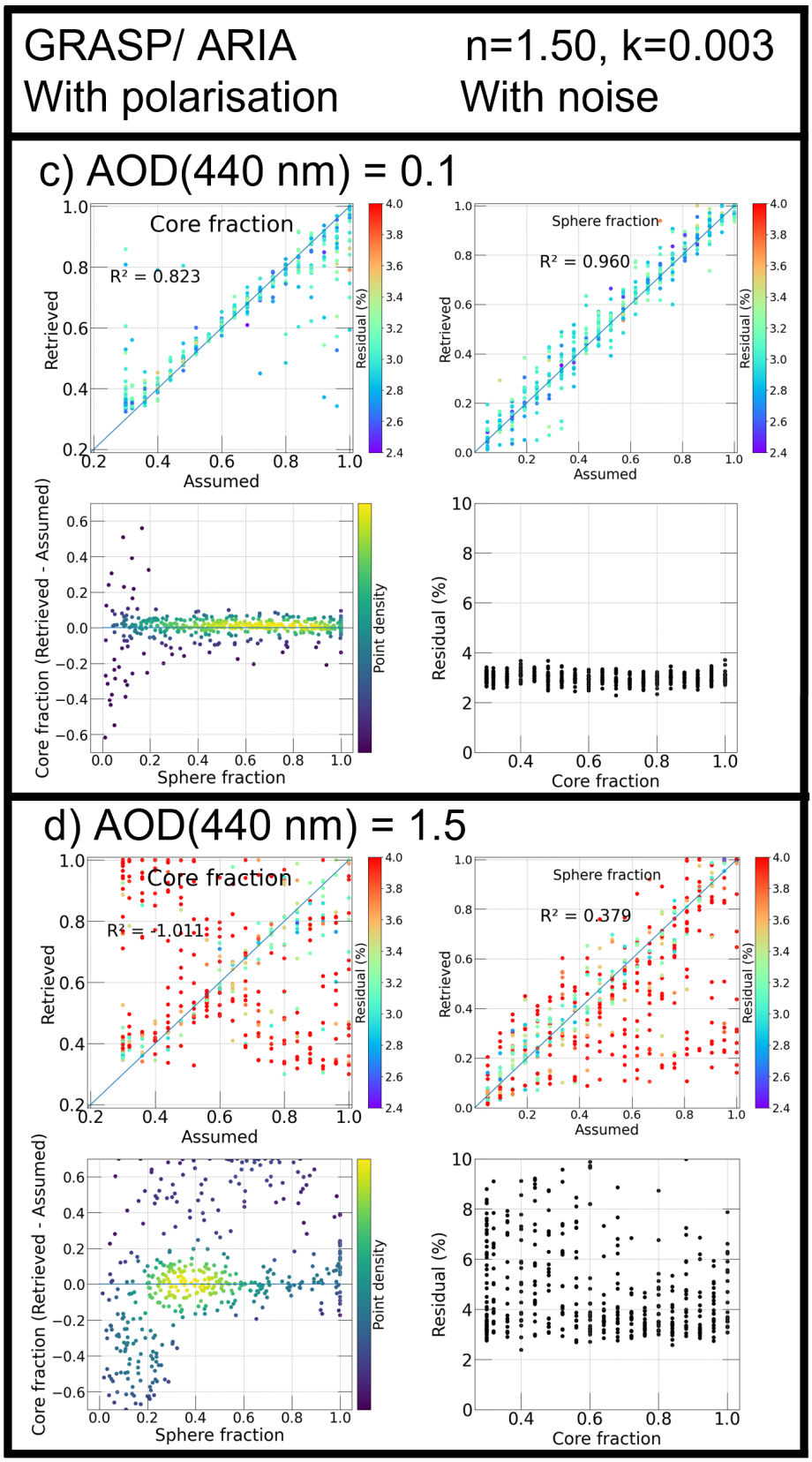

(4.12.2) Core and sphericity fractions, radiance residual. c) and d)

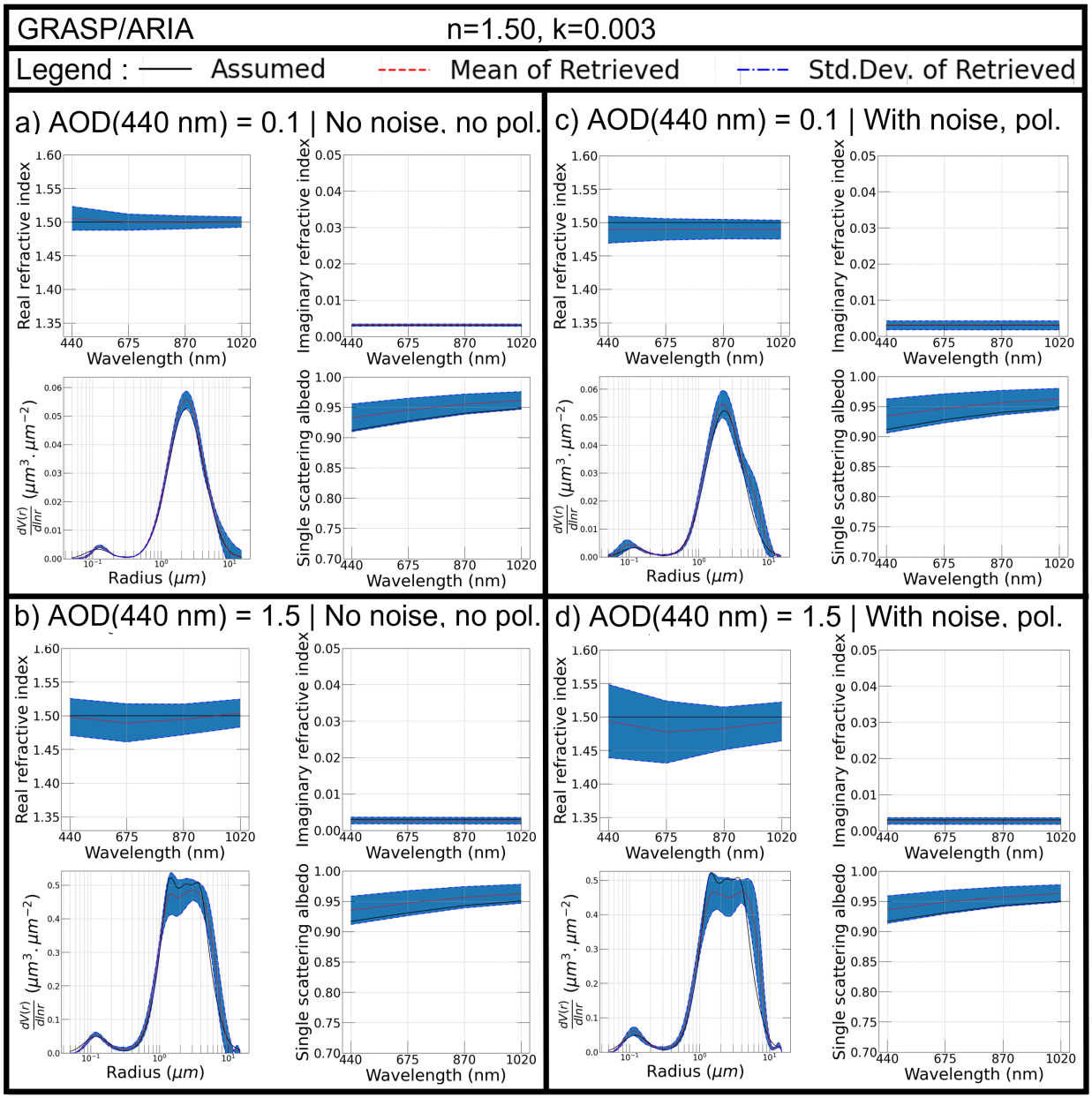

(4.12.3) Refractive index, Size distribution, SSA.

Figure 4.12: Same as 4.11, but for coarse mode dominated size distribution.

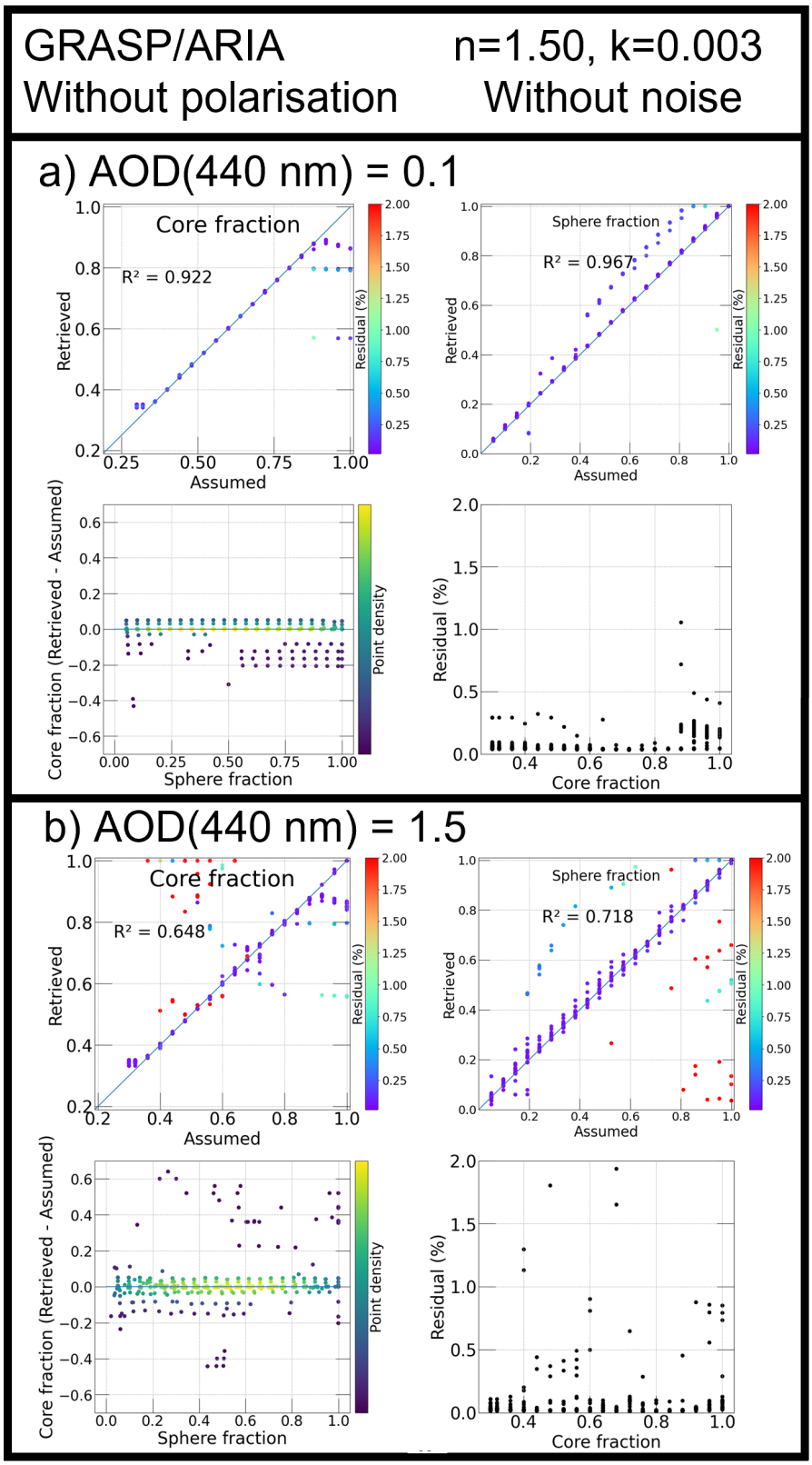

(4.13.1) Core and sphericity fractions, radiance residual. a) and b)

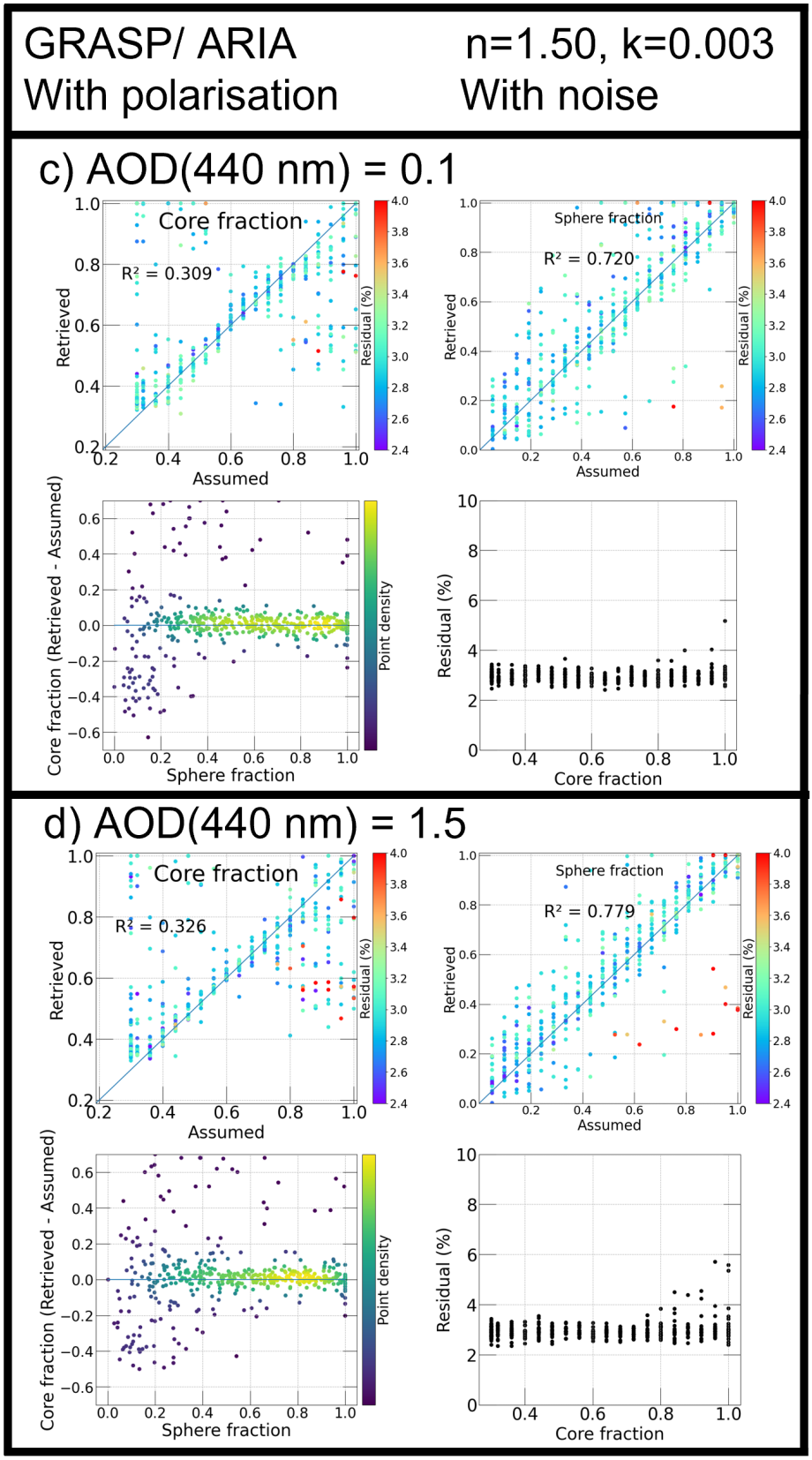

(4.13.2) Core and sphericity fractions, radiance residual. c) and d)

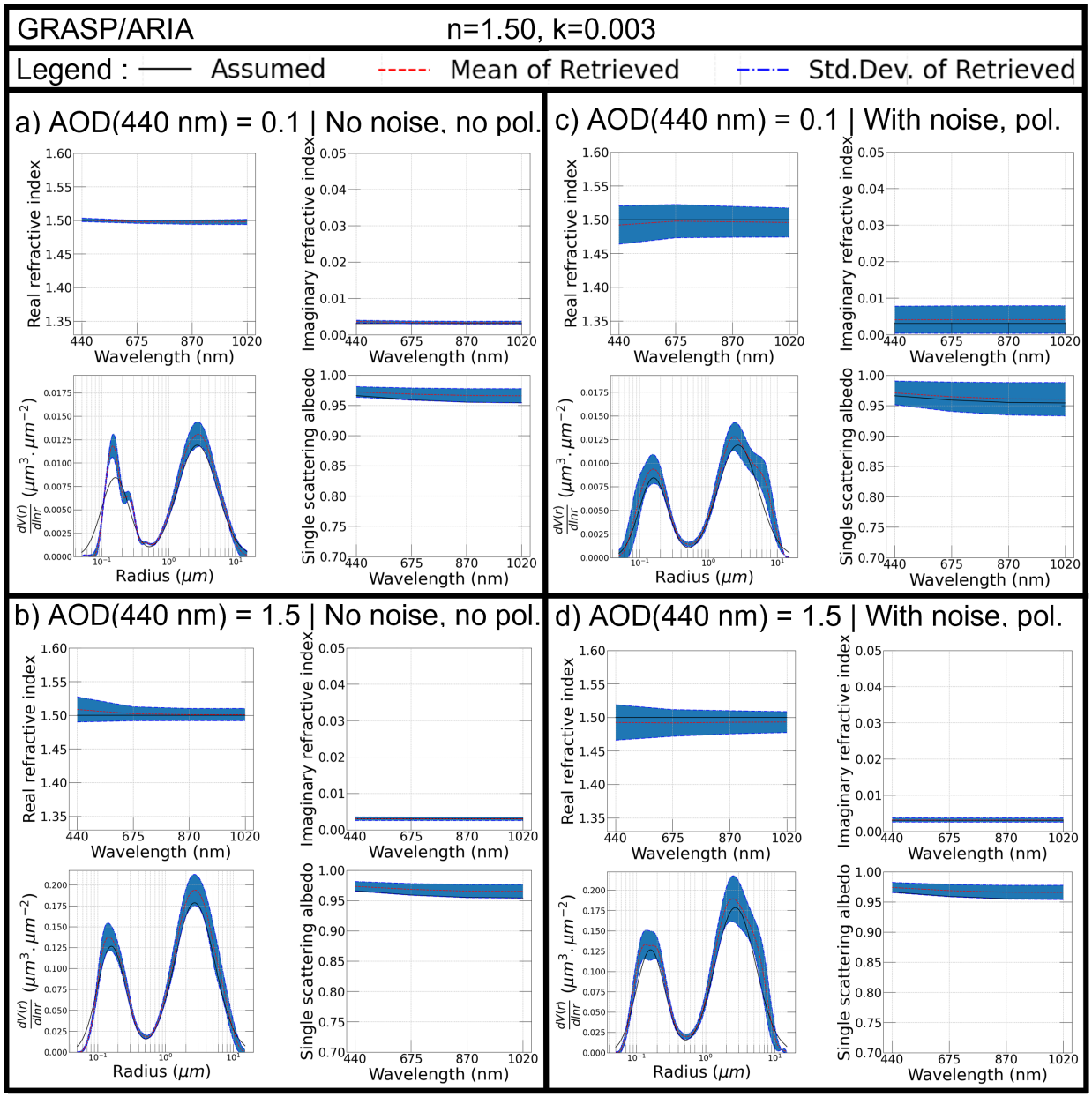

(4.13.3) Refractive index, Size distribution, SSA.

Figure 4.13: Same as 4.11, but for bimodal size distribution.

general degradation of the retrievals, as for coarse mode dominated size distribution. However, the degradation is much less important. Measurements with noise and polarisation, however, show an improvement like for fine mode dominated size distribution.

Intermediate conclusions

The effect of aerosol concentration on retrieval of aerosol inhomogeneity and distinction between core/shell and sphericity fractions was found to behave differently, depending on the dominated particles size. When fine mode dominates in aerosol size distribution, the increasing of AOD somewhat improves the retrieval of not only core/shell and sphericity fractions, but also of all other characteristics. However, in case of coarse mode dominated size distribution, progressive increasing of AOD and thus multiple scattering effect appears to be more important for smoothing the unique features of core/shell aerosol structure. The retrievals of core/shell and sphericity fractions fail completely at AOD(440 nm) of 1.5. Moreover, the results suggest loss of sensitivity and degradation in retrievals of all other parameters as well. The sensitivity is not improved even by involving of the polarisation measurements.

4.6 Conclusion

A general conclusion which can be drawn from these tests is that the quality of core/shell and sphericity fraction retrievals is related to the ability to separate these two features, while the rest of the retrieved aerosol characteristics is generally well in agreement with the initially assumed ones in these synthetic tests. In some regimes of dominate aerosol sizes, contrast in core/shell real refractive index, AOD and fractions of sphericity and core radius fraction, the retrievals work quite successfully even if polarised radiances are not involved in the retrievals. Including polarisation improves significantly the range of applicability of aerosol core/shell parameterisation and retrievals become valid in a wider range of regimes. The main advantage of polarisation is appearance sensitivity in case of fine mode dominated particles, which is the most difficult case for separating from non-sphericity.

Adding noise, which is mimicking real measurements, greatly impacts the quality of core fraction retrieval; for fine mode dominated particles, it can even reduce sensitivity as to not be able to define a scope where the core fraction can be retrieved simultaneously within a certain margin of error. Information on polarisation increases sensitivity in this case enough to regain

or increase the scope of applicability.

The main takeaway from tests on contrast is that the evolution of core fraction retrieval quality is not linear, there is a real refractive index threshold around 1.43 above which maximum sensitivity is reached, then there is even a slight decrease for the values above 1.60. Nevertheless, the most important contrasts in core/shell refractive indices have a positive effect on core fraction retrieval. Even if it produces some fluctuations in retrieval of all other parameters, like real refractive index, size distribution, sphere fraction, the results are still very satisfactory. Filtering of the results by the residual of fit also helps to select the cases when the contrast is sufficient and all parameters are reasonably retrieved.

The tests conducted with varying aerosol concentrations have shown that fine and coarse mode dominated cases, and bimodal size distributions respond differently in regimes of low and high aerosol loading. Fine mode dominated SDs have more sensitivity to increasing concentrations, i.e., increasing role of multiple scattering. In the case of coarse mode dominated SDs, increasing effect of multiple scattering can even cause a complete loss of sensitivity. The case of bimodal size distribution is generally less dependent on varying aerosol concentration than the coarse mode and is kind of compromise situation between two types of size distributions.

Chapter 5

GRASP/ARIA application to real AERONET measurements

5.1 Selected sites and their description

After assessing the theoretical potential of aerosol core/shell structure optical properties distinction and after inversion of synthetic measurements, the algorithm is now applied to real sunphotometric measurements from AERONET. This application and the results are presented and discussed in the current section. The selected AERONET sites for the algorithm application, also described in section 2.3, belong to two groups; those that provide light intensity measurements only and those that, in addition, provide information on light polarisation. Indeed, the study of synthetic photometric measurements with DoLP demonstrated a substantial improvement of the core/shell fraction retrieval, however, the number of sites that provide polarisation measurements represent only a small fraction of all AERONET sites. Moreover, the number of measurements that satisfies the quality criteria and can be used for the inversion are even more limited. All AERONET sites that provide polarisation measurements have been used or at least examined in this work. Nevertheless, because the number of such sites is very limited, the sunphotometric measurements without information on polarisation are also considered and the performance of the core/shell structure retrieval is evaluated.

It is important to remind here that the inversions of real AERONET measurements are performed with the same algorithmic settings as it was for inversion of the synthetic measurements. This approach, first of all, implies the use of unique settings and secondly it implies consistency that ensures the comparative analysis between the results of synthetic and real inversions. In the study employing synthetic measurements, the data was divided according to the size distribution, i.e., fine, coarse and bimodal, to mimic the variety of real conditions. In the case of real measurements in this section, the analysis will be conducted for the sites that represent different dominant aerosol type. In addition, the aerosol size dominance will also be classified based on the Angström exponent (α). For instance, fine particles dominated size distributions generally correspond to $\alpha > 2$, coarse as $\alpha < 0.5$ and bimodal in between these two values.

5.2 Inversion quality assessment

Approach and results analysis

Before addressing the specific figures of this section (cf. figures 5.1), their general structure is presented as following. The figures are composed of panels corresponding to ensembles of graphs describing aerosol microphysical and optical characteristics resulted from inversion of real AERONET measurements using GRASP/ARIA and GRASP/Standard algorithms. The data points in these graphs correspond to specific AERONET measurements. As presented above, GRASP/ARIA refers to the newly developed algorithm, where reproducing the measured radiances is handled by kernels that incorporate the newly presented aerosol core/shell structure parameterisation (inhomogeneous particles), while GRASP/Standard refers to the usage of kernels that are similar to operational AERONET algorithm (homogeneous particles). Besides the fraction of core, the figures present intercomparison of the retrieved sphericity fractions, size distributions and refractive indices using two algorithms, GRASP/ARIA and GRASP/Standard, aiming to analyse differences, possible compensations of optical or microphysical properties or some tendencies. Analysis of each of these parameters has for objective to understand the impact of the new core/shell parameterisation model on the retrievals.

- The first graph in the panel compares the percentage of the residual in fitting the measured radiances by GRASP/ARIA and by GRASP/standard. It represents the quality of the retrieval, the one-to-one line is the marker of equal results; the dots below the line mean that GRASP/ARIA demonstrates better reproduction of radiances and worse when above. Three ranges of the quality of the residual can be considered here: the "equivalent

residuals" corresponding to the difference $residual_{ARIA} - residual_{standard} = 0 \pm 0.5\%$; the "worse residuals" corresponding to $residual_{ARIA} > residual_{standard} + 0.5\%$ and the "better residuals" corresponding to $residual_{ARIA} < residual_{standard} - 0.5\%$. The colour of the dots display the value of the core fraction retrieved by GRASP/ARIA. The second displays the most impacted factor by the change of model and the most important to interpret core fraction values as it only concerns the spherical part. The colour of the dots display the value of the radiance residual of the GRASP/ARIA retrieval.

- The second graph, that displays the retrieved fraction of spherical aerosol by GRASP/ARIA and by GRASP/standard, shows the results most impacted by the change of the aerosol model. This graph is in fact the most important for interpreting the core fraction values because of an interplay between the effects of inhomogeneity and non-sphericity on the directional light scattering, as discussed above.

- The third graph shows the number of sphericity fractions equal to zero and one, i.e., the algorithmic limits, considering the aerosol population either fully spherical or fully non-spherical. More often, reaching the algorithmic limit indicates a lower dynamic of the retrieved parameters and possibly indicates that convergence has reached a local minimum of the gradient descent. The decrease in the number of data points reaching this limit does not necessarily equate to an improvement due to the introduction of the new aerosol parametrisation, but still indicates a better dynamic of the retrievals and is rather positively contributing to the algorithm convergence.

- The fourth, fifth and sixths graphs are respectively the size distribution, the spectral dependence of real and imaginary refractive indices, presented in a similar manner to that in Chapter 4. The purpose of these graphs is an intercomparison between two versions of the algorithm, i.e. GRASP/ARIA and GRASP/Standard. However, as previously explained, in the case of the core/shell model, the retrieved refractive index is one of the core, whereas in the case of the “standard” aerosol model, the retrieved is an effective refractive index for the entire particles. At the same time, depending on the average size of the shell, the proportion of inhomogeneous spherical aerosol (core/shell model concerns spherical particles only) and homogeneous non-spherical model, the refractive index retrieved by GRASP/ARIA can approach or deviate to a greater or lesser extent from the one of GRASP/Standard. For example, if the ensemble of the retrieved particles

will be non-spherical in GRASP/ARIA, the retrieved refractive index will be the one of an effective homogeneous particle.

Measurements without polarisation

The GRASP/ARIA algorithm was applied to quite large number of sites, however, from all the studied sites, only a few representative cases are finally displayed here; essentially the cases of urban, desert and mixed aerosol types; each representing different aerosol size range and potentially composition.

Figure 5.1 shows an intercomparison between the retrievals performed with GRASP/ARIA and GRASP/Standard for the AERONET sites of Lille and GSFC, i.e. urban aerosol dominated sites. In both cases, the use of GRASP/ARIA led to an improvement in residuals for approximately 72% of the total measurements, with about 30% showing an improvement greater than 0.5%. This overall reduction in residuals is encouraging and suggests that the model provides more accurate representation of atmospheric aerosols. It should be mentioned, however, that reduction in the residual can be also due to introducing an additional retrieved parameter which increases the number of degree of freedom in the inversion. This added flexibility allows for a finer adjustment of the radiance and thus can facilitate convergence. This situation can be defined as "overfitting", but in this case the inversion results would become very sensitive to the initial guess. The sensitivity to initial guess was thus verified by running inversions with different initial guess assumptions. The conclusion was that the obtained results are practically the same whatever initial guess is, i.e. do not depend on the initial guess. The former indicates that the improvement in the residual of fit is not due to an overfitting. Despite this general improvement, relative to the employment of homogeneous aerosols model only, approximately 28% of the radiance fitting is still exhibiting somewhat degraded residuals, with about 12% exceeding the degradation of 0.5%. At the same time, the change of aerosol model also implicitly means a change in the effect of the constraints imposed and it is quite normal that the new parameterisation does not improve the retrievals in all situations.

An examination of the population of the retrievals associated with higher residuals (degradation in the residual exceeds 0.5%) revealed that, in this case, the predominately retrieved core fractions is ranging between 0.6 and 0.8 (see graph 1). This range of core fractions accounts for 76% of the cases for Lille and 80% for GSFC. In contrast, for measurements with

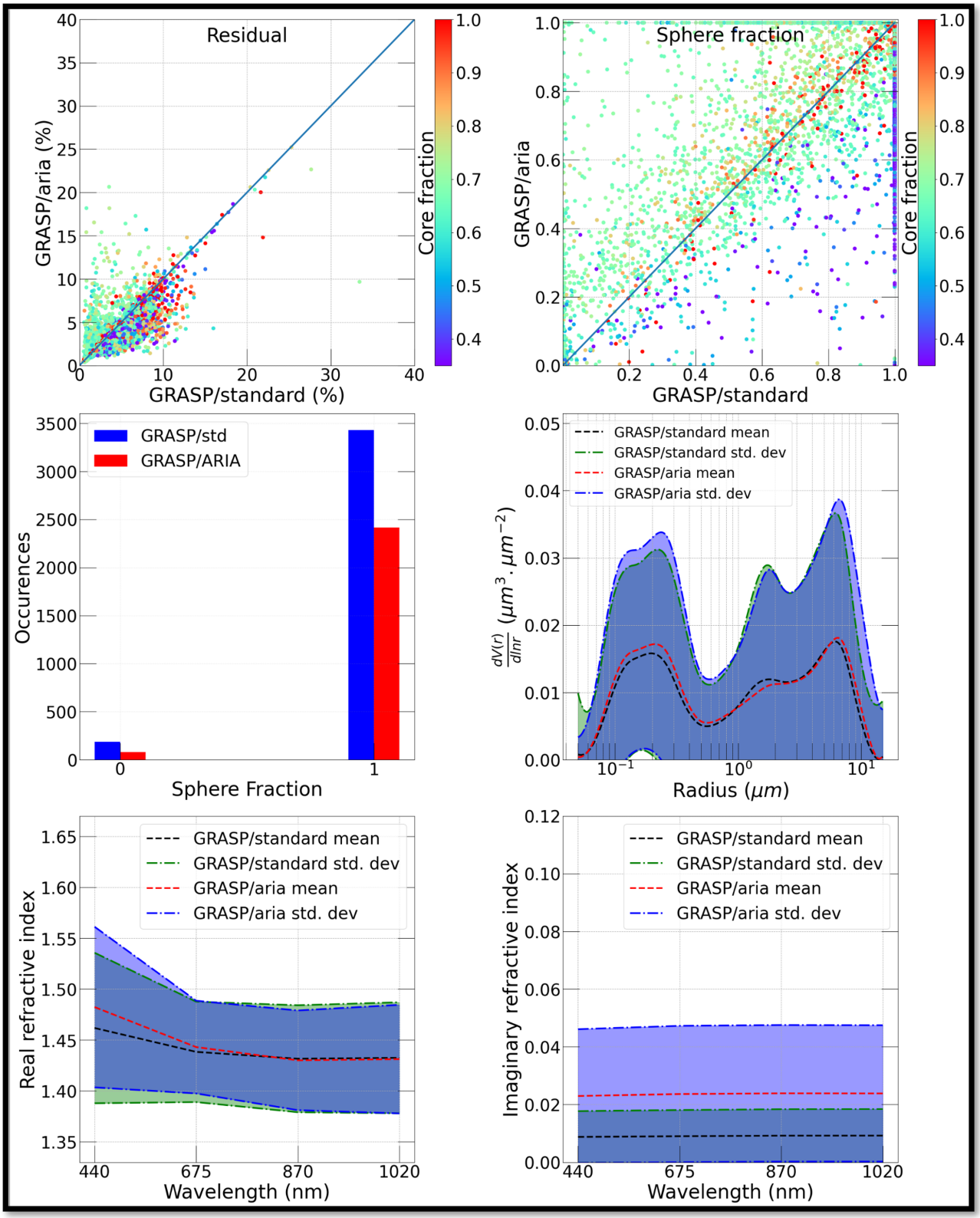

(5.1.1) Lille AERONET site

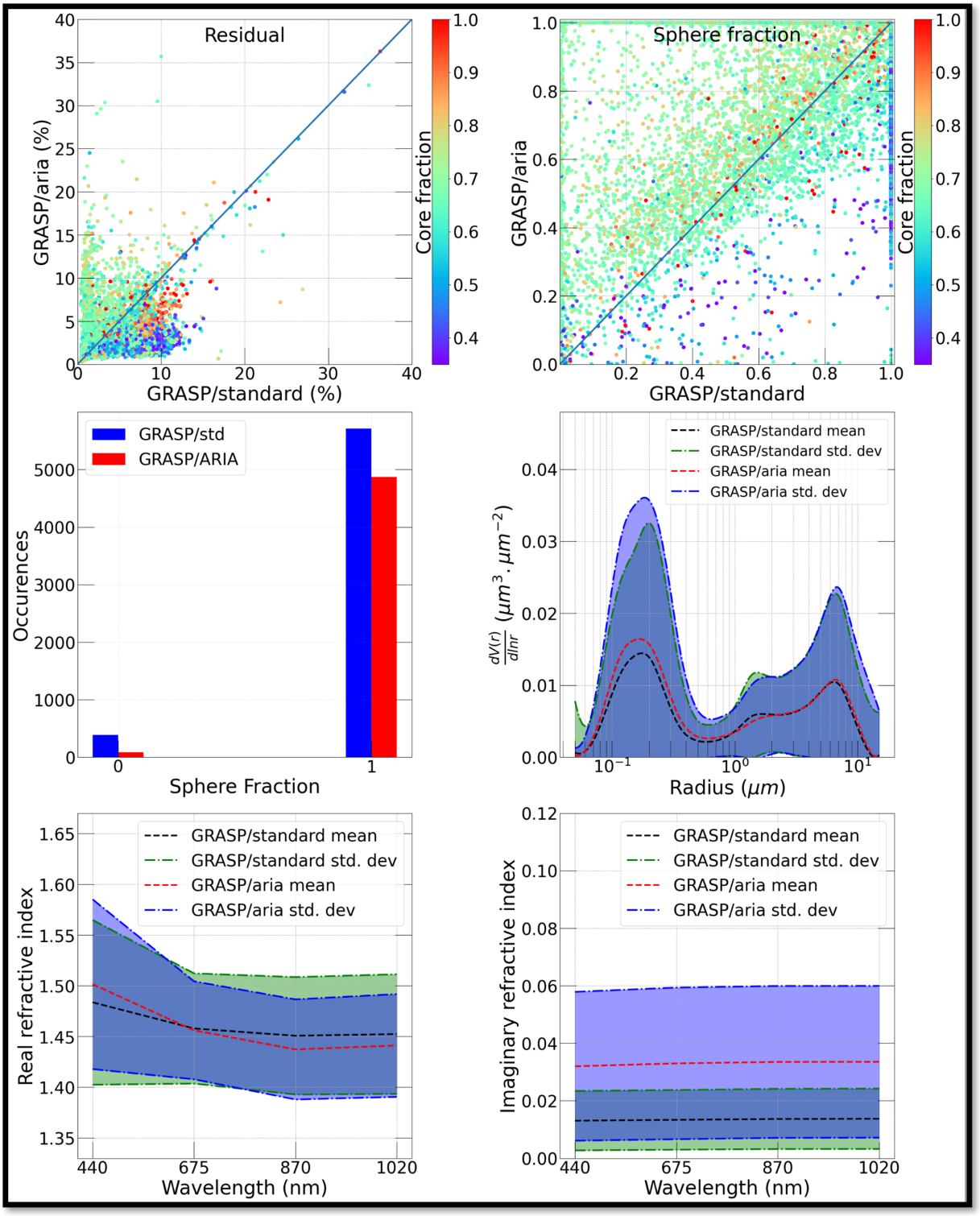

(5.1.2) GSFC AERONET site

Figure 5.1: Collection of plots of aerosol optical and microphysical characteristics retrieved by GRAS/ARIA and GRASP/Standard using real AERONET measurements for the period from 2008 to 2025, for the sites representing urban aerosol.

lower residuals (improvement in the residual exceeds 0.5%), the representation of this core fraction range decreases substantially, to 41% for Lille and 46% for GSFC. This observation is consistent with the results of tests using synthetic measurements, especially for a bimodal size distribution (see Fig. 4.5). That is, the retrieved core fraction appears to "get stuck" around 0.7 without improving the residual of the radiance fit, indicating a regime of a combination of aerosol parameters where the sensitivity is lost. The retrieved sphere fraction shown in graph 2 is generally similar for GRASP/ARIA and GRASP/Standard, with the exception of cases where the retrieved values reach the algorithmic bounds. Up to half of the measurements retrieved with GRASP/Standard display the sphericity fraction values reaching unity, whereas GRASP/ARIA reduces this proportion (cf. graph 3), yet both models rather agree on the retrieved sphericity fraction in 50% of those cases. The parts were the two algorithms disagree, strongly correlates with the general quality of the retrieval - better retrievals (as defined in 5.2) coincide with a wider range of sphericities where the standard model reached algorithmic bounds; the worse quality of the retrievals coincide with the core/shell model reaching algorithmic bounds where the standard model exhibits a variability of the sphericity fraction (cf. appendix A.4.2).

This is in line with the previous analyses using synthetic measurements that showed the situations of limited sensitivity - the retrieved core fraction tends to fall within the range of 0.6 – 0.8, consequently, the sphericity fraction retrieval becomes affected as well. When the range of 0.6 – 0.8 of the core fraction is excluded from the analysis, similar sphericity fractions by GRASP/ARIA and GRASP/Standard are generally associated with core fractions close to unity, i.e., both algorithms find the same homogeneous aerosol model. This agreement between two versions of the algorithm weakens when stronger fraction of non-spherical particles appear, which means that presence of non-sphericity starts to influence the core/shell model retrieval. It was also noted that more important sphericity fraction estimates are predominantly associated with the core fractions ranging between 0.6 and 0.8, which is in line with the previous analysis showing a tendency of the algorithm to overestimate sphericity when there is a lack of the measurements sensitivity in the aerosol inhomogeneous model. The study of synthetic measurements without involving the polarisation, leads to believe that an important part of the measurements still lack sensitivity to the inhomogeneous aerosol model and that core fraction retrievals may strongly differ from the expected one, even if the residual of the fit is improved.

The mean size distributions (graph 4) show quite the same shapes except for a slight increase in

fine mode concentration, although, it is not persistent through all measurements. It should be noted that the shape of the retrieved SD is influenced by the degree of fit of the radiances and also known to be correlated with the retrieved real part of refractive index (graph 5), as both influence the light refraction. Nevertheless, equivalent residuals generally display the same SD; for the worse residuals however was observed a tendency to shift the particle radius towards smaller sizes, while for the better, towards bigger. The increase in the particle size is eventually in line with adding a liquid shell and consistent with an improved residual when the core/shell model is employed, however, it is associated with an unexpected spectral dependency of the refractive index (cf. appendix A.4.2). Hence, there remains a possibility that the increase in particle size and in refractive with a spectral dependency could originate in an algorithmic optimisation and does not represent reality.

Besides, the diminusion of particle size for worse residual cases could be the cause of the algorithmic path leading to a local minimum in the gradient descent where sphericity, core fraction, refractive index and size distribution can compensate one another enough for the algorithm to be unable to escape from this minimum. The conditions are, most likely, in the majority of the cases, an overestimation of the sphericity, a core fraction in the interval from 0.6 to 0.8 and an underestimation of the particle size coupled with an underestimation of the real refractive index (cf. appendix A.4.2). The imaginary part of the refractive index (graph 6) generally corresponds to the expected values, that is a value superior to the one of GRASP/Standard and an increasing difference with growing size of the shell and sphericity. It, however, does not seem to be less influenced by the interplay with the size, inhomogeneity and sphericity fraction.

Figure 5.2 shows the intercomparison between retrievals by GRASP/ARIA and GRASP/Standard for the AERONET sites Sede Boker and Kanpur representing mixed types of aerosol. For the Sede Boker site, residual of the radiance fit was improved in approximately 85% of the total measurements, with about 16% showing an improvement greater than 0.5%; whereas for Kanpur, it is respectively 51% and 9% . As for the measurements that show a degradation greater than 0.5%, it concerns around 1% of the measurements for Sede Boker and 25% for Kanpur.

A closer look on the retrieval results from Sede Boker showed that in the cases with worse fitting of the radiances by GRASP/ARIA than by GRASP/Standard, more than half of them have the sphericity fraction reaching the unity. It is also interesting to note that when the sphericity fraction is unity in the retrievals by GRASP/Standard, the retrieved size distributions can

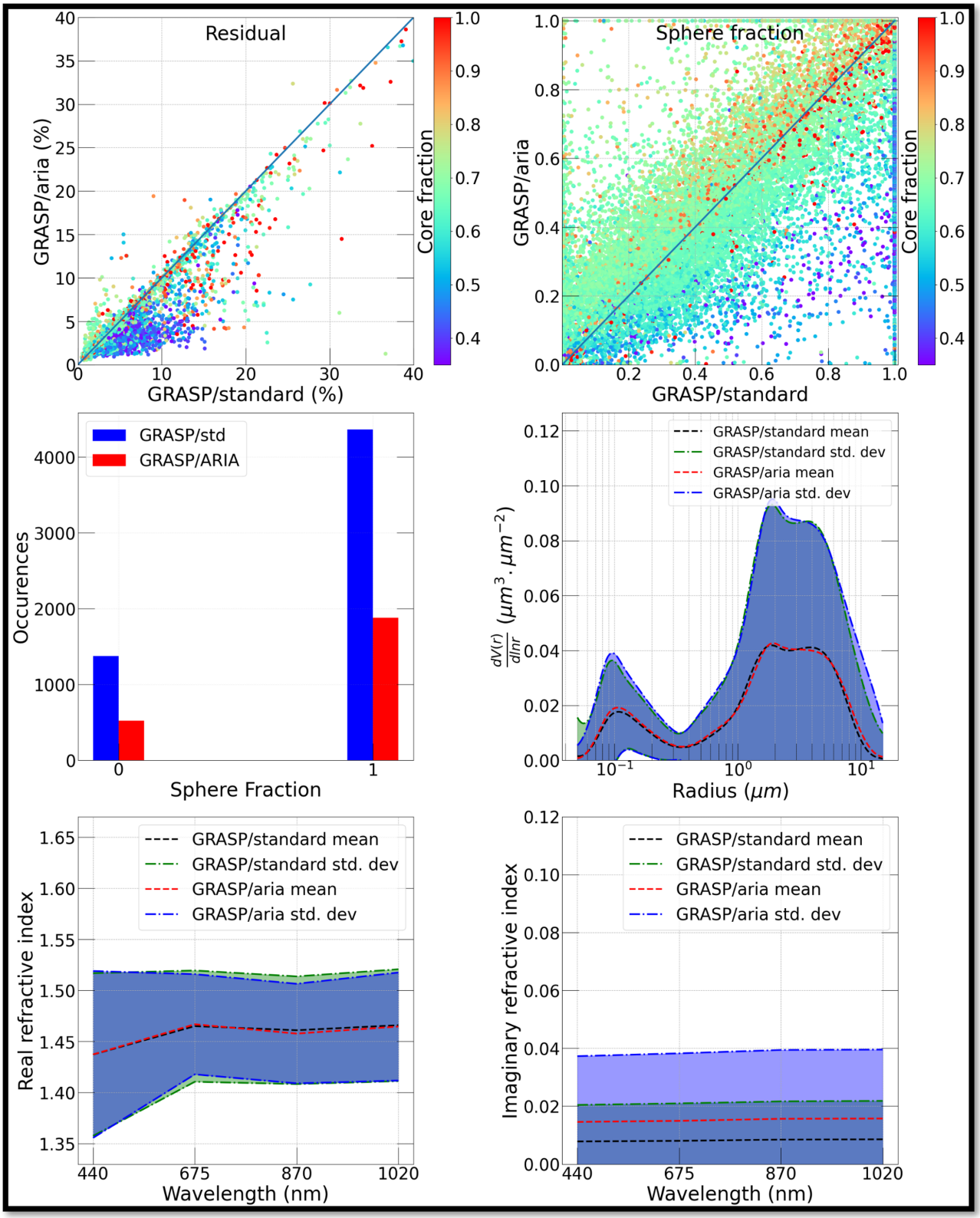

(5.2.1) SEDE_BOKER AERONET site

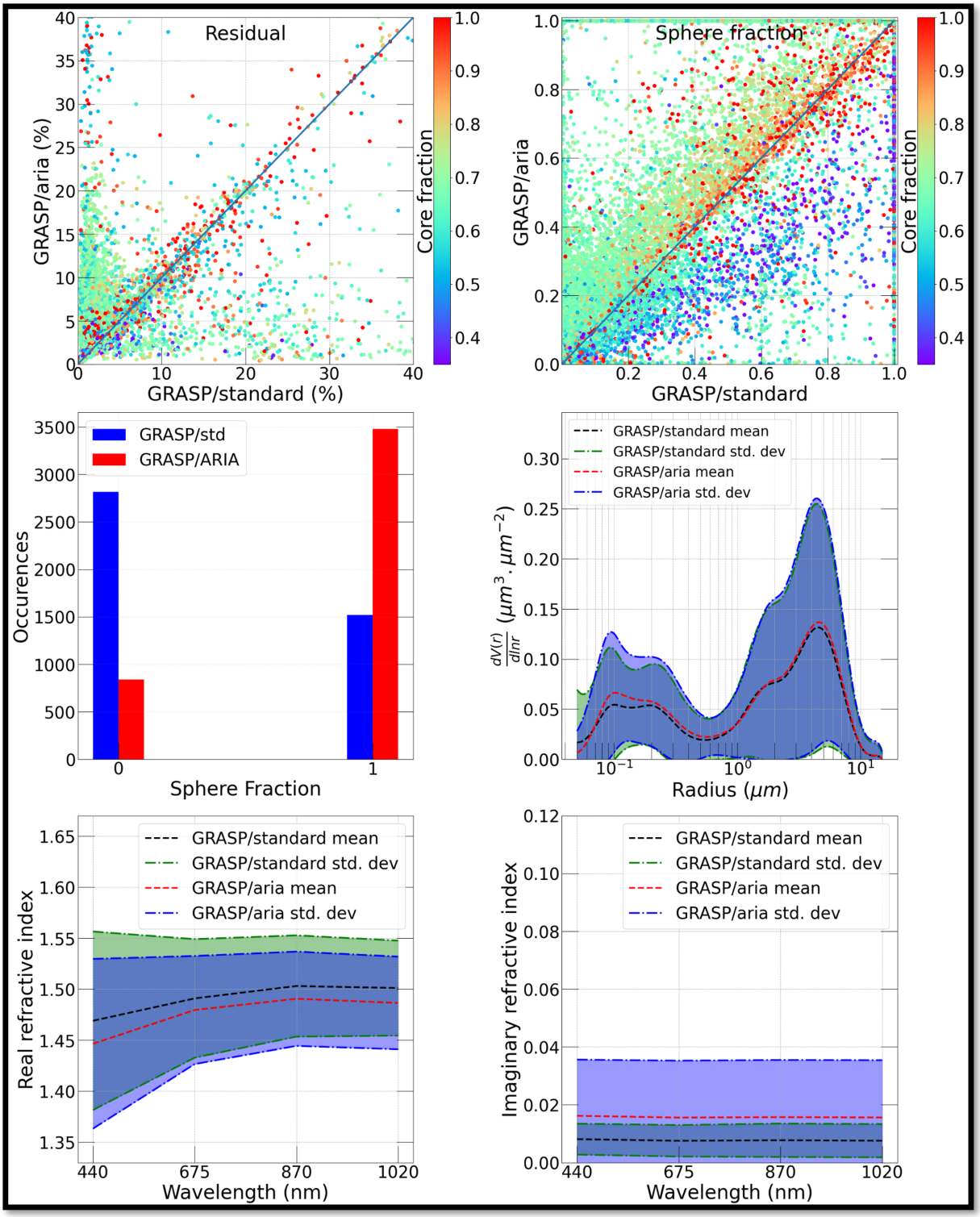

(5.2.2) Kanpur AERONET site

Figure 5.2: Same as Figure 5.1, but for AERONET sites representing mixed aerosol type.

present unexpectedly high concentrations in the first and the last bin which corresponds to an algorithmic attempt to compensate some non-existing microphysics (cf. 4.1). Thus, this could not be so much GRASP/ARIA retrieving worse radiance residuals as GRASP/Standard that attempts to fit the measurements by unrealistic microphysics without having a better description of the aerosol model. Contrarily to the previous sites, worse residuals show an increased radius for fine particles, equally for coarse ones, yet the real refractive index is still smaller for GRASP/ARIA than for GRASP/Standard.

Besides, the overwhelming majority of the measurements show equivalent radiance residuals in the case of both algorithm versions and have the same sphericity fraction. The sphericity fractions reaching the algorithmic bounds are however reduced by half in the case of GRASP/ARIA. The SD is quite similarly retrieved for two algorithms. The residual improvement was found to be related to a better dynamic in the retrieved sphericity fraction that reached the algorithmic bounds for the standard model but not for core/shell. An artificial increase of the last bins of SD was however still appearing for GRASP/ARIA, but in only a few cases and the residual was worse than of GRASP/Standard. For the Sede Boker site, the majority of the measurements (82%) show a very limited impact of adding the inhomogeneous aerosol model, meaning that the homogeneous aerosol model satisfies well the measured radiation field in these cases. Nevertheless, the measurements that do have an improvement in the residual, display a supposedly good sensitivity to core fraction for improvements greater than 1%. While in cases when the improvement in residual is bellow 1%, we find that the sphericity fractions agree well between the models, that is also paired with the core fraction between 0.6 and 0.8, strongly advocating for a lack of sensitivity to core fraction, as discussed previously. This conclusion is similar for the Kanpur site.

However, the results for the Kanpur site are more difficult to interpret because in many cases the convergence is generally hard to attain in the retrievals from both models. Looking at the measurements below 10% of residuals in radiance fit, graph 1 doesn't show any correlation between the proximity of the residuals and the core fraction, yet, the sphere fraction graph displays the same characteristics as for the previous case and for the other optical characteristics. The lack of dependency between residuals and core fraction may, then, reside in the ability, or lack thereof, of both model to describe the observed aerosols.

Figure 5.3 shows the comparison between retrieval results for Tamanrasset and Dakar, i.e.

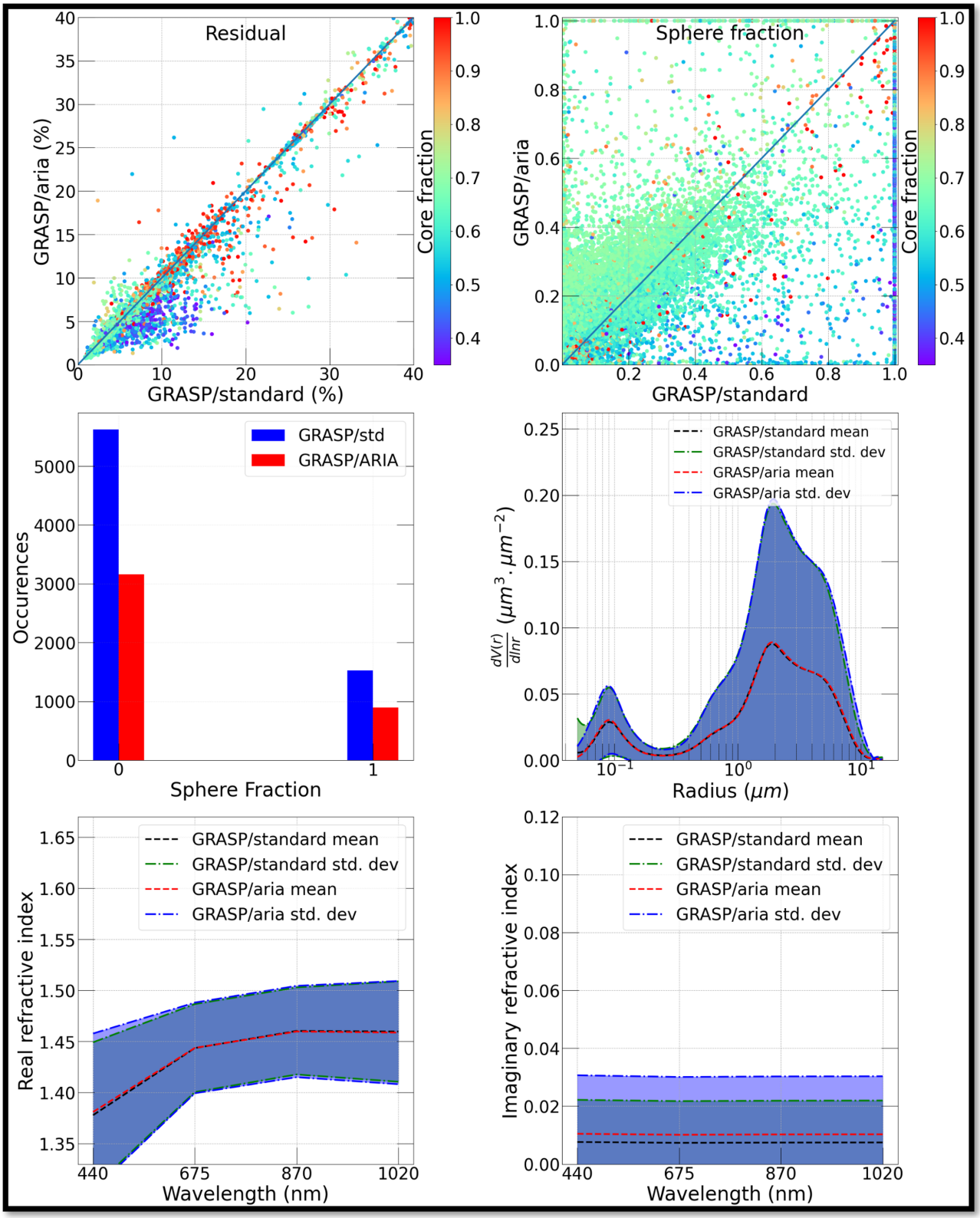

(5.3.1) Tamanrasset AERONET site

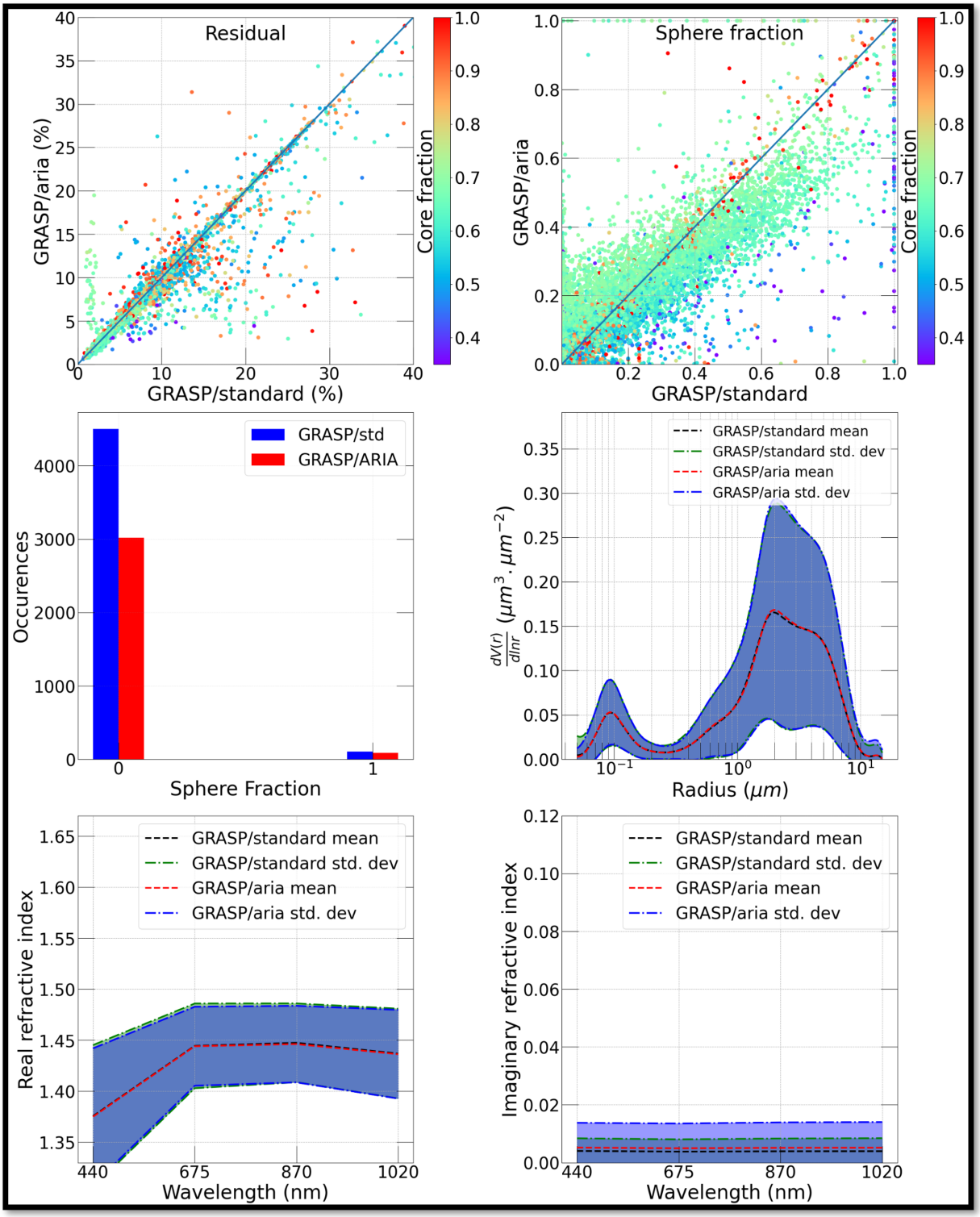

(5.3.2) Dakar AERONET site

Figure 5.3: Same as Figure 5.1, but for AERONET site dominated by desert dust aerosol.

desert aerosol dominated sites. Polarisation measurements are not available for these two sites. For these desert sites, application of GRASP/ARIA generates similar results. Contrarily to the previous sites, those present smaller fractions of aerosol sphericity and more coarse mode dominated size distributions. The radiance fitting residual is quite similar in about 85% of cases and in about 12% of cases the residual is improved, while only in about 2% is degraded when the GRASP/ARIA algorithm is used. Similarly to the Kanpur site analysis, the conclusions are derived for the cases when the residuals are below 10% because, in the cases of lack of convergence, the interpretations can be misleading. The measurements with residuals that show improvements, display a consistency between the core fraction and the sphericity fraction retrievals in the regimes that were found as favourable for sensitivity in the study using synthetic measurements for coarse mode dominated size distributions. The results also display expected values for the refractive index; the derived by both versions of the algorithm SDs are very similar.

With information on polarisation

As discussed above, the degree of linear polarisation of light provides an important information content for aerosol retrievals, especially for fine particles. Indeed, it increases the ability to separate between non-sphericity and core/shell aerosol model, as found in the tests with synthetic measurements. As only few AERONET sites provide measurements with polarisation, the results available for the analysis are quite limited, unfortunately.

Figure 5.4 shows the results for the same urban sites as previously presented without information on polarisation, i.e., Lille and GSFC. However, the measurements in Lille can hardly be used to draw definitive conclusions because of very limited number of available observations. Nevertheless, interesting characteristics can still be witnessed for GSFC. Indeed, the GSFC site possesses much more measurements and patterns seem to emerge. First of all, the residuals, like for measurements without polarisation, are typically improved by the use of the core/shell aerosol model; for GSFC it is better in 46% of cases, 44% equivalent and 10% worse. This is another clue that the model can better describe aerosol interaction with light as the inversion procedure has to fit not only the intensity of light scattering, but also the DoLP. Looking at the residuals, it emerges that the higher the residual is in case of GRASP/Standard, the smaller the core fraction is. This is in favour of sensitivity to core/shell as the standard model tends to struggle more to reproduce measurements with high impact of inhomogeneity. In the

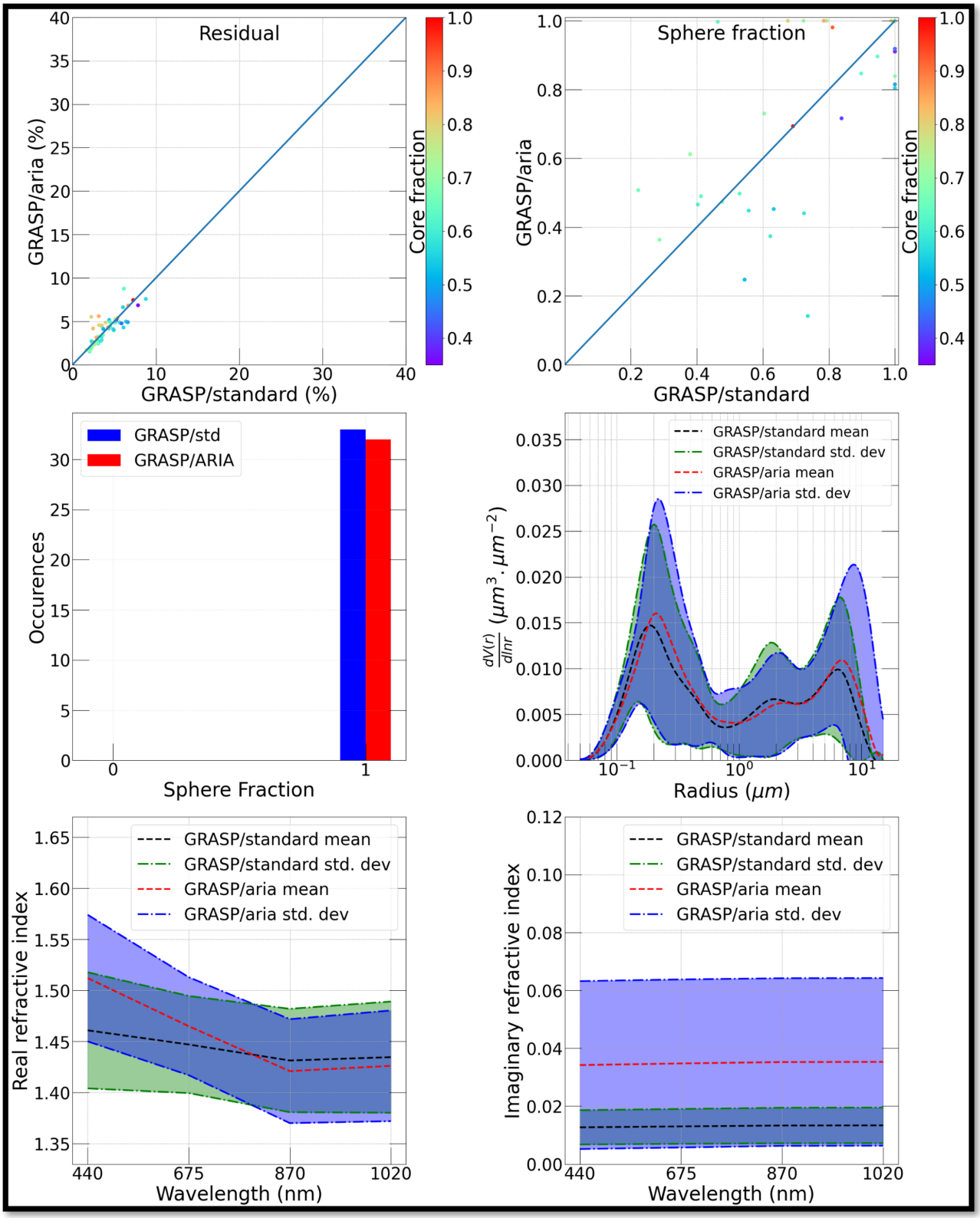

(5.4.1) Lille AERONET site

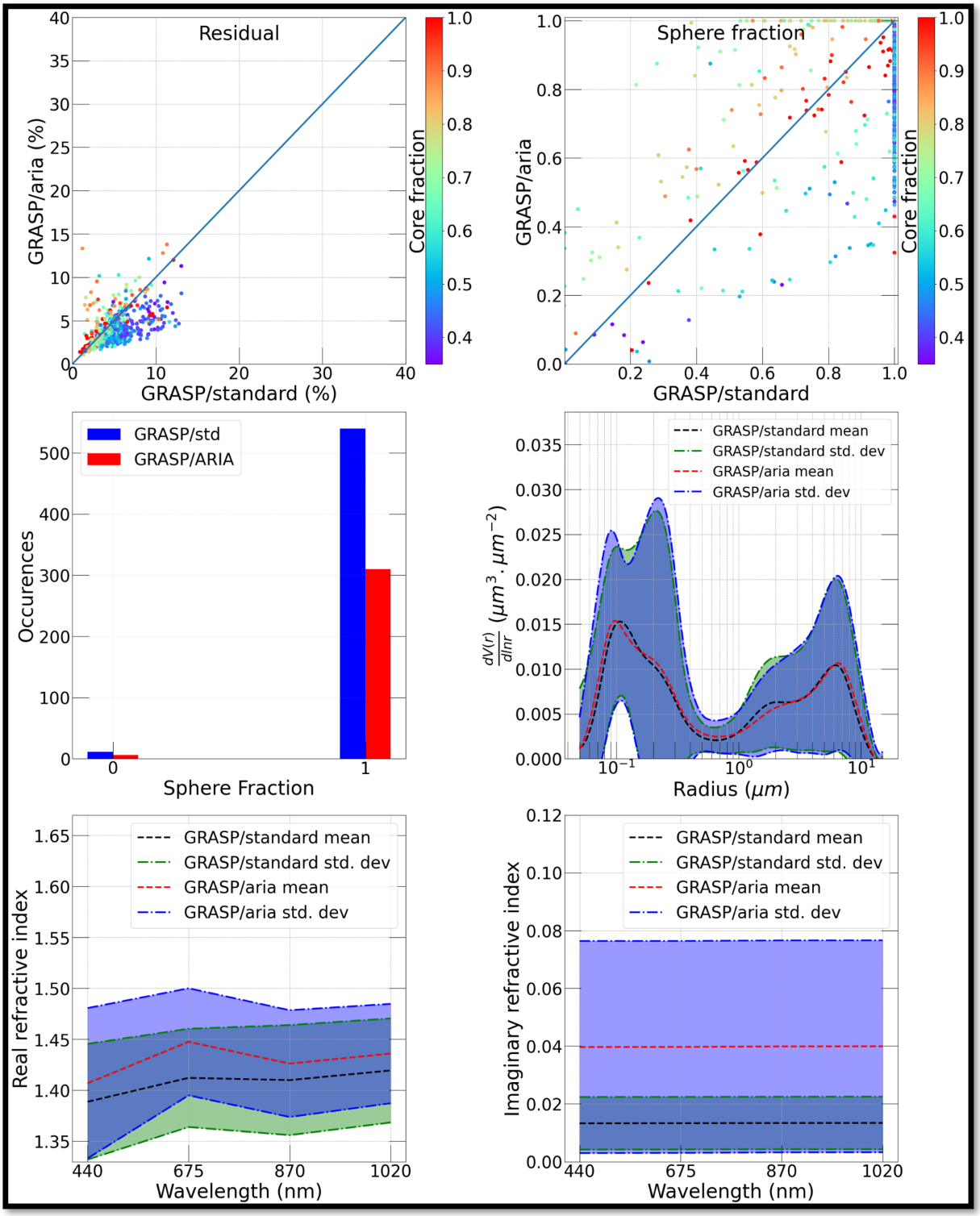

(5.4.2) GSFC AERONET site

Figure 5.4: Collection of plots of aerosol optical and microphysical characteristics derived using GRASP/ARIA (parameterisation of inhomogeneity included) of all available inversible observations for AERONET sites representing domination of urban aerosol (Lille and GSFC sites). The data covers the perid of 2008 to 2025.

same fashion as the measurements without DoLP, the number of sphere fractions reaching the algorithmic bounds is reduced. The size distribution evolves differently with a decrease in fine mode particle size and an increase for coarse mode. Finally, the refractive index is represented accordingly with what it expected from the change in the aerosol model with, however, a small increase in the spectral dependency.

Finally, despite that the Lille and GSFC sites are mostly dominated by fine particles, which situation was found to be the least sensitive to core fraction, the results of real measurement inversion with polarisation information showed quite good performance.

Figure 5.5 presents the results for the sites Barcelona and Tel-Aviv University that are equipped with polarimetric photometers. These sites also represent mixed aerosol type with however a general dominance of coarse particles. This implies, according to the tests with synthetic measurements, that in this combination of the measurements capacity and particles size should be favourable for sensitivity to aerosol core/shell structure.

The results for these sites show that the majority (about 60% of total measurements) of the retrievals by both versions of the algorithm have quite equivalent residuals, while in the other (about 30%) retrievals, the GRASP/ARIA showed improvement of the residual relative to GRASP/Standard. The retrievals for the Tel-Aviv University site show however much more moderate improvement than the Barcelona site. Interesting also to note that the retrieval improvement by GRASP/ARIA relative to GRASP/Standard are practically the same whatever the DoLP is used or not. This is because the considered sites are dominated by coarse mode aerosol, but the main improvement from involving the DoLP is expected for the case of fine mode particles. It is also interesting to note that the retrieved fraction of spherical aerosol is equal to unity in 90% of cases for Barcelona and only in 45% for Tel-Aviv University. This is in line with the fact that GRASP/ARIA shows stronger improvement for the Barcelona site - core/shell applied to spherical aerosol only. The retrieved core fraction was found to be generally slightly higher (thinner shell) for these sites than for the sites dominated by fine particles, which is also in line with the fact that Barcelona and Tel-Aviv are more strongly affected by generally hydrophobic desert dust. Besides, variability of the optical properties are quite similar to what was observed for other sites, i.e., increase in particle size for measurements with improved residuals and increase in refractive index with a slight exacerbation of the spectral dependency.

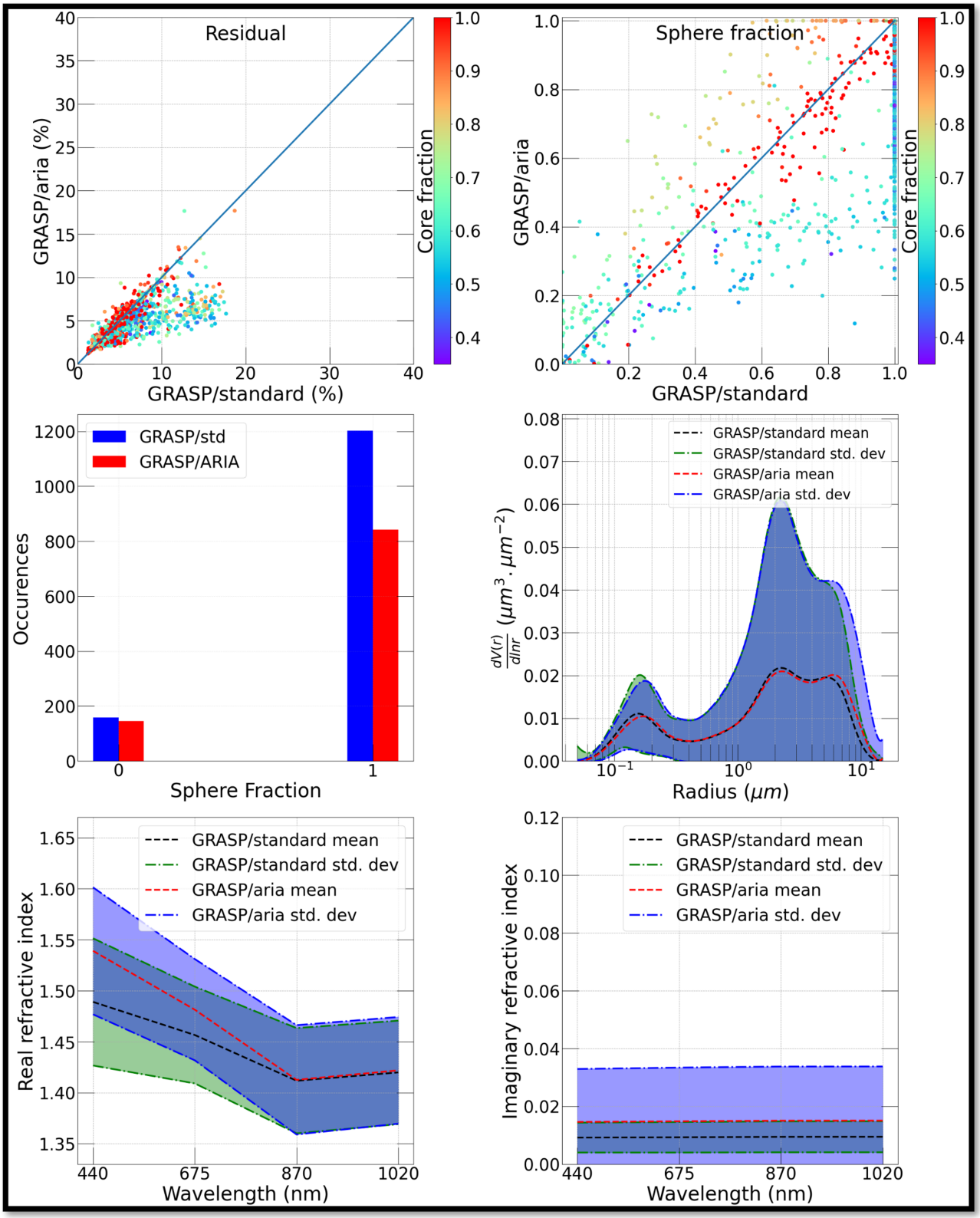

(5.5.1) Barcelona AERONET site

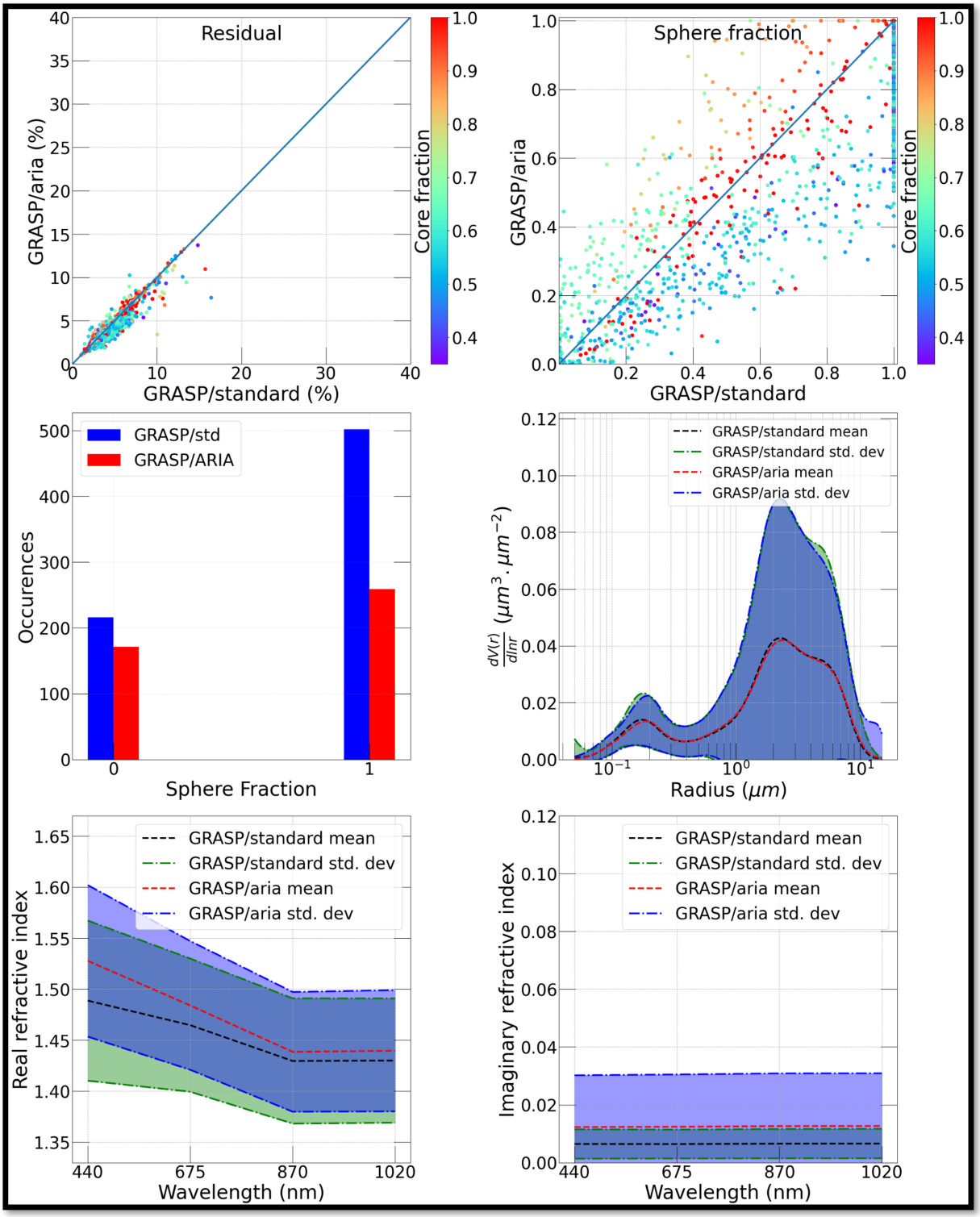

(5.5.2) Tel_Aviv_University AERONET site

Figure 5.5: Same as 5.1 for AERONET sites with mixed aerosols.

Intercomparison of retrievals by GRASP/ARIA with and without DoLP

The inversion results of the GRASP/ARIA algorithm obtained from measurements with and without polarization information show that the core fraction retrieved from the measurements including the DoLP has a generally better dynamic of values and is less concentrated within the range of 0.6 – 0.8. Recall that his range of values was identified as typically picked up by the inversion when the sensitivity is limited.

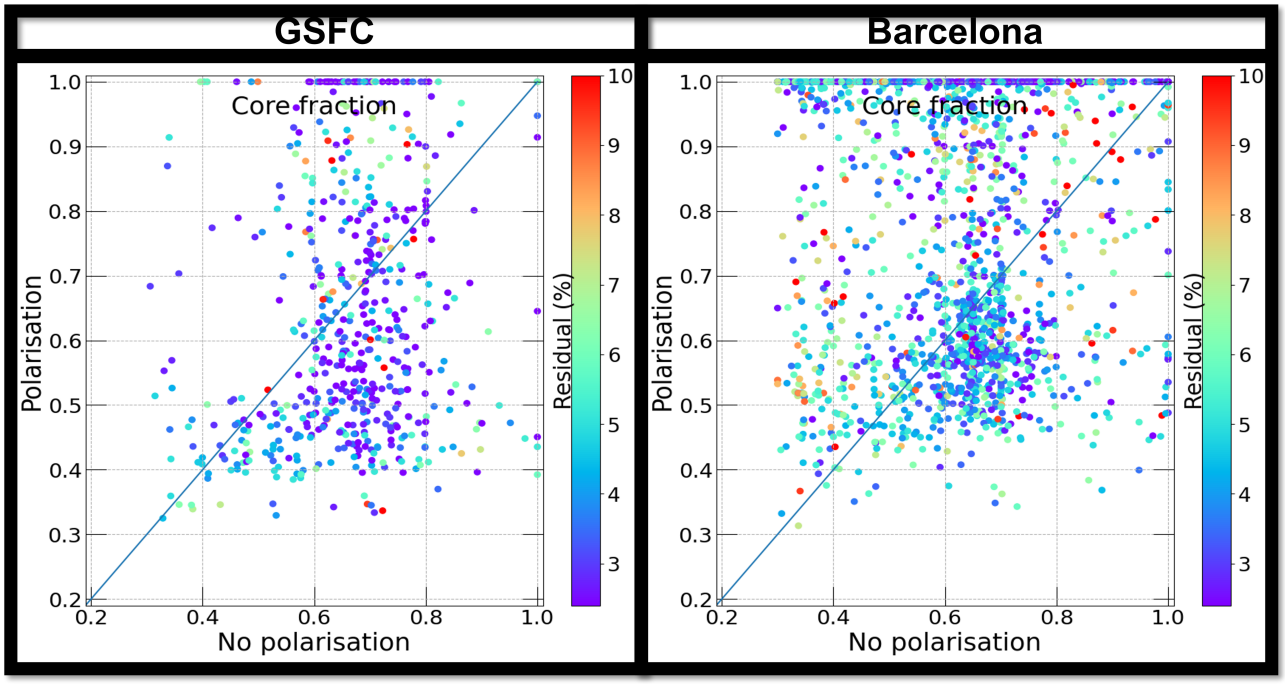

Figure 5.6: Comparison of retrieved core fraction from inversions of measurements with and without information on polarisation for the sites of GSFC and Barcelona.

Figure 5.6 presents an intercomparison of core fractions retrieved by GRASP/ARIA with and without involving the DoLP for the sites of GSFC and Barcelona. The inversions were conducted using exactly the same observations, but involving or excluding the polarisation measurements. The GSFC and Barcelona sites represent urban and mixed aerosol types, respectively. Two main patterns can be observed. When the DoLP is not used, the majority of the points are concentrated in the range of values 0.6 – 0.8, which seems to be result of lack of sensitivity so that the core fraction remains without a significant change during the inversion procedure. While involving polarisation, improves the dynamic of the retrieved core fraction values.

If we assume that the measurements with information on polarisation are sensitive to core

fraction, the disagreements of retrieved core fraction between measurements with and without polarisation imply that the absence of polarisation in the measurements is correlated with an absence of sensitivity to core fraction. Yet, improvements in the radiance residuals for measurements without polarisation correspond, most of the time, to measurements with polarisation where the core fraction is most sensitive (between 0.4 and 0.5). Whereas equivalent and worse residuals cover the whole range; most of them are in the range 0.6-0.8 for measurements without polarisation. Suggesting that improvement of residuals for measurements without polarisation is related to thicker shells, even if core fraction is not properly retrieved.

For Barcelona, it is more complicated to witness patterns as there is a bigger dispersion of points. Looking at the quality of the residuals, for equivalent and worse residuals, core fractions of measurements inverted without polarisation are mostly within the range 0.6-0.8, indicating a lack of sensitivity. As for better residuals, contrary to GSFC, they correspond to a wide range of core fractions which could be divided in three parts, the first concerns the nearly homogeneous or homogeneous (35% of cases) which are displaying an improvement with polarisation, then the ones that demonstrate a relative agreement (30% of cases with ± 0.1; 42% for ± 0.15) and finally, random differences mostly concentrated for smaller core fractions from measurements without polarisation, potentially displaying an overestimation of the core fraction.

Intermediate conclusions

In a general manner, tests showed that implementation of the core/shell aerosol model helps to reproduce the measured radiances better than the standard aerosol model. Moreover, including the additional core fraction inversion parameter did not destabilise the algorithm. The former was concluded based on several tests with different initial guesses that have demonstrated the uniqueness of the inversion result. It was found however that sensitivity to core/shell can be not sufficient in some cases of combination of aerosol properties and measurement configuration. The abundance of the retrieved core fraction values in the range of 0.6 to 0.8 was found as related to the situation of the lack of sensitivity. It specially happens when fine mode particles are dominant and the light polarisation information is not included in the inversion procedure. Successful retrieval of core fraction was found to influence retrievals of aerosol sphericity fraction, i.e., better dynamic in the derived values.

The results have shown that better reproducing radiances (above 0.5% relative to the case

of standard aerosol model use) was associated with a wider range of the sphere fraction. The size distributions retrieved either by GRASP/ARIA or GRASP/Standard are generally very similar. The derived by both versions of the algorithm refractive indices may have some slight fluctuation in spectral dependance, however are consistent with expectations related to the facts that GRASP/ARIA retrieves refractive index of core part only and that the values are also dependant on relative contribution of homogeneous non-spherical particles.

Overall, the core/shell model appeared to provide benefits for the retrievals, but the measurements without polarisation don't seem to have enough sensitivity to core/shell aerosol model in every situation. The validity of the retrieved core fraction values, even with the employment of polarisation, still needs to be assessed, e.g., by studying the associated atmospheric conditions.

Results have also been analysed separating AODs at 440 nm in several groups (separation in 2 groups presented in Appendix A.4.3). The motivation for this is that AERONET assigns Level 2 labels to retrievals from measurements with AOD (440) larger than 0.4, so the real part of refractive index and sphericity fraction for smaller AODs are not of Level 2 with uncertainties being larger than for higher values of AOD. The two groups don't present significative differences except for that it is harder to converge for GRASP/ARIA with higher AODs and smaller wavelength of real refractive index (440 and 675 nm) present on overestimation in lower AODs compared to GRASP/Standard which is absent from higher AODs.

5.3 Evaluation of consistency between retrieved core/shell fraction and other aerosol characteristics

Evaluation of core/shell fraction retrievals using in situ measurements, including sampling and laboratory analysis will require specially dedicated studies. It would need to be done through multiple seasons, sites and throughout the entire atmospheric column. Indeed, the main complexity of employing the in situ sampling techniques is comparing it to telemetric data by assumption that aerosol properties at ground level are representative for entire atmospheric column, however, aerosols can have different origins and aged differently. An indirect evaluation however can be done analysing the other retrieved aerosol characteristics and tracking consistencies between aerosol microphysical and optical properties. For instance, a physical expectation is that appearance of shell will be associated with increase of aerosol particles

size, a thicker shell should be attributed to more hygroscopic particles, i.e. typically small urban/industrial aerosol type, and finally some seasonal dependencies can appear reflecting different environmental conditions.

The retrieved core/shell fraction is also expected to be related to ambient relative humidity as condensation requires. The deliquescence point and water adsorption by aerosol however depends on particles chemical composition and microphysical properties (cf. 1.1.2). The amount of the water adsorbed on the aerosol surface might also depend on the total atmospheric water availability, meaning that the relative humidity only might not be indicative to validate the size of the shell, but rather verify the plausibility of absence or presence of aerosol coating. Furthermore, history of air masses transport, varying relative humidity and ageing processes that aerosols went through, will also influence the core/shell structure dimensions.

The performance of the new algorithm can also be evaluated using intercomparison of climatological aerosol properties for a specific site, like the type of particles, shape, size etc., trying to evaluate the consistency of the core fraction retrieval. However, this approach would rely on the assumption that the standard model describes aerosol properties without interfering with other parameters; e.g., core fraction of non-spherical particles.

The use of simulated properties could be a means of validation, i.e. like for the tests on synthetic measurements. However, the problem of validation with synthetic data is that it is generated with a model that does not fully represent the complexities of real atmospheric aerosols and, hence, the behaviour of the algorithm inverting these synthetic measurements might be different from the one inverting real measurements. This is why, the intercomparisons with the results of synthetic measurements can be done only as part of a body of evidences.

Approach and results analysis

The figures of this section are thus aiming to examine the consistency of the core/shell retrievals with other retrieved aerosol microphysical and optical properties, including using the results on subsamples of the observations. Figures 5.7 are composed of ensembles of graphs describing the core fraction distribution and characteristics of the aerosol relative to the core fraction.

- The first graph presents the probability density of the retrieved core fraction sorted by

the residual quality relative to the retrievals using the standard (without core/shell parameterisation) aerosol model. The second graph shows the probability density of the retrieved core fraction for the different seasons and only for the cases when the residual is improved by incorporating the core/shell parameterisation. The goal with the first is to observe the differences in the density between the retrieval qualities. If the better residuals show the same probability density as equivalent or worse residuals, this would hint at a general lack of sensitivity. The goal of the second graph is to analyse the measurements that improve the quality of the radiance retrieval; these are the measurements that are generally expected to have sensitivity to the core/shell fraction. The seasonal variability of the core fraction probability density can be considered as more representative in this case and the corresponding analysis is more meaningful.

- The third graph shows the repartition of core fractions, still limited to measurements with improved residuals, according to the values of Angström exponent and real part of refractive index. The idea is that Angström exponent indicates the dominance of the aerosol size mode, fine to coarse, in the total size distribution, and the real refractive index hints at the chemical nature of the aerosol. The goal is thus to analyse if derived core fraction logically follows the dominate aerosol size and composition. The logic is in expectation that small particles with lower real refractive index should be more hygroscopic and thus the shell size more important, and vice versa for the coarse mode dominated aerosol.

- The fourth graph represents the size distributions sorted by two ranges of core fractions, i.e. below and above 0.5, still for ensemble of measurements where residual is improved due to employment of core/shell parameterisation. The logic here is that particles that experienced coating due to water uptake will present a larger size. The difference in size could then be imputed to the size of the shell.

The data for this analysis is filtered in order to keep only the cases with the radiance fit residual below 10%, as an educated threshold enabling meaningful retrievals in general and also sufficient quality of the core/shell retrieval.

No information on polarisation

Figure 5.7 presents the introduced above characteristics for the AERONET measurements without information on polarisation. Recall that most of presently available AERONET measurements do not involve information on polarisation, but, despite the limited sensitivity to

core/shell, the analysis is still of importance as the sensitivity exists in some regimes. Moreover, despite the lack of measurements with polarisation in desert sites, it was shown that coarse mode dominated cases do present good sensitivity to core/shell even without polarisation. The AERONET sites such as GSFC, Kanpur, Tamanrasset and Dakar are considered here.

The first presented is GSFC, which is an urban aerosol dominated site with a significant proportion of fine particles. According to previous test using synthetic measurements and first analysis of real measurements for this site, sensitivity to core fraction exists in the case of combinations of very inhomogeneous (very low core fractions) and mostly spherical aerosols (sphericity fraction close to unity). The first graph displays that a wider dynamic and more extreme values of the core fractions (that could be part of the domain of sensitivity) correspond to the measurements were the core/shell model improves the quality of radiance retrieval compared to the standard aerosol model, which is in favour of core fraction sensitivity. The second graph shows the probability density of core fraction per season. The graph shows that summer and spring are characterised by mild core fractions with a strong frequency of occurance in the range 0.6-0.8, whereas, winter and autumn are characterised by more diverse core fractions, displaying a higher density of highly inhomogeneous and more homogeneous particles. Climatology of meteorological data (cf. appendix A.4.1) shows that the GSFC site is characterised by highest mean relative humidity (60-65%) during summer and spring, while the winter and autumn seasons are characterised by somewhat lower mean relative humidity (50-55%), but also by a larger variation. Seasonal relative humidity and core fraction thus show coherence with one another. The third graph shows a group of quite homogeneous fine mode dominated particles with real refractive index around 1.35 (red dots in downright conner). However, for rather bimodal size distributions cases (Angström Exp. of 1.0 to 1.5), the shell size become more important (more green and blue dots from right down to left up), which means thicker shell for fine mode dominated particles. The former is in line with the knowledge that fine mode anthropogenic particles are generally more hygroscopic. The real refractive index of core in these cases has a majority of values between about 1.4 to 1.45 that corresponds well to anthropogenic aerosol. The size distributions in the fourth graph don't present a particle radius shift towards bigger radii, which is not consistent with an increasing importance of the shell (Core fraction ≤ 0.5).

The Kanpur site represents the mixed aerosol type with bimodal and coarse mode dominated size distributions. According to previous tests, dominance of coarse mode should correspond to

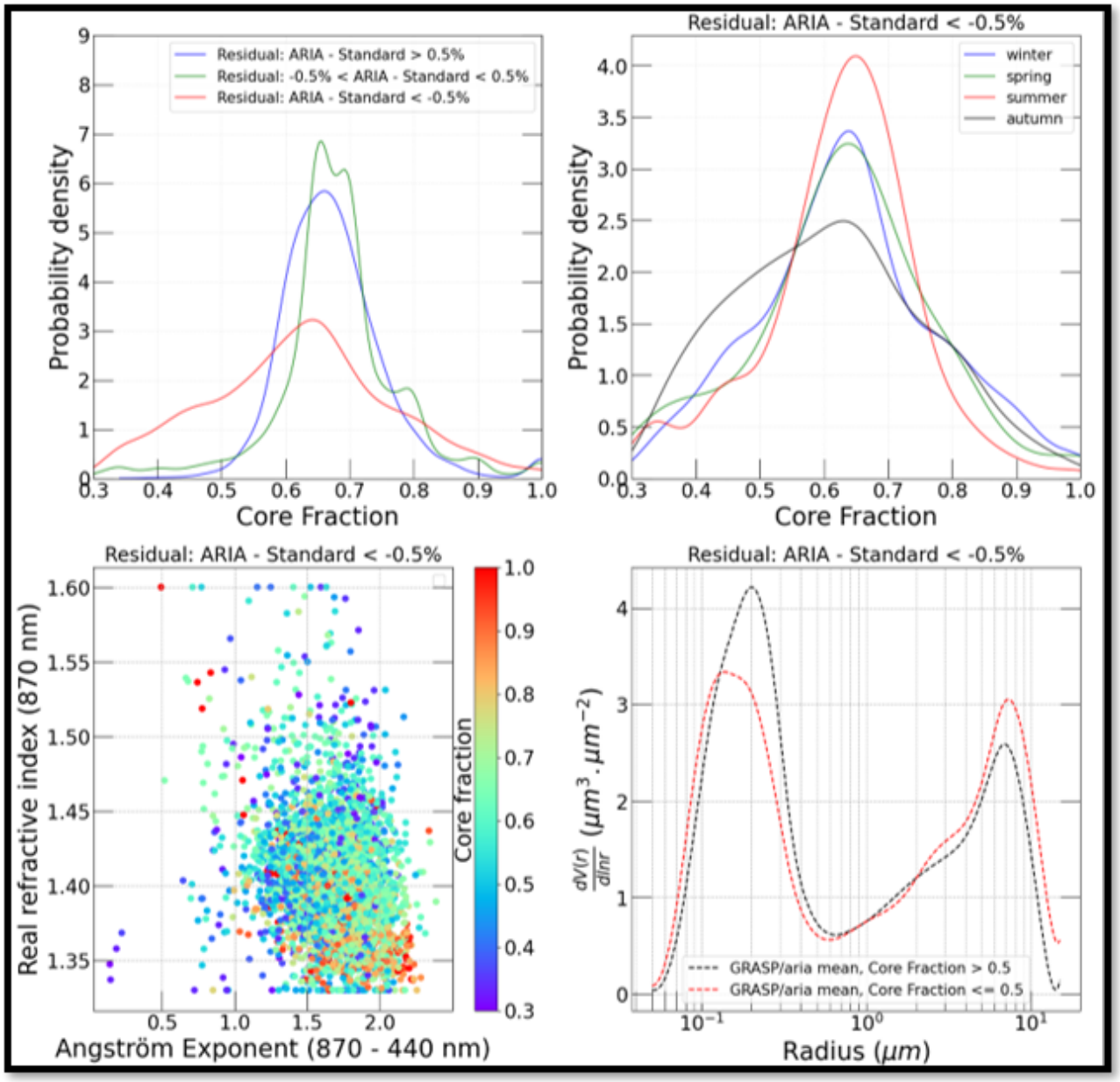

(5.7.1) GSFC AERONET site

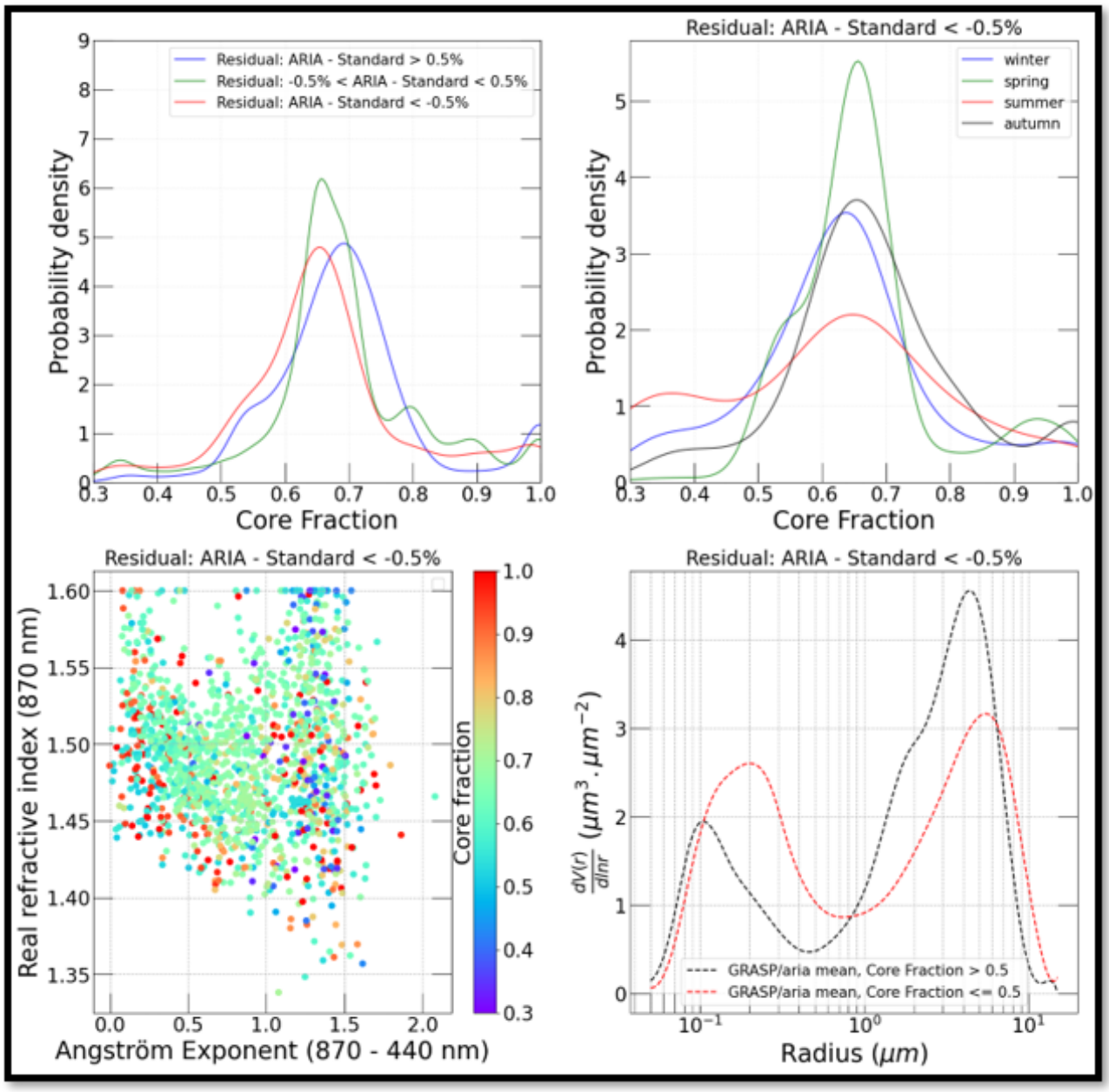

(5.7.2) Kanpur AERONET site

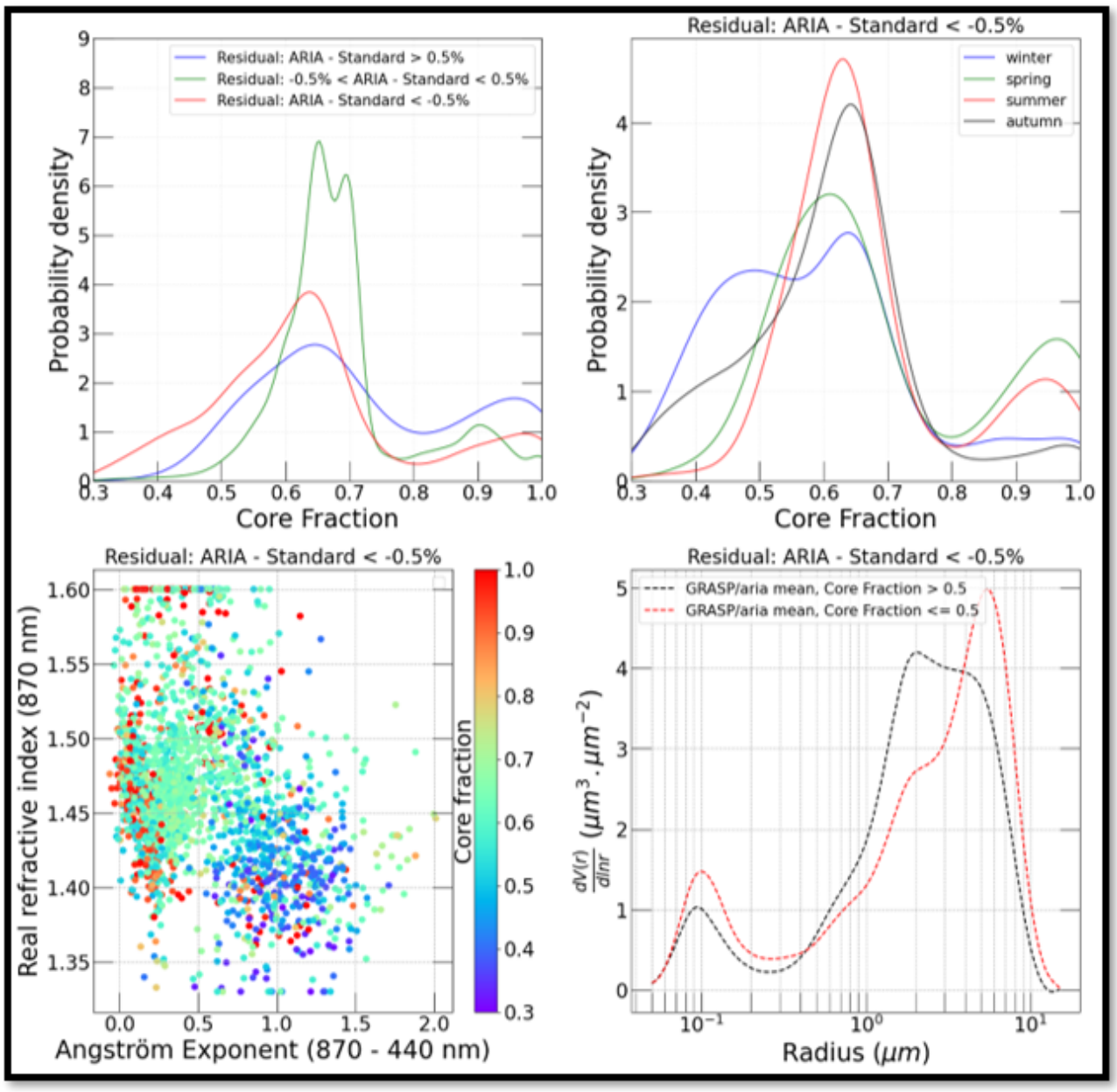

(5.7.3) Tamanrasset_INM AERONET site

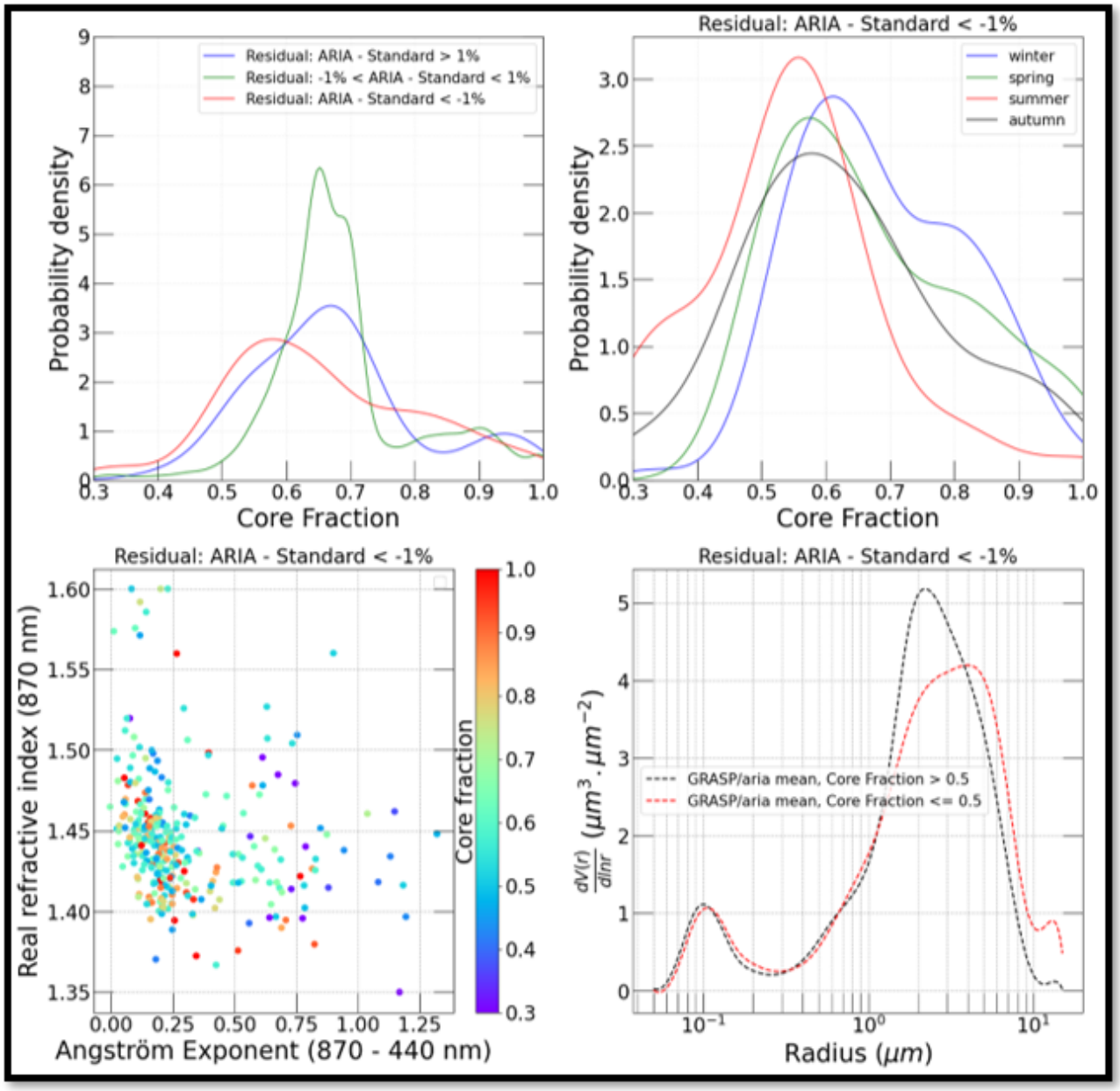

(5.7.4) Dakar AERONET site

Figure 5.7: Collection of plots illustrating the interpretation of core fraction retrievals in the context of residual improvement, seasonality, dominant particle size (represented by the Ångström exponent), composition (represented by the real refractive index), and shifts in the particle size distribution. The plots show results of GRASP/ARIA retrievals for real AERONET measurements from the period 2008 to 2025, which do not include information on light polarisation. The data are filtered by quality of radiance fit. The AERONET sites GSFC, Kanpur, Tamanrasset INM and Dakar represent a variety of urban, industrial, desert, and mixed aerosol types.

better sensitivity to the core/shell structure. The first graph indicates that the quality of the residual fit does not really depend on the core fraction retrievals. The quality of radiance thus might not be a good filter to assess a lack of sensitivity to the core fraction retrieval in this case. The Kanpur site is also characterised by quite a high variability of the relative humidity throughout the year (between 25% and 80%) (cf. appendix A.4.1). Summer is the most humid season of the year and, in the first graph, summer is shown as the season with the highest probability density for smaller core fractions then other seasons. The third graph shows that the majority of the small core fractions (blue dots) are associated with bimodal size distributions particles (Angström exponent around 1.0 to 1.5). There is an another important group of dots representing homogeneous (core fraction close to unity – red dots) coarse mode dominated size distributions (Angström exponent ranging between 0 to about 0.7) that is logically correlated with increasing real refractive index (larger particles have higher real refractive index typical for dust). The refractive index thus seems to be coherent with aerosol sizes and, accurately retrieved. Finally, the range of the retrieved real refractive indices for the particle core is favourable for the regime where the contrast between core and shell is high enough to maximise sensitivity to core fraction retrievals. The fourth graph logically shows that the increase in shell size is followed by an increase in particle size. Moreover, the radius shift towards larger sizes for the fine mode is more important than for the coarse mode which is consistent with the fact that smaller particles are more hygroscopic and grow faster. This body of evidence is in favour of a good sensitivity to the core fraction retrieval, which might even extend to retrievals with a worse or equivalent quality of radiance fitting, as there seem to be other complexities influencing the optical properties.

The Tamanrasset site is deeply inland in the south of Algeria, in the heart of the Sahara Desert. The study of Guirado et al. (2014) describes the aerosol characterisation at this site based over a two-year period of observations. The meteorological conditions in this location are divided in two main periods, the "dry-cool season (November–February)" and the "wet-hot season (April–September)" with the two remaining months being transition month (characterized by 20% to 30% relative humidity). Wet season is characterised by moist air masses (monsoon) brought by easterly winds. The aerosol burden is characterised by low AOD during dry season and heavy dust storms during wet season. Looking at the first graph, the core fraction histograms are quite similar for better and worse residuals relative to the residuals of the standard aerosol model. This observation hints at the possibility of another characteristic, not taken into account by the model, influencing the quality of the retrievals. The second graph presents

results that are quite in line with the climatological description of the Tamanrasset site. That is, autumn and winter have quite a different distribution of core fractions than spring and summer. Spring and summer include the transition from dry to wet seasons, with an increased inhomogeneity (core fraction around 0.6) and a second mode of histogram showing homogeneous aerosol (core fraction between 0.9 to 1.0). During wet season (autumn and winter), measurements show an increase in inhomogeneity, which is in line with is expected. The third graph show a clear dependence of the core fraction on Angström exponent, where the thicker shell corresponds to presence of bimodal size distribution (Angström exponent around 1.0) and more homogeneous particles are attributed to coarse mode dominated aerosol (Angström exponent close to zero). The aerosol size distribution, especially the coarse mode, is logically shifted towards larger sizes when the core fraction is ≤ 0.5, showing the particles grow due to presence of liquid shell.

The Dakar site is different from Tamanrasset by its proximity to ocean and higher influence of atmospheric water content. The seasonal dynamic is however not different from Tamanrasset, with higher relative humidity in spring and summer. For the retrievals in the Dakar site, it was noted that the core fraction histograms (first graph) start to differentiate when the improvement in the residual is above 1%. This 1% threshold is thus used in the figure for the following analysis. The first graph shows that core fractions probability density for better residuals are distributed in a wide range of values. The second graph shows that the core fractions in the summer period are quite different from winter, while it is known that summer is characterised as wet season and by presence of only dust aerosol type, while in winter, the site is often influenced by biomass burning aerosol transport. The third graph shows dominance of coarse mode aerosol and a correlation between lower Angström exponent and increasing real refractive index, while the dependence of the core fraction cannot be clearly identified, except for a group of dots indicating thicker shell (blue dots) for somewhat increasing contribution of fine mode aerosol (Angström exponent between 0.5 and 1.25). It should also be mentioned that in case of coarse mode domination in size distributions, the core fraction variability can also be affected by variety of sphericity fractions because only spherical aerosol have core/shell parameterisation. This fact complicates the core fraction interpretation as function of size and refractive index for all desert sites. Indeed, the fraction of particles concerned by the core/shell model will be limited. Finally, the fourth graph shows particle radius shift towards larger sizes for the case with smaller core fractions, which is in line with the hygroscopic growth phenomena which is

apparently captured by the algorithm.

With information on polarisation

Figure 5.8 presents the characteristics for Urban aerosol when the measurements include information on light polarisation.

Polarimetric measurements at the Lille site accounted for only a few weeks, during winter of 2025, in the time of this study and thus the number of usable measurements is very limited. However, the obtained inversions still showed several interesting conclusions. First is that the core fractions corresponding to better, relative to use of standard aerosol model, residual are notably smaller. Second, the obtained, for these cases, mean size distribution shows clear fine mode dominance. However, while the residuals are degraded, the size distribution shows a split (bimodality) of the coarse mode, which visibly attempts to compensate the luck of convergence.

The demarcation is even more pronounced for GSFC, with a great proportion of core fraction between 0.35 and 0.6. Like for measurements without information on polarisation, winter and autumn are the months with the highest core fractions. These are the months with the smallest mean relative humidity, at the same time, these months also present the largest dispersion of the values (cf. appendix A.4.1). The third graph shows particles with a higher real refractive index that tend to have a larger core fraction along with an increasing size. There are also some case of fully homogeneous and liquid particles (red dots). The fourth graph suggests a slight size shift towards bigger radius when shell contribution increases. Overall, the results for these real measurements that include polarisation information seem to show an increase sensitivity to the aerosol core/shell structure retrievals, compared to measurements without polarisation.

Figure 5.9 presents the characteristics derived from the measurements that include polarisation for the sites with mixed aerosol type. Namely, the Barcelona and Tel Aviv University sites are considered.

Barcelona is a coastal site influenced by marine air mass and relative humidity varying around 70% (cf. appendix A.4.1). The first graph shows an important range of variability of the core fractions where the highly inhomogeneous particles present an important part, along with a

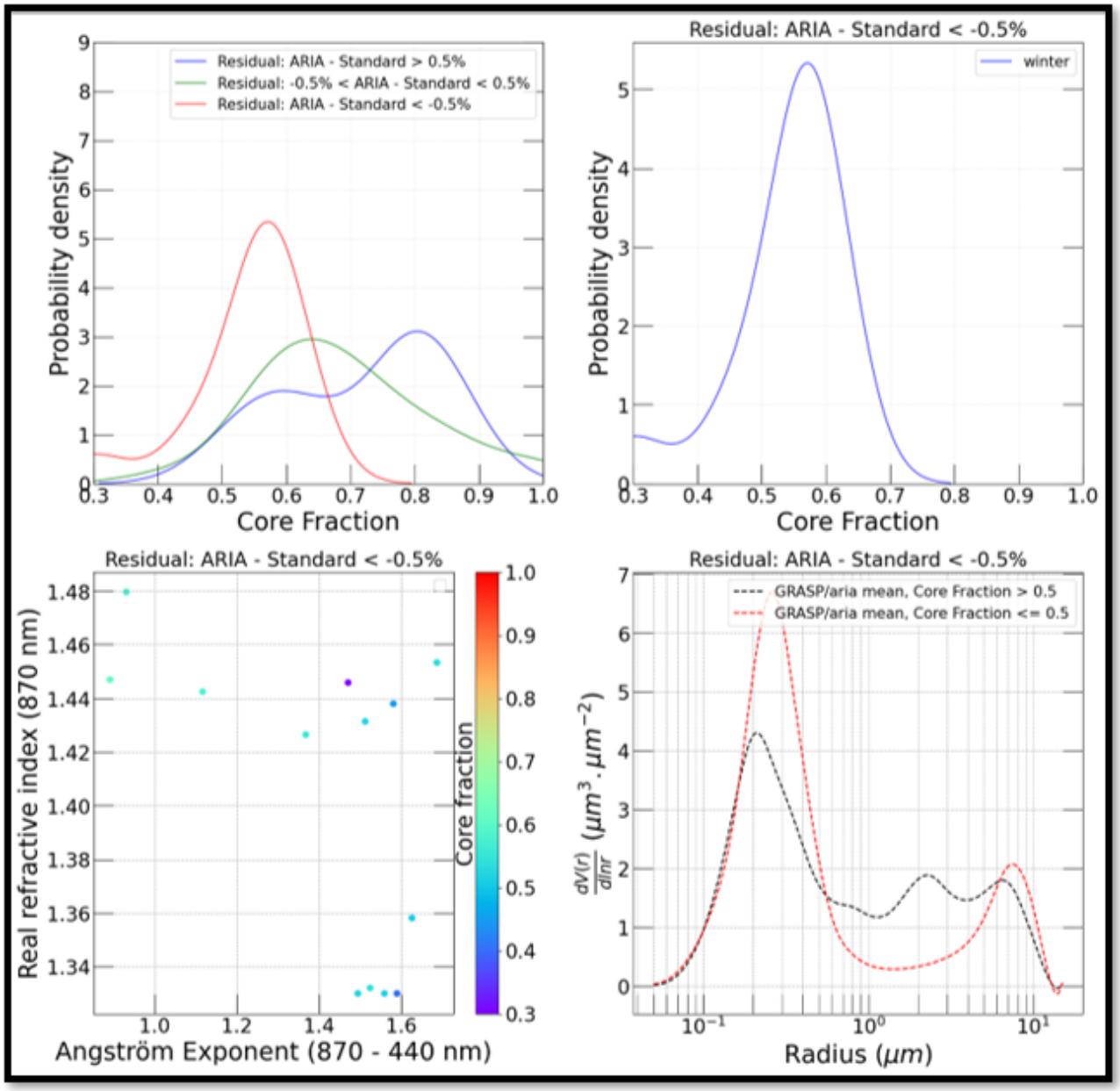

(5.8.1) Lille AERONET site

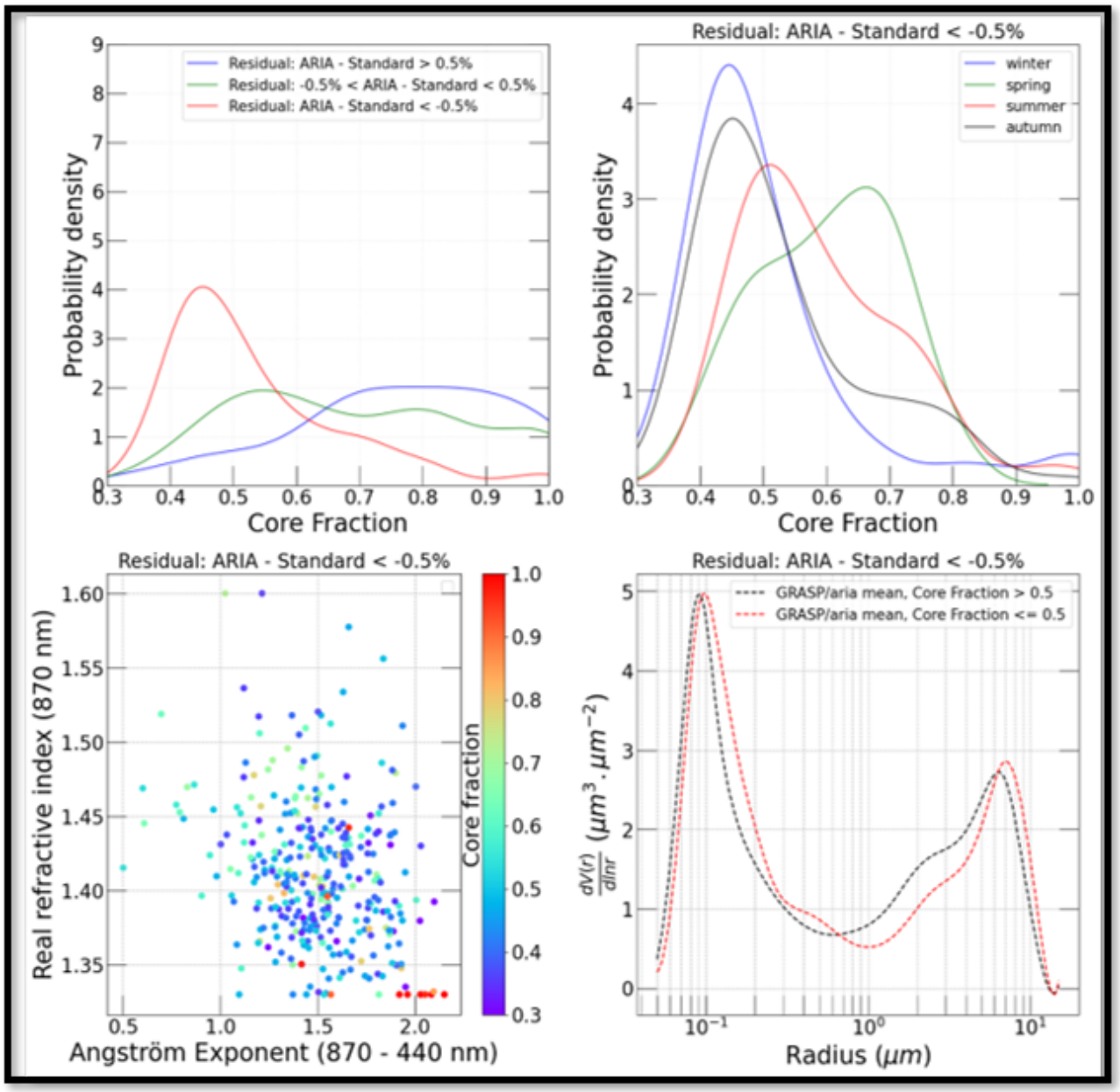

(5.8.2) GSFC AERONET site

Figure 5.8: Same as Figure 5.7, but for AERONET sites representing urban aerosol and for measurements that include information on light polarization. The time period is, however, much more limited.

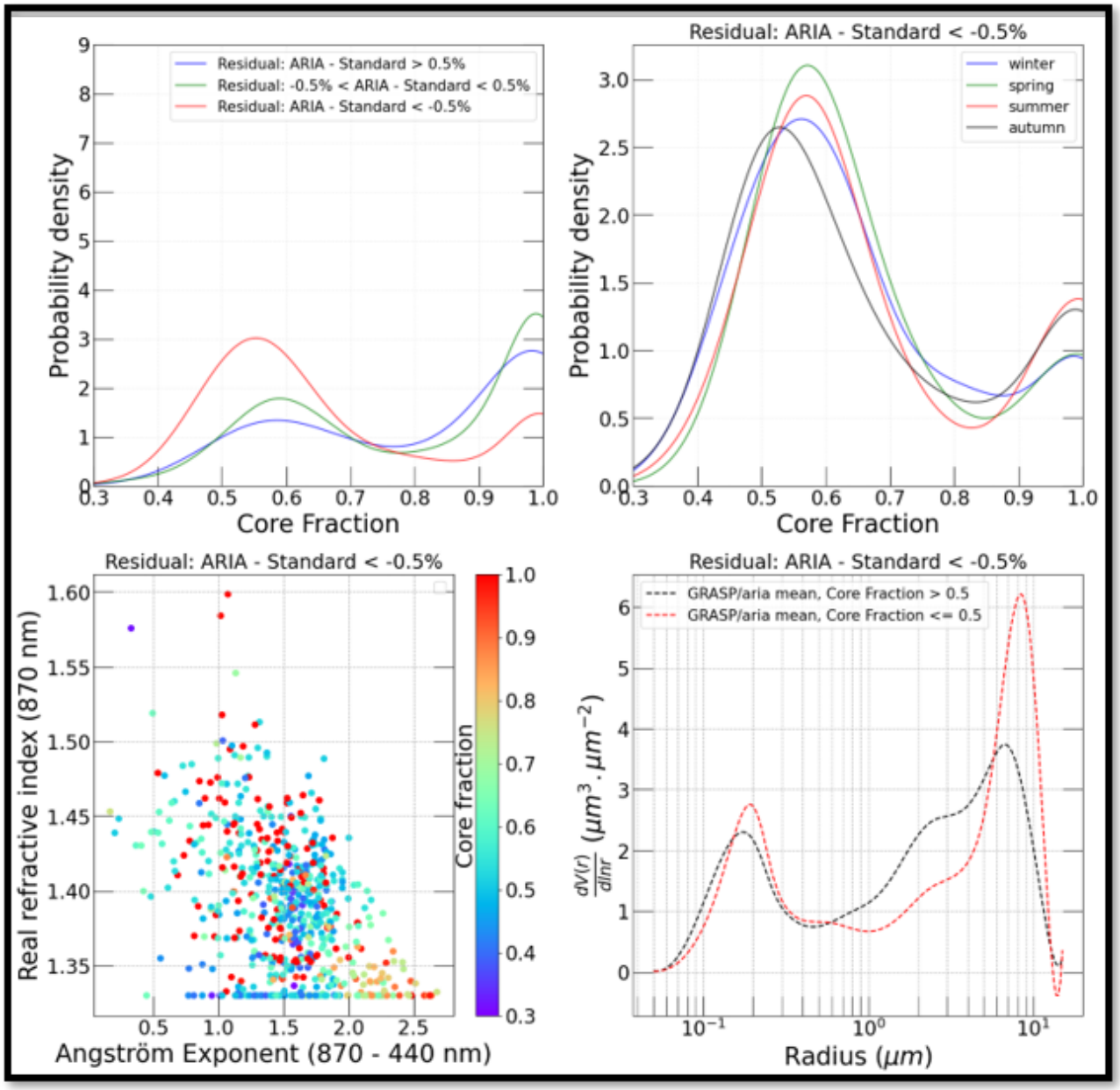

(5.9.1) Barcelona AERONET site

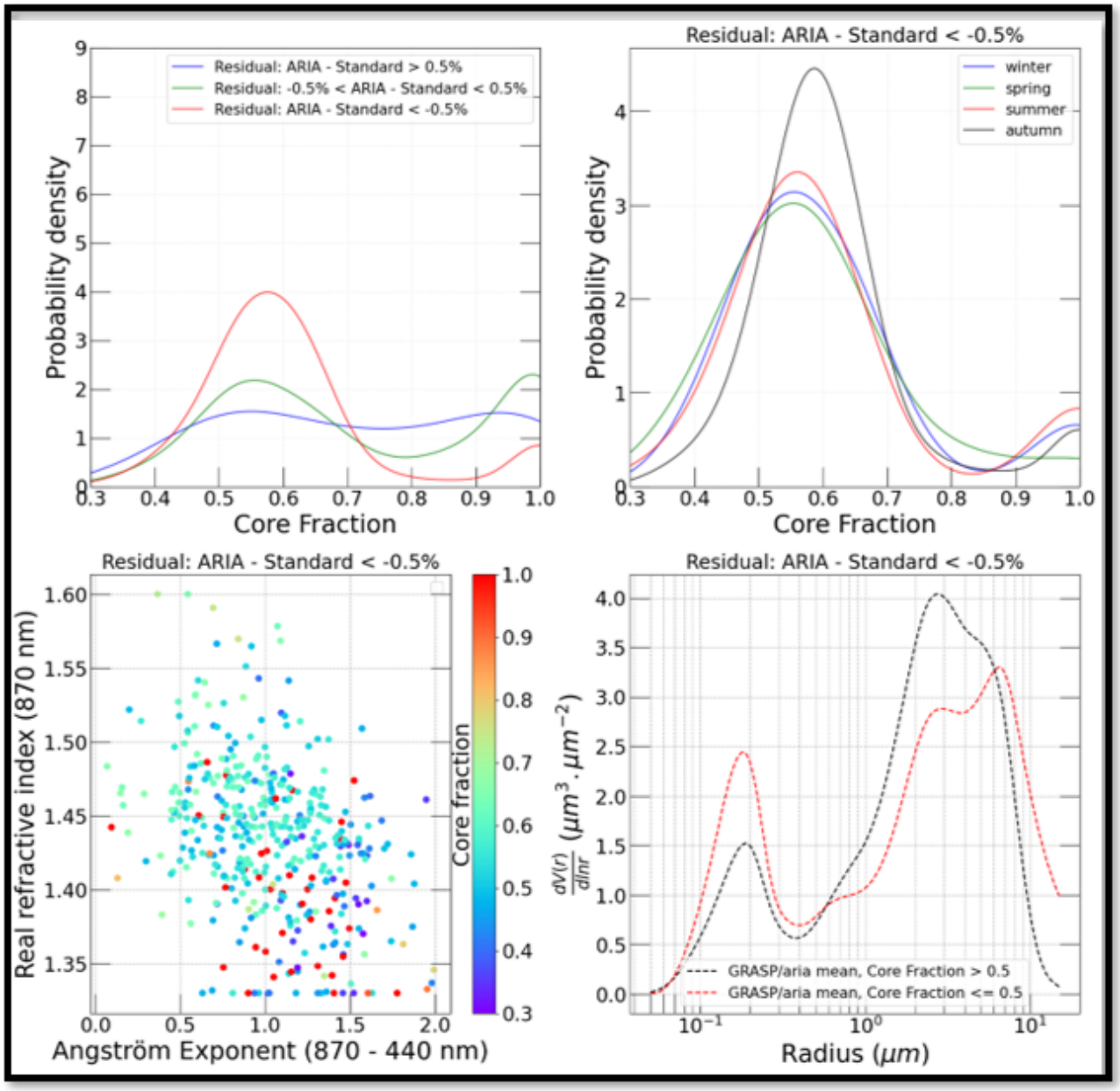

(5.9.2) Tel-Aviv_University AERONET site

Figure 5.9: Same as Figure 5.8 (information on polarisation is included), but for AERONET sites representing mixed aerosol type.

second peak in the histogram that corresponds to nearly homogeneous particles. The probability density of core fraction is practically similar for all seasons, which is most probably dictated by the marine air masses influence and not seasonal variabilities of relative humidity. The third graph is difficult to interpret in respect to the core fraction, which does not seem to clearly depend on the dominant aerosol size or refractive index. The high number of retrieved real refractive indices around 1.33 to 1.4 might indicate a predominance of liquid aerosol that is consistent with the marine air mass influence. The fourth graph displays the expected size distribution shift demarcation. Most of the clues indicate sensitivity to core fraction retrieval, however some more analysis might be needed to understand why no pattern emerges from the third graph. The Tel-Aviv site is in a similar situation with Barcelona, as it is a coastal city of the Mediterranean Sea with a high relative humidity (mean around 70%). The consistency of the obtained results with what was obtained in Barcelona is encouraging. The main difference between two sites is seen in the third graph that shows the majority of real refractive index values is higher in Tel Aviv. This agrees with proximity to desert regions and thus stronger influence by dust transport. Besides, stronger core/shell contrast (core fraction around 0.5 – 0.7) in Tel Aviv is rather attributed to the real refractive index of core in range 1.4 to 1.5, which would produce a strong inhomogeneous aerosol case. The cases of thick shell or homogeneous particles, core fraction around 0.3 – 0.4 or 1, respectively, have tendency to present for real refractive index of core below 1.4, which, in both cases will be nearly homogeneous liquid aerosol.

Intermediate conclusions

The core fraction retrievals from real AERONET measurements were analysed in the context of consistency with other retrieved aerosol microphysical and optical properties. This is intended to provide an indirect validation, or at least to verify consistency with physical expectations. Namely, the hypotheses were: important shell fractions should be associated with particles growth; shell thickness should depend on size and composition of core; fine mode dominated particles should be more hygroscopic; and finally, liquid coating may vary seasonally, depending on meteorological conditions. In order to focus on the cases with better sensitivity of the retrievals to the particle core/shell fraction, the selected measurements are only those where the residual of the radiance fit is improved relative to the use of a standard aerosol model (i.e., without core/shell parameterisation). Indeed, in most of the cases, the probability density of the retrieved core fraction for the improved residuals is different from those of equivalent and

worst residuals, which implies that the sensitivity exists and the core/shell model improves the quality of radiance fit.

The main and quite encouraging founding is almost systematic shift of size distributions towards larger particle radius, when an important thickness of shell was derived by the algorithm (core fraction ≤ 0.5). The core fraction dependence on dominant particles size (Angström exponent) or composition (real refractive index) of core were less pronounced or difficult to identify for some sites. Nevertheless, logical clusters of values and tendencies can be seen for the sites of GSFC and Tamanrasset. The seasonal variabilities exist and generally consistent with the related relative humidities, but clear linkage to environmental conditions will need a more focused approach. It should be mentioned that other attempts to analyse the results in terms of relative humidity and atmospheric water vapour were done, but clear and persistent correlations were not observed. Another important conclusion is that even without information on polarisation, the core/shell retrievals from real measurements show logical results. It agrees with the previous conclusions from the synthetic tests, showing that for some combination of aerosol properties the sensitivity to core/shell structure exists even for only directional radiances intensities. The measurements with polarisation however should provide more confident results. For instance, in the case of GSFC, the differences between the retrievals when polarisation is used or not, are very pronounced for the probability density distributions of the core fraction. Yet, the AERONET polarimetric measurements are not numerous, in fact, only GSFC, Barcelona and Tel-Aviv University sites provides significant statistics of polarimetric AERONET measurements.

5.4 Conclusion

This chapter presented application of the newly developed GRASP/ARIA algorithm to real AERONET measurements. Employment of the core/shell parameterisation clearly showed improvement of the ability to reproduce the measured radiances either of only directional intensities, or of the combination with the polarized radiances as well. The conclusions are based on the intercomparison of the GRASP/ARIA retrievals with those of GRASP/Standard, i.e., version that employs an aerosol model similar to the operational AERONET algorithm. Including the core fraction were found to influence the retrieval of sphericity fraction, which can be considered as improved because a better dynamic in the derived sphericity fraction is generally observed. Involvement of the core fraction parameter did not significantly impact the

derived size distribution. It also has a moderate impact on the retrieved complex refractive index, which in most of the cases is consistent with the difference in its formulation in both versions of the algorithm. That is, in GRASP/ARIA the refractive index is for the particle core only, while in GRASP/Standard it is an equivalent value for the entire particle. Retrievals from real measurements that include polarisation showed generally larger range of core fractions.

Attribution of the retrieved core fraction to atmospheric water vapour, or relative humidity was not evident. The histograms of the derived core fraction however showed seasonal variability and are generally in line with environmental conditions of different seasons for the analysed sites. The conclusion is however that direct link to relative humidity should be studied with a more focused and detailed approach. Nevertheless, the dynamic in the retrieved size distributions is highly consistent with appearance of an important fraction of liquid particle shell. Note that there is no imbedded dependence in the algorithm between the particles size and the core/shell fraction. The fact that more important shell fraction retrievals are associated with the size distributions shifted towards larger particles is particularly encouraging in this context. The consistency of the core/shell fraction dimensions with general more hygroscopic fine mode dominate particles or rather hydrophobic coarse mode dominated is also observed.

Chapter 6

Summary and perspectives

6.1 Summary and Conclusions

This work is dedicated to the study of the feasibility and to the first attempt of applying a remote sensing approach to evaluate the internal inhomogeneity of atmospheric aerosol particles. The work was subdivided into three main steps. The first focused on a theoretical assessment of the potential for implementing the proposed approach. The second step was dedicated to the formulation of a parameterisation of aerosol inhomogeneity and its implementation in the remote sensing algorithm GRASP. In the third step, the algorithm was applied to real measurements from the AERONET network of sun/sky photometers.

Aerosol internal inhomogeneity was modelled in this work using a core/shell particle structure. A study of changes in the elements of the scattering matrix under the single scattering approximation was conducted to evaluate the differences between the core/shell particle structure and homogeneous particles. Because coating of particles is associated with not only structural change, but also a change in size, a comparative study was conducted while varying the thickness of particles shell, contrast in complex refractive index of particle core and shell, as well as an equivalent change of the total particle radius. Attention was dedicated to the difference in angular scattering and degree of linear polarisation related to the changes in the above-mentioned microphysical properties of particles. Then, the possibility of compensation

or equivalence in the optical signature resulting from changes in structure, composition, or size was examined. The final objective of this study was to estimate the pertinence of using core/shell precomputed tables of optical characteristics (kernels) calculated under single scattering approximation for its insertion in the GRASP remote sensing retrieval algorithm.

Calculations of the angular scattering and degree of linear polarisation were realised for two changes in contrast of complex refractive index of particle core and shell, and for a change of particle size. The results demonstrated that particles of the same size and different structure share an almost indistinguishable forward scattering, but the differences are emerging in backward and side scattering directions. These differences increase with contrast in refractive index and particle size. The effects on scattering due to a change in structure were found to be different in absolute value as well as in angular behaviour. Furthermore, for every aforementioned difference in scattering, the degree of linear polarisation offers increased distinctions across wider ranges of angles. The calculation of kernels, was, therefore, deemed pertinent for an implementation of the core/shell model in the retrieval algorithm.

Using the newly defined aerosol parameterisation and new precomputed kernels, the retrieval algorithm was then modified to enable the retrieval of an additional core/shell fraction parameter. The new kernels however use the same structure as original GRASP kernels for spherical and spheroidal homogeneous particles. Furthermore, the spherical homogeneous kernel is used in the algorithm to simulate a core fraction equal to unity. The calculated kernels were made for core fractions ranging from 0.2 to 0.95 with a step of 0.05. Intermediate core fractions are calculated by linear interpolation of optical characteristics between the two closest kernels.

To test the sensitivity to core/shell fraction and calibrate the new inversion model, studies using synthetic measurements were realised. The main objectives were to test the sensitivity of the algorithm to core fraction retrieval in case of atmospheric radiances and draw outliers to the domain of applicability. To achieve this goal, synthetic measurements were created for the whole range of core fractions, but also combinations of particle sphericity fraction, varying refractive indices, size distributions and aerosol concentrations. Several supplementary tests were conducted, e.g., synthetic measurements' creation using the core/shell model and inversion of these measurements while using the "standard" (homogeneous particles) model to understand the potential effects of aerosol models' equivalence. One of the major results was a finding

that the core fraction has an influence on sphericity fraction retrieval, with a general underestimation of the sphericity for large core fraction values and overestimation for small core fractions.

The other tests consisted in varying another parameter, the real part of refractive index, to examine the algorithm response to the contrast in the core/shell materials. In addition, variation in the aerosol concentration was examined to estimate the effect of multiple scattering on smoothing the angular information and the sensitivity to the core fraction retrieval. The tests on the contrast in the core/shell materials have shown that the quality of core fraction retrieval rises with contrast until the real refractive index is around 1.5 then slowly decreases when approaching 1.6; the physical or algorithmic reasons should be examined further. For measurements without noise, the core fraction retrievals have shown good results no matter the sphericity, except for fine mode dominated size distributions. Fine mode particles case is one with the least sensitivity to the particles structural changes, to accurately retrieve the core fraction in this case is possible for only a limited range (domain of applicability) of core fraction and sphericity, unless polarisation measurements are used. The quality of core fraction reproduction from measurements with noise is heavily degraded. The precision is reduced, as well as the domain of applicability, and the core/shell materials contrast also becomes more influential on the retrieval quality. The effects of concentration, however, was found also dependent on the size of the particles. To improve the retrieval quality, the concentrations must be high for fine particles, whereas, retrieval degrades for high concentration of coarse particles; for bimodal distributions, the degradation is tempered. Finally, involvement of polarisation measurements was found as tremendously improving the retrieval quality, not only increasing the domain of applicability, but also increasing the precision. The major benefit of the information on polarisation is observed for fine mode dominated size distributions. This significantly increases the domain of applicability.

Inversions of real AERONET measurements were realised using selected representative sites such as: AgiaMarina Xyliatou, Banizoumbou, Barcelona, Beijing, Dakar, Dunkerque, GSFC, Kanpur, Lille, Paris, Sede Boker, Tamanrasset and Tel-Aviv University; from which, Barcelona, GSFC, Lille and Tel-Aviv University have measurements with information on the degree of linear polarisation. The measurements from the period 2008 to 2025 were processed. The preparation of the inversion files was realised through the existing tools of the GRASP codes. However, an important additional work was still needed, and a new tool for the integration of polarised AERONET measurements was created, including numerous tests and verifications prior to the

use for the retrievals. Moreover, while the intensity measurement quality criteria are well established in AERONET, there is no fixed standard on the almucantar symmetry quality control and angular measurement requirements for the polarisation measurements. The polarisation measurement quality control criteria and code had thus to be created, and numerous tests were conducted. The best was found to replicate the angular measurement requirements of the intensity almucantar measurements, but for the radiance reconstructed, as described in (Fedarenka et al., 2016), from the polarisation measurements.

As discussed, measurements without polarisation information have shown limited sensitivity to the core fraction, especially for fine mode dominated size distributions; however, they are still usable under a more restrictive filter on product quality.

6.2 Perspectives

GRASP/ARIA implementations

The accomplished work employed the AERONET measurements with, but also without polarisation because only few sites realise polarised almucantar measurements. Nevertheless, other measurement protocol also exists, and some other sites apply so-called "hybrid" measurements including polarisation, which, instead of measuring radiances only in the principal plane, measurements are also done in the intersecting plane to the sun. Handling of hybrid polarised measurements for the creation of input data need to be integrated in the processing, which will significantly increase the geographical and temporal domain of applicability of the newly developed algorithm. Another perspective, which should improve applicability of the algorithm is coupling of the AERONET measurements with other instruments. For instance, pairing with LIDAR or in situ measurements. The polarimetric satellite observation, like POLDER and the recently launched 3MI, is definitely the most relevant for the future application. These satellite observations gather the spectral information on light polarisation and directionality, especially in side and backward scattering angles, and could be of great utility for the particles internal structure retrieval on a global scale. The space-borne observations however require a different handling of the currently calculated kernels because the satellite observations miss an important part of information on the forward light scattering and are less sensitive to the details in the aerosol size distribution.

Another important aspect to mention is the assumption, used in this work, that only spherical particles have core/shell structure. Thus, all the tests on real AERONET measurements that had predominantly coarse particles and small sphericity fraction, and demonstrated high residuals of radiance fit, can potentially be improved. Therefore, now that sensitivity to the presence of inhomogeneity has been demonstrated, the next step might be to extend inhomogeneity to the non-spherical particles as well.

Dissemination of knowledge

One of the objectives of this thesis was to share this new model with the scientific community for use in modelling, climatology, and other scientific applications. During the work on the thesis, this objective took concrete form through participation in a community effort to recreate a database of optical computations (extinction, absorption, single-scattering albedo, lidar ratio, etc.) useful for global models and remote sensing applications. In particular, there is an international project dedicated to the tabulation of such optical computations, called the *Table of Aerosol Optics* (TAO).

Context:
Lookup tables for aerosol optical properties are an essential component of high-resolution global aerosol modelling because they gather calculations that would take too much time to perform on the fly for most purposes. The currently used aerosol tables are often taken from an old computation of aerosol properties (Shettle and Fenn, 1979) that were made open for the public. Decades later, it took form in a database with a software package called *Optical Properties of Aerosols and Clouds* (OPAC) (Köpke et al., 1997; Hess et al., 1998). The tables were later improved with Koepke et al. (2015), who re-computed the optical properties of the OPAC dust using spheroid shapes (instead of spheres) and added their results to the OPAC database.

Nevertheless, instrumentation, models and calculation techniques have evolved tremendously since Shettle and Fenn (1979), there are worldwide observation networks (e.g, AERONET), decades of satellite measurements, new ways to account for particle shape (e.g., hexahedrons) etc. The main objectives of TAO are to immediately provide updated aerosol optical lookup tables to the scientific community on an open platform, and create a flexible framework for the lookup tables that allows the scientific community to continuously update TAO as new measurements and computational techniques become available. The tables generated in this thesis,

containing extensive optical characteristics of core/shell inhomogeneous particles, correspond to one of the updates and developments that can be shared with the wider scientific community through the TAO project.

TAO project:
TAO is a project initiated as part of the MIRA working group (), which was meant, as originally conceived, to be a community repository where specialists could put their computations for other scientists to use. However, with my implication, the project significantly evolved to become a relational database in an effort to facilitate usage and maintenance, as well as extending it to also gather cloud optics in a future version : *Table of Aerosol and Cloud Optics* (TACO).

My background in data science and new skills in computation and understanding of atmospheric aerosol optical properties allowed me to suggest an approach on the creation of a relational database with the aim to be able to handle data from different contributors all over the world and be able to make it easily available for users in standardised formats. One of the advantages of working with a relational database is that it allows for the creation of an *Application Programming Interface* (API) to automatise the processes of data gathering and usage, allowing to "connect" the database to a software or computer program. The project was also thought with a web interface (using the API) that could guide the user through the database and help them to dynamically appreciate the content of the database.

My contribution to the project was in the conception and implementation of the structure of the database (backend), see appendix A.5, and the data insertion methods with the Testing First methodology. The main objective during the construction was to have a flexible database that could acquire properties from different calculations, measurements climatologies, instrument etc. and for different kind of aerosol grouping (e.g., urban aerosols or black carbon). The choice was made to work with a python interface supported by the package "SQLAlchemy", which is a package translating the python code into the language of the database. This choice allows the possibility to change the type of database, to adapt to the current need, without having to adapt large portions of the code. The database was implemented and constructed with tests files in order to communicate the prototype in several scientific conferences (EGU, AGU, Aerocom/Aerosat etc.). The implementation began with the leadership of Fabrice Ducos, currently a technical director of the AERIS/ICARE data and services centre hosted by the University of Lille. The project is now submitted to ICARE with the already implemented

architecture to host the database and build an API and a website. The tables of core/shell particles optical characteristics that I computed during my thesis will be made available to the scientists worldwide via this community tool, to the development of which I made a significant contribution.

References

Angela Benedetti, J.-J. M.: Aerosol analysis and forecast in the ECMWF Integrated Forecast System: Data assimilation., https://doi.org/10.21957/g3bogeske, 2008. [Cited on page 13]

Bauer, S. E., Ault, A., and Prather, K. A.: Evaluation of aerosol mixing state classes in the GISS modelE-MATRIX climate model using single-particle mass spectrometry measurements, Journal of Geophysical Research: Atmospheres, 118, 9834–9844, https://doi.org/10.1002/jgrd.50700, _eprint: https://agupubs.onlinelibrary.wiley.com/doi/pdf/10.1002/jgrd.50700, 2013. [Cited on page 13]

Boichu, M., Grandin, R., Blarel, L., Torres, B., Derimian, Y., Goloub, P., Brogniez, C., Chiapello, I., Dubovik, O., Mathurin, T., Pascal, N., Patou, M., and Riedi, J.: Growth and Global Persistence of Stratospheric Sulfate Aerosols From the 2022 Hunga Tonga–Hunga Ha'apai Volcanic Eruption, Journal of Geophysical Research: Atmospheres, 128, e2023JD039 010, https://doi.org/10.1029/2023JD039010, _eprint: https://agupubs.onlinelibrary.wiley.com/doi/pdf/10.1029/2023JD039010, 2023. [Cited on pages 2 and 5]

Bond, T. and Bergstrom: Light Absorption by Carbonaceous Particles: An Investigative Review, Aerosol Sci. Tecnol., 40, 27–67, https://doi.org/10.1080/02786820500421521, 2006. [Cited on page 18]

Bond, T. C., Doherty, S. J., Fahey, D. W., Forster, P. M., Berntsen, T., DeAngelo, B. J., Flanner, M. G., Ghan, S., Kärcher, B., Koch, D., Kinne, S., Kondo, Y., Quinn, P. K., Sarofim, M. C., Schultz, M. G., Schulz, M., Venkataraman, C., Zhang, H., Zhang, S., Bellouin, N., Guttikunda, S. K., Hopke, P. K., Jacobson, M. Z., Kaiser, J. W., Klimont, Z., Lohmann, U., Schwarz, J. P., Shindell, D., Storelvmo, T., Warren, S. G., and Zender, C. S.: Bounding the role of black carbon in the climate system: A scientific assessment, Journal of Geophysical Research: Atmospheres, 118, 5380–5552, https://doi.org/10.1002/jgrd.50171, _eprint: https://agupubs.onlinelibrary.wiley.com/doi/pdf/10.1002/jgrd.50171, 2013. [Cited on pages 2 and 6]

Boucher, O.: Atmospheric Aerosols, in: Atmospheric Aerosols: Properties and Climate Impacts, edited by Boucher, O., pp. 9–24, Springer Netherlands, Dordrecht, ISBN 978-94-017-9649-1, https://doi.org/10.1007/978-94-017-9649-1_2, 2015. [Cited on page 1]

Burton, S. P., Hair, J. W., Kahnert, M., Ferrare, R. A., Hostetler, C. A., Cook, A. L., Harper, D. B., Berkoff, T. A., Seaman, S. T., Collins, J. E., Fenn, M. A., and Rogers, R. R.: Observations of the spectral dependence of linear particle depolarization ratio of aerosols using NASA Langley airborne High Spectral Resolution Lidar, Atmospheric Chemistry and Physics, 15, 13 453–13 473, https://doi.org/10.5194/acp-15-13453-2015, publisher: Copernicus GmbH, 2015. [Cited on page 20]

Calvo, A. I., Alves, C., Castro, A., Pont, V., Vicente, A. M., and Fraile, R.: Research on aerosol sources and chemical composition: Past, current and emerging issues, Atmospheric Research, 120-121, 1–28, https://doi.org/10.1016/j.atmosres.2012.09.021, 2013. [Cited on page 6]

Cappa, C. D., Lovejoy, E. R., and Ravishankara, A. R.: Evidence for liquid-like and nonideal behavior of a mixture of organic aerosol components, Proceedings of the National Academy of Sciences, 105, 18 687–18 691, https://doi.org/10.1073/pnas.0802144105, publisher: Proceedings of the National Academy of Sciences, 2008. [Cited on page 9]

Chaboureau, J.-P., Labbouz, L., Flamant, C., and Hodzic, A.: Acceleration of the southern African easterly jet driven by the radiative effect of biomass burning aerosols and its impact on transport during AEROCLO-sA, Atmospheric Chemistry and Physics, 22, 8639–8658, https://doi.org/10.5194/acp-22-8639-2022, publisher: Copernicus GmbH, 2022. [Cited on page 6]

Chen, L., Peng, C., Gu, W., Fu, H., Jian, X., Zhang, H., Zhang, G., Zhu, J., Wang, X., and Tang, M.: On mineral dust aerosol hygroscopicity, Atmospheric Chemistry and Physics, 20, 13 611–13 626, https://doi.org/10.5194/acp-20-13611-2020, publisher: Copernicus GmbH, 2020. [Cited on page 5]

Chin, M. and Jacob, D. J.: Anthropogenic and natural contributions to tropospheric sulfate: A global model analysis, Journal of Geophysical Research: Atmospheres, 101, 18 691–18 699, https://doi.org/10.1029/96JD01222, _eprint: https://agupubs.onlinelibrary.wiley.com/doi/pdf/10.1029/96JD01222, 1996. [Cited on page 5]

Cohen, A. J., Brauer, M., Burnett, R., Anderson, H. R., Frostad, J., Estep, K., Balakrishnan, K., Brunekreef, B., Dandona, L., Dandona, R., Feigin, V., Freedman, G., Hubbell, B., Jobling, A., Kan, H., Knibbs, L., Liu, Y., Martin, R., Morawska, L., Pope, C. A., Shin, H., Straif, K., Shaddick, G., Thomas, M., Dingenen, R. v., Donkelaar, A. v., Vos, T., Murray, C. J. L., and Forouzanfar, M. H.: Estimates and 25-year trends of the global burden of disease attributable to ambient air pollution: an analysis of data from the Global Burden of Diseases Study 2015, The Lancet, 389, 1907–1918, https://doi.org/10.1016/S0140-6736(17)30505-6, publisher: Elsevier, 2017. [Cited on page 11]

Cook, P. A., Savage, N. H., Turquety, S., Carver, G. D., O'Connor, F. M., Heckel, A., Stewart, D., Whalley, L. K., Parker, A. E., Schlager, H., Singh, H. B., Avery, M. A., Sachse, G. W., Brune, W., Richter, A., Burrows, J. P., Purvis, R., Lewis, A. C., Reeves, C. E., Monks, P. S., Levine, J. G., and Pyle, J. A.: Forest fire plumes over the North Atlantic: p-TOMCAT model simulations with aircraft and satellite measurements from the ITOP/ICARTT campaign, Journal of Geophysical Research: Atmospheres, 112, https://doi.org/10.1029/2006JD007563, _eprint: https://agupubs.onlinelibrary.wiley.com/doi/pdf/10.1029/2006JD007563, 2007. [Cited on page 6]

Craig F. Bohren, D. R. H.: Absorption and Scattering by a Sphere, chap. 4, pp. 82–129, John Wiley & Sons, Ltd, ISBN 9783527618156, https://doi.org/https://doi.org/10.1002/9783527618156.ch4, 1998a. [Cited on page 15]

Craig F. Bohren, D. R. H.: A Potpourri of Particles, chap. 8, pp. 181–223, John Wiley & Sons, Ltd, ISBN 9783527618156, https://doi.org/https://doi.org/10.1002/9783527618156.ch8, 1998b. [Cited on page 16]

De Leeuw, G., Andreas, E. L., Anguelova, M. D., Fairall, C. W., Lewis, E. R., O'Dowd, C., Schulz, M., and Schwartz, S. E.: Production flux of sea spray aerosol, Reviews of Geophysics, 49, 2010RG000 349, https://doi.org/10.1029/2010RG000349, 2011. [Cited on page 3]

Derimian, Y., Choël, M., Rudich, Y., Deboudt, K., Dubovik, O., Laskin, A., Legrand, M., Damiri, B., Koren, I., Unga, F., Moreau, M., Andreae, M. O., and Karnieli, A.: Effect of sea breeze circulation on aerosol mixing state and radiative properties in a desert setting, Atmospheric Chemistry and Physics, 17, 11 331–11 353, https://doi.org/10.5194/acp-17-11331-2017, publisher: Copernicus GmbH, 2017. [Cited on pages 18 and 20]

Dubovik, O., Smirnov, A., Holben, B. N., King, M. D., Kaufman, Y. J., Eck, T. F., and Slutsker, I.: Accuracy assessments of aerosol optical properties retrieved from Aerosol Robotic Network (AERONET) Sun and sky radiance measurements, Journal of Geophysical Research: Atmospheres, 105, 9791–9806, https://doi.org/10.1029/2000JD900040, _eprint: https://agupubs.onlinelibrary.wiley.com/doi/pdf/10.1029/2000JD900040, 2000. [Cited on pages 17 and 19]

Dubovik, O., Holben, B., Eck, T. F., Smirnov, A., Kaufman, Y. J., King, M. D., Tanré, D., and Slutsker, I.: Variability of Absorption and Optical Properties of Key Aerosol Types Observed in Worldwide Locations, Journal of the Atmospheric Sciences, 59, 590–608, https://doi.org/10.1175/1520-0469(2002)059<0590:VOAAOP>2.0.CO;2, publisher: American Meteorological Society Section: Journal of the Atmospheric Sciences, 2002. [Cited on pages 2, 43, 44, and 56]

Dubovik, O., Sinyuk, A., Lapyonok, T., Holben, B. N., Mishchenko, M., Yang, P., Eck, T. F., Volten, H., Muñoz, O., Veihelmann, B., van der Zande, W. J., Leon, J.-F., Sorokin, M., and Slutsker, I.: Application of spheroid models to account for aerosol particle nonsphericity in remote sensing of desert dust, Journal of Geophysical Research: Atmospheres, 111, https://doi.org/10.1029/2005JD006619, _eprint: https://agupubs.onlinelibrary.wiley.com/doi/pdf/10.1029/2005JD006619, 2006. [Cited on pages 13 and 34]

Dubovik, O., Fuertes, D., Litvinov, P., Lopatin, A., Lapyonok, T., Doubovik, I., Xu, F., Ducos, F., Chen, C., Torres, B., Derimian, Y., Li, L., Herreras-Giralda, M., Herrera, M., Karol, Y., Matar, C., Schuster, G. L., Espinosa, R., Puthukkudy, A., Li, Z., Fischer, J., Preusker, R., Cuesta, J., Kreuter, A., Cede, A., Aspetsberger, M., Marth, D., Bindreiter, L., Hangler, A., Lanzinger, V., Holter, C., and Federspiel, C.: A Comprehensive Description of Multi-Term LSM for Applying Multiple a Priori Constraints in Problems of Atmospheric Remote Sensing: GRASP Algorithm, Concept, and Applications, Frontiers in Remote Sensing, 2, https://doi.org/10.3389/frsen.2021.706851, publisher: Frontiers, 2021. [Cited on pages 28 and 173]

Eck, T. F., Holben, B. N., Reid, J. S., Xian, P., Giles, D. M., Sinyuk, A., Smirnov, A., Schafer, J. S., Slutsker, I., Kim, J., Koo, J.-H., Choi, M., Kim, K. C., Sano, I., Arola, A., Sayer, A. M., Levy, R. C., Munchak, L. A., O'Neill, N. T., Lyapustin, A., Hsu, N. C., Randles, C. A., Da Silva, A. M., Buchard, V., Govindaraju,

R. C., Hyer, E., Crawford, J. H., Wang, P., and Xia, X.: Observations of the Interaction and Transport of Fine Mode Aerosols With Cloud and/or Fog in Northeast Asia From Aerosol Robotic Network and Satellite Remote Sensing, Journal of Geophysical Research: Atmospheres, 123, 5560–5587, https://doi.org/10.1029/2018JD028313, _eprint: https://agupubs.onlinelibrary.wiley.com/doi/pdf/10.1029/2018JD028313, 2018. [Cited on page 10]

Fang, T., Guo, H., Zeng, L., Verma, V., Nenes, A., and Weber, R. J.: Highly Acidic Ambient Particles, Soluble Metals, and Oxidative Potential: A Link between Sulfate and Aerosol Toxicity, Environmental Science & Technology, 51, 2611–2620, https://doi.org/10.1021/acs.est.6b06151, publisher: American Chemical Society, 2017. [Cited on page 11]

Fedarenka, A., Dubovik, O., Goloub, P., Li, Z., Lapyonok, T., Litvinov, P., Barel, L., Gonzalez, L., Podvin, T., and Crozel, D.: Utilization of AERONET polarimetric measurements for improving retrieval of aerosol microphysics: GSFC, Beijing and Dakar data analysis, Journal of Quantitative Spectroscopy and Radiative Transfer, 179, 72–97, https://doi.org/10.1016/j.jqsrt.2016.03.021, 2016. [Cited on pages 37, 38, and 148]

Formenti, P., Schütz, L., Balkanski, Y., Desboeufs, K., Ebert, M., Kandler, K., Petzold, A., Scheuvens, D., Weinbruch, S., and Zhang, D.: Recent progress in understanding physical and chemical properties of African and Asian mineral dust, Atmospheric Chemistry and Physics, 11, 8231–8256, https://doi.org/10.5194/acp-11-8231-2011, publisher: Copernicus GmbH, 2011. [Cited on page 4]

Friedlander, S. K. and Friedlander, P. P. C. E. D. A. Q. A. T. L. S. K.: Smoke, Dust, and Haze: Fundamentals of Aerosol Dynamics, Oxford University Press, ISBN 978-0-19-512999-1, `https://books.google.fr/books?id=uxDcwAEACAAJ`, 2000. [Cited on page 8]

Fuller, K. A.: Scattering and absorption cross sections of compounded spheres. III. Spheres containing arbitrarily located spherical inhomogeneities, JOSA A, Vol. 12, Issue 5, pp. 893-904, https://doi.org/10.1364/JOSAA.12.000893, publisher: Optica Publishing Group, 1995. [Cited on page 18]

Fuzzi, S., Baltensperger, U., Carslaw, K., Decesari, S., Denier van der Gon, H., Facchini, M. C., Fowler, D., Koren, I., Langford, B., Lohmann, U., Nemitz, E., Pandis, S., Riipinen, I., Rudich, Y., Schaap, M., Slowik, J. G., Spracklen, D. V., Vignati, E., Wild, M., Williams, M., and Gilardoni, S.: Particulate matter, air quality and climate: lessons learned and

future needs, Atmospheric Chemistry and Physics, 15, 8217–8299, https://doi.org/10.5194/acp-15-8217-2015, publisher: Copernicus GmbH, 2015. [Cited on page 11]

Gliß, J., Mortier, A., Schulz, M., Andrews, E., Balkanski, Y., Bauer, S. E., Benedictow, A. M. K., Bian, H., Checa-Garcia, R., Chin, M., Ginoux, P., Griesfeller, J. J., Heckel, A., Kipling, Z., Kirkevåg, A., Kokkola, H., Laj, P., Le Sager, P., Lund, M. T., Lund Myhre, C., Matsui, H., Myhre, G., Neubauer, D., van Noije, T., North, P., Olivié, D. J. L., Rémy, S., Sogacheva, L., Takemura, T., Tsigaridis, K., and Tsyro, S. G.: AeroCom phase III multi-model evaluation of the aerosol life cycle and optical properties using ground- and space-based remote sensing as well as surface in situ observations, Atmospheric Chemistry and Physics, 21, 87–128, https://doi.org/10.5194/acp-21-87-2021, publisher: Copernicus GmbH, 2021. [Cited on page 9]

Grandey, B. S., Rothenberg, D., Avramov, A., Jin, Q., Lee, H.-H., Liu, X., Lu, Z., Albani, S., and Wang, C.: Effective radiative forcing in the aerosol-climate model CAM5.3-MARC-ARG, Atmospheric Chemistry and Physics, 18, 15 783–15 810, https://doi.org/10.5194/acp-18-15783-2018, arXiv:1804.06158 [physics.ao-ph], 2018. [Cited on page 1]

Grant-Jacob, J. and Mills, B.: Deep learning in airborne particulate matter sensing: a review, Journal of Physics Communications, 6, 122 001, https://doi.org/10.1088/2399-6528/aca45e, 2022. [Cited on page 11]

Guirado, C., Cuevas, E., Cachorro, V. E., Toledano, C., Alonso-Pérez, S., Bustos, J. J., Basart, S., Romero, P. M., Camino, C., Mimouni, M., Zeudmi, L., Goloub, P., Baldasano, J. M., and de Frutos, A. M.: Aerosol characterization at the Saharan AERONET site Tamanrasset, Atmospheric Chemistry and Physics, 14, 11 753–11 773, https://doi.org/10.5194/acp-14-11753-2014, publisher: Copernicus GmbH, 2014. [Cited on page 134]

Guo, L., Gu, W., Peng, C., Wang, W., Li, Y. J., Zong, T., Tang, Y., Wu, Z., Lin, Q., Ge, M., Zhang, G., Hu, M., Bi, X., Wang, X., and Tang, M.: A comprehensive study of hygroscopic properties of calcium- and magnesium-containing salts: implication for hygroscopicity of mineral dust and sea salt aerosols, Atmospheric Chemistry and Physics, 19, 2115–2133, https://doi.org/10.5194/acp-19-2115-2019, publisher: Copernicus GmbH, 2019. [Cited on page 5]

Herrera, M. E., Dubovik, O., Torres, B., Lapyonok, T., Fuertes, D., Lopatin, A., Litvinov, P., Chen, C., Benavent-Oltra, J. A., Bali, J. L., and Ristori, P. R.: Estimates of remote sensing

retrieval errors by the GRASP algorithm: application to ground-based observations, concept and validation, Atmospheric Measurement Techniques, 15, 6075–6126, https://doi.org/10.5194/amt-15-6075-2022, publisher: Copernicus GmbH, 2022. [Cited on page 21]

Hess, M., Koepke, P., and Schult, I.: Optical Properties of Aerosols and Clouds: The Software Package OPAC, Bulletin of the American Meteorological Society, 79, 831–844, https://doi.org/10.1175/1520-0477(1998)079<0831:OPOAAC>2.0.CO;2, publisher: American Meteorological Society Section: Bulletin of the American Meteorological Society, 1998. [Cited on page 149]

JACOB, D. J.: Introduction to Atmospheric Chemistry, Princeton University Press, `http://www.jstor.org/stable/j.ctt7t8hg`, 1999. [Cited on page 9]

Jacobson, M. Z., Turco, R. P., Jensen, E. J., and Toon, O. B.: Modeling coagulation among particles of different composition and size, Atmospheric Environment, 28, 1327–1338, https://doi.org/10.1016/1352-2310(94)90280-1, 1994. [Cited on page 8]

Kahnert, M.: Modelling radiometric properties of inhomogeneous mineral dust particles: Applicability and limitations of effective medium theories, Journal of Quantitative Spectroscopy and Radiative Transfer, 152, 16–27, https://doi.org/10.1016/j.jqsrt.2014.10.025, 2015. [Cited on page 18]

Kaufman, Y. J., Gitelson, A., Karnieli, A., Granor, E., Fraser, R. S., Nakajima, T., Mattoo, S., and Holben, B. N.: Size distribution and scattering phase function of aerosol particles retrieved from sky brightness measurements, Journal of Geophysical Research: Atmospheres, 99, 10 341–10 356, https://doi.org/10.1029/94JD00229, _eprint: https://agupubs.onlinelibrary.wiley.com/doi/pdf/10.1029/94JD00229, 1994. [Cited on page 46]

Khaykin, S., Legras, B., Bucci, S., Sellitto, P., Isaksen, L., Tencé, F., Bekki, S., Bourassa, A., Rieger, L., Zawada, D., Jumelet, J., and Godin-Beekmann, S.: The 2019/20 Australian wildfires generated a persistent smoke-charged vortex rising up to 35 km altitude, Communications Earth & Environment, 1, 22, https://doi.org/10.1038/s43247-020-00022-5, publisher: Nature Publishing Group, 2020. [Cited on page 2]

Khaykin, S., Bekki, S., Godin-Beekmann, S., Fromm, M. D., Goloub, P., Hu, Q., Josse, B., Laeng, A., Meziane, M., Peterson, D. A., Pelletier, S., and Thouret, V.: Stratospheric impact of the anomalous 2023 Canadian wildfires: the two vertical pathways of smoke, Atmospheric

Chemistry and Physics, 25, 14 551–14 571, https://doi.org/10.5194/acp-25-14551-2025, publisher: Copernicus GmbH, 2025. [Cited on page 2]

Kinne, S., Lohmann, U., Feichter, J., Schulz, M., Timmreck, C., Ghan, S., Easter, R., Chin, M., Ginoux, P., Takemura, T., Tegen, I., Koch, D., Herzog, M., Penner, J., Pitari, G., Holben, B., Eck, T., Smirnov, A., Dubovik, O., Slutsker, I., Tanre, D., Torres, O., Mishchenko, M., Geogdzhayev, I., Chu, D. A., and Kaufman, Y.: Monthly averages of aerosol properties: A global comparison among models, satellite data, and AERONET ground data, Journal of Geophysical Research: Atmospheres, 108, 2001JD001 253, https://doi.org/10.1029/2001JD001253, 2003. [Cited on page 9]

Koepke, P., Gasteiger, J., and Hess, M.: Technical Note: Optical properties of desert aerosol with non-spherical mineral particles: data incorporated to OPAC, Atmos. Chem. Phys., https://doi.org/10.5194/acp-15-5947-2015, 2015. [Cited on page 149]

Konovalov, I. B., Beekmann, M., Berezin, E. V., Formenti, P., and Andreae, M. O.: Probing into the aging dynamics of biomass burning aerosol by using satellite measurements of aerosol optical depth and carbon monoxide, Atmospheric Chemistry and Physics, 17, 4513–4537, https://doi.org/10.5194/acp-17-4513-2017, publisher: Copernicus GmbH, 2017. [Cited on page 6]

Köpke, P., Hess, M., Schult, I., and Shettle, E.: Global Aerosol Data Set, Tech. Rep. 243, MPI Meteorologie Hamburg, 1997. [Cited on page 149]

Kroll, J. H. and Seinfeld, J. H.: Chemistry of secondary organic aerosol: Formation and evolution of low-volatility organics in the atmosphere, Atmospheric Environment, 42, 3593–3624, https://doi.org/10.1016/j.atmosenv.2008.01.003, 2008. [Cited on page 1]

Lang-Yona, N., Abo-Riziq, A., Haspel, C., Segre, E., Trainic, M., and Rudich, Y.: Interaction of internally mixed aerosols with light, Physical chemistry chemical physics : PCCP, 12, 21–31, https://doi.org/10.1039/b913176k, 2010. [Cited on page 18]

Laskin, A., Wietsma, T. W., Krueger, B. J., and Grassian, V. H.: Heterogeneous chemistry of individual mineral dust particles with nitric acid: A combined CCSEM/EDX, ESEM, and ICP-MS study, Journal of Geophysical Research: Atmospheres, 110, https://doi.org/10.1029/2004JD005206, _eprint: https://agupubs.onlinelibrary.wiley.com/doi/pdf/10.1029/2004JD005206, 2005. [Cited on page 9]

LeGrand, S. L., Polashenski, C., Letcher, T. W., Creighton, G. A., Peckham, S. E., and Cetola, J. D.: The AFWA dust emission scheme for the GOCART aerosol model in WRF-Chem v3.8.1, Geoscientific Model Development, 12, 131–166, https://doi.org/10.5194/gmd-12-131-2019, publisher: Copernicus GmbH, 2019. [Cited on page 4]

Lenoble, J., Herman, M., Deuzé, J. L., Lafrance, B., Santer, R., and Tanré, D.: A successive order of scattering code for solving the vector equation of transfer in the earth's atmosphere with aerosols, Journal of Quantitative Spectroscopy and Radiative Transfer, 107, 479–507, https://doi.org/10.1016/j.jqsrt.2007.03.010, 2007. [Cited on page 28]

Li, L., Dubovik, O., Derimian, Y., Schuster, G. L., Lapyonok, T., Litvinov, P., Ducos, F., Fuertes, D., Chen, C., Li, Z., Lopatin, A., Torres, B., and Che, H.: Retrieval of aerosol components directly from satellite and ground-based measurements, Atmospheric Chemistry and Physics, 19, 13 409–13 443, https://doi.org/10.5194/acp-19-13409-2019, publisher: Copernicus GmbH, 2019. [Cited on pages 10 and 28]

Li, Z., Gu, X., Wang, L., Li, D., Xie, Y., Li, K., Dubovik, O., Schuster, G., Goloub, P., Zhang, Y., Li, L., Ma, Y., and Xu, H.: Aerosol physical and chemical properties retrieved from ground-based remote sensing measurements during heavy haze days in Beijing winter, Atmospheric Chemistry and Physics, 13, 10 171–10 183, https://doi.org/10.5194/acp-13-10171-2013, publisher: Copernicus GmbH, 2013. [Cited on page 18]

Liu, J., Lin, P., Laskin, A., Laskin, J., Kathmann, S. M., Wise, M., Caylor, R., Imholt, F., Selimovic, V., and Shilling, J. E.: Optical properties and aging of light-absorbing secondary organic aerosol, Atmospheric Chemistry and Physics, 16, 12 815–12 827, https://doi.org/10.5194/acp-16-12815-2016, publisher: Copernicus GmbH, 2016. [Cited on page 6]

Mie, G.: Beiträge zur Optik trüber Medien, speziell kolloidaler Metallösungen, Annalen der Physik, 330, 377–445, https://doi.org/10.1002/andp.19083300302, _eprint: https://onlinelibrary.wiley.com/doi/pdf/10.1002/andp.19083300302, 1908. [Cited on page 14]

Mishchenko, M. I. and Travis, L. D.: Satellite retrieval of aerosol properties over the ocean using polarization as well as intensity of reflected sunlight, Journal of Geophysical Research, 102, 16 989–17 013, https://doi.org/10.1029/96JD02425, 1997. [Cited on page 17]

Mishchenko, M. I., Hovenier, J. W., and Travis, L. D., eds.: Light Scattering by Nonspherical Particles: Theory, Measurements, and Applications, Academic Press, San Diego, 2000. [Cited on page 22]

Mishchenko, M. I., Liu, L., Cairns, B., and Mackowski, D. W.: Optics of water cloud droplets mixed with black-carbon aerosols, Opt. Lett., 39, 2607–2610, https://doi.org/10.1364/OL.39.002607, 2014. [Cited on page 18]

Mishchenko, M. I., Dlugach, J. M., and Liu, L.: Linear depolarization of lidar returns by aged smoke particles, Applied Optics, 55, 9968–9973, https://doi.org/10.1364/AO.55.009968, publisher: Optica Publishing Group, 2016. [Cited on page 20]

Morawska, L., Thomas, S., Jamriska, M., and Johnson, G.: The modality of particle size distributions of environmental aerosols, Atmospheric Environment, 33, 4401–4411, https://doi.org/10.1016/S1352-2310(99)00217-4, 1999. [Cited on page 2]

Muller, P.: Glossary of terms used in physical organic chemistry (IUPAC Recommendations 1994), Pure and Applied Chemistry, 66, 1077–1184, https://doi.org/10.1351/pac199466051077, publisher: De Gruyter, 1994. [Cited on page 8]

Peterson, D. A., Campbell, J. R., Hyer, E. J., Fromm, M. D., Kablick, G. P., Cossuth, J. H., and DeLand, M. T.: Wildfire-driven thunderstorms cause a volcano-like stratospheric injection of smoke, npj Climate and Atmospheric Science, 1, 30, https://doi.org/10.1038/s41612-018-0039-3, publisher: Nature Publishing Group, 2018. [Cited on page 2]

Petters, M. D. and Kreidenweis, S. M.: A single parameter representation of hygroscopic growth and cloud condensation nucleus activity, Atmospheric Chemistry and Physics, 7, 1961–1971, https://doi.org/10.5194/acp-7-1961-2007, publisher: Copernicus GmbH, 2007. [Cited on page 8]

Prospero, J. M., Barkley, A. E., Gaston, C. J., Gatineau, A., Campos y Sansano, A., and Panechou, K.: Characterizing and Quantifying African Dust Transport and Deposition to South America: Implications for the Phosphorus Budget in the Amazon Basin, Global Biogeochemical Cycles, 34, e2020GB006 536, https://doi.org/10.1029/2020GB006536, _eprint: https://agupubs.onlinelibrary.wiley.com/doi/pdf/10.1029/2020GB006536, 2020. [Cited on page 4]

Pöschl, U.: Atmospheric Aerosols: Composition, Transformation, Climate and Health Effects, Angewandte Chemie International Edition, 44, 7520–7540, https://doi.org/10.1002/anie.200501122, _eprint: https://onlinelibrary.wiley.com/doi/pdf/10.1002/anie.200501122, 2005. [Cited on page 5]

Rosenfeld, D., Andreae, M. O., Asmi, A., Chin, M., de Leeuw, G., Donovan, D. P., Kahn, R., Kinne, S., Kivekäs, N., Kulmala, M., Lau, W., Schmidt, K. S., Suni, T., Wagner, T., Wild, M., and Quaas, J.: Global observations of aerosol-cloud-precipitation-climate interactions, Reviews of Geophysics, 52, 750–808, https://doi.org/https://doi.org/10.1002/2013RG000441, 2014. [Cited on page 10]

Rudich, Y., Donahue, N. M., and Mentel, T. F.: Aging of Organic Aerosol: Bridging the Gap Between Laboratory and Field Studies, Annual Review of Physical Chemistry, 58, 321–352, https://doi.org/10.1146/annurev.physchem.58.032806.104432, publisher: Annual Reviews, 2007. [Cited on page 6]

Schuster, G. L., Lin, B., and Dubovik, O.: Remote sensing of aerosol water uptake, Geophysical Research Letters, 36, https://doi.org/10.1029/2008GL036576, _eprint: https://agupubs.onlinelibrary.wiley.com/doi/pdf/10.1029/2008GL036576, 2009. [Cited on page 18]

Seinfeld, J. H. and Pandis, S. N.: Atmospheric Chemistry and Physics: From Air Pollution to Climate Change, Wiley, ISBN 978-1-118-94740-1, `https://books.google.fr/books?id=n_RmCgAAQBAJ`, 2016. [Cited on page 8]

Shettle, E. and Fenn, R.: Models for the Aerosols of the Lower Atmosphere and the Effects of Humidity on Their Optical Properties, Tech. Rep. AFGL-TR-790214, Air Force Geophysics Laboratory, 1979. [Cited on page 149]

Si, Y., Lu, Q., Zhang, X., Hu, X., Wang, F., Li, L., and Gu, S.: A review of advances in the retrieval of aerosol properties by remote sensing multi-angle technology, Atmospheric Environment, 244, 117 928, https://doi.org/10.1016/j.atmosenv.2020.117928, 2021. [Cited on page 7]

Stamnes, K., Tsay, S. C., Wiscombe, W., and Jayaweera, K.: Numerically stable algorithm for discrete-ordinate-method radiative transfer in multiple scattering and emitting layered media, Applied Optics, 27, 2502–2509, https://doi.org/10.1364/AO.27.002502, 1988. [Cited on page 18]

Stocker, T. F., Dahe, Q., and Plattner, G.-K.: Technical Summary, AR5 Climate Change 2013: The Physical Science Basis — IPCC, `https://www.ipcc.ch/report/ar5/wg1/`, 2013. [Cited on page 3]

Sun, J. and Ariya, P. A.: Atmospheric organic and bio-aerosols as cloud condensation nuclei (CCN): A review, Atmospheric Environment, 40, 795–820, https://doi.org/10.1016/j.atmosenv.2005.05.052, 2006. [Cited on page 5]

Textor, C., Schulz, M., Guibert, S., Kinne, S., Balkanski, Y., Bauer, S., Berntsen, T., Berglen, T., Boucher, O., Chin, M., Dentener, F., Diehl, T., Easter, R., Feichter, H., Fillmore, D., Ghan, S., Ginoux, P., Gong, S., Grini, A., Hendricks, J., Horowitz, L., Huang, P., Isaksen, I., Iversen, I., Kloster, S., Koch, D., Kirkevåg, A., Kristjansson, J. E., Krol, M., Lauer, A., Lamarque, J. F., Liu, X., Montanaro, V., Myhre, G., Penner, J., Pitari, G., Reddy, S., Seland, , Stier, P., Takemura, T., and Tie, X.: Analysis and quantification of the diversities of aerosol life cycles within AeroCom, Atmospheric Chemistry and Physics, 6, 1777–1813, https://doi.org/10.5194/acp-6-1777-2006, publisher: Copernicus GmbH, 2006. [Cited on page 2]

Toon, O. B. and Ackerman, T. P.: Algorithms for the calculation of scattering by stratified spheres, Applied Optics, 20, 3657–3660, https://doi.org/10.1364/AO.20.003657, publisher: Optica Publishing Group, 1981. [Cited on page 42]

Toon O. B., A. T. P.: Algorithms for the calculation of scattering by stratified spheres, Applied optics, 20, 3657–3660, https://doi.org/https://doi.org/10.1364/AO.20.003657, publisher: Copernicus GmbH, 1981. [Cited on page 29]

Twomey, S.: The Influence of Pollution on the Shortwave Albedo of Clouds, Journal of the Atmospheric Sciences, 34, 1149–1152, https://doi.org/10.1175/1520-0469(1977)034<1149:TIOPOT>2.0.CO;2, publisher: American Meteorological Society Section: Journal of the Atmospheric Sciences, 1977. [Cited on page 10]

Unga, F., Choël, M., Derimian, Y., Deboudt, K., Dubovik, O., and Goloub, P.: Microscopic Observations of Core-Shell Particle Structure and Implications for Atmospheric Aerosol Remote Sensing, Journal of Geophysical Research: Atmospheres, 123, 13,944–13,962, https://doi.org/10.1029/2018JD028602, _eprint: https://agupubs.onlinelibrary.wiley.com/doi/pdf/10.1029/2018JD028602, 2018. [Cited on pages 18, 20, 26, 35, 43, 57, and 172]

Urbanski, S. P., Hao, W. M., and Nordgren, B.: The wildland fire emission inventory: western United States emission estimates and an evaluation of uncertainty, Atmospheric Chemistry and Physics, 11, 12 973–13 000, https://doi.org/10.5194/acp-11-12973-2011, publisher: Copernicus GmbH, 2011. [Cited on page 6]

Waquet, F. and Herman, M.: The truncation problem, Journal of Quantitative Spectroscopy and Radiative Transfer, 229, 80–91, https://doi.org/10.1016/j.jqsrt.2019.02.001, 2019. [Cited on page 28]

Watanabe, M., Iwasaka, Y., Shibata, T., Hayashi, M., Fujiwara, M., and Neuber, R.: The evolution of Pinatubo aerosols in the Arctic stratosphere during 1994–2000, Atmospheric Research, 69, 199–215, https://doi.org/10.1016/j.atmosres.2003.09.006, 2004. [Cited on page 5]

White, W. H.: Chemical markers for sea salt in IMPROVE aerosol data, Atmospheric Environment, 42, 261–274, https://doi.org/10.1016/j.atmosenv.2007.09.040, 2008. [Cited on page 3]

Winiwarter, W., Kuhlbusch, T. A. J., Viana, M., and Hitzenberger, R.: Quality considerations of European PM emission inventories, Atmospheric Environment, 43, 3819–3828, https://doi.org/10.1016/j.atmosenv.2009.05.023, 2009. [Cited on page 5]

Appendix A

A.1 In depth description of GRASP algorithm settings file

The first elements composing the settings file are:

```
input:
    driver: sdata
    file:  /path/to/a.sdata
    segment:
        x: 1
        y: 1
        t: 1

    transformer: [segment_imagedat]
    transformer_settings:
        segment_imagedat:
            file: /path/to/a.dat
```

This part handles the input data from which we want to retrieve the aerosol properties where "driver" designates the type of the measurements file and "file", its path. "segment" describes how to handle the dimensionality of the inputted data during inversion; here every measurement is considered independent in space and time. "transformer" is an optional additional file that initialises the values of every retrieved characteristic, dynamically overwriting the initial guesses to adapt initial conditions to each measurement. The practical aspects of this feature will be discussed later; nonetheless, transformers are useful to have individual initial guesses,

should it be for, e.g., surface reflectance that need to be adapted to every location or volume concentrations of the size distribution that can be adapted according to the measured TOD, as an educated a priori information. The next part handles outputs:

```
output:
    sdata:
        dump: /path/to/a.sdata
    segment:
        function: csv # csv, plot, none
        stream: /path/to/a.csv  #screen #
```

where the "sdata"-"dump" part designates the optical measurement simulated by the forward model at the end of the inversion, it is mostly useful for the creation of synthetic data with the forward mode or when the quality of angular reproduction needs to be assessed. "segment"-" function" and "stream" refer to the format of output to be generated and where to. It can be a file or a textual output on a command prompt. The most useful format for this kind of study is the csv which stores data in tables that can be easily used to generate graphics.

The following part defines the operational properties of the algorithm itself:

```
retrieval:
    general:
        path_to_internal_files:
         ↪ "/workspace/repos/grasp/src/retrieval/internal_files/"

    mode: inversion

    inversion:
        regime: single_pixel

        convergence:
            minimization_convention: logarithm
            maximum_iterations_for_stopping: 35
            maximum_iterations_of_Levenberg-Marquardt: 35
            threshold_for_stopping: 1.0e-4
            threshold_for_stopping_Q_iterations: 1e-12
            scale_for_finite_difference: 5.0e-3

        noises:
            #add_random_noise : measurement_fitting
```

```
        noise[1]:
            standard_deviation_synthetic: 0.0 #0.03
            error_type:  relative
            standard_deviation:  0.03
            measurement_type[1]:
                type: I
                index_of_wavelength_involved: [ 1, 2, 3, 4 ]
        noise[2]:
            standard_deviation_synthetic: 0.0 #0.005
            error_type:  absolute
            standard_deviation:  0.005
            measurement_type[1]:
                type: tod
                index_of_wavelength_involved: [ 1, 2, 3, 4 ]
        noise[3]:
            standard_deviation_synthetic: 0.0 #0.005
            error_type:  absolute
            standard_deviation:  0.005
            measurement_type[1]:
                type: P_rel
                index_of_wavelength_involved: [ 1, 2, 3, 4 ]

    measurement_fitting:
        polarization: degree_of_polarization
        ↪ #absolute_polarization_components,
        ↪ relative_polarization_components, polarized_reflectance, and
        ↪ degree_of_polarization
```

As was mentioned, the GRASP algorithm is modular and can adapt to different configurations to enable this functionality, some paths are given in the settings file like the path to internal files, which includes kernels and other resources necessary for the forward model. The option "path_to_internal_files", then defines the root folder for the following paths. "mode" sets the purpose of the algorithm, the inversion mode uses an iterative procedure to adjust some defined aerosol properties to reproduce the input data with the forward model through the minimalisation of the reproduction differences between markers defined in "noises"; the forward mode runs the forward model once with fixed values for the defined aerosol properties. The forward mode can be used, for example, to synthetically generate the measurements of an instrument. This synthetic data grants a way to assess the quality and stability of an inversion model assessing its capacity to reproduce a result for which the aerosol model is known, i.e., initially assumed in

the calculation. The inversion "regime" can be defined as single pixel or multi pixel. Single pixel treats every measurement individually, whereas multi pixel enables the different measurements to be constrained in respect to a certain coherence between aerosol properties, may it be from a spacial or temporal proximity.

The “convergence” part defines the precision of the algorithm in the following way:

```
convergence:
    minimization_convention: logarithm
    maximum_iterations_for_stopping: 35
    maximum_iterations_of_Levenberg-Marquardt: 35
    threshold_for_stopping: 1.0e-4
    threshold_for_stopping_Q_iterations: 1e-12
    scale_for_finite_difference: 5.0e-3
```

This part defines the intended limits and precision of the gradient descent, which can impact calculation results and inversion time. Indeed, results may be affected by an over-fitting problem in some rare cases because of a high number of iterations because, to converge, the algorithm is built to relax some of the constraints after several iterations without a clear improvement in the quality of the retrieval. "minimization_convention" gives the scale of those expected improvements. "maximum_iterations_for_stopping" is self-explanatory, while "maximum_iterations_of_Levenberg-Marquardt" is the number of iteration where the Levenberg-Marquardt correction is applied; this convergence algorithm, though precise, may slow the convergence speed. "threshold_for_stopping" designates the change of the score between two p - iterations (main iterations), if the change in score is below the threshold, this algorithm comes to an end. This value is important for the previously mentioned over-fitting issue. "threshold_for_stopping_Q_iterations" is the same for q - iterations (smaller iterations set inside p - iterations).
"scale_for_finite_difference" corresponds to the scale of the changes in the variables of the vector "a" between q - iterations.

Description of the noises is formulated as follows:

```
noises:
    #add_random_noise : measurement_fitting
    noise[1]:
        standard_deviation_synthetic: 0.0 #0.03
        error_type:  relative
        standard_deviation:  0.03
        measurement_type[1]:
```

```
                type: I
                index_of_wavelength_involved: [ 1, 2, 3, 4 ]
        noise[2]:
            standard_deviation_synthetic: 0.0 #0.005
            error_type:  absolute
            standard_deviation:  0.005
            measurement_type[1]:
                type: tod
                index_of_wavelength_involved: [ 1, 2, 3, 4 ]
        noise[3]:
            standard_deviation_synthetic: 0.0 #0.005
            error_type:  absolute
            standard_deviation:  0.005
            measurement_type[1]:
                type: P_rel
                index_of_wavelength_involved: [ 1, 2, 3, 4 ]

    measurement_fitting:
        polarization: degree_of_polarization
        ↪ #absolute_polarization_components,
        ↪ relative_polarization_components, polarized_reflectance, and
        ↪ degree_of_polarization
```

"noises" correspond to two things, the first is the "standard_deviation" which is an expected noise caused by a supposed instrumental imprecision in the data collection. The second is the "standard_deviation_synthetic" which represents noise that can be applied to synthetic (simulated) measurements in order to estimate impact of inconsistencies in the measured radiances on the retrieved aerosol model. The noises are linked to the type of measurements present in the input file and that should be reproduced by the forward model computation. Three "type" of measurements are considered here: "I" is the sky irradiance, tod is the Total Optical Depth (TOD) and "P_rel" is the light polarisation. "measurement_fitting"-"polarization" is there to define which type of polarisation parameter is used. "error_type" defines if the associated noise value is based on the relative difference between measured and retrieved or the absolute one. The absence of a measurement type requires the removal of its associated noise from the settings file.

The forward radiative transfer calculation settings are the following:

```
forward_model:
    aerosol:
```

```
        sphere_core:
            kernels_folder: kernels_sphere_core/
            value:
                mode[1]: [0.9, 0.8, 0.7, 0.65, 0.6, 0.55, 0.5, 0.45, 0.4,
                ↪  0.35]
        use_layered_spheres: true
    phase_matrix:
        size_binning_method_for_triangle_bins: logarithm
        number_of_elements: 4
        kernels_folder: "KERNELS_BASE/"
        radius:
            mode[1]:
                min: 0.05
                max: 15.0
```

"forward_model" handles the modules employed by the forward model, gathered in the internal files. "sphere_core"-"value" defines the list of kernels to load inside the algorithm. "mode[1]", standing alone, indicates that the SD of this settings file uses a single mode of 22 triangle bins, which are defined in "phase_matrix". Another format exists with a bi-modality represented by 15 bins for the fine mode and 10 bins for the coarse mode. This distinction may have meaning in our application if, for example, as seen in Unga et al. (2018), the mean relative shell radius is different for coarse and for fine particles. In that case, loading specific kernels for coarse and for fine particles might be a sensible option to ensure better precision in the retrieval; the realisation, however, is subjected to measurement sensitivity and potential overfitting issues, which have to be tested. "phase_matrix" corresponds to the default handling of the kernels in their globality, homogeneous and inhomogeneous alike; defining the logarithmic scale of the SD bins with "size_binning_method_for_triangle_bins". "number_of_elements" is the number of used scattering elements to contribute to the inversion process. "radius" defines bin limits for each mode.

The radiative transfer settings are:

```
radiative_transfer:
    number_of_layers: 50
    aerosol_profile_vertical_type:    exponential
    molecular_profile_vertical_type: standard_atmosphere
    reference_plane_for_polarization: meridian
    gaussian_quadrature_type: double
    radiance_theoretical_interpolation: true
```

```
        double_precision_in_single_scattering: true
        simulating_observation:
            order_of_scattering: multiple_scattering
            number_of_gaussian_quadratures_for_expansion_coefficients:  41
            ↪ number_of_guassian_quadratures_for_fourier_expansion_coefficients:
            ↪ 20
            number_of_fourier_expansion_coefficients:  20
        simulating_derivatives:
            order_of_scattering: single_scattering
            number_of_gaussian_quadratures_for_expansion_coefficients:  21
            ↪ number_of_guassian_quadratures_for_fourier_expansion_coefficients:
            ↪ 10
            number_of_fourier_expansion_coefficients: 10
        phase_matrix_truncation: true
```

"number_of_layers" is the number of vertical layers resolved in radiative transfer calculations. "aerosol_profile_vertical_type" is the type of distribution used to model aerosol concentration vertical profile; exponential calculation is only based on altitude : $\frac{\exp(\frac{h}{HM})}{HM}$. Gaussian uses the normal distribution $\frac{\exp(h-HM)}{\sqrt{rpi}} \times \sigma$. "molecular_profile_vertical_type" is the type of calculation used to model molecular vertical profile; exponential calculation is only based on altitude : $\frac{\exp(\frac{h}{8})}{8}$. [standard_atmosphere] is another type using predefined temperature and pressure profiles to calculate molecular density at each altitude. "simulating_observation", in the case of most remote sensing instruments, uses [multiple_scattering] as assumed for aerosol scattering in the atmosphere. "simulating_derivatives" is the step of the derivative used to integrate "simulating_observations", meaning the [multiple_scattering] calculation is composed of single_scattering calculations elements. The corresponding number of Gaussian quadratures and expansion coefficients is used for the balance between accuracy and calculation speed, as described in (Dubovik et al., 2021). The "phase_matrix_truncation" option allows the separation of the forward peak from the rest of the phase function to reduce computational time (without heavily impacting the accuracy of the model).

The output products definition:

```
    products:
        configuration:
            wavelength_indices_for_angstrom: [1, 3]
            aerosol_particulate_matter_diameter: 10.0
```

```
        aerosol:
            chemistry: false
            lidar: false
            optical_properties: true
            phase_matrix: false
            refractive_index: true
            theoretical_bimodal_extinction: true
            theoretical_bimodal_parameters: true
        error_estimation:
            aerosol:
                lidar: false
                optical_properties: false
            parameters: false
        forcing:
            broadband_flux: false
            forcing: false
        retrieval:
            fitting: true
            parameters: true
            residual: true
```

"products" defines the received parameters in the output, such as "wavelength_indices_for_angstrom" defines the indices of the wavelength used to calculate the outputted Angström exponent; "aerosol_particulate_matter_diameter" defines the diameter in μm used to calculate PM; and "aerosol", "error_estimation", "forcing" and "retrieval" describe which type of information should be returned.

There is also a "debug" option used to visualise key elements of the inversion process to check if the algorithm is functioning as intended.

The final part "constraints" defines the initial guesses and constrains definition, where, alongside with the aforementioned loading of the Core/Shell kernels, a characteristic related to the newly developed Core/Shell parameterisation option now appears:

```
    constraints:
        characteristic[1]: #1
            type: size_distribution_triangle_bins
            retrieved: true
            mode[1]:
```

```
initial_guess:                          #1        #2        #3
↪ #4        #5        #6        #7        #8        #9
↪ #10       #11       #12       #13       #14       #15
↪ #16       #17       #18       #19       #20       #21
↪ #22
    value:                          [ 0.000011,  0.0011,
    ↪ 0.0011,  0.0011,  0.0011,  0.0011,  0.0011,  0.0011,
    ↪ 0.0011,  0.0011,  0.0011,  0.0011,  0.0011,  0.0011,
    ↪ 0.0011,  0.0011,  0.0011, 0.0011, 0.0011, 0.0011,
    ↪ 0.0011, 0.000011]
    min:                            [0.000005, 0.000005,
    ↪ 0.000005, 0.000005, 0.000005, 0.000005, 0.000005,
    ↪ 0.000005, 0.000005, 0.000005, 0.000005, 0.000005,
    ↪ 0.000005, 0.000005, 0.000005, 0.000005, 0.000005,
    ↪ 0.000005, 0.000005, 0.000005, 0.000005, 0.000005  ]
    max:                            [0.3,  0.5,      0.5,
    ↪ 0.5,      0.5,      0.5,      0.5,     0.5,      0.5,
    ↪ 0.5,      0.5,      0.5,      0.5,      0.5,      0.5,
    ↪ 0.5,      0.5,      0.5,      0.5,      0.5,      0.5,
    ↪ 0.3   ] #0.1
    index_of_wavelength_involved:   [0,        0,        0,
    ↪ 0,        0,        0,        0,        0 ,       0,
    ↪ 0,        0,        0,        0,        0,        0 ,
    ↪ 0,        0,        0,        0,        0,        0,
    ↪ 0         ]
single_pixel:
    smoothness_constraints:
        difference_order: 3
        lagrange_multiplier: 0.3 #1.0e-0
    a_priori_estimates:
        lagrange_multiplier: [1.0e-4, 5.0e-8, 0, 0, 0, 0, 0,
        ↪ 0 , 0, 0, 0, 0, 0, 0, 0, 0, 0, 0, 0, 5.0e-8,
        ↪ 1.0e-4 ] #1.0e-3
multi_pixel:
    smoothness_constraints:
       derivative_order_of_X_variability:    0
       lagrange_multiplier_of_X_variability: 0.0
       derivative_order_of_Y_variability:    0
```

```
                lagrange_multiplier_of_Y_variability: 0.0
                derivative_order_of_T_variability:    0
                lagrange_multiplier_of_T_variability: 0.0

    characteristic[5]: #4
        type: sphere_core
        retrieved: true
        mode[1]:
            initial_guess:                          #1
                value:                             [0.3]
                min:                               [0.2]
                max:                               [1.0]
                index_of_wavelength_involved:      [0]
            single_pixel:
                smoothness_constraints:
                    difference_order: 0
                    lagrange_multiplier: 0.0
            multi_pixel:
                smoothness_constraints:
                    derivative_order_of_X_variability:    0
                    lagrange_multiplier_of_X_variability: 0.0
                    derivative_order_of_Y_variability:    0
                    lagrange_multiplier_of_Y_variability: 0.0
                    derivative_order_of_T_variability:    0
                    lagrange_multiplier_of_T_variability: 0.0

    characteristic[8]: #7
        type: surface_land_polarized_maignan_breon
        retrieved: false
        mode[1]:
            initial_guess:                          #1          #2          #3
            ↪ #4
                value:                             [2.1,       2.1,        2.1,
                ↪ 2.1    ]
                min:                               [0.01,      0.01,
                ↪ 0.01,       0.01   ]
                max:                               [10.,       10.,        10.,
                ↪ 10.    ]
```

```
        index_of_wavelength_involved:   [1,         2,         3,
        ↪ 4    ]
    single_pixel:
        smoothness_constraints:
            difference_order: 0
            lagrange_multiplier: 0.0
    multi_pixel:
        smoothness_constraints:
            derivative_order_of_T_variability:    0
            lagrange_multiplier_of_T_variability: 0.0
            derivative_order_of_X_variability:    0
            lagrange_multiplier_of_X_variability: 0.0
            derivative_order_of_Y_variability:    0
            lagrange_multiplier_of_Y_variability: 0.0
```

"characteristics" are the elements of the vector of aerosol parameters "a" and "type" defines the element of the vector attributed to the characteristic. "retrieved" gives the statute of the characteristic in the inversion, if set to true, the algorithm will modify the value during the numerical inversion to try to find the optimal value for the fit of the inputted radiances; if set to false, the value is fixed throughout the inversion as defined in the settings file for the forward model calculations. "mode" has the same purpose as previously discussed, to separate calculations for different SD modes, which is usually mono-modal or bi-modal.

A.2 Optical properties of core/shell particles under single scattering approximation

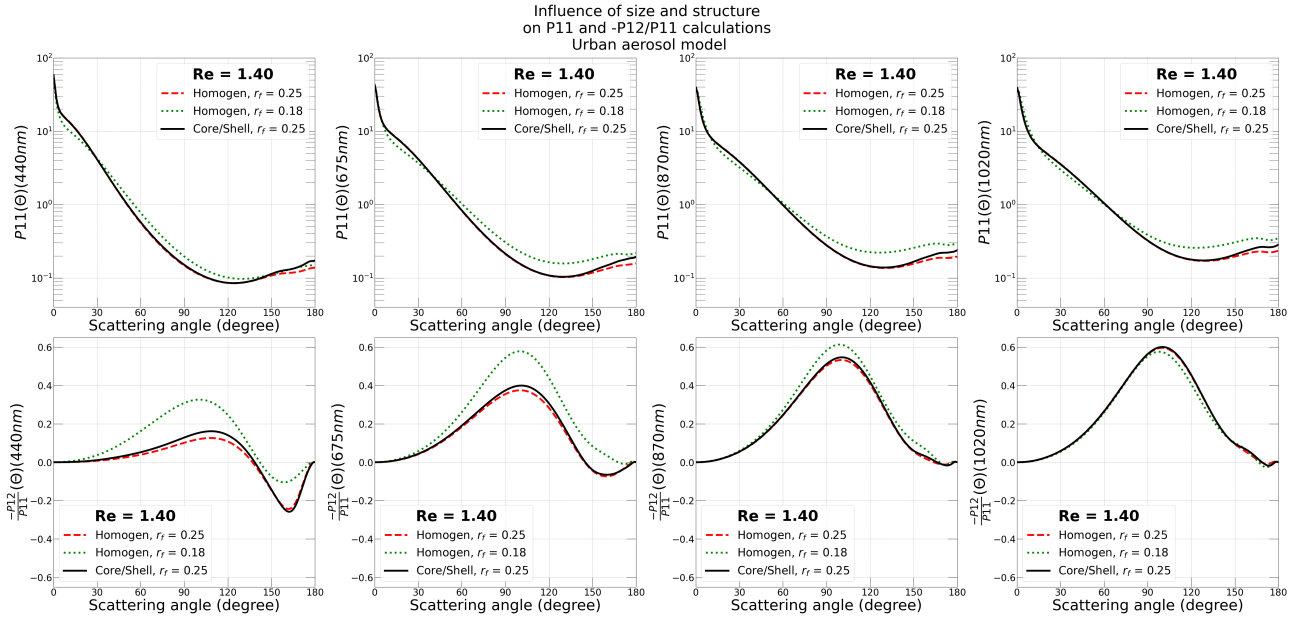

Figure A.1: Phase function (P_{11}) and degree of linear polarisation ($\frac{-P_{12}}{P_{11}}$) with refractive indexes corresponding to urban aerosol model (n=1.40) with a fine mode dominated size distribution.

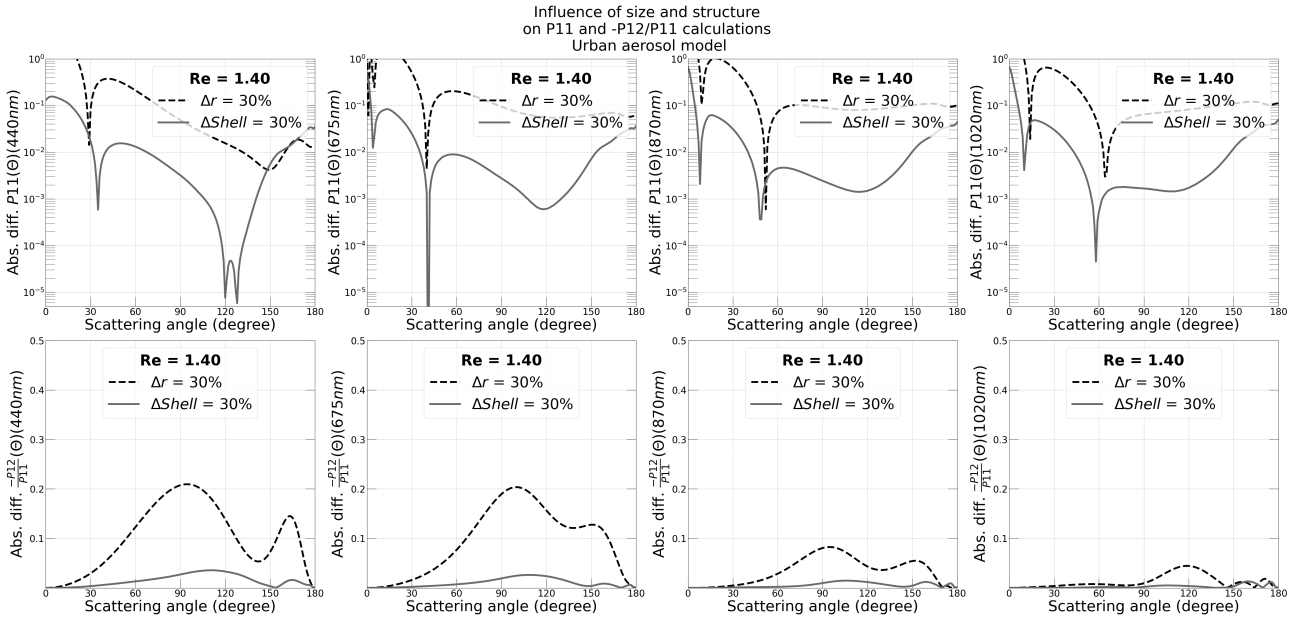

Figure A.2: Impacts of changes in size and structure on the phase function ($\mid P_{1x^{homog.}}(rm) - P_{1x^{homog.}}(0.7rm) \mid \Rightarrow \Delta r$ and $\mid P_{1x^{inhomog.}}(rm) - P_{1x^{homog.}}(rm) \mid \Rightarrow \Delta shell$). Urban aerosol model, fine mode dominated size distribution.

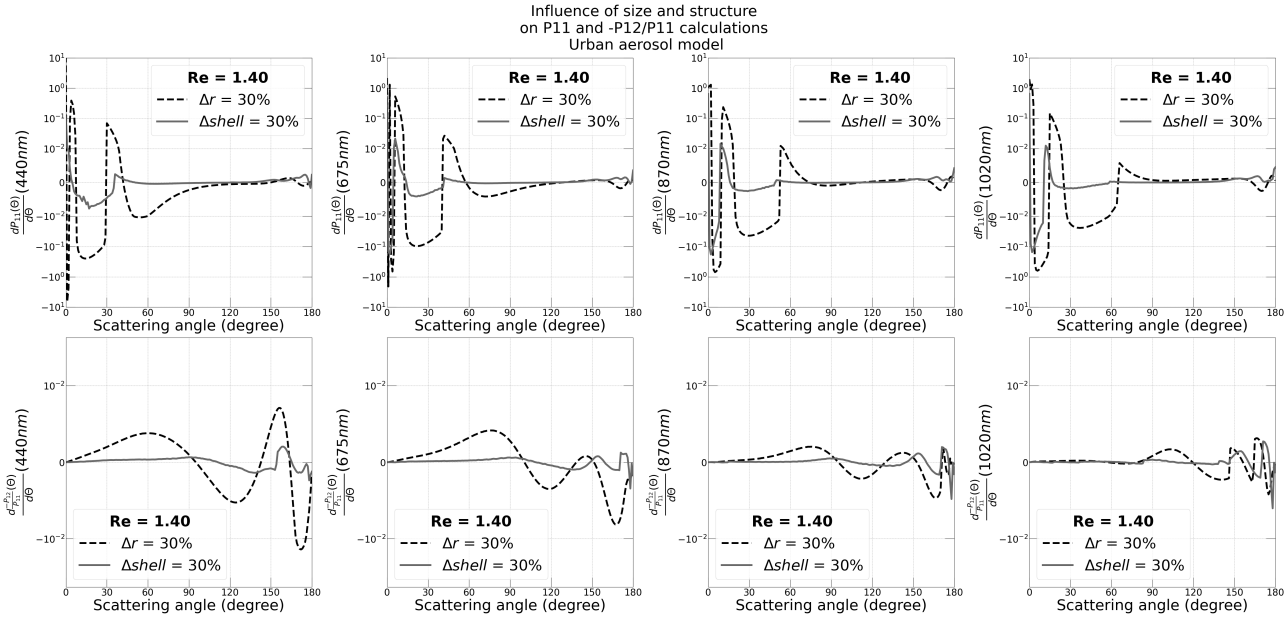

Figure A.3: Angular variation of impacts of changes in size and structure on the phase function for Urban aerosol model representing fine mode dominated size distribution.

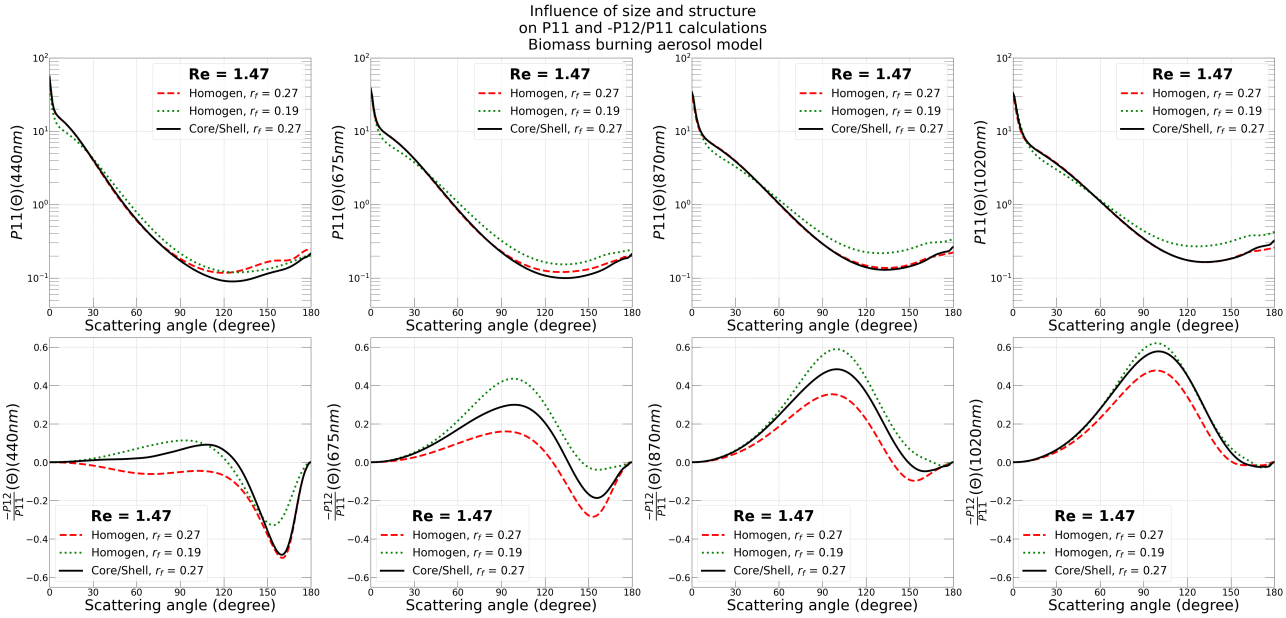

Figure A.4: Phase function (P_{11}) and degree of linear polarisation ($\frac{-P_{12}}{P_{11}}$) with refractive indexes corresponding to biomass burning aerosol model (n=1.47) with a fine mode dominated size distribution.

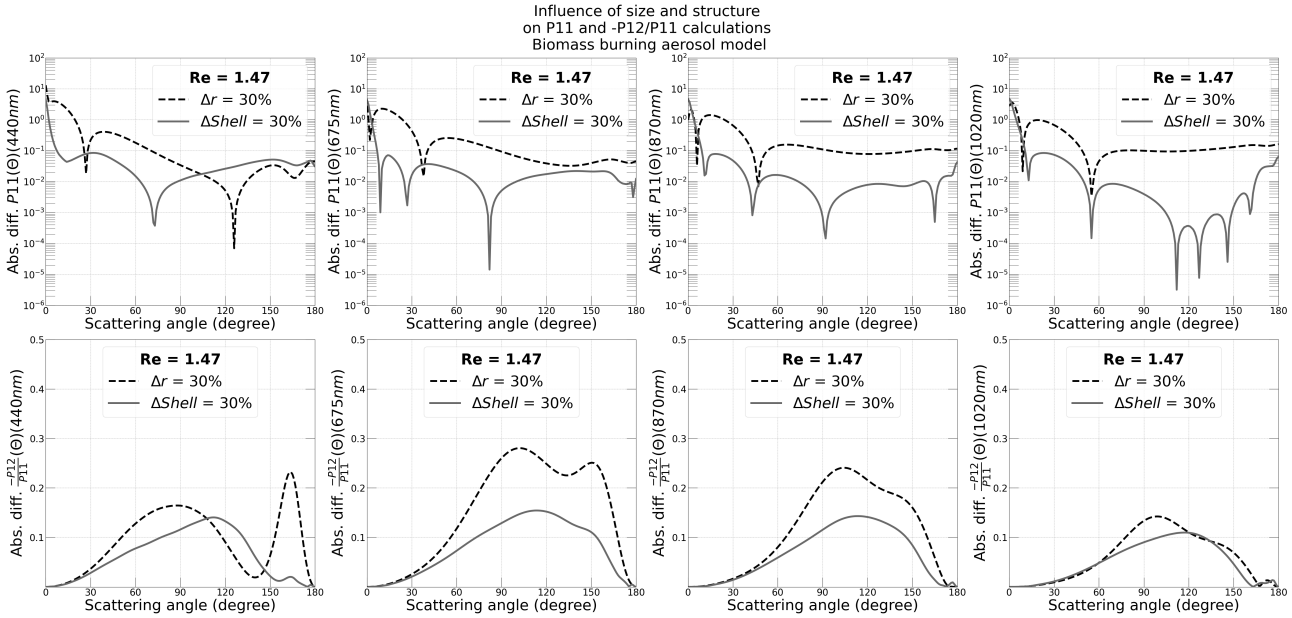

Figure A.5: Impacts of changes in size and structure on the phase function ($\mid P_{1x^{homog.}}(rm) - P_{1x^{homog.}}(0.7rm) \mid \Rightarrow \Delta r$ and $\mid P_{1x^{inhomog.}}(rm) - P_{1x^{homog.}}(rm) \mid \Rightarrow \Delta shell$). Biomass burning aerosol model, fine mode dominated size distribution.

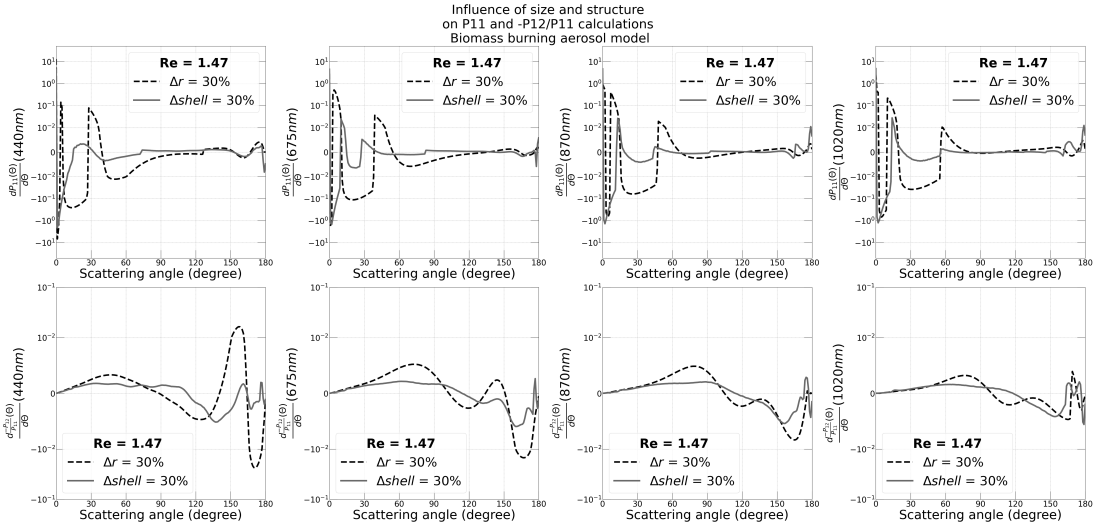

Figure A.6: Angular variation of impacts of changes in size and structure on the phase function for biomass burning aerosol model representing fine mode dominated size distribution.

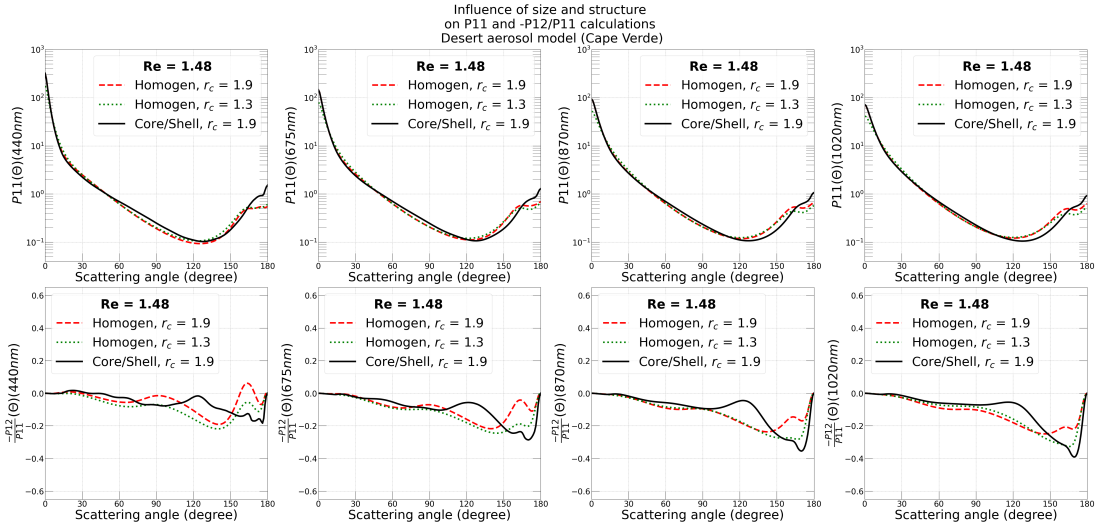

Figure A.7: Phase function (P_{11}) and degree of linear polarisation ($\frac{-P_{12}}{P_{11}}$) with refractive indexes corresponding to desert aerosol model (n=1.48) with a coarse mode dominated size distribution.

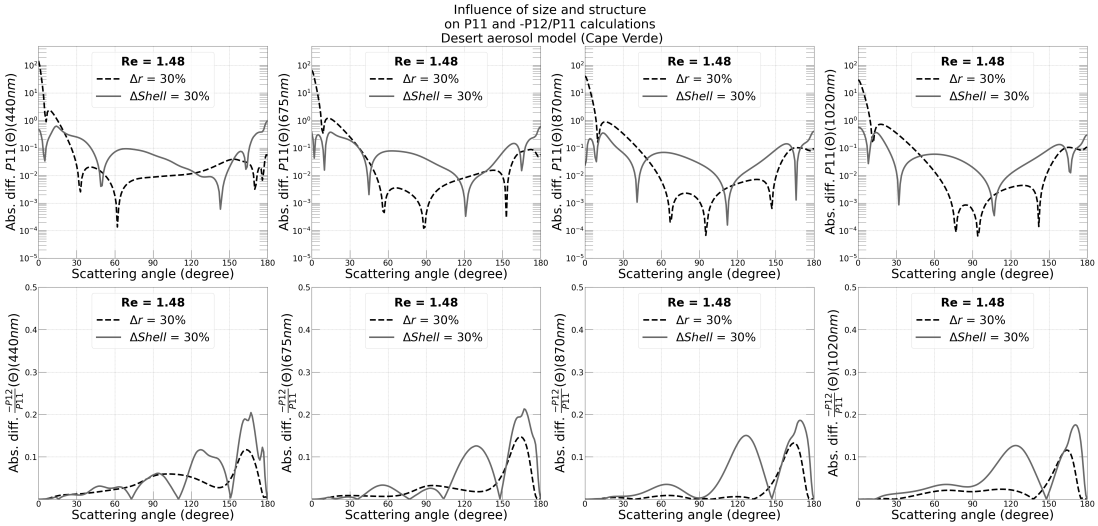

Figure A.8: Impacts of changes in size and structure on the phase function ($\mid P_{1x^{homog.}}(rm) - P_{1x^{homog.}}(0.7rm) \mid \Rightarrow \Delta r$ and $\mid P_{1x^{inhomog.}}(rm) - P_{1x^{homog.}}(rm) \mid \Rightarrow \Delta shell$). Desert aerosol model, coarse mode dominated size distribution.

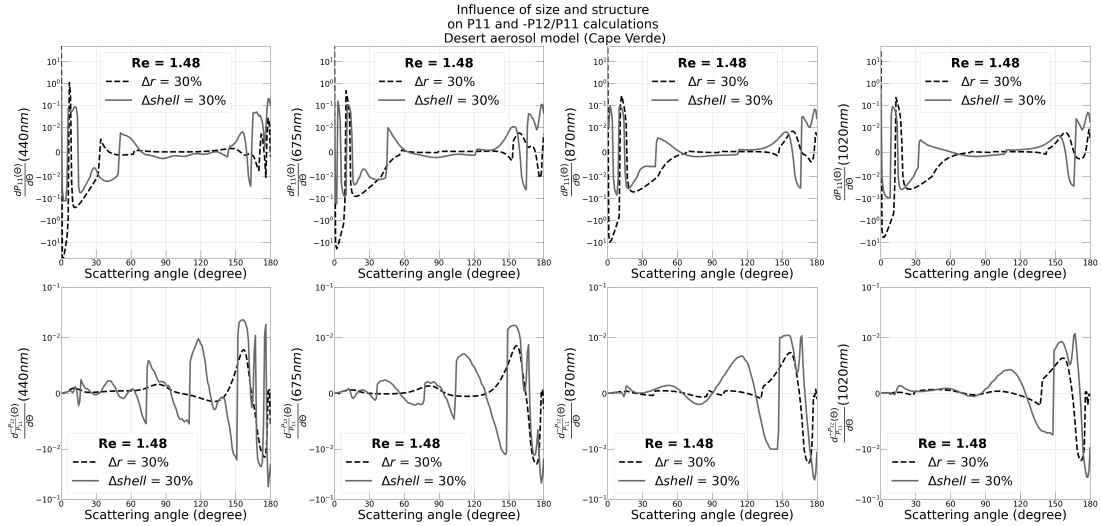

Figure A.9: Angular variation of impacts of changes in size and structure on the phase function for desert aerosol model representing coarse mode dominated size distribution.

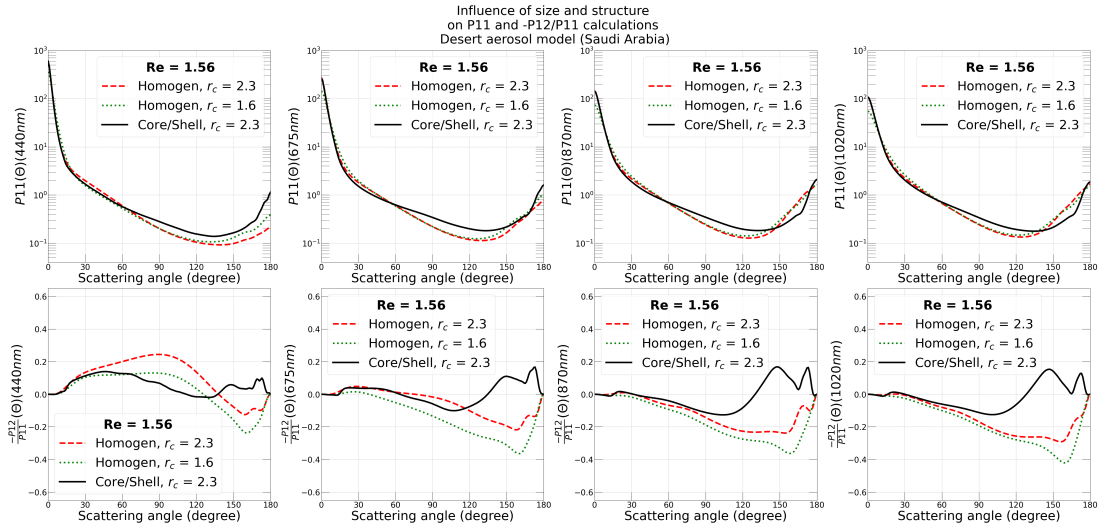

Figure A.10: Phase function (P_{11}) and degree of linear polarisation ($\frac{-P_{12}}{P_{11}}$) with refractive indexes corresponding to desert aerosol model (n=1.56) with a coarse mode dominated size distribution.

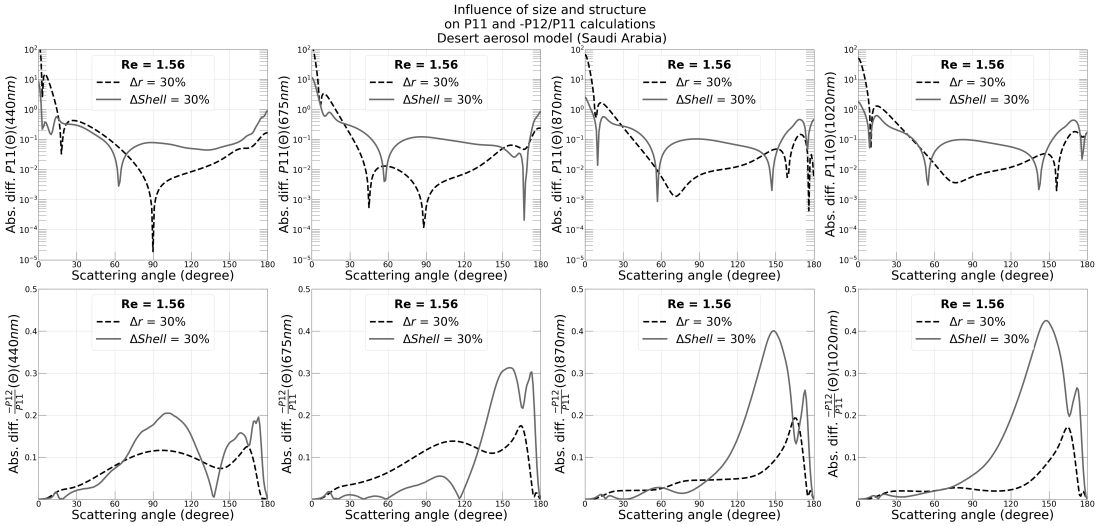

Figure A.11: Impacts of changes in size and structure on the phase function ($\mid P_{1x^{homog.}}(rm) - P_{1x^{homog.}}(0.7rm) \mid \Rightarrow \Delta r$ and $\mid P_{1x^{inhomog.}}(rm) - P_{1x^{homog.}}(rm) \mid \Rightarrow \Delta shell$). Desert aerosol model, coarse mode dominated size distribution.

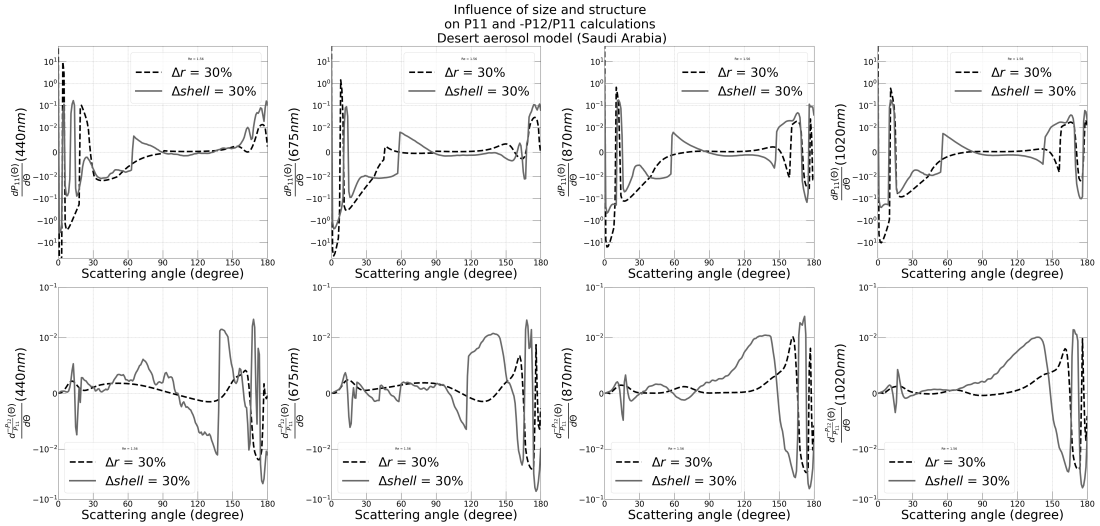

Figure A.12: Angular variation of impacts of changes in size and structure on the phase function for desert aerosol model representing coarse mode dominated size distribution.

A.3 Synthetic tests with GRASP/ARIA

A.3.1 Inversion of inhomogeneous aerosol signal with a homogeneous model

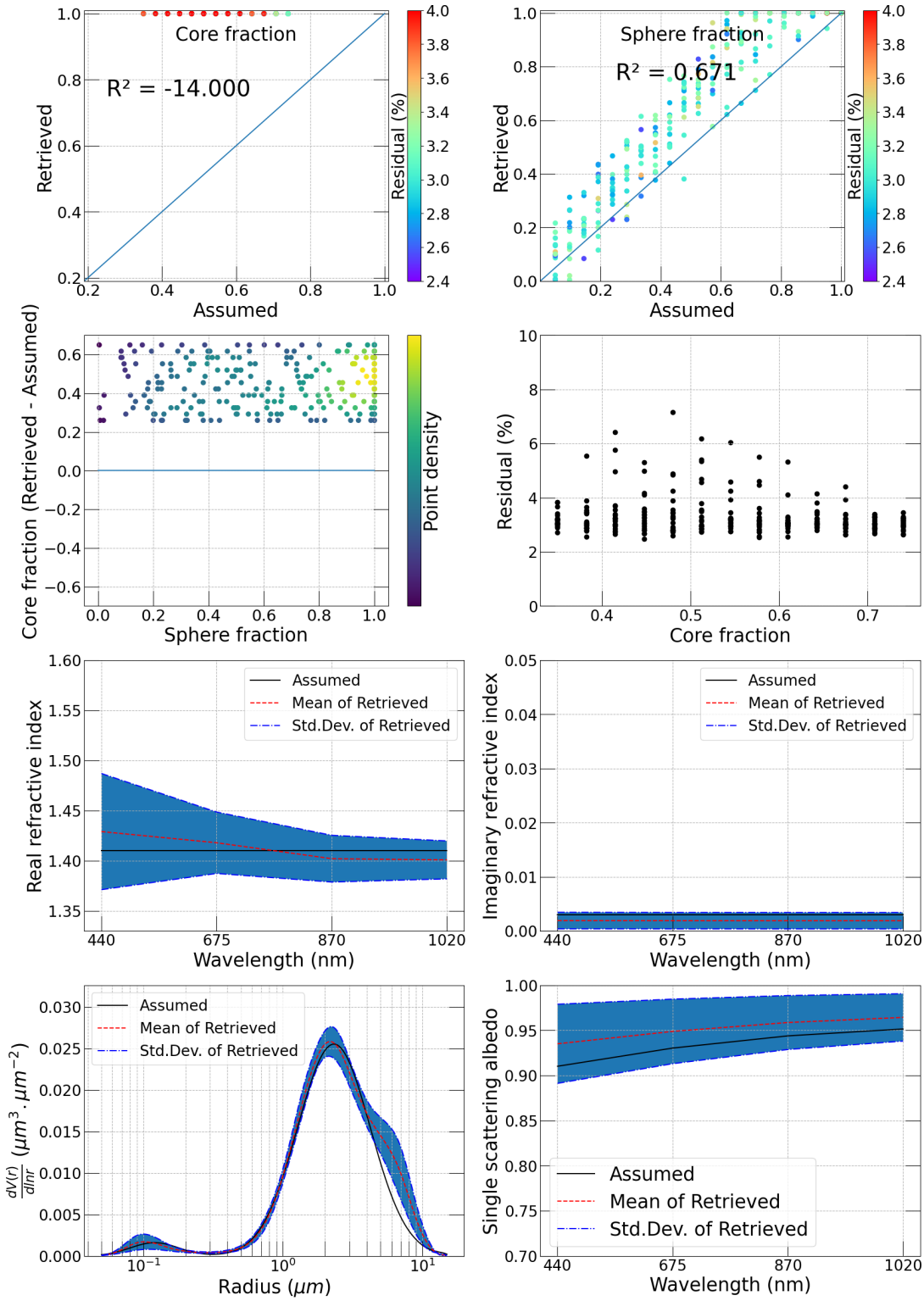

Figure A.13: Collection of plots of aerosol optical and microphysical characteristics derived by inversion of synthetic AERONET measurements. The case of coarse mode dominated aerosol size distribution. The radiances, are generated using GRASP/ARIA (with inhomogeneous aerosol model) and inverted using GRASP/Standard (with homogeneous aerosol only). Results only use radiance intensity (no polarisation), with added noise in the measurements, the refractive index is n=1.41, k=0.003 and presented core fraction < 0.75

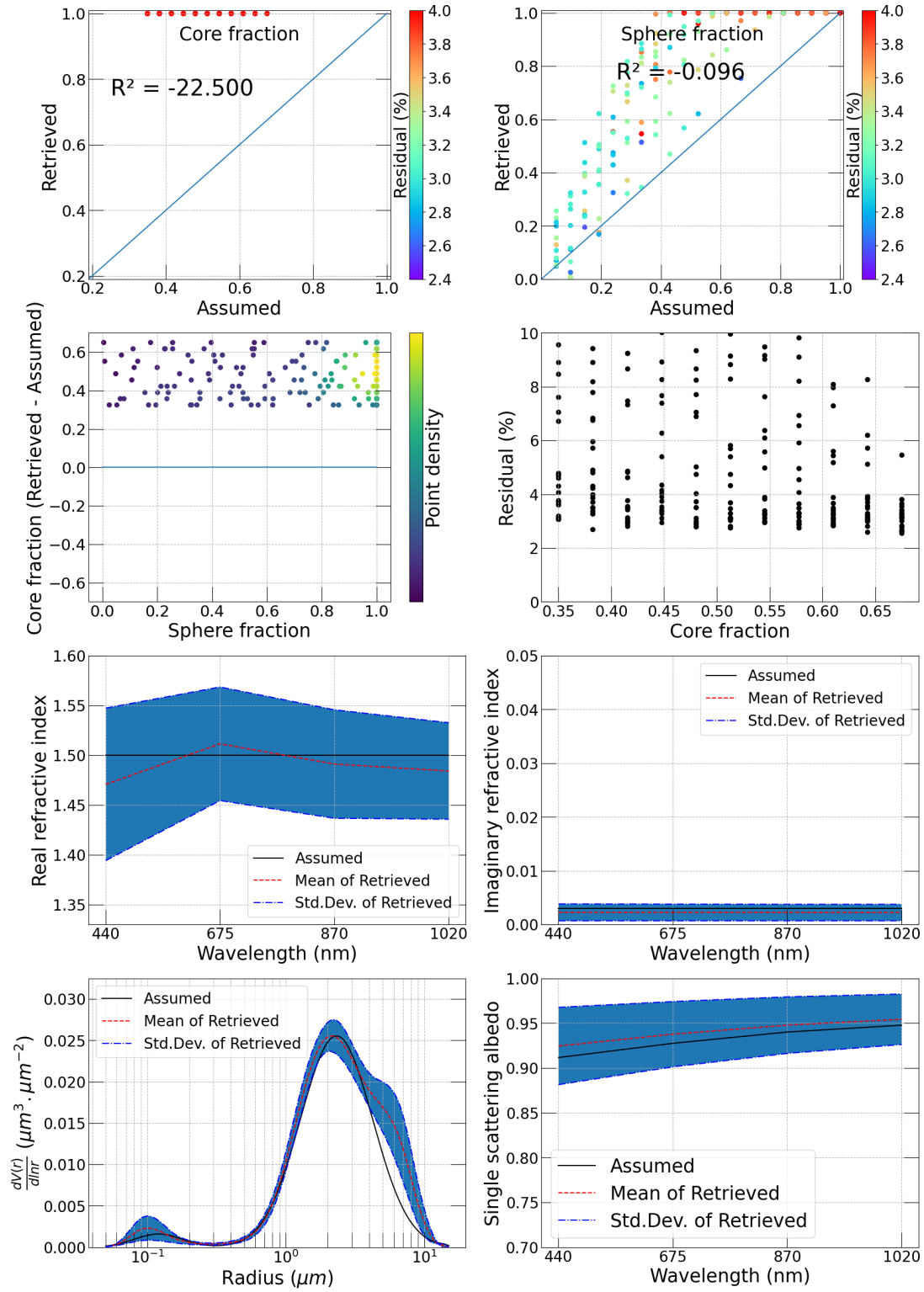

Figure A.14: Collection of plots of aerosol optical and microphysical characteristics derived by inversion of synthetic AERONET measurements. The case of coarse mode dominated aerosol size distribution. The radiances, are generated using GRASP/ARIA (with inhomogeneous aerosol model) and inverted using GRASP/Standard (with homogeneous aerosol only). Results only use radiance intensity (no polarisation), with added noise in the measurements, the refractive index is n=1.50, k=0.003 and presented core fraction < 0.7

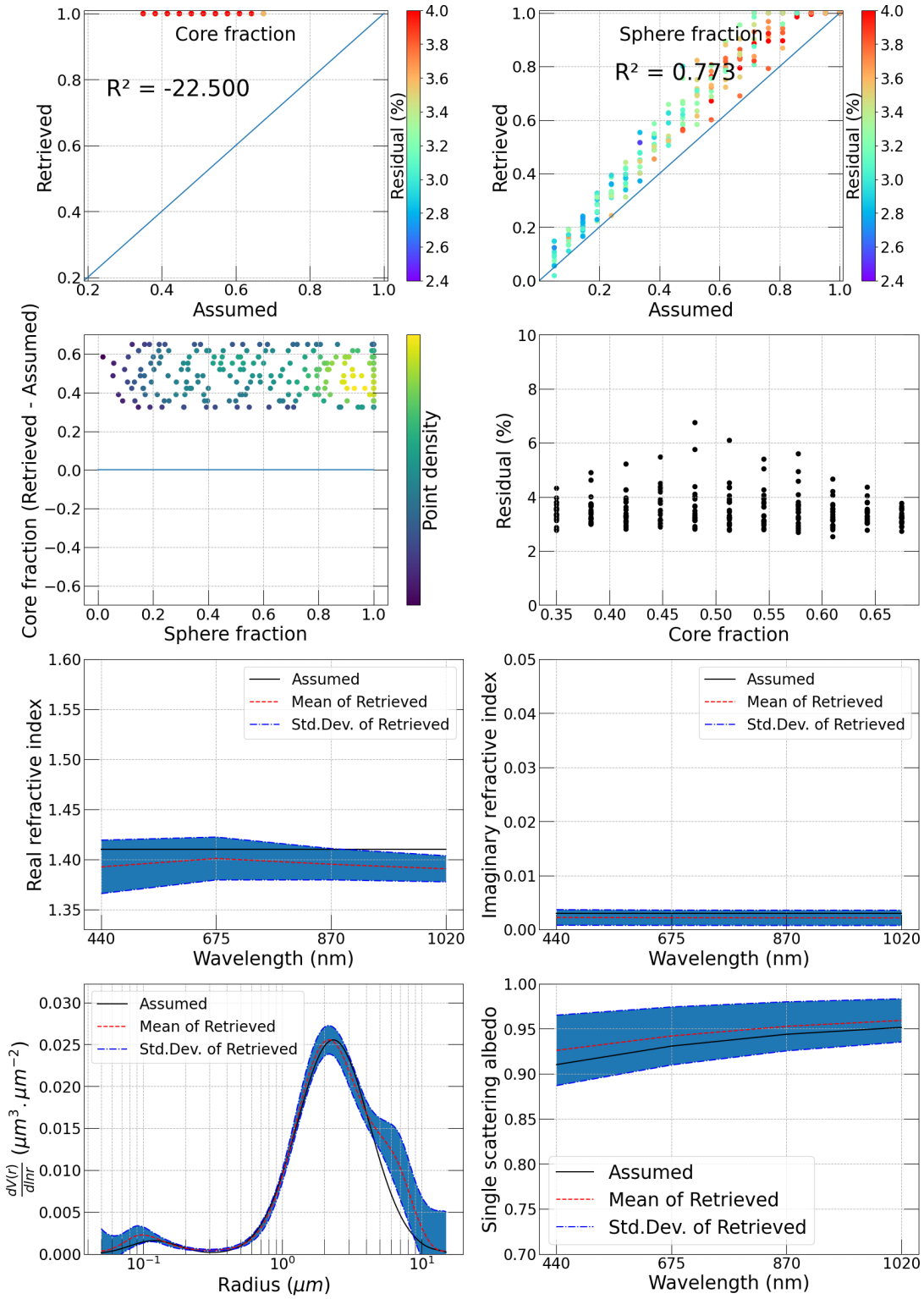

Figure A.15: Collection of plots of aerosol optical and microphysical characteristics derived by inversion of synthetic AERONET measurements. The case of coarse mode dominated aerosol size distribution. The radiances, are generated using GRASP/ARIA (with inhomogeneous aerosol model) and inverted using GRASP/Standard (with homogeneous aerosol only). Results use radiance intensity and polarisation, with added noise in the measurements, the refractive index is n=1.41, k=0.003 and presented core fraction < 0.7

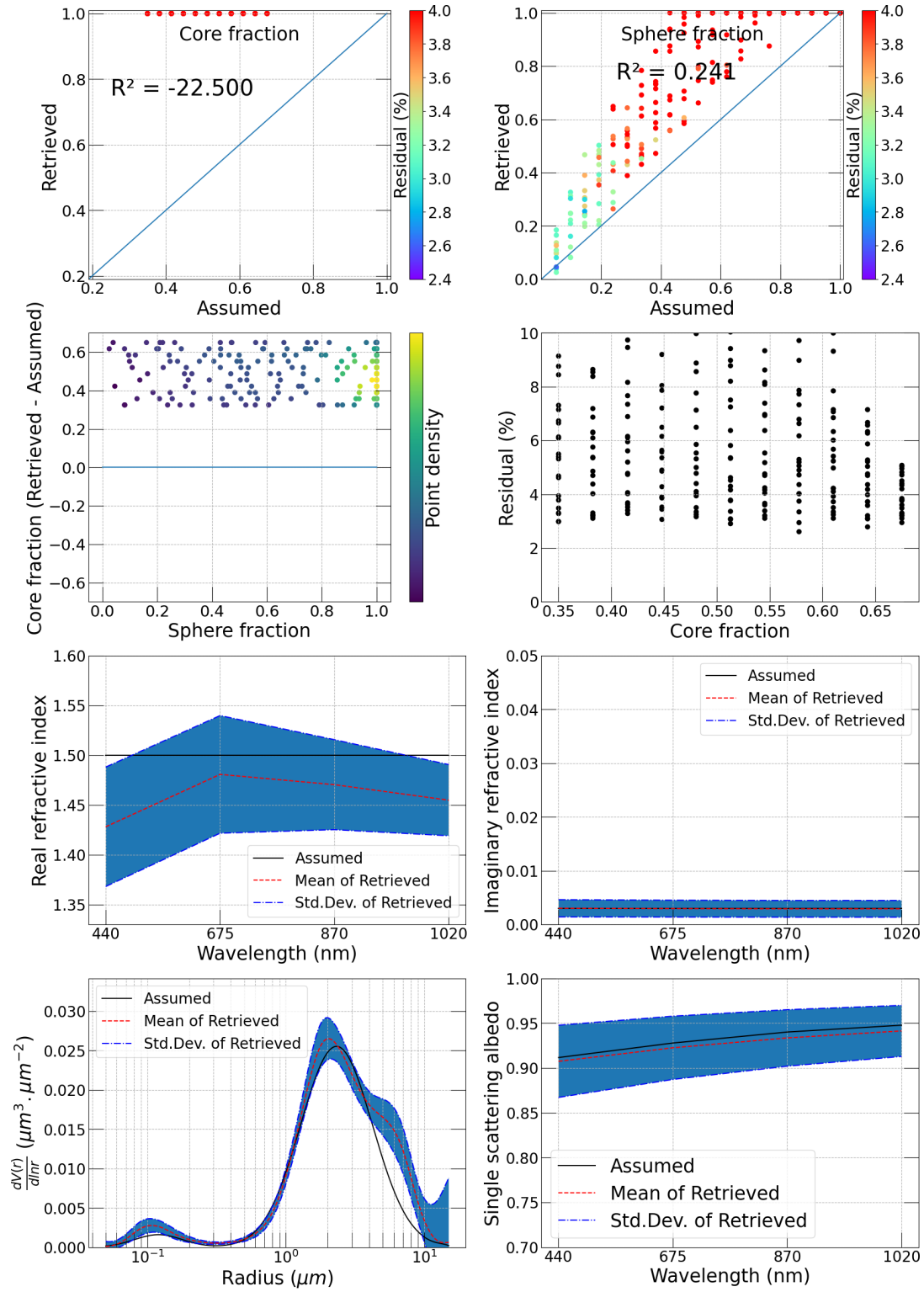

Figure A.16: Collection of plots of aerosol optical and microphysical characteristics derived by inversion of synthetic AERONET measurements. The case of coarse mode dominated aerosol size distribution. The radiances, are generated using GRASP/ARIA (with inhomogeneous aerosol model) and inverted using GRASP/Standard (with homogeneous aerosol only). Results use radiance intensity and polarisation, with added noise in the measurements, the refractive index is n=1.50, k=0.003 and presented core fraction < 0.7

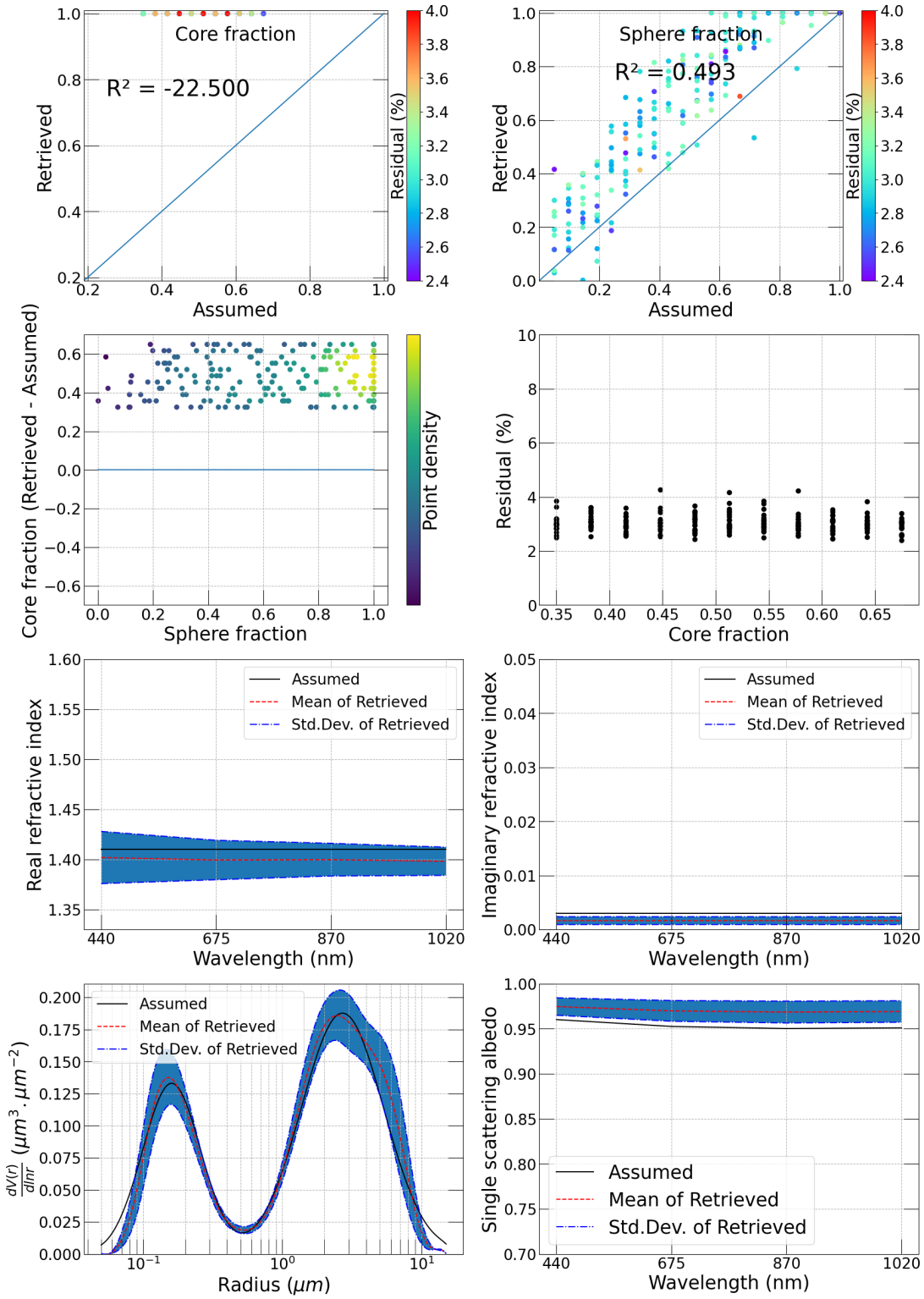

Figure A.17: Collection of plots of aerosol optical and microphysical characteristics derived by inversion of synthetic AERONET measurements. The case of bimodal aerosol size distribution. The radiances, are generated using GRASP/ARIA (with inhomogeneous aerosol model) and inverted using GRASP/Standard (with homogeneous aerosol only). Results only use radiance intensity (no polarisation), with added noise in the measurements, the refractive index is n=1.41, k=0.003 and presented core fraction < 0.7

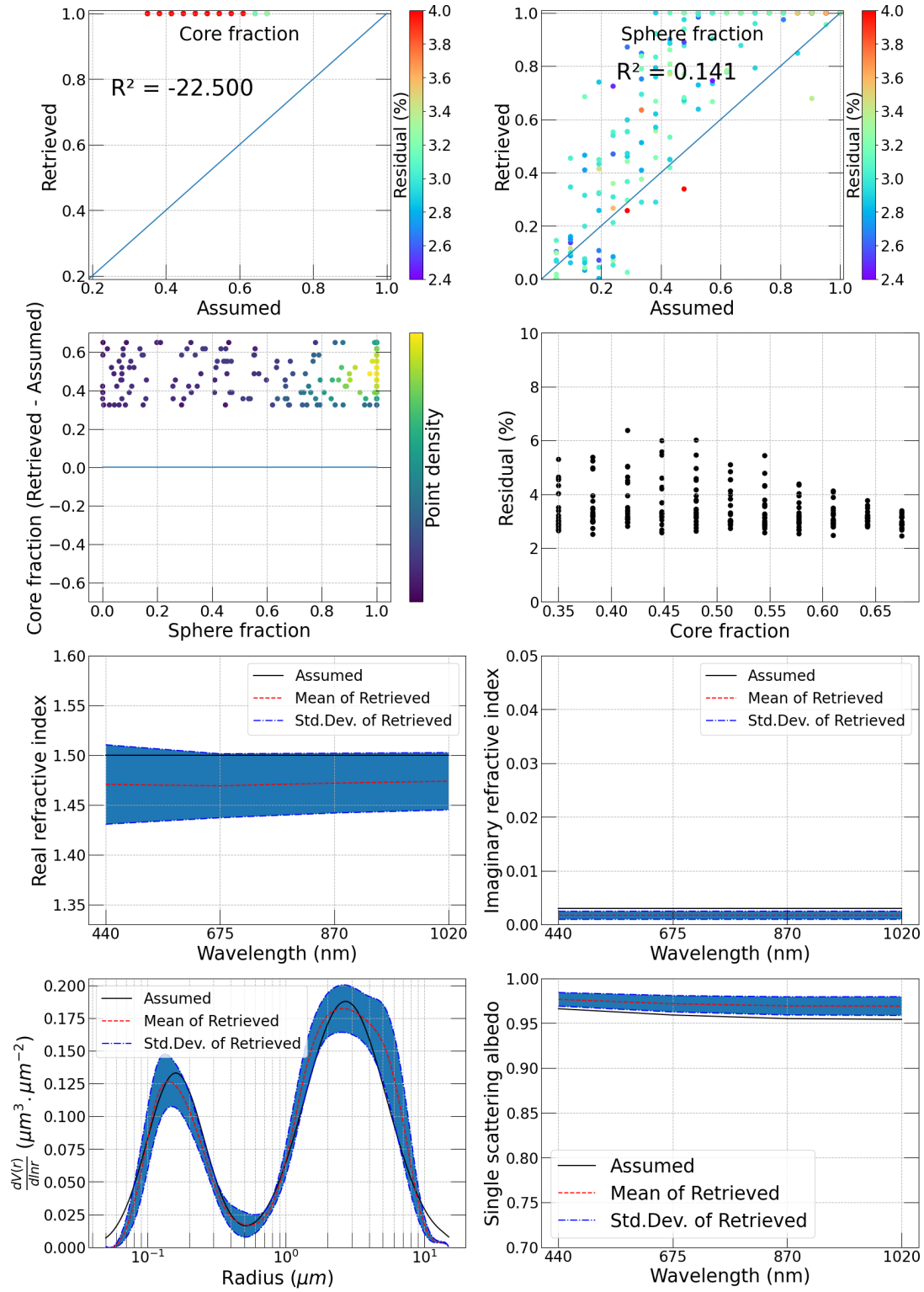

Figure A.18: Collection of plots of aerosol optical and microphysical characteristics derived by inversion of synthetic AERONET measurements. The case of bimodal aerosol size distribution. The radiances, are generated using GRASP/ARIA (with inhomogeneous aerosol model) and inverted using GRASP/Standard (with homogeneous aerosol only). Results only use radiance intensity (no polarisation), with added noise in the measurements, the refractive index is n=1.50, k=0.003 and presented core fraction < 0.7

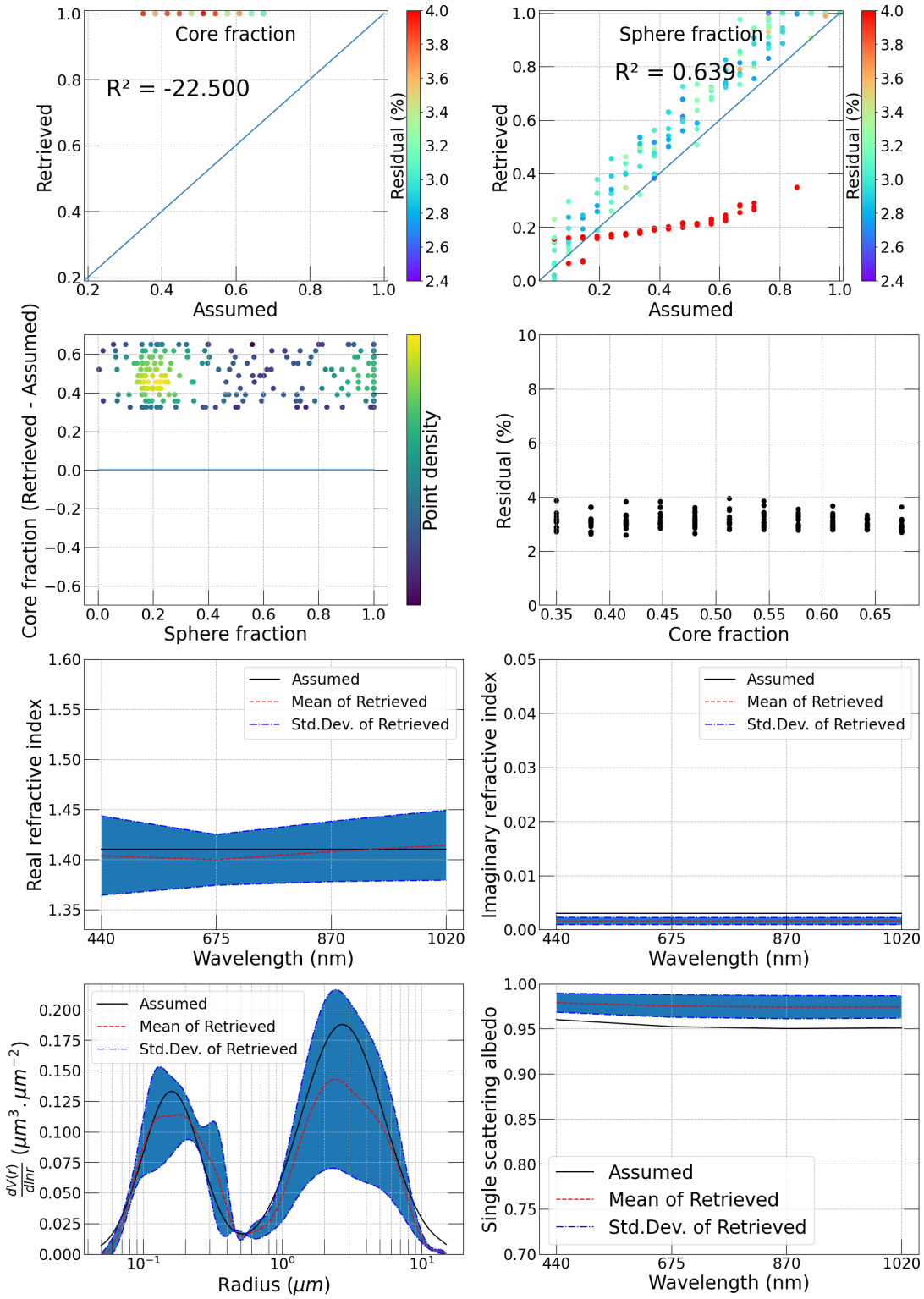

Figure A.19: Collection of plots of aerosol optical and microphysical characteristics derived by inversion of synthetic AERONET measurements. The case of bimodal aerosol size distribution. The radiances, are generated using GRASP/ARIA (with inhomogeneous aerosol model) and inverted using GRASP/Standard (with homogeneous aerosol only). Results use radiance intensity and polarisation, with added noise in the measurements, the refractive index is n=1.41, k=0.003 and presented core fraction < 0.7

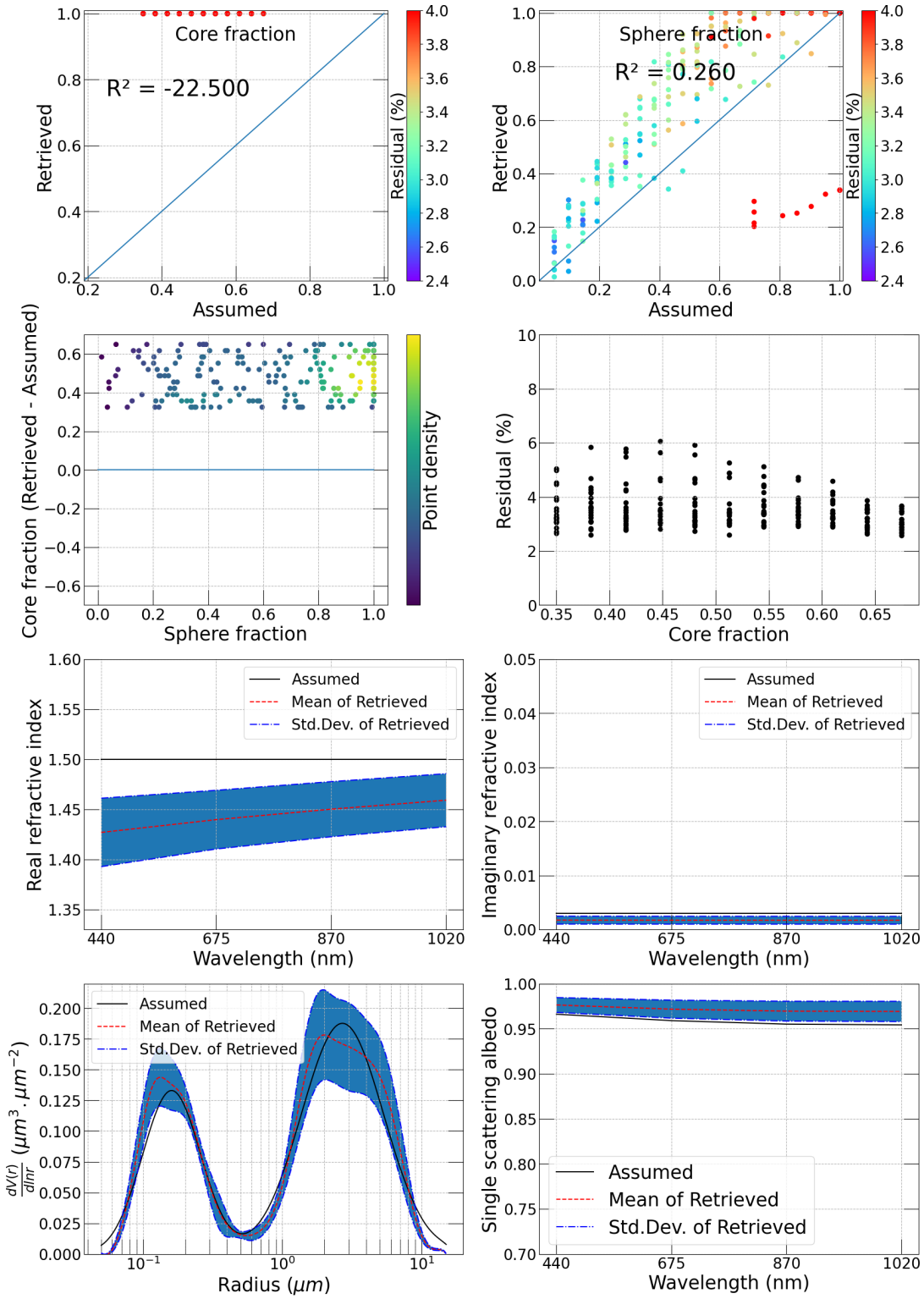

Figure A.20: Collection of plots of aerosol optical and microphysical characteristics derived by inversion of synthetic AERONET measurements. The case of bimodal aerosol size distribution. The radiances, are generated using GRASP/ARIA (with inhomogeneous aerosol model) and inverted using GRASP/Standard (with homogeneous aerosol only). Results use radiance intensity and polarisation, with added noise in the measurements, the refractive index is n=1.50, k=0.003 and presented core fraction < 0.7

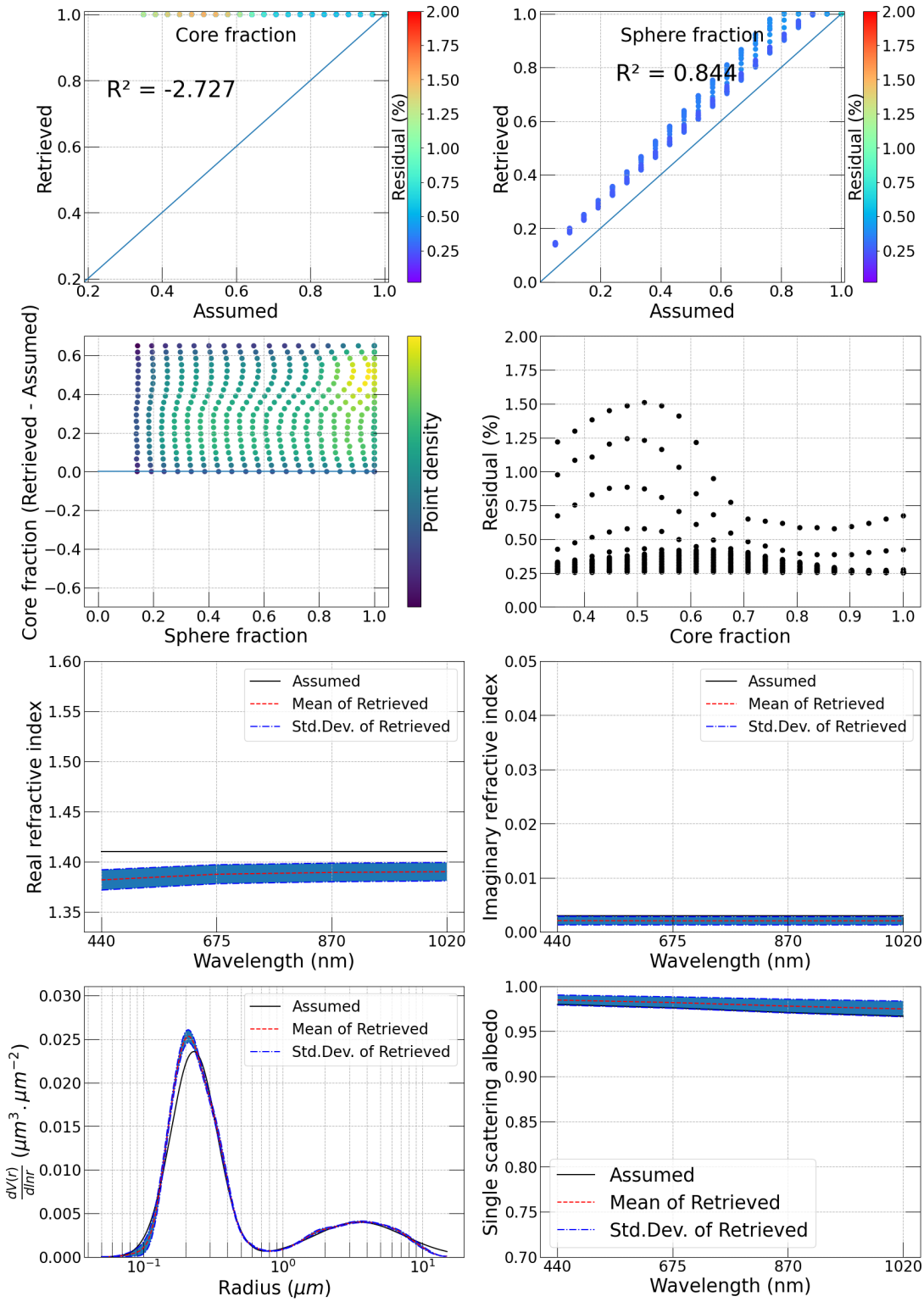

Figure A.21: Collection of plots of aerosol optical and microphysical characteristics derived by inversion of synthetic AERONET measurements. The case of fine mode dominated aerosol size distribution. The radiances, are generated using GRASP/ARIA (with inhomogeneous aerosol model) and inverted using GRASP/Standard (with homogeneous aerosol only). Results use radiance intensity only (no polarisation), the refractive index is n=1.41, k=0.003

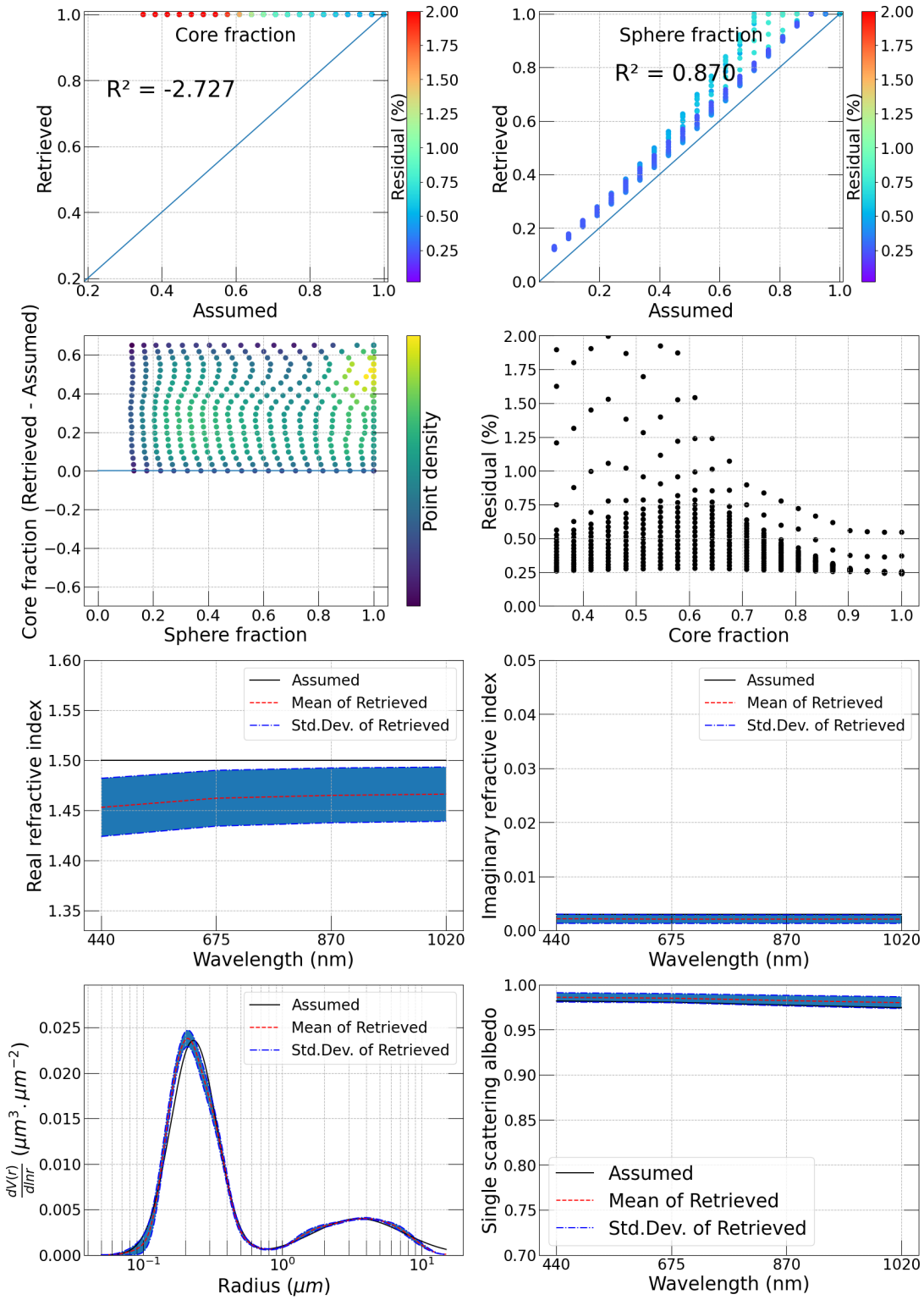

Figure A.22: Collection of plots of aerosol optical and microphysical characteristics derived by inversion of synthetic AERONET measurements. The case of fine mode dominated aerosol size distribution. The radiances, are generated using GRASP/ARIA (with inhomogeneous aerosol model) and inverted using GRASP/Standard (with homogeneous aerosol only). Results use radiance intensity only (no polarisation), the refractive index is n=1.50, k=0.003

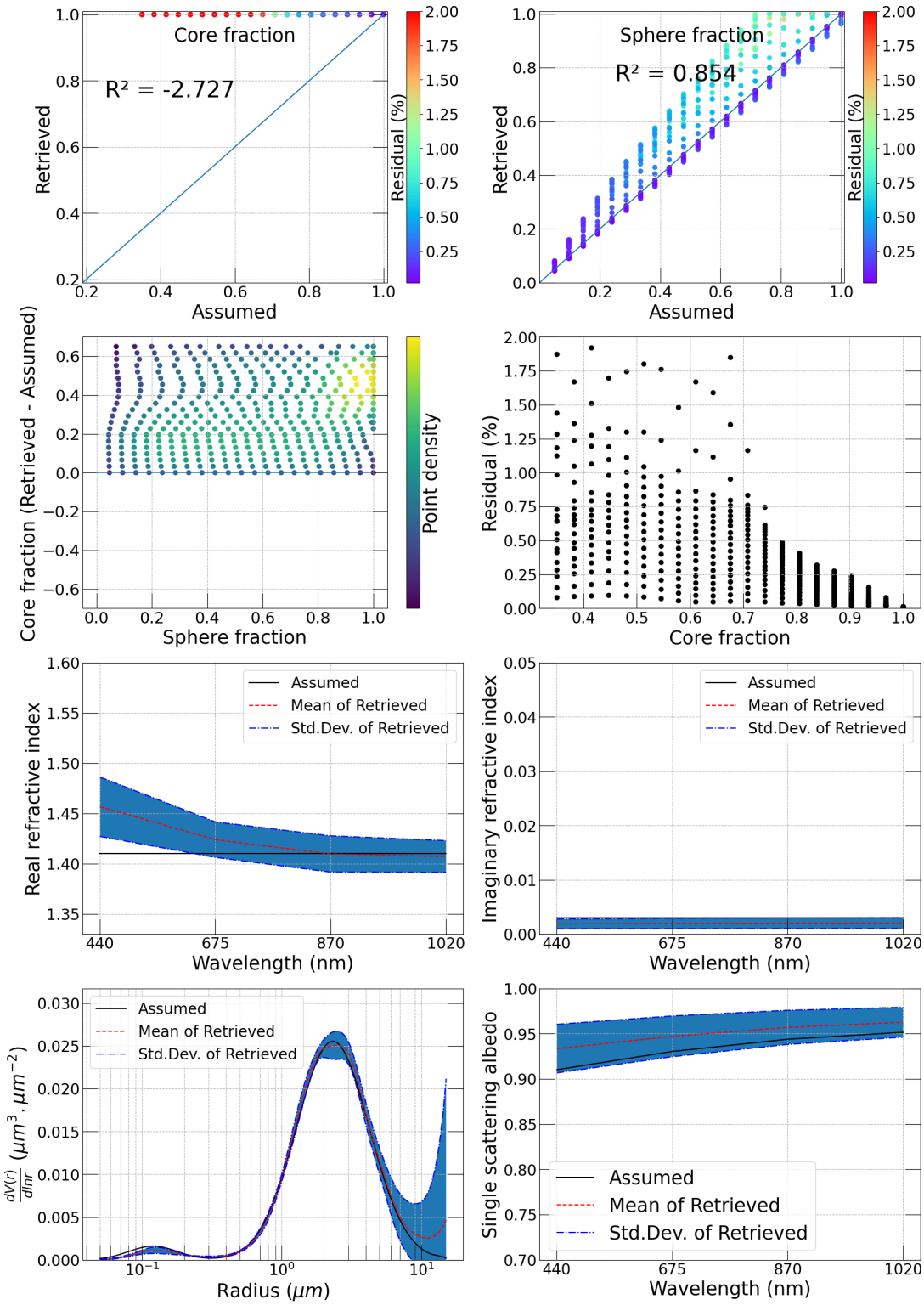

Figure A.23: Collection of plots of aerosol optical and microphysical characteristics derived by inversion of synthetic AERONET measurements. The case of coarse mode dominated aerosol size distribution. The radiances, are generated using GRASP/ARIA (with inhomogeneous aerosol model) and inverted using GRASP/Standard (with homogeneous aerosol only). Results use radiance intensity only (no polarisation), the refractive index is n=1.41, k=0.003

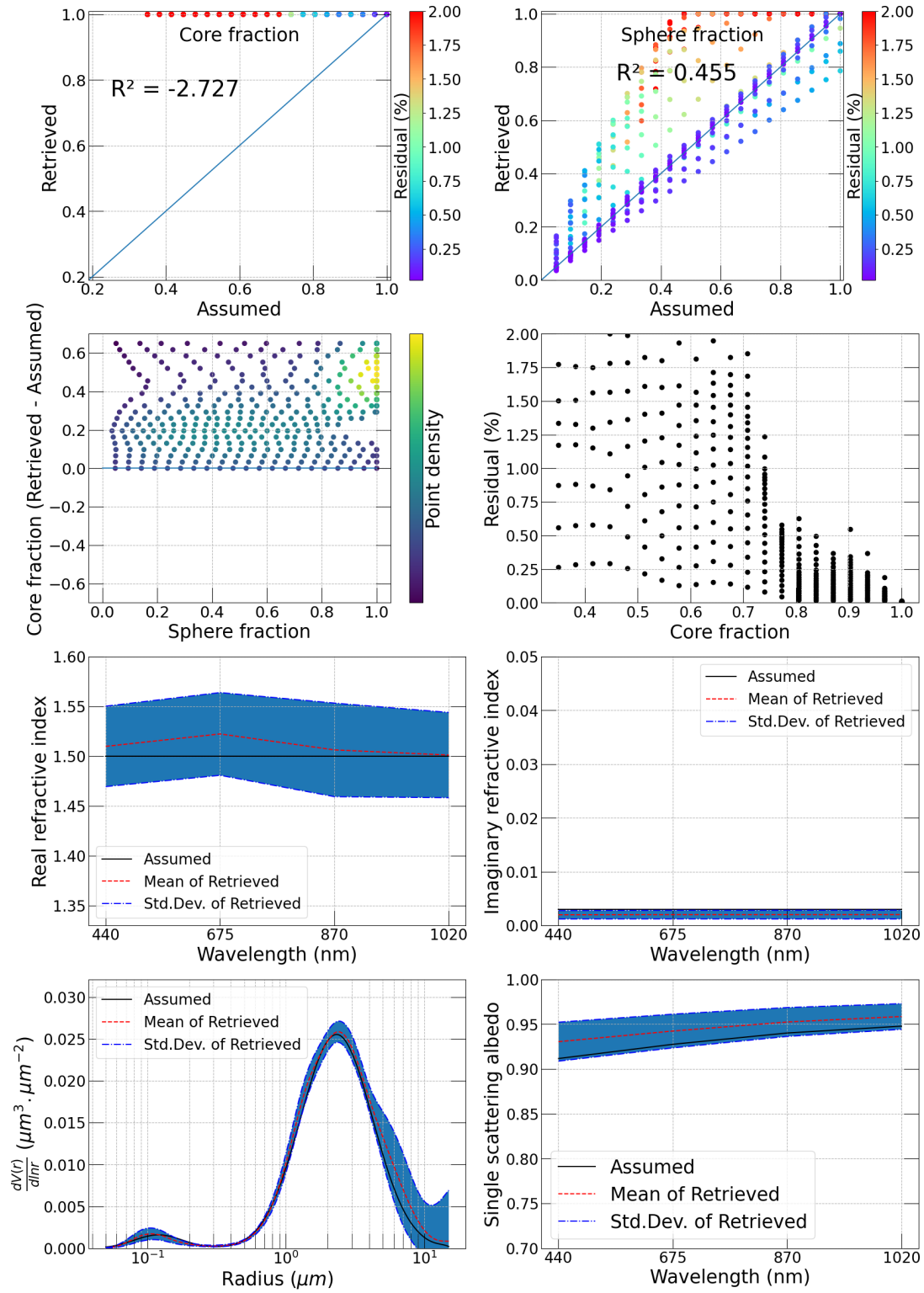

Figure A.24: Collection of plots of aerosol optical and microphysical characteristics derived by inversion of synthetic AERONET measurements. The case of coarse mode dominated aerosol size distribution. The radiances, are generated using GRASP/ARIA (with inhomogeneous aerosol model) and inverted using GRASP/Standard (with homogeneous aerosol only). Results use radiance intensity only (no polarisation), the refractive index is n=1.50, k=0.003

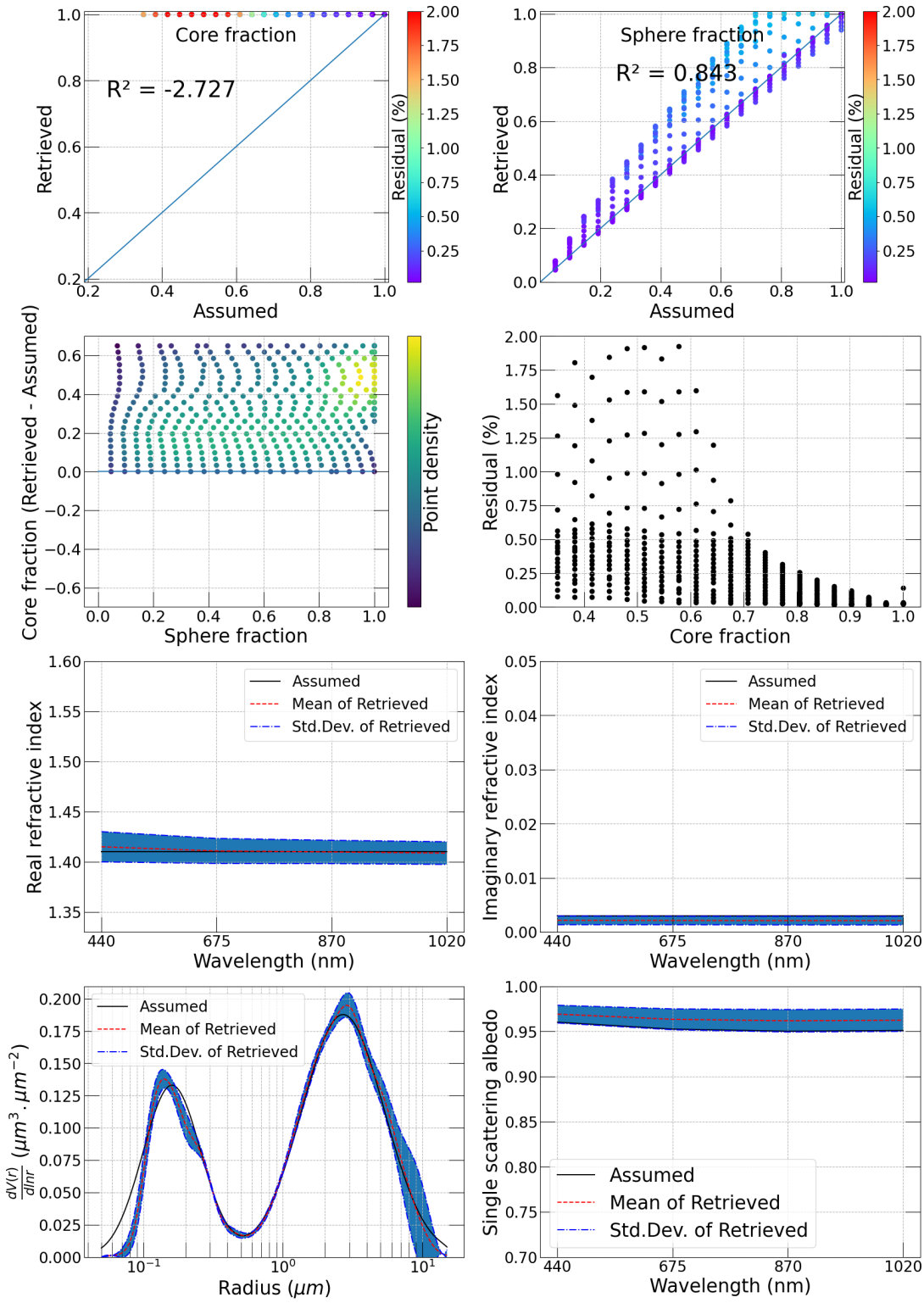

Figure A.25: Collection of plots of aerosol optical and microphysical characteristics derived by inversion of synthetic AERONET measurements. The case of bimodal aerosol size distribution. The radiances, are generated using GRASP/ARIA (with inhomogeneous aerosol model) and inverted using GRASP/Standard (with homogeneous aerosol only). Results use radiance intensity only (no polarisation), the refractive index is n=1.41, k=0.003

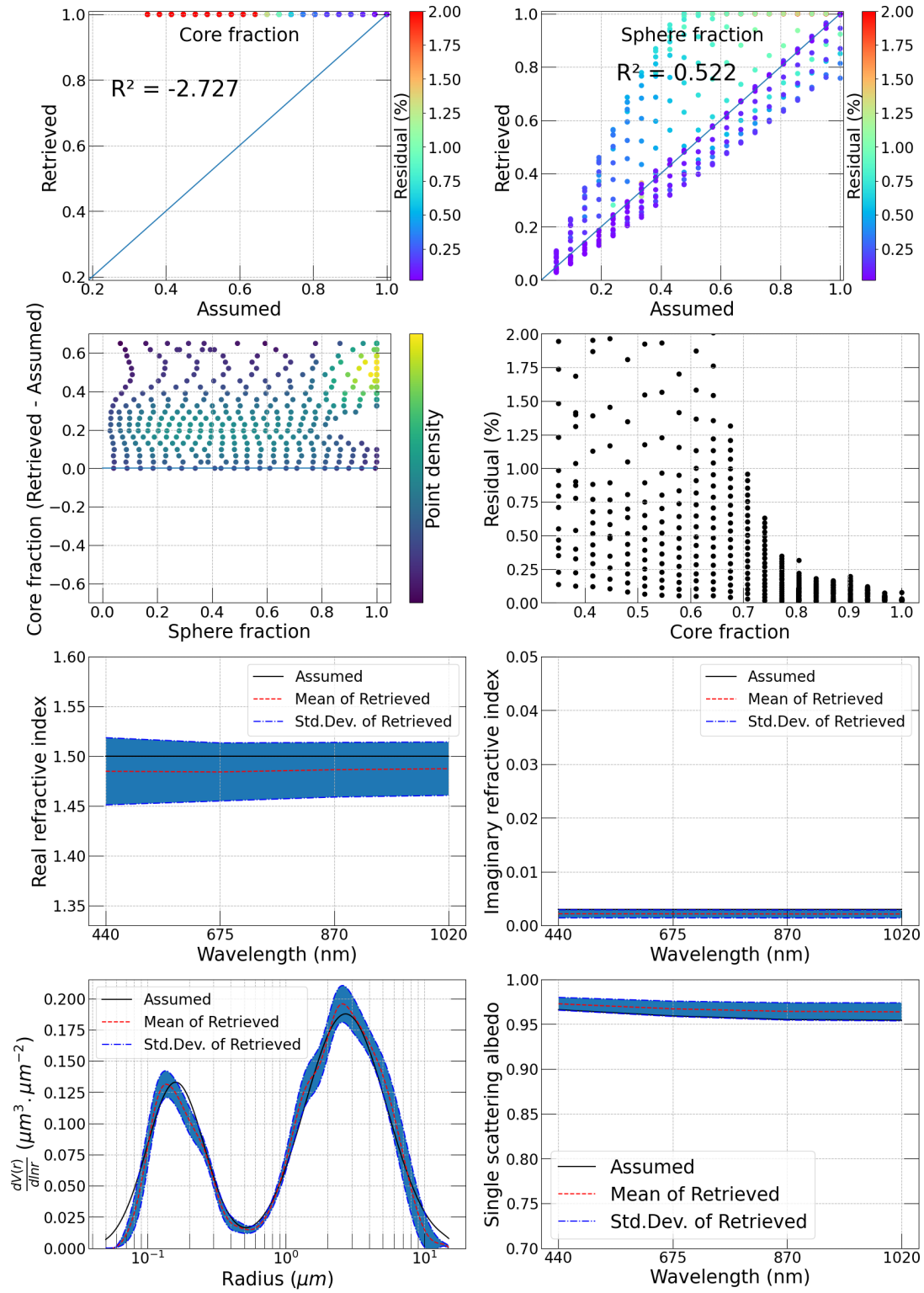

Figure A.26: Collection of plots of aerosol optical and microphysical characteristics derived by inversion of synthetic AERONET measurements. The case of bimodal aerosol size distribution. The radiances, are generated using GRASP/ARIA (with inhomogeneous aerosol model) and inverted using GRASP/Standard (with homogeneous aerosol only). Results use radiance intensity only (no polarisation), the refractive index is n=1.50, k=0.003

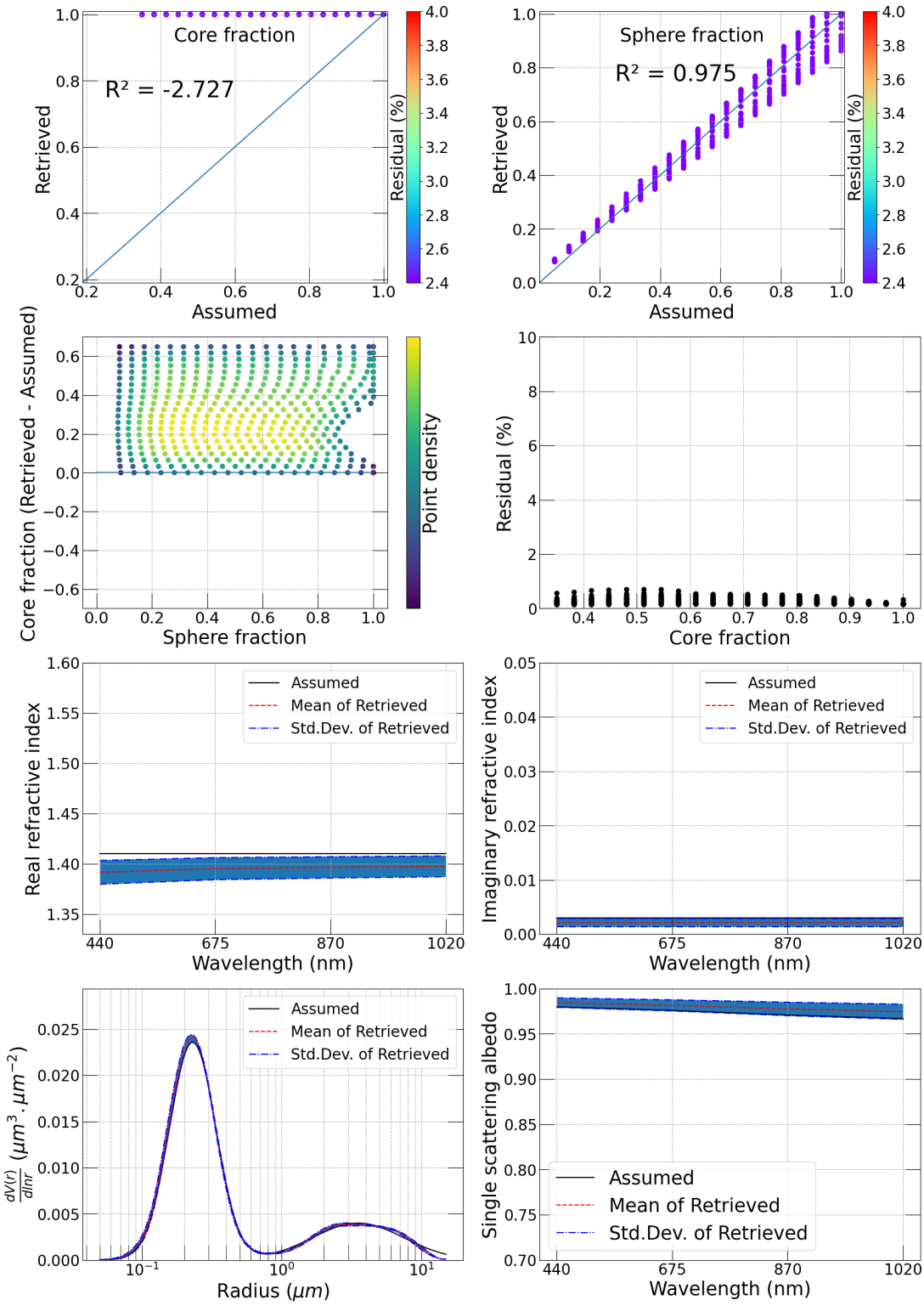

Figure A.27: Collection of plots of aerosol optical and microphysical characteristics derived by inversion of synthetic AERONET measurements. The case of fine mode dominated aerosol size distribution. The radiances, are generated using GRASP/ARIA (with inhomogeneous aerosol model) and inverted using GRASP/Standard (with homogeneous aerosol only).Results use radiance intensity and polarisation, the refractive index is n=1.41, k=0.003

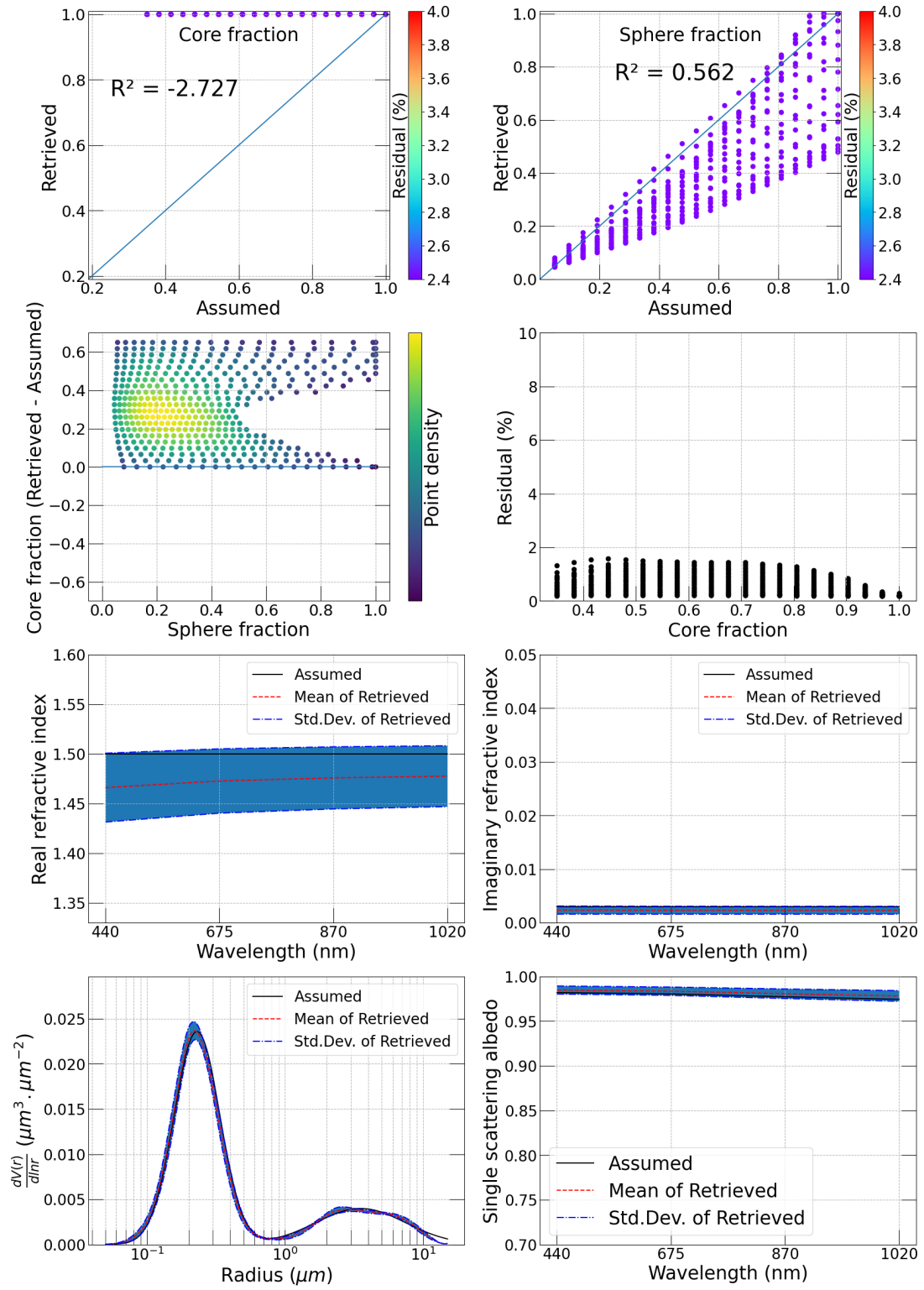

Figure A.28: Collection of plots of aerosol optical and microphysical characteristics derived by inversion of synthetic AERONET measurements. The case of fine mode dominated aerosol size distribution. The radiances, are generated using GRASP/ARIA (with inhomogeneous aerosol model) and inverted using GRASP/Standard (with homogeneous aerosol only). Results use radiance intensity and polarisation, the refractive index is n=1.50, k=0.003

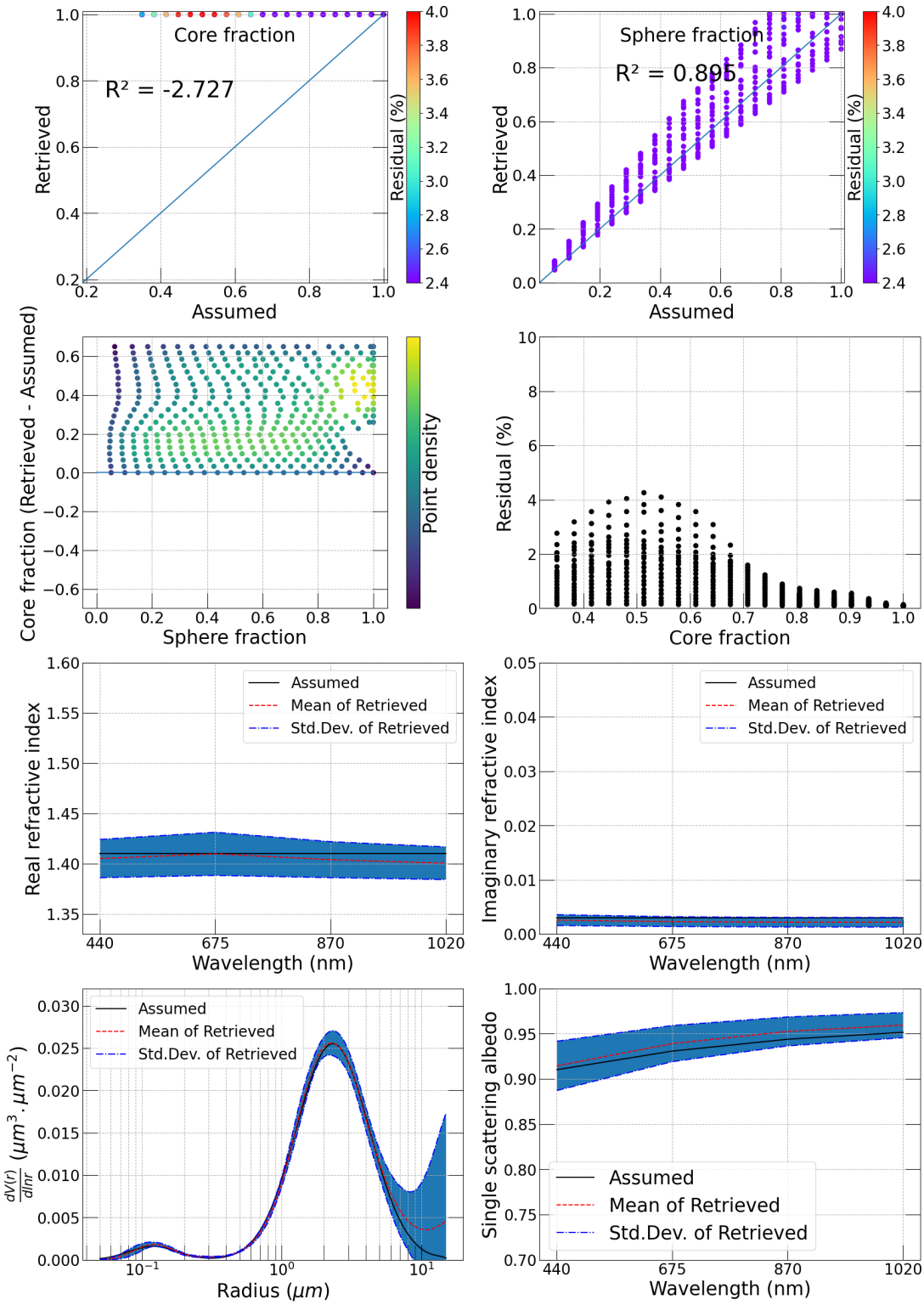

Figure A.29: Collection of plots of aerosol optical and microphysical characteristics derived by inversion of synthetic AERONET measurements. The case of coarse mode dominated aerosol size distribution. The radiances, are generated using GRASP/ARIA (with inhomogeneous aerosol model) and inverted using GRASP/Standard (with homogeneous aerosol only). Results use radiance intensity and polarisation, the refractive index is n=1.41, k=0.003

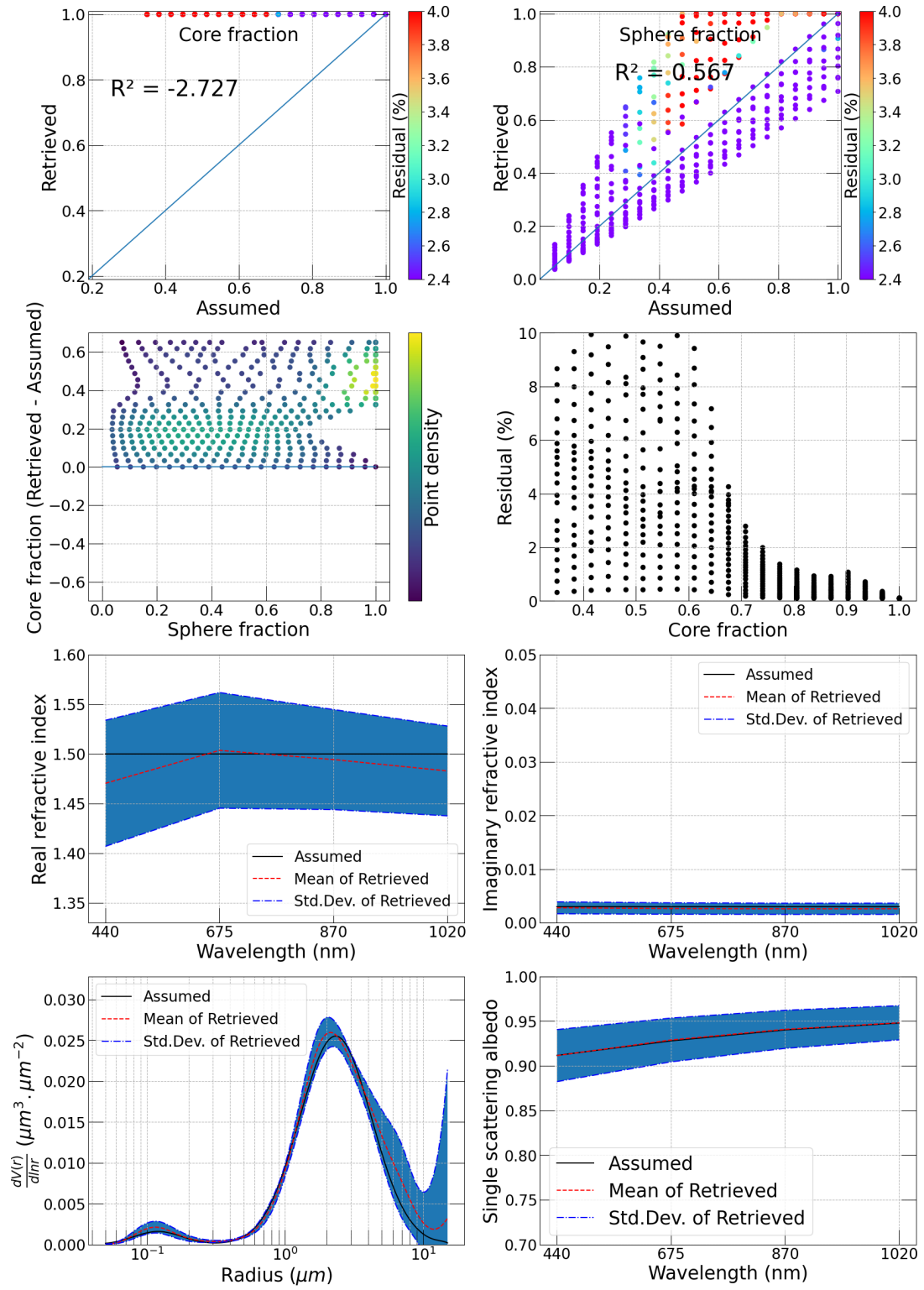

Figure A.30: Collection of plots of aerosol optical and microphysical characteristics derived by inversion of synthetic AERONET measurements. The case of coarse mode dominated aerosol size distribution. The radiances, are generated using GRASP/ARIA (with inhomogeneous aerosol model) and inverted using GRASP/Standard (with homogeneous aerosol only). Results use radiance intensity and polarisation, the refractive index is n=1.50, k=0.003

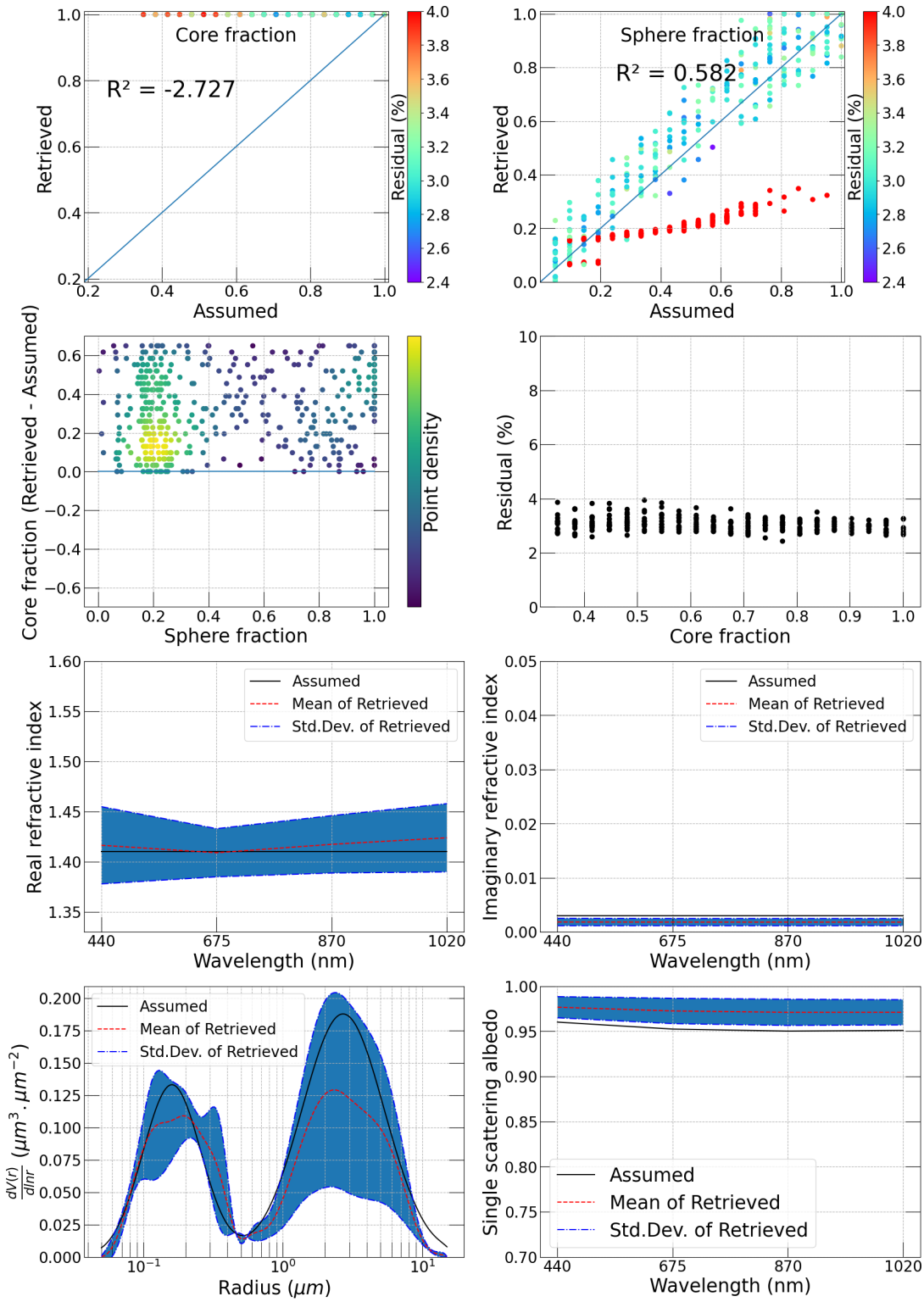

Figure A.31: Collection of plots of aerosol optical and microphysical characteristics derived by inversion of synthetic AERONET measurements. The case of bimodal aerosol size distribution. The radiances, are generated using GRASP/ARIA (with inhomogeneous aerosol model) and inverted using GRASP/Standard (with homogeneous aerosol only). Results use radiance intensity and polarisation, the refractive index is n=1.41, k=0.003

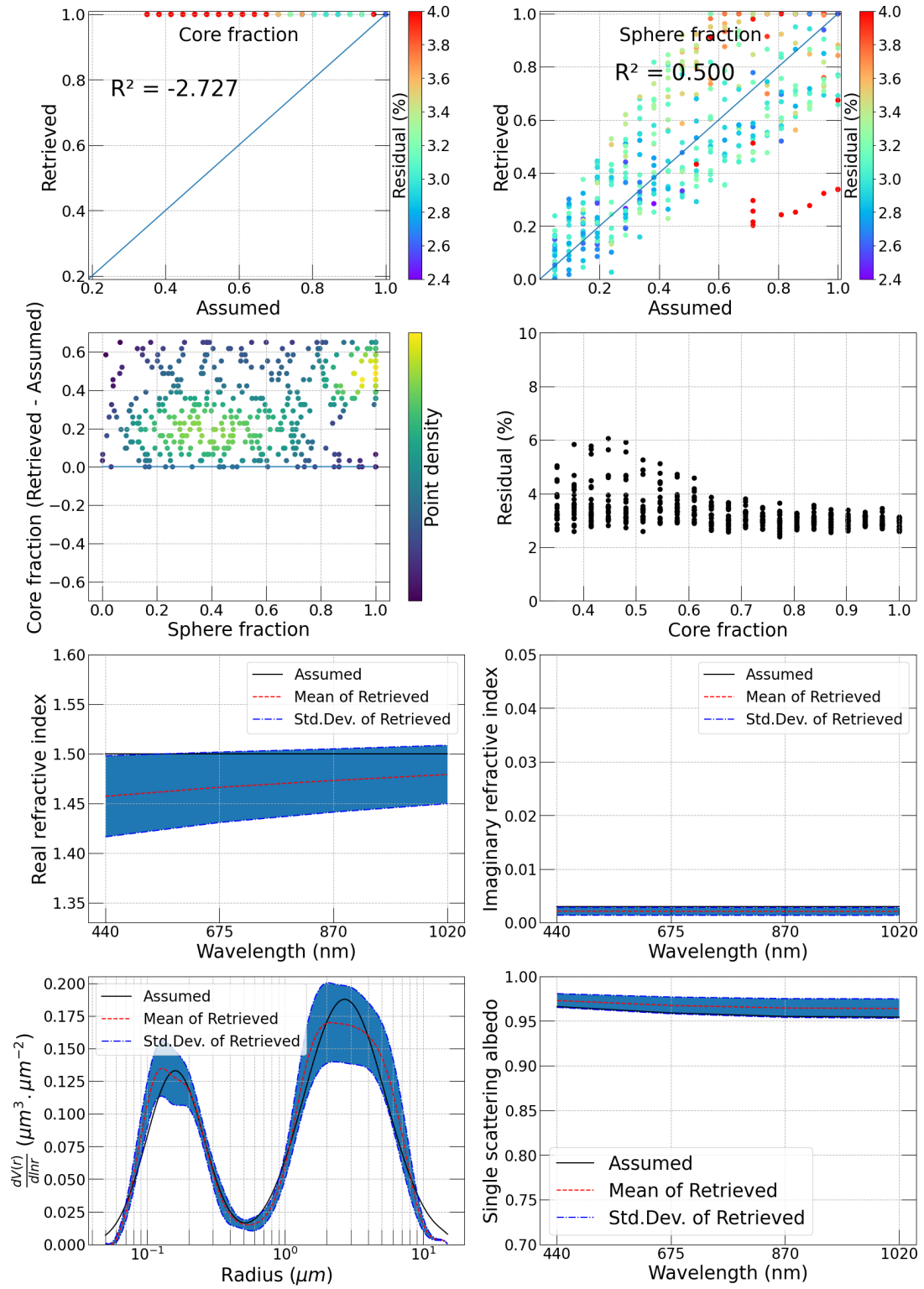

Figure A.32: Collection of plots of aerosol optical and microphysical characteristics derived by inversion of synthetic AERONET measurements. The case of bimodal aerosol size distribution. The radiances, are generated using GRASP/ARIA (with inhomogeneous aerosol model) and inverted using GRASP/Standard (with homogeneous aerosol only). Results use radiance intensity and polarisation, the refractive index is n=1.50, k=0.003

A.3.2 Scope of applicability

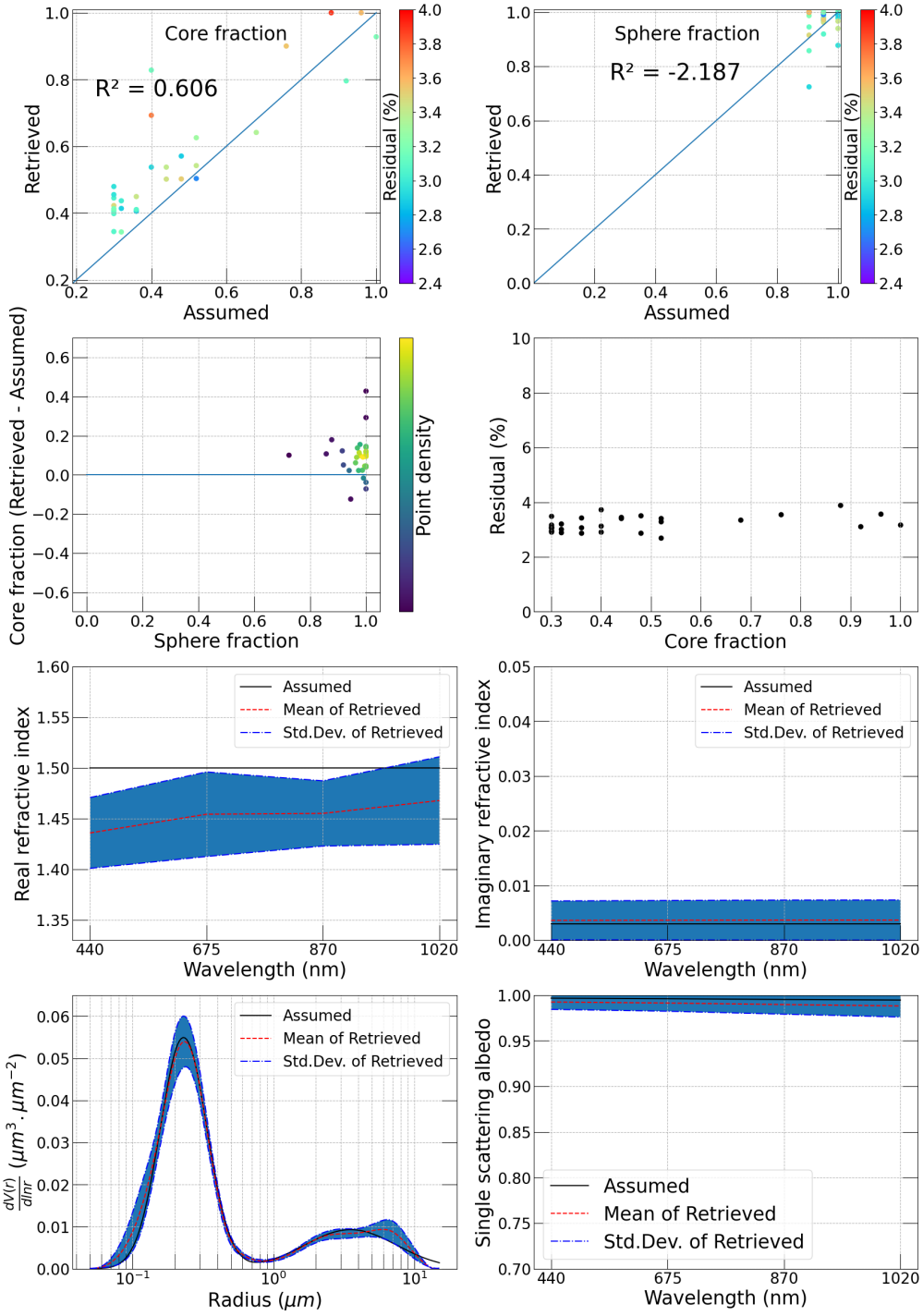

Figure A.33: Collection of plots of aerosol optical and microphysical characteristics derived by inversion of synthetic AERONET measurements. The case of coarse mode dominated aerosol size distribution. The radiances, are generated and inverted GRASP/ARIA (with inhomogeneous aerosol model). Results use radiance intensity only (no polarisation), with added noise in the measurements, the refractive index is n=1.50, k=0.003

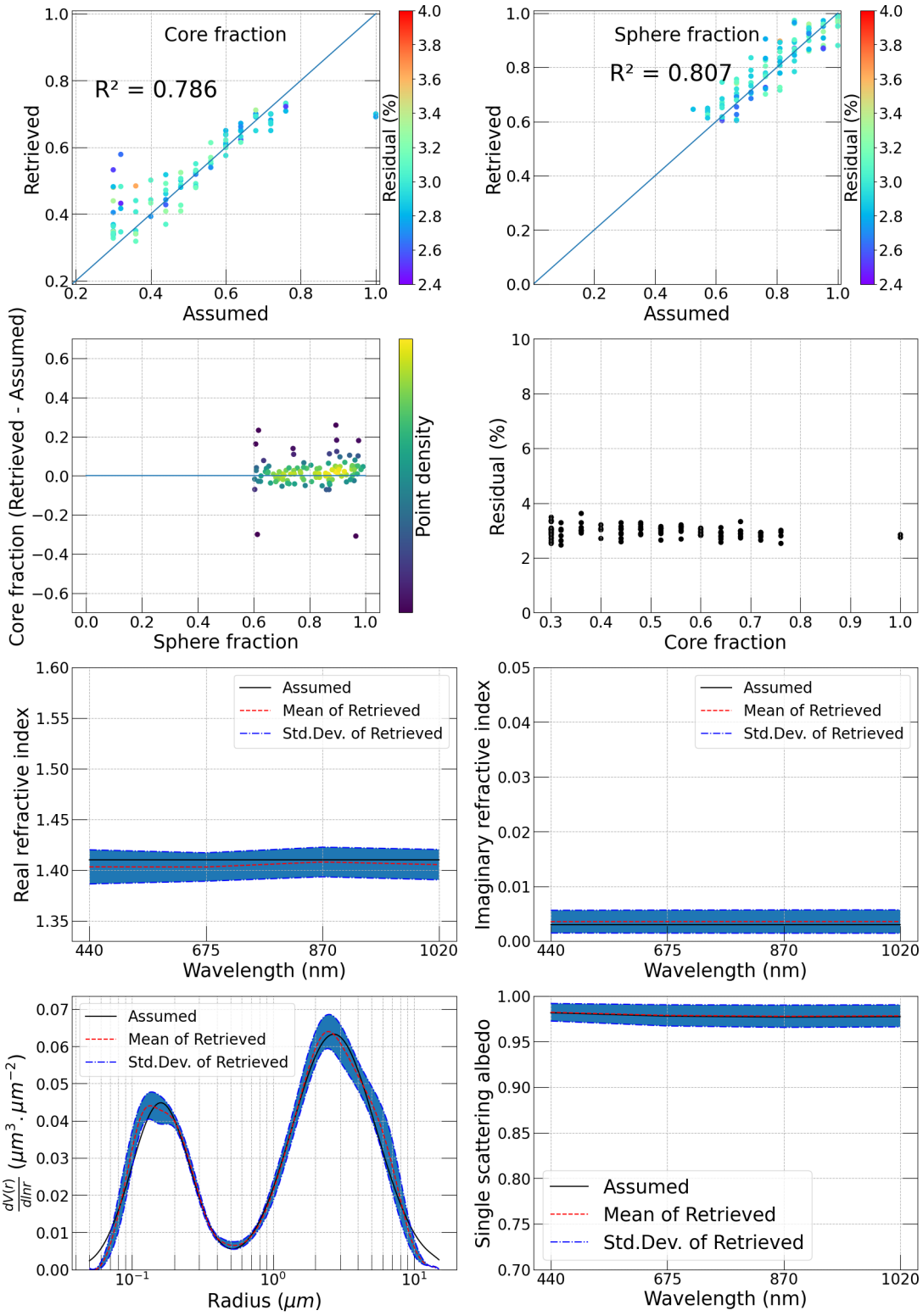

Figure A.34: Collection of plots of aerosol optical and microphysical characteristics derived by inversion of synthetic AERONET measurements. The case of bimodal aerosol size distribution. The radiances, are generated and inverted GRASP/ARIA (with inhomogeneous aerosol model). Results use radiance intensity only (no polarisation), with added noise in the measurements, the refractive index is n=1.41, k=0.003

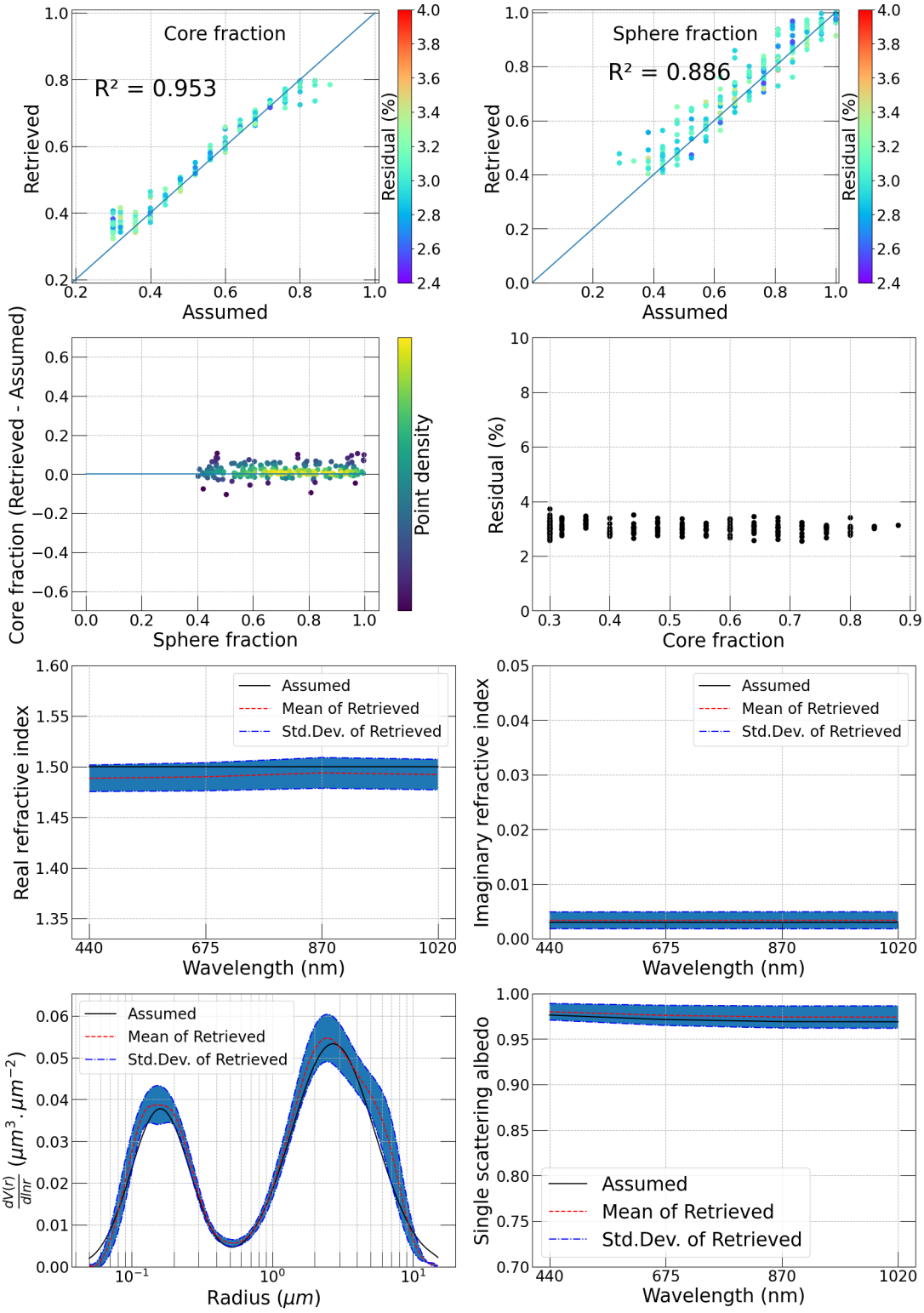

Figure A.35: Collection of plots of aerosol optical and microphysical characteristics derived by inversion of synthetic AERONET measurements. The case of bimodal aerosol size distribution. The radiances, are generated and inverted GRASP/ARIA (with inhomogeneous aerosol model). Results use radiance intensity only (no polarisation), with added noise in the measurements, the refractive index is n=1.50, k=0.003

A.3.3 Complementary figures

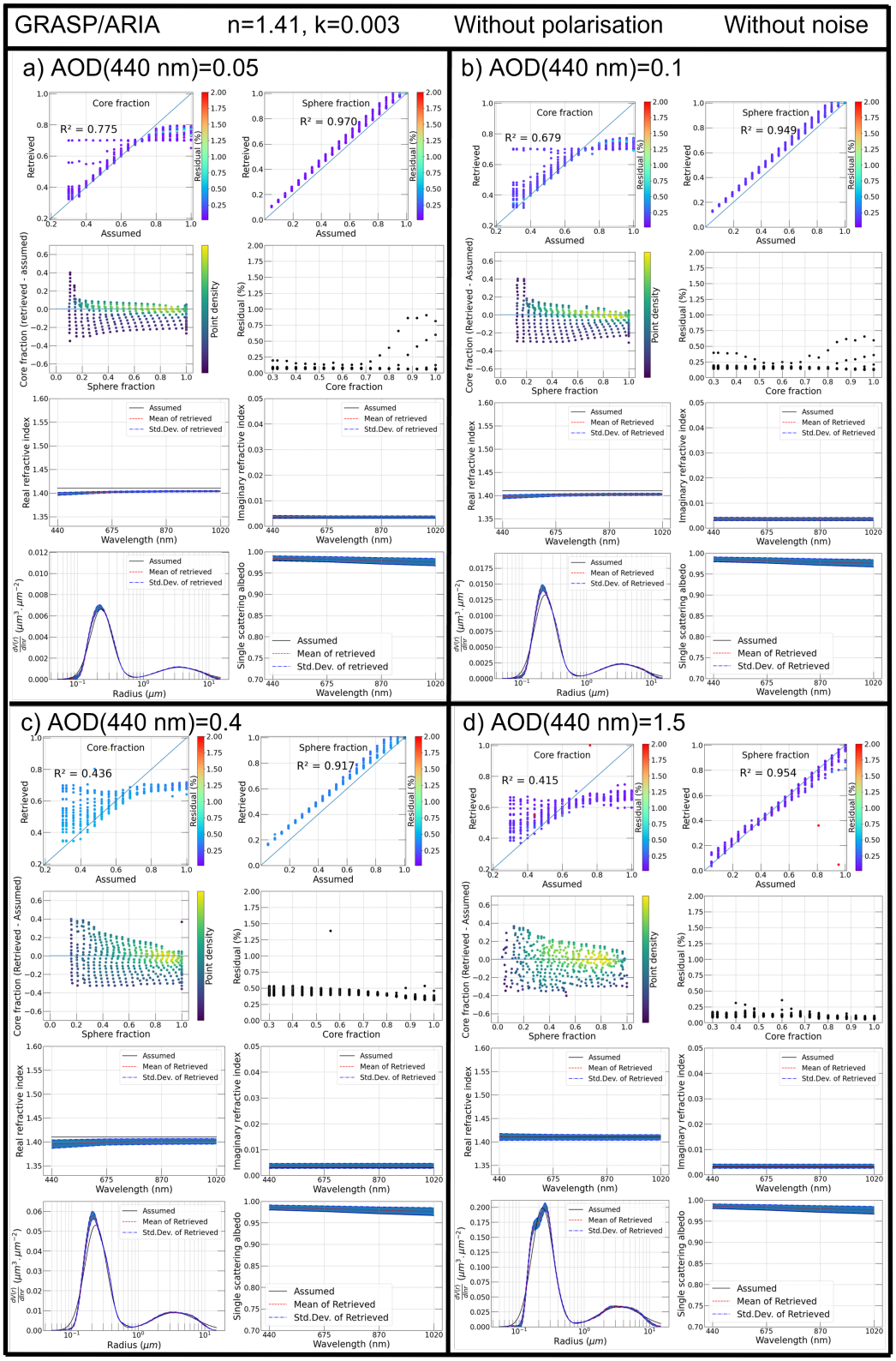

Figure A.36: Collection of plots of aerosol optical and microphysical characteristics derived by inversion of synthetic AERONET measurements. The case of fine mode dominated aerosol size distribution and of refractive index n=1.41 and k=0.003. The radiances, are generated and inverted using GRASP/ARIA (with inhomogeneous aerosol model), simulation of measurements noise and polarisation are not included. In panels, the AOD at 440 nm are a) 0.05, b) 0.1, c) 0.4 d) 1.5.

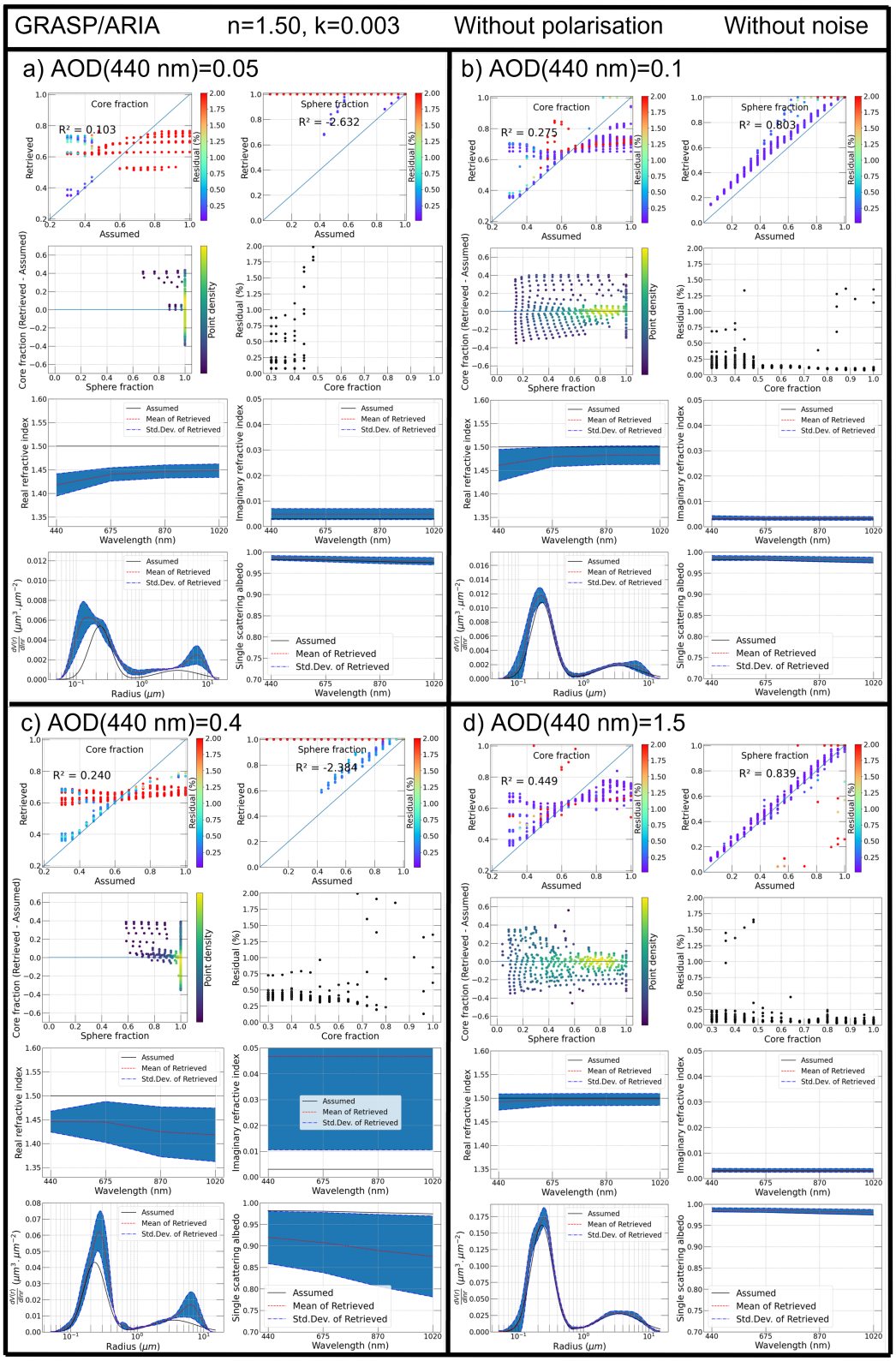

Figure A.37: Collection of plots of aerosol optical and microphysical characteristics derived by inversion of synthetic AERONET measurements. The case of fine mode dominated aerosol size distribution and of refractive index n=1.50 and k=0.003. The radiances, are generated and inverted using GRASP/ARIA (with inhomogeneous aerosol model), simulation of measurements noise and polarisation are not included. In panels, the AOD at 440 nm are a) 0.05, b) 0.1, c) 0.4, d) 1.5.

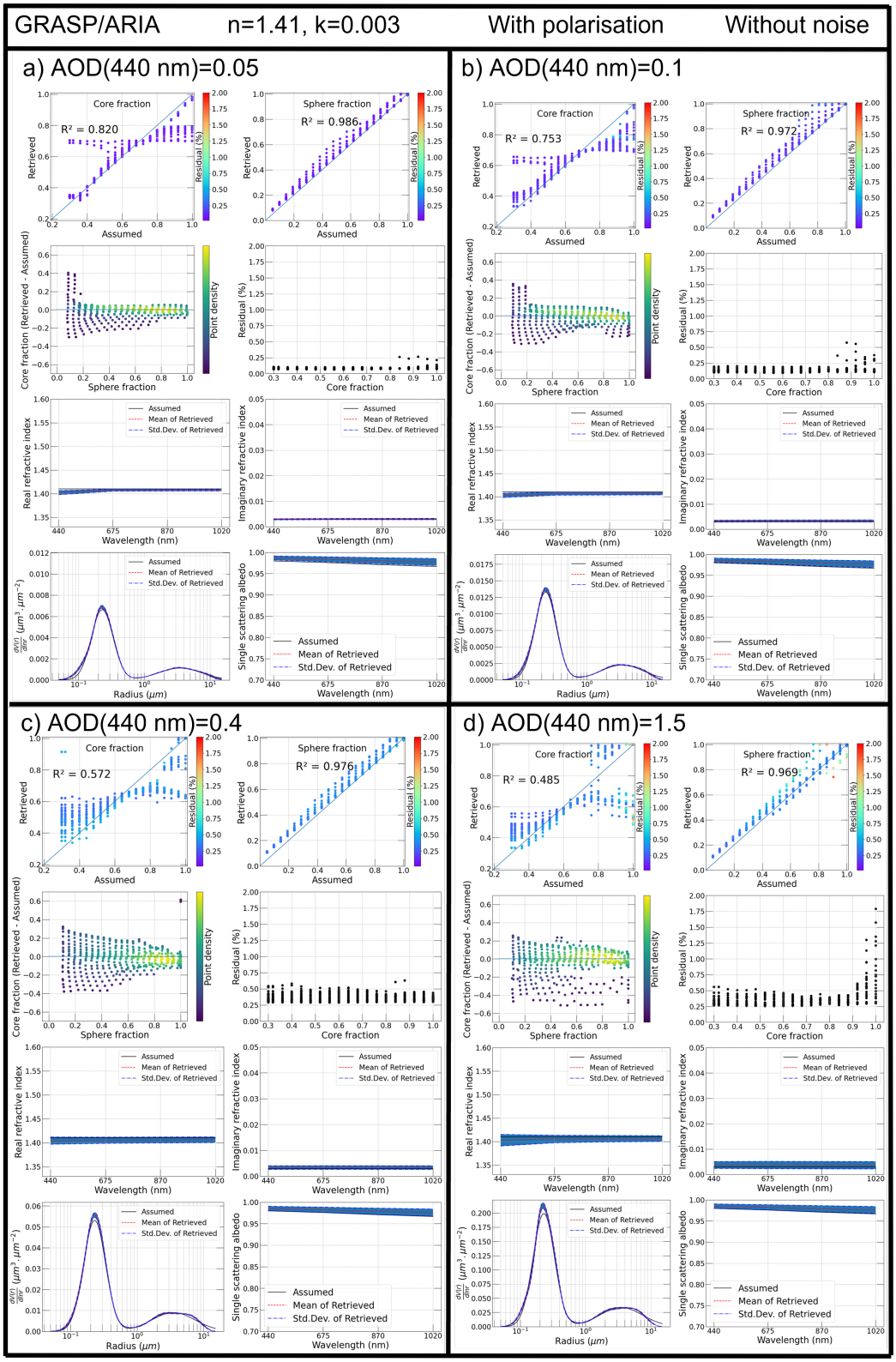

Figure A.38: Collection of plots of aerosol optical and microphysical characteristics derived by inversion of synthetic AERONET measurements. The case of fine mode dominated aerosol size distribution and of refractive index n=1.41 and k=0.003. The radiances, are generated and inverted using GRASP/ARIA (with inhomogeneous aerosol model), simulation of measurements noise is not included and polarisation is included. In panels, the AOD at 440 nm are a) 0.05, b) 0.1, c) 0.4, d) 1.5.

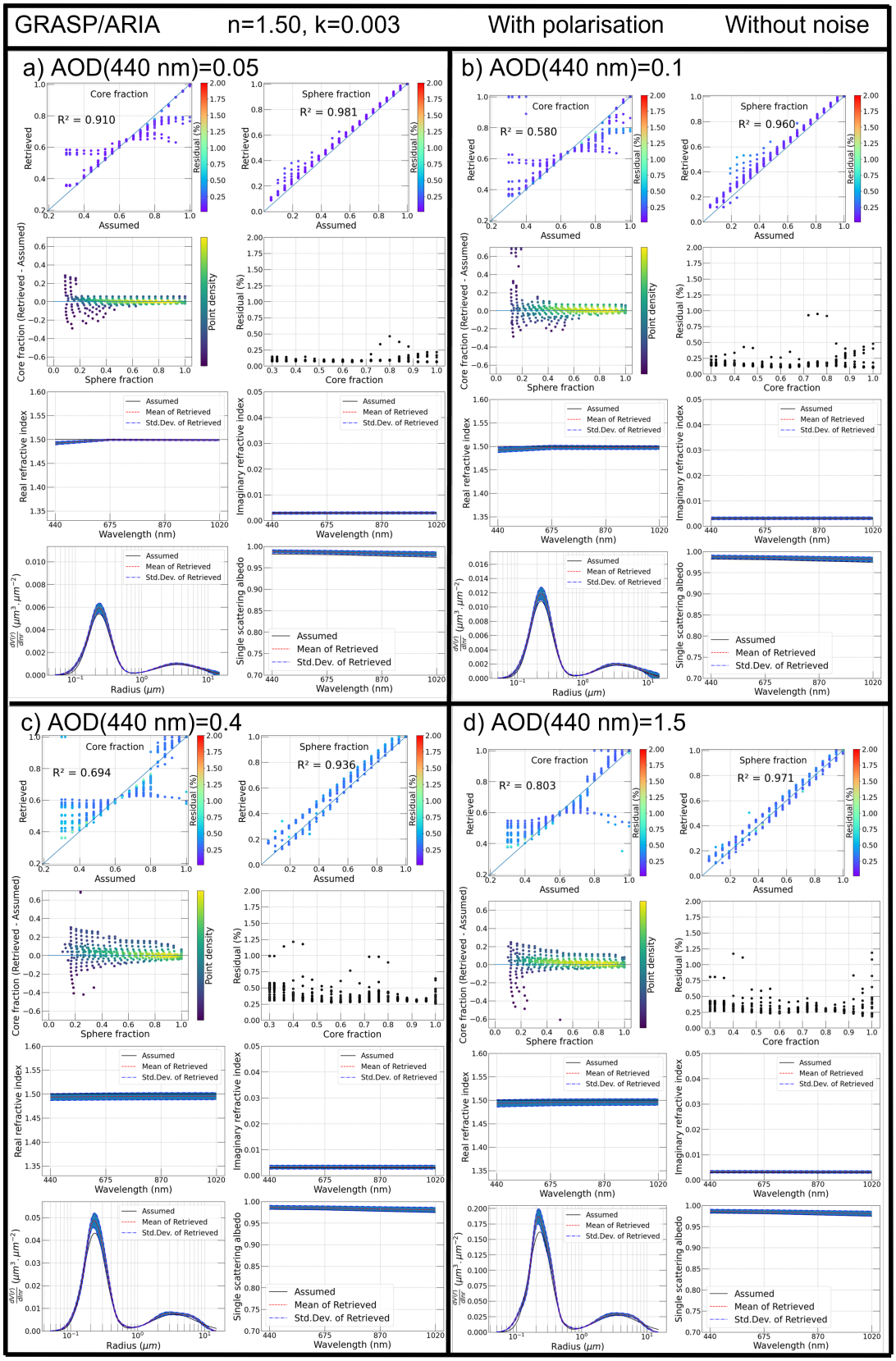

Figure A.39: Collection of plots of aerosol optical and microphysical characteristics derived by inversion of synthetic AERONET measurements. The case of fine mode dominated aerosol size distribution and of refractive index n=1.50 and k=0.003. The radiances, are generated and inverted using GRASP/ARIA (with inhomogeneous aerosol model), simulation of measurements noise is not included and polarisation is included. In panels, the AOD at 440 nm are a) 0.05, b) 0.1, c) 0.4, d) 1.5.

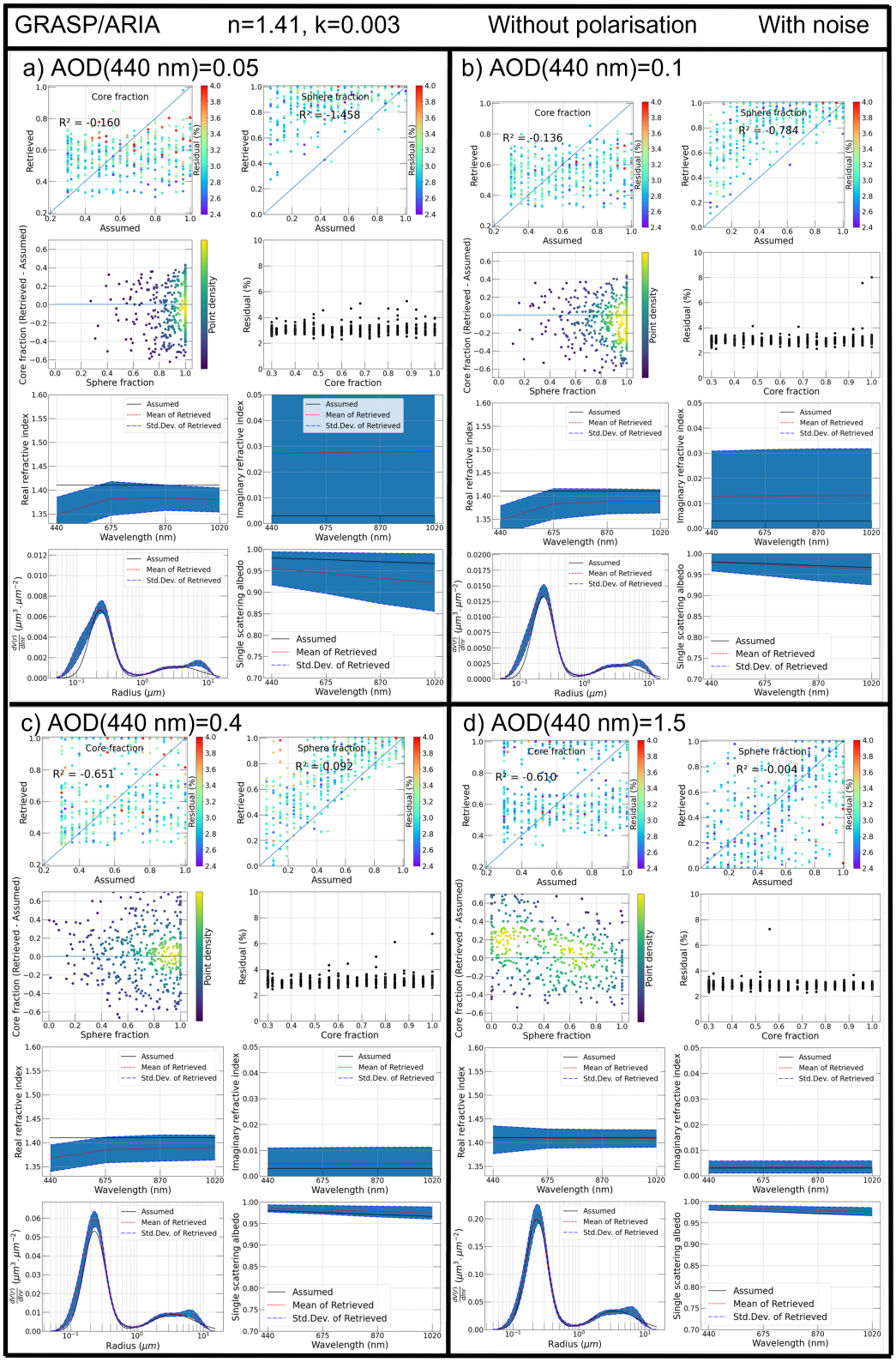

Figure A.40: Collection of plots of aerosol optical and microphysical characteristics derived by inversion of synthetic AERONET measurements. The case of fine mode dominated aerosol size distribution and of refractive index n=1.41 and k=0.003. The radiances, are generated and inverted using GRASP/ARIA (with inhomogeneous aerosol model), simulation of measurements polarisation is not included and noise is included. In panels, the AOD at 440 nm are a) 0.05, b) 0.1, c) 0.4, d) 1.5.

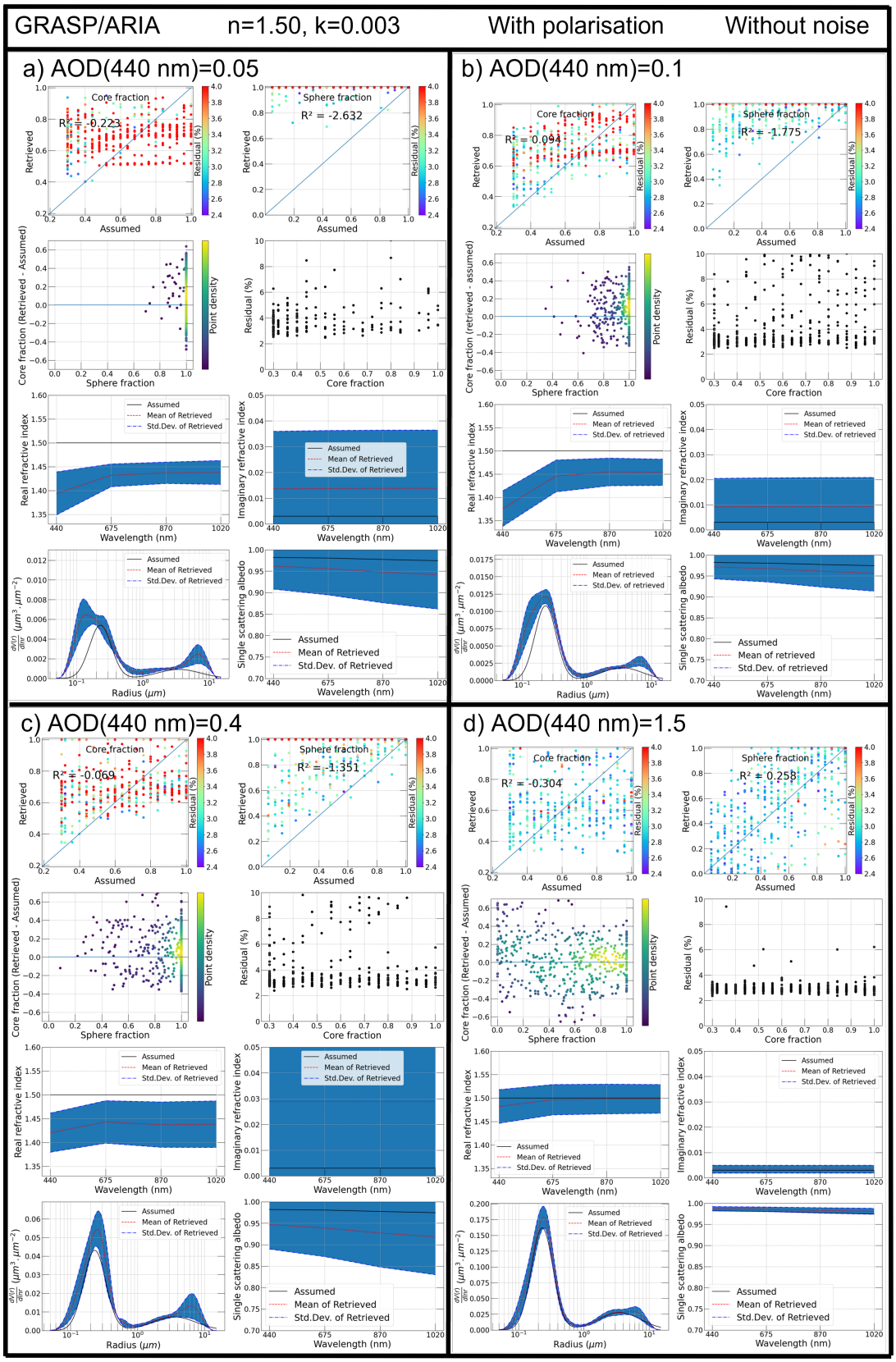

Figure A.41: Collection of plots of aerosol optical and microphysical characteristics derived by inversion of synthetic AERONET measurements. The case of fine mode dominated aerosol size distribution and of refractive index n=1.50 and k=0.003. The radiances, are generated and inverted using GRASP/ARIA (with inhomogeneous aerosol model), simulation of measurements polarisation is not included and noise is included. In panels, the AOD at 440 nm are a) 0.05, b) 0.1, c) 0.4, d) 1.5.

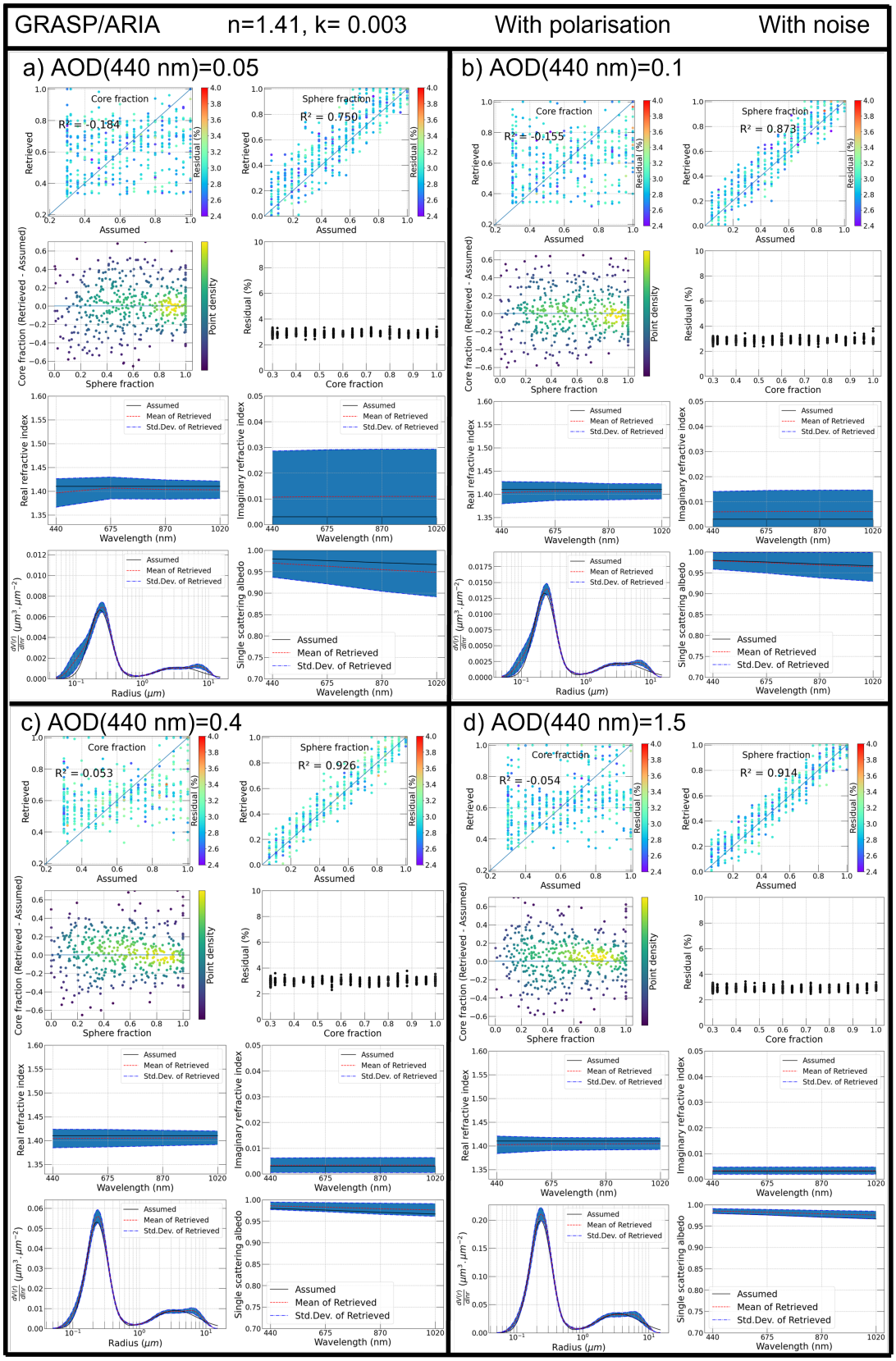

Figure A.42: Collection of plots of aerosol optical and microphysical characteristics derived by inversion of synthetic AERONET measurements. The case of fine mode dominated aerosol size distribution and of refractive index n=1.41 and k=0.003. The radiances, are generated and inverted using GRASP/ARIA (with inhomogeneous aerosol model), simulation of measurements noise and polarisation are included. In panels, the AOD at 440 nm are a) 0.05, b) 0.1, c) 0.4, d) 1.5.

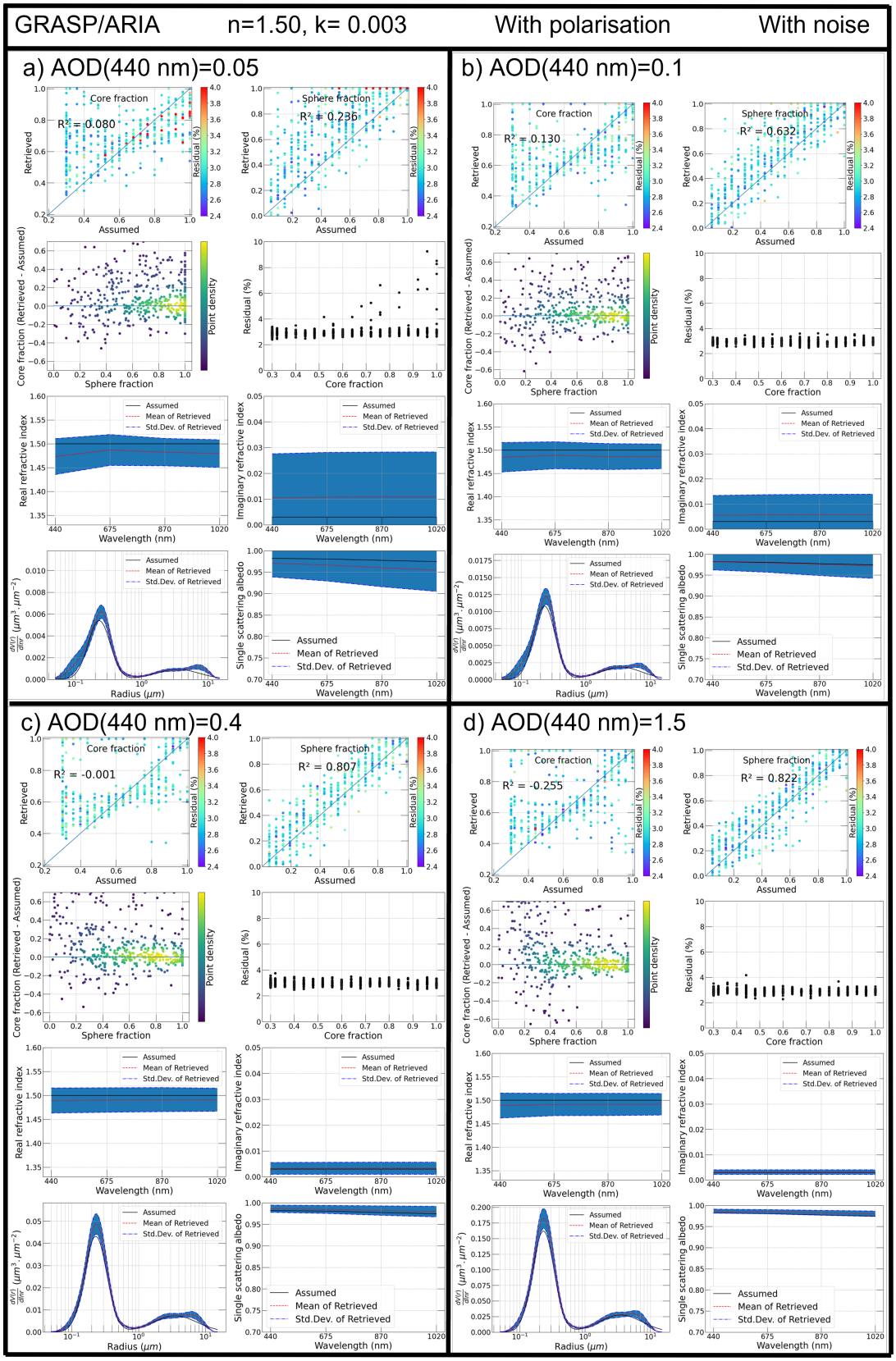

Figure A.43: Collection of plots of aerosol optical and microphysical characteristics derived by inversion of synthetic AERONET measurements. The case of fine mode dominated aerosol size distribution and of refractive index n=1.50 and k=0.003. The radiances, are generated and inverted using GRASP/ARIA (with inhomogeneous aerosol model), simulation of measurements noise and polarisation are included. In panels, the AOD at 440 nm are a) 0.05, b) 0.1, c) 0.4, d) 1.5.

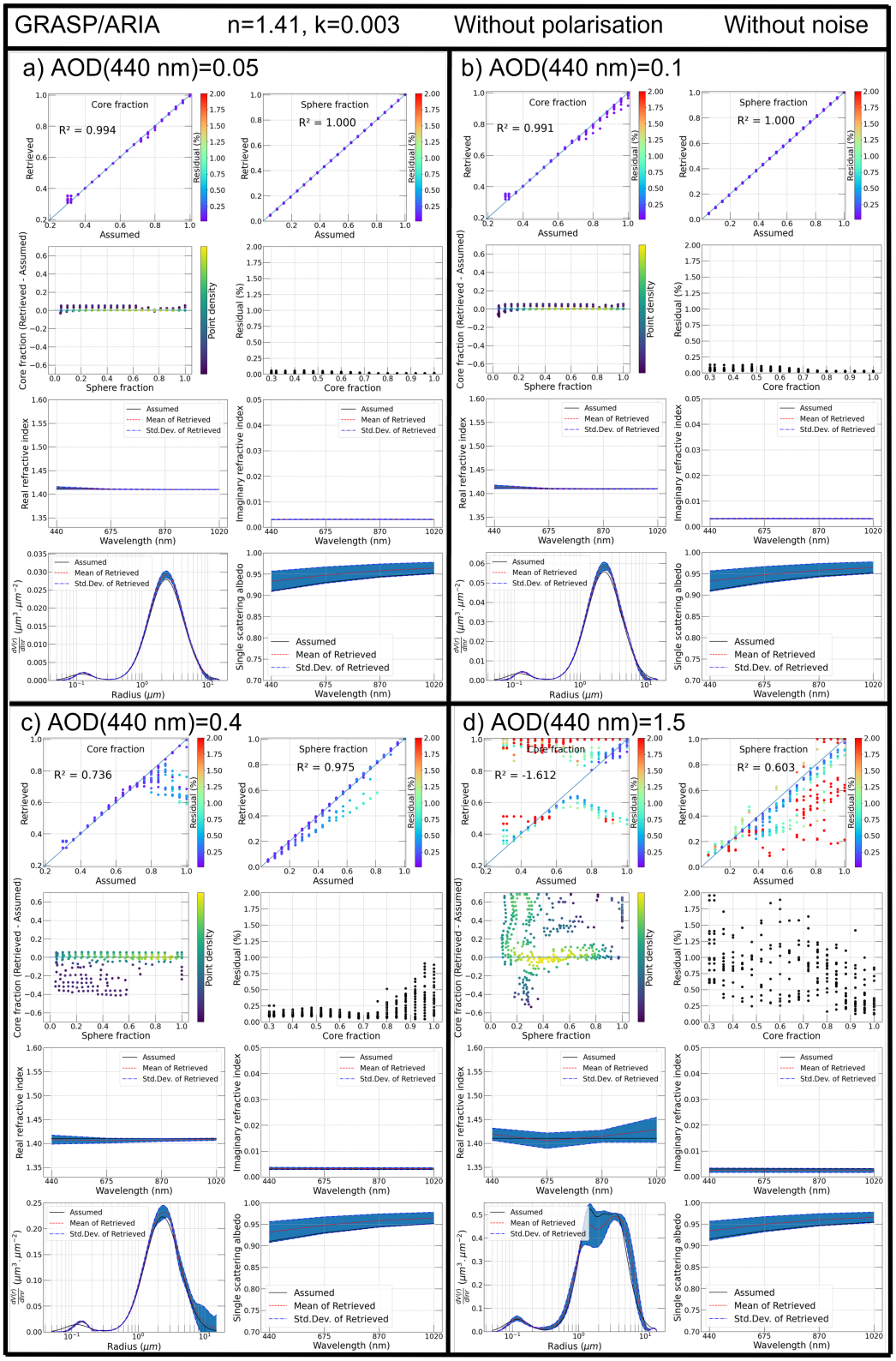

Figure A.44: Collection of plots of aerosol optical and microphysical characteristics derived by inversion of synthetic AERONET measurements. The case of coarse mode dominated aerosol size distribution and of refractive index n=1.41 and k=0.003. The radiances, are generated and inverted using GRASP/ARIA (with inhomogeneous aerosol model), simulation of measurements noise and polarisation are not included. In panels, the AOD at 440 nm are a) 0.05, b) 0.1, c) 0.4, d) 1.5.

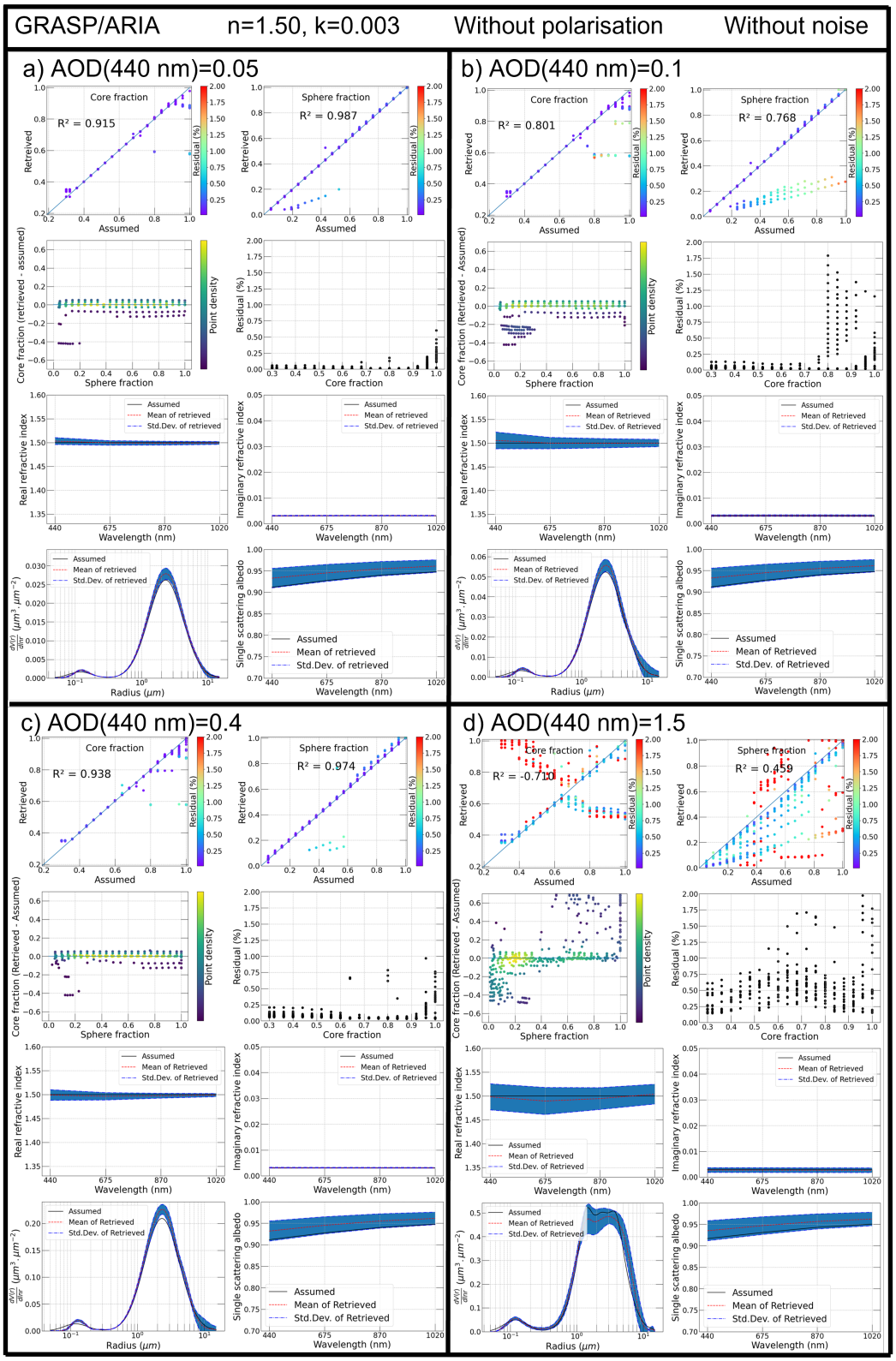

Figure A.45: Collection of plots of aerosol optical and microphysical characteristics derived by inversion of synthetic AERONET measurements. The case of coarse mode dominated aerosol size distribution and of refractive index n=1.50 and k=0.003. The radiances, are generated and inverted using GRASP/ARIA (with inhomogeneous aerosol model), simulation of measurements noise and polarisation are not included. In panels, the AOD at 440 nm are a) 0.05, b) 0.1, c) 0.4, d) 1.5.

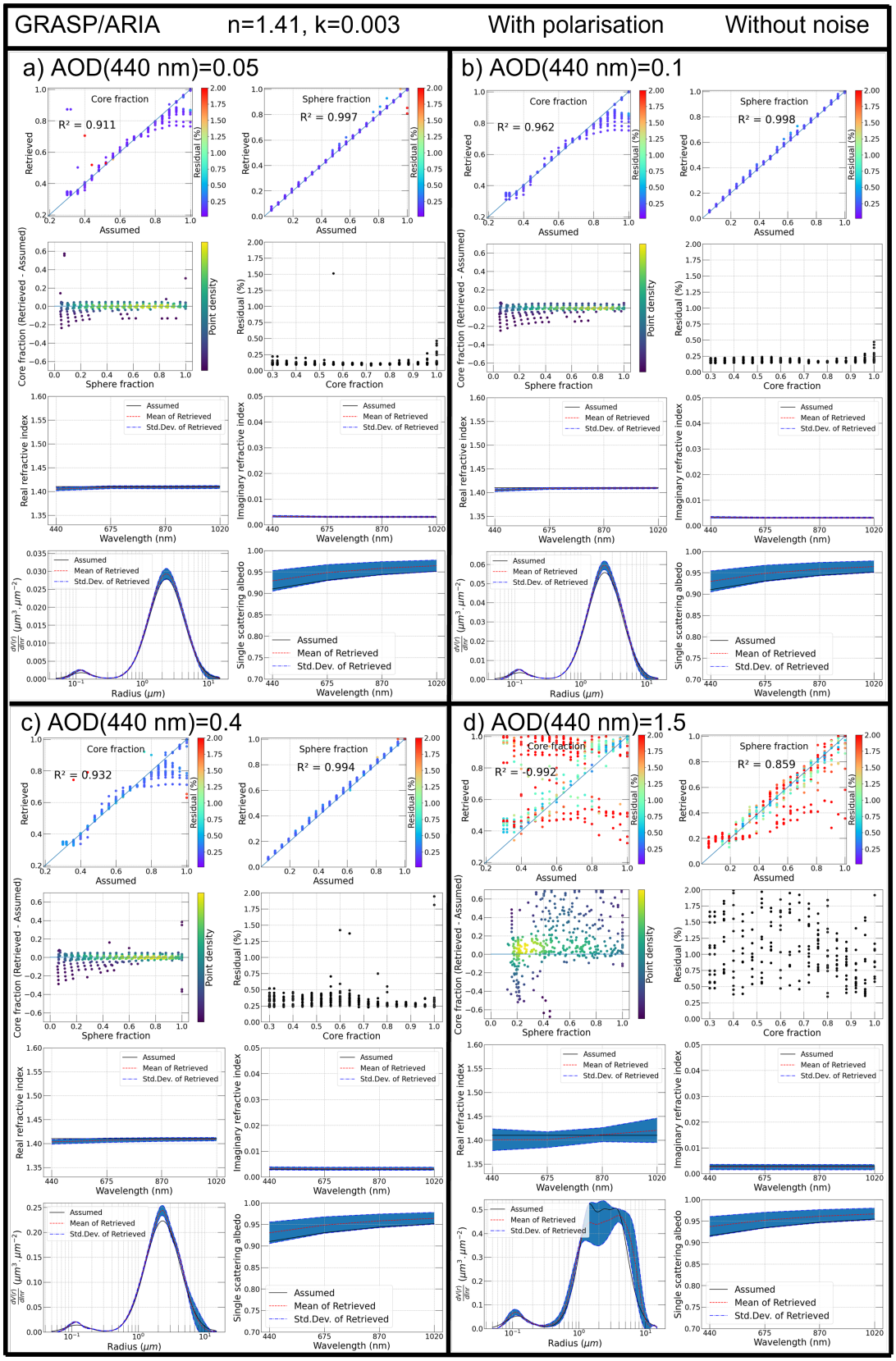

Figure A.46: Collection of plots of aerosol optical and microphysical characteristics derived by inversion of synthetic AERONET measurements. The case of coarse mode dominated aerosol size distribution and of refractive index n=1.41 and k=0.003. The radiances, are generated and inverted using GRASP/ARIA (with inhomogeneous aerosol model), simulation of measurements noise is not included and polarisation is included. In panels, the AOD at 440 nm are a) 0.05, b) 0.1, c) 0.4, d) 1.5.

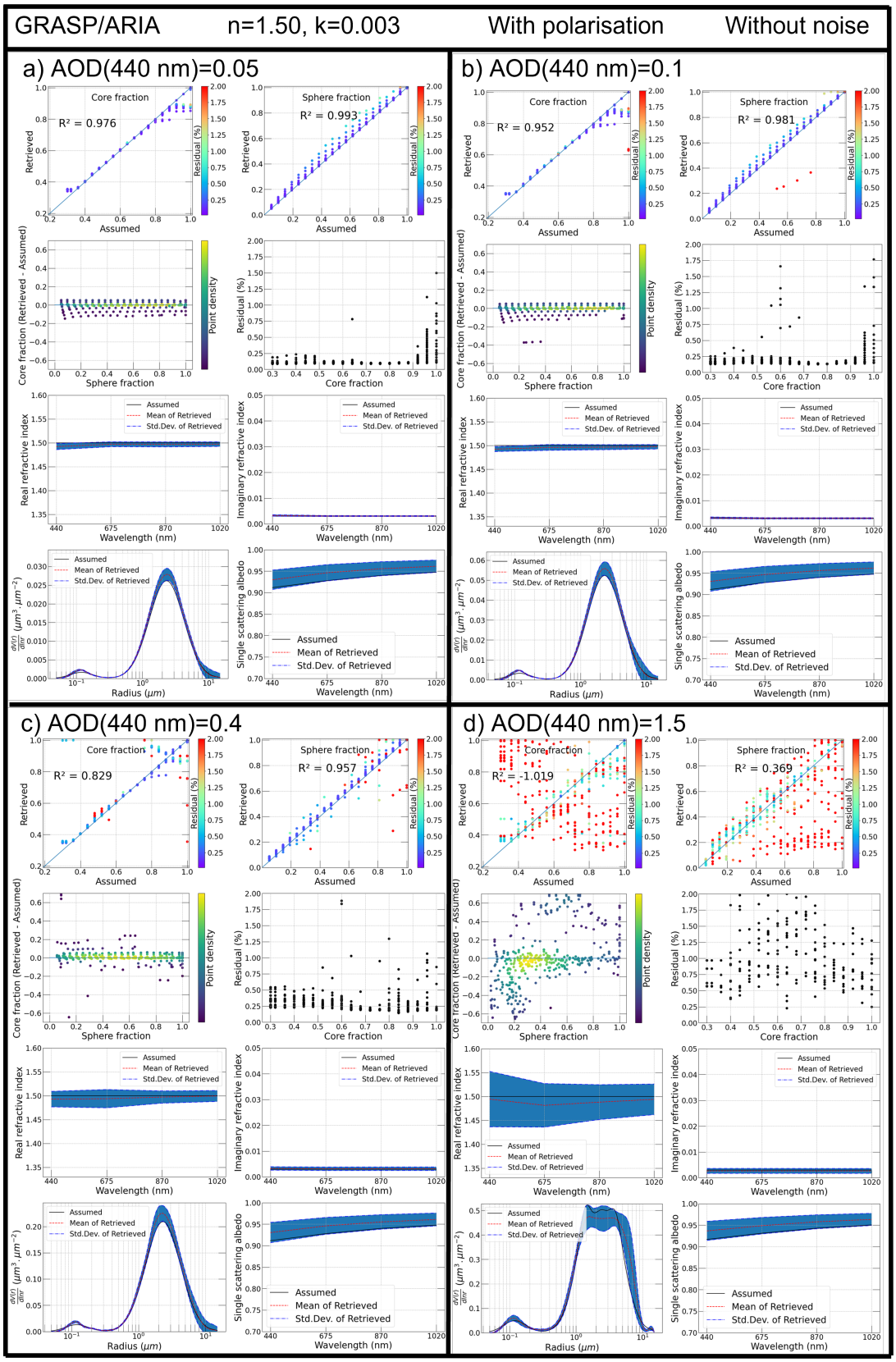

Figure A.47: Collection of plots of aerosol optical and microphysical characteristics derived by inversion of synthetic AERONET measurements. The case of coarse mode dominated aerosol size distribution and of refractive index n=1.50 and k=0.003. The radiances, are generated and inverted using GRASP/ARIA (with inhomogeneous aerosol model), simulation of measurements noise is not included and polarisation is included. In panels, the AOD at 440 nm are a) 0.05, b) 0.1, c) 0.4, d) 1.5.

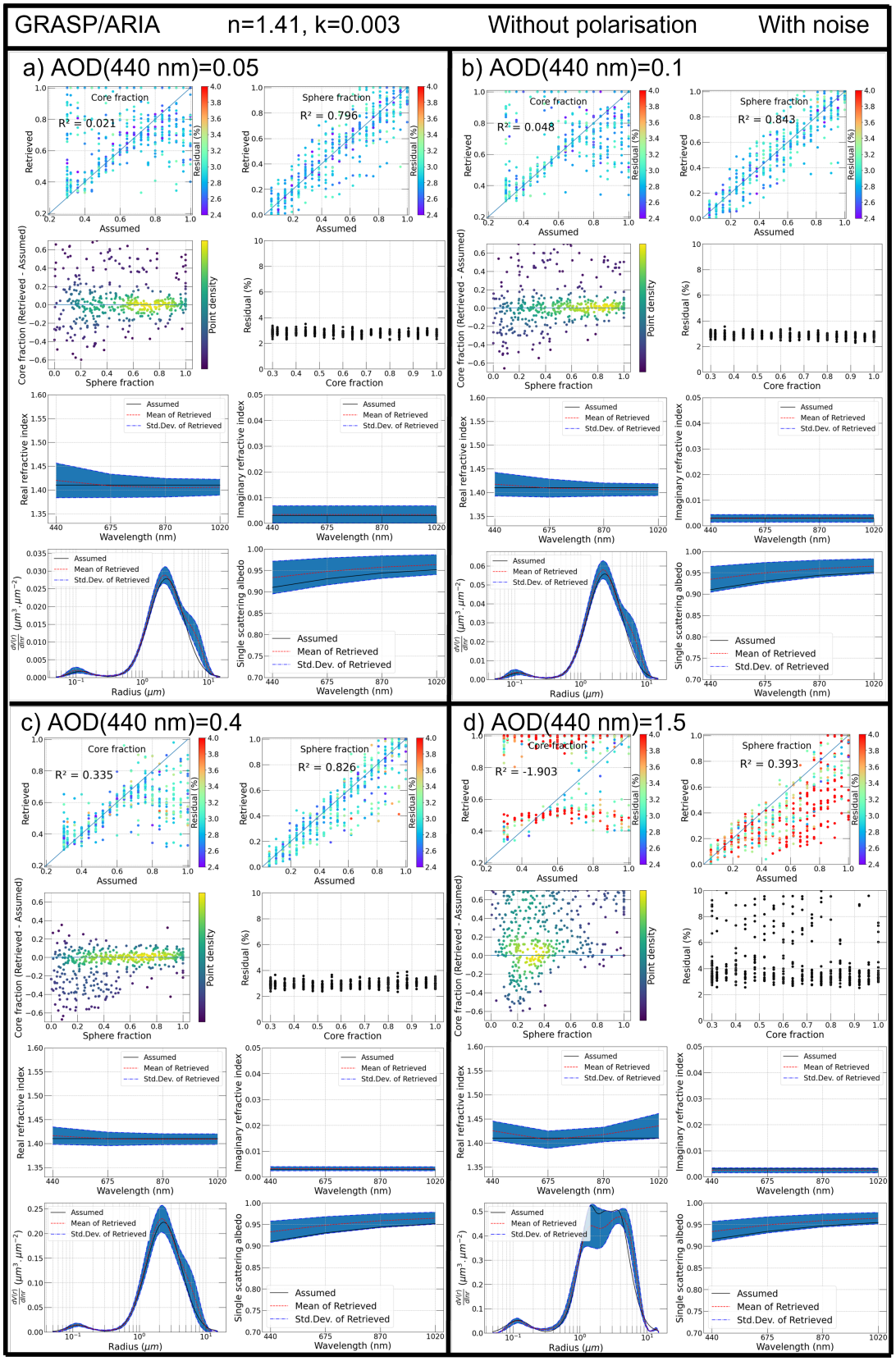

Figure A.48: Collection of plots of aerosol optical and microphysical characteristics derived by inversion of synthetic AERONET measurements. The case of coarse mode dominated aerosol size distribution and of refractive index n=1.41 and k=0.003. The radiances, are generated and inverted using GRASP/ARIA (with inhomogeneous aerosol model), simulation of measurements polarisation is not included and noise is included. In panels, the AOD at 440 nm are a) 0.05, b) 0.1, c) 0.4, d) 1.5.

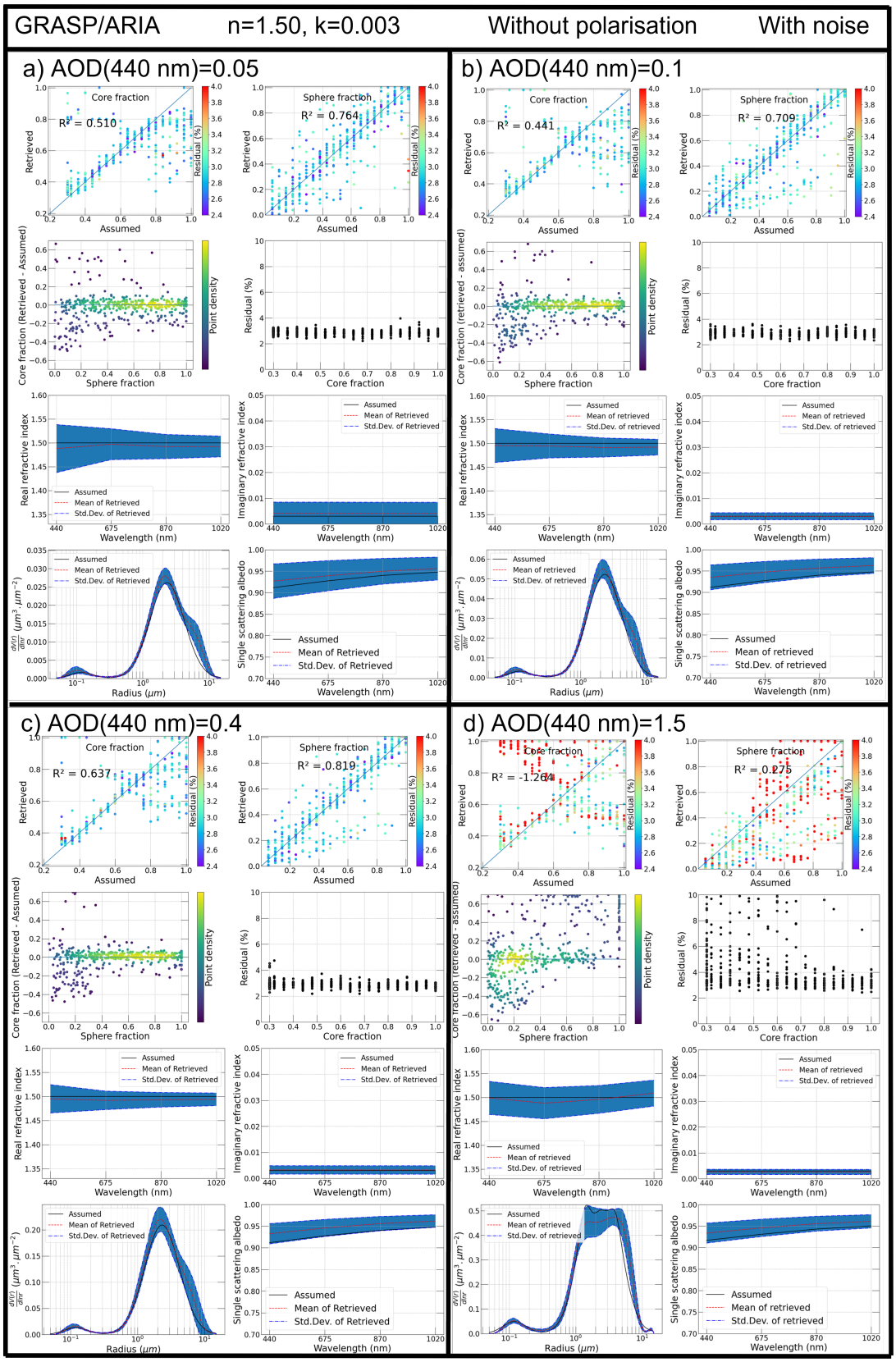

Figure A.49: Collection of plots of aerosol optical and microphysical characteristics derived by inversion of synthetic AERONET measurements. The case of coarse mode dominated aerosol size distribution and of refractive index n=1.50 and k=0.003. The radiances, are generated and inverted using GRASP/ARIA (with inhomogeneous aerosol model), simulation of measurements polarisation is not included and noise is included. In panels, the AOD at 440 nm are a) 0.05, b) 0.1, c) 0.4, d) 1.5.

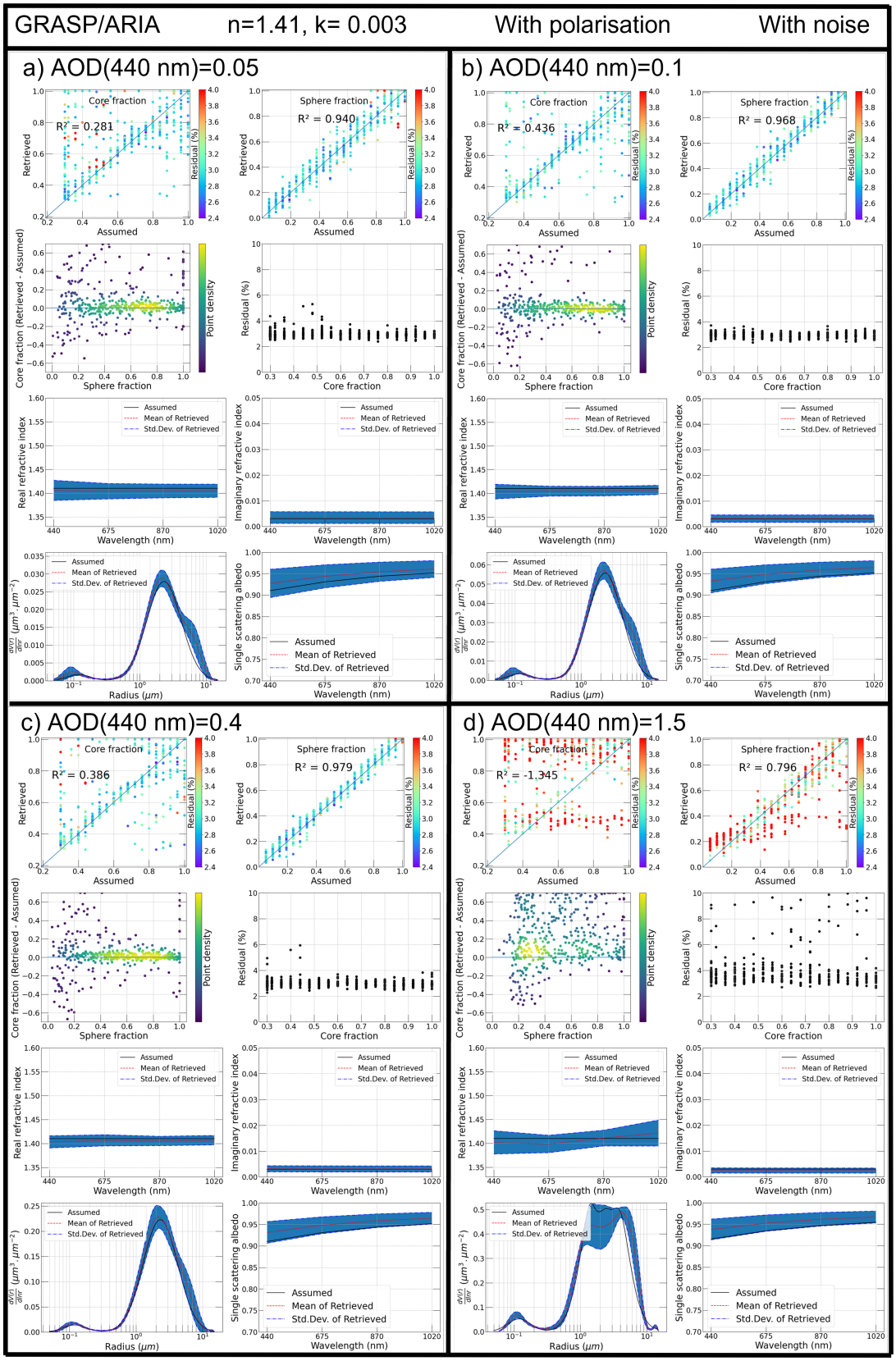

Figure A.50: Collection of plots of aerosol optical and microphysical characteristics derived by inversion of synthetic AERONET measurements. The case of coarse mode dominated aerosol size distribution and of refractive index n=1.41 and k=0.003. The radiances, are generated and inverted using GRASP/ARIA (with inhomogeneous aerosol model), simulation of measurements noise and polarisation are included. In panels, the AOD at 440 nm are a) 0.05, b) 0.1, c) 0.4, d) 1.5.

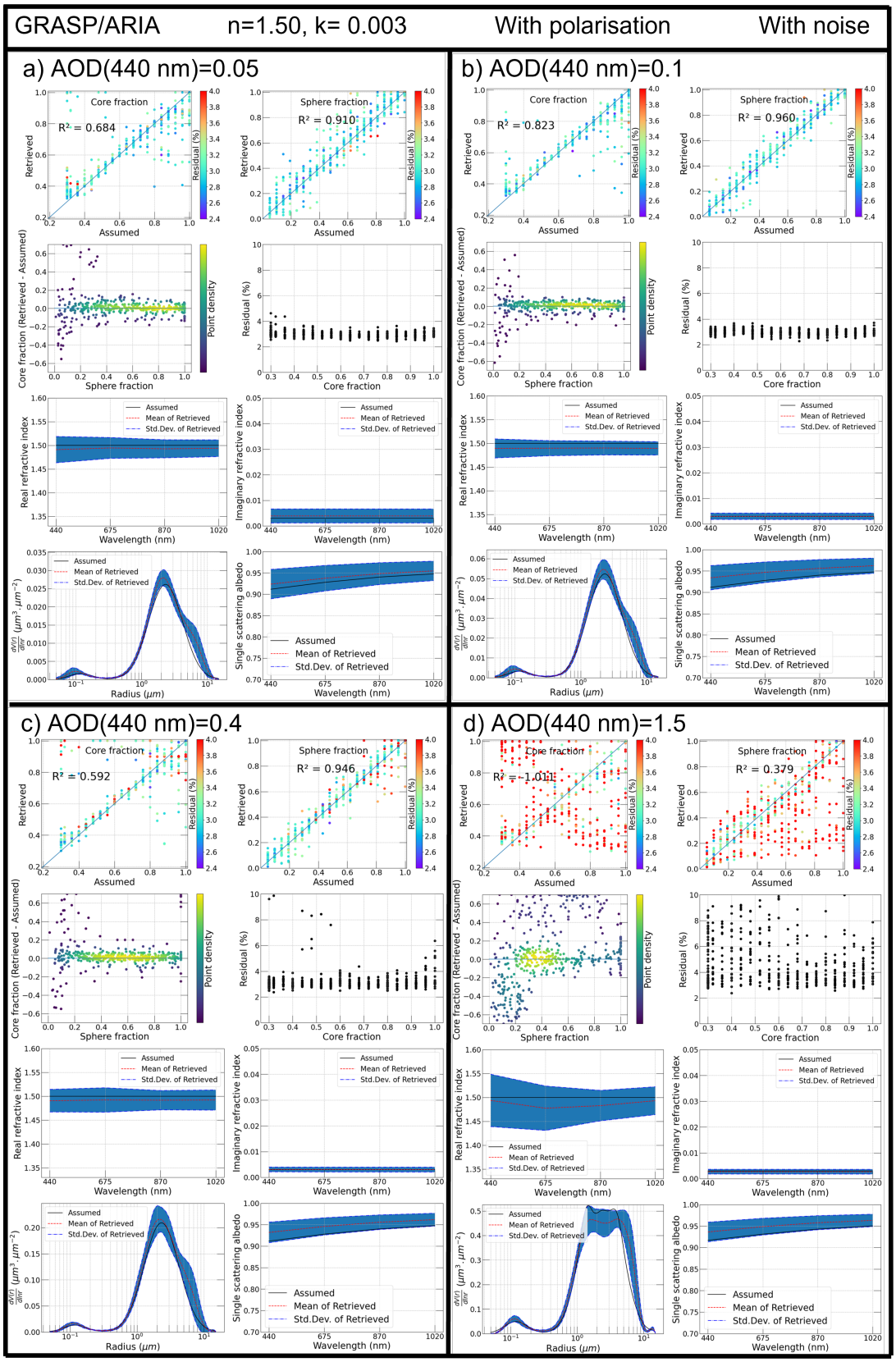

Figure A.51: Collection of plots of aerosol optical and microphysical characteristics derived by inversion of synthetic AERONET measurements. The case of coarse mode dominated aerosol size distribution and of refractive index n=1.50 and k=0.003. The radiances, are generated and inverted using GRASP/ARIA (with inhomogeneous aerosol model), simulation of measurements noise and polarisation are included. In panels, the AOD at 440 nm are a) 0.05, b) 0.1, c) 0.4, d) 1.5.

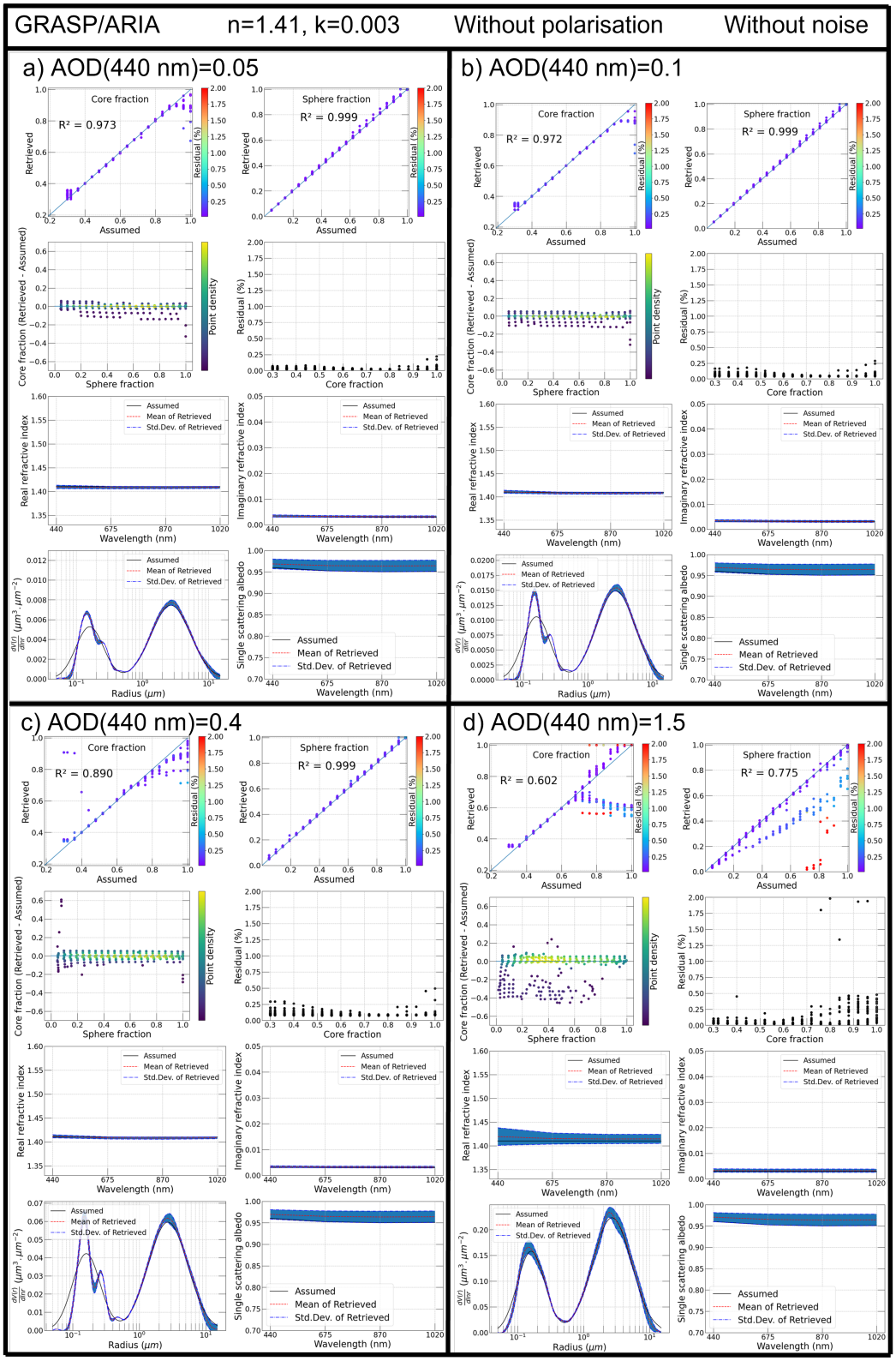

Figure A.52: Collection of plots of aerosol optical and microphysical characteristics derived by inversion of synthetic AERONET measurements. The case of bimodal aerosol size distribution and of refractive index n=1.41 and k=0.003. The radiances, are generated and inverted using GRASP/ARIA (with inhomogeneous aerosol model), simulation of measurements noise and polarisation are not included. In panels, the AOD at 440 nm are a) 0.05, b) 0.1, c) 0.4, d) 1.5.

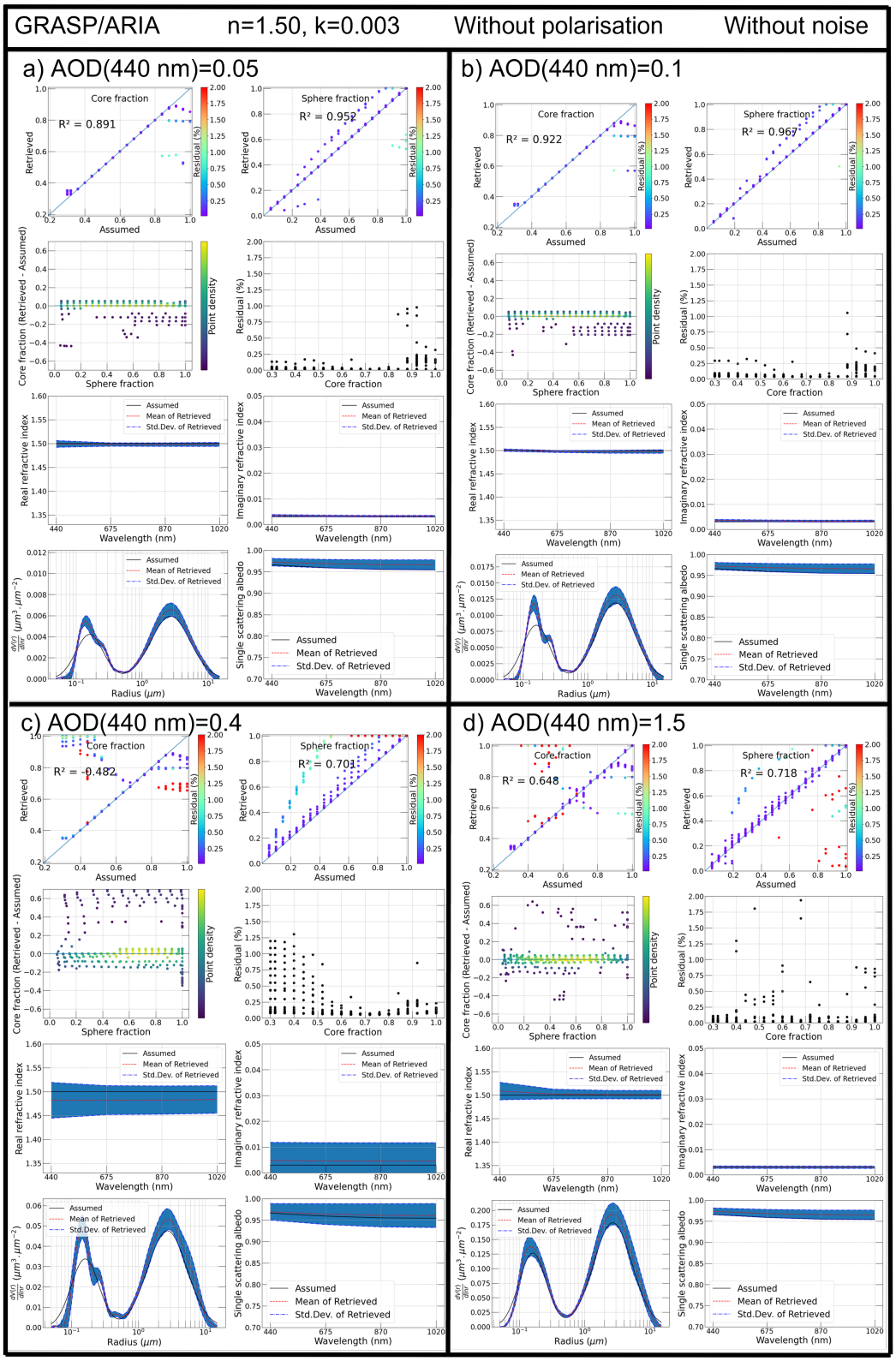

Figure A.53: Collection of plots of aerosol optical and microphysical characteristics derived by inversion of synthetic AERONET measurements. The case of bimodal aerosol size distribution and of refractive index n=1.50 and k=0.003. The radiances, are generated and inverted using GRASP/ARIA (with inhomogeneous aerosol model), simulation of measurements noise and polarisation are not included. In panels, the AOD at 440 nm are a) 0.05, b) 0.1, c) 0.4, d) 1.5.

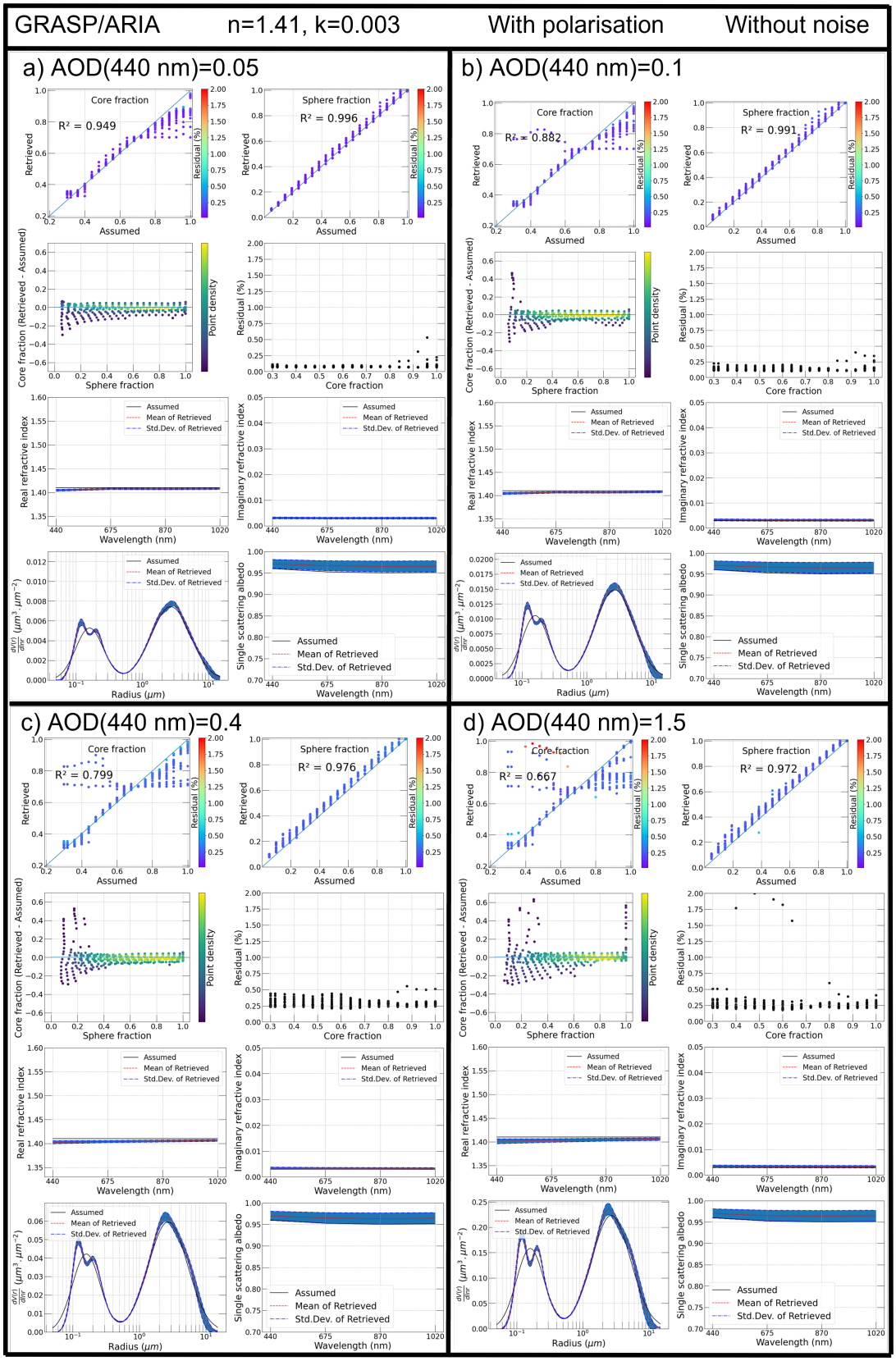

Figure A.54: Collection of plots of aerosol optical and microphysical characteristics derived by inversion of synthetic AERONET measurements. The case of bimodal aerosol size distribution and of refractive index n=1.41 and k=0.003. The radiances, are generated and inverted using GRASP/ARIA (with inhomogeneous aerosol model), simulation of measurements noise is not included and polarisation is included. In panels, the AOD at 440 nm are a) 0.05, b) 0.1, c) 0.4, d) 1.5.

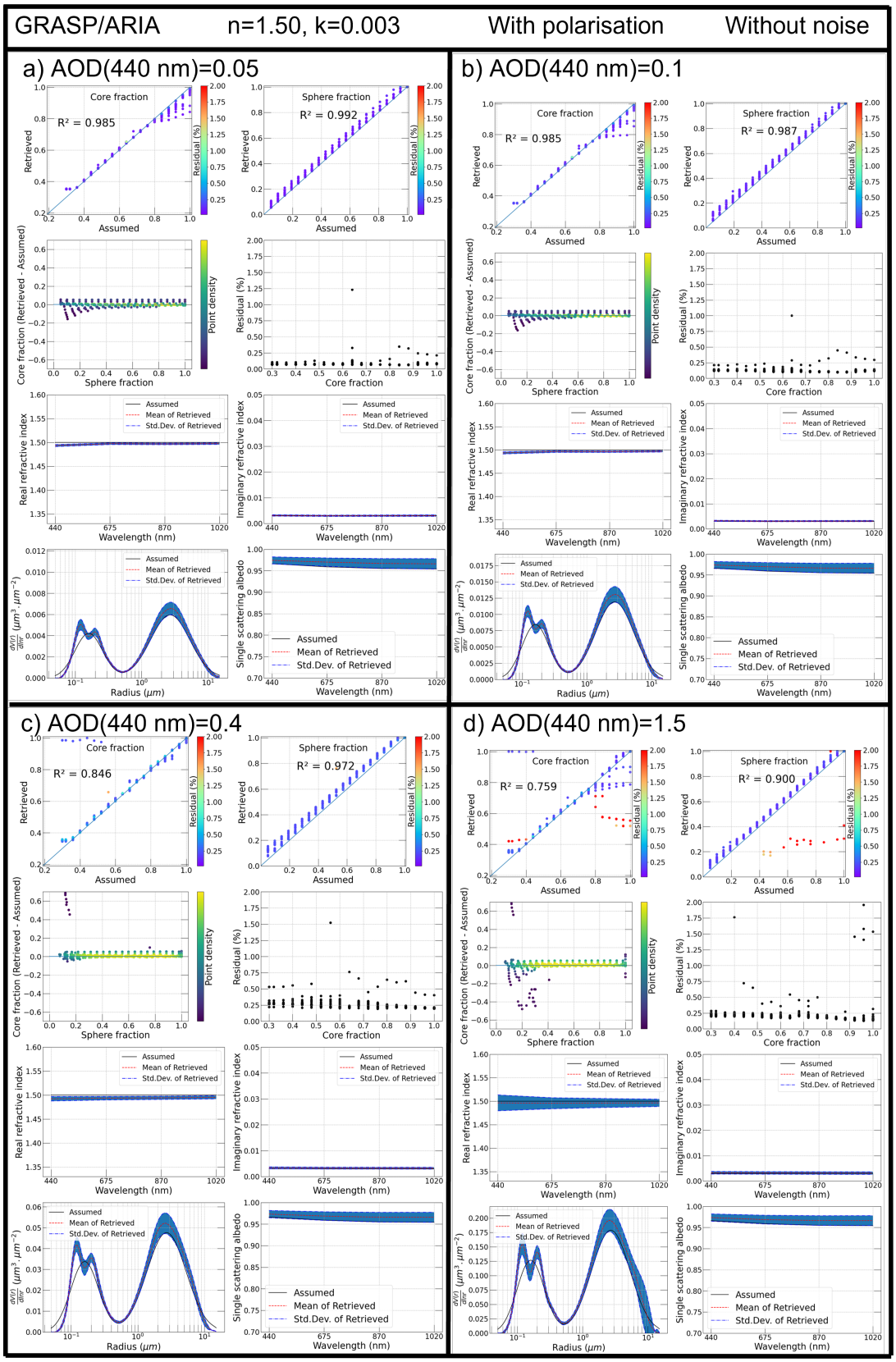

Figure A.55: Collection of plots of aerosol optical and microphysical characteristics derived by inversion of synthetic AERONET measurements. The case of bimodal aerosol size distribution and of refractive index n=1.50 and k=0.003. The radiances, are generated and inverted using GRASP/ARIA (with inhomogeneous aerosol model), simulation of measurements noise is not included and polarisation is included. In panels, the AOD at 440 nm are a) 0.05, b) 0.1, c) 0.4, d) 1.5.

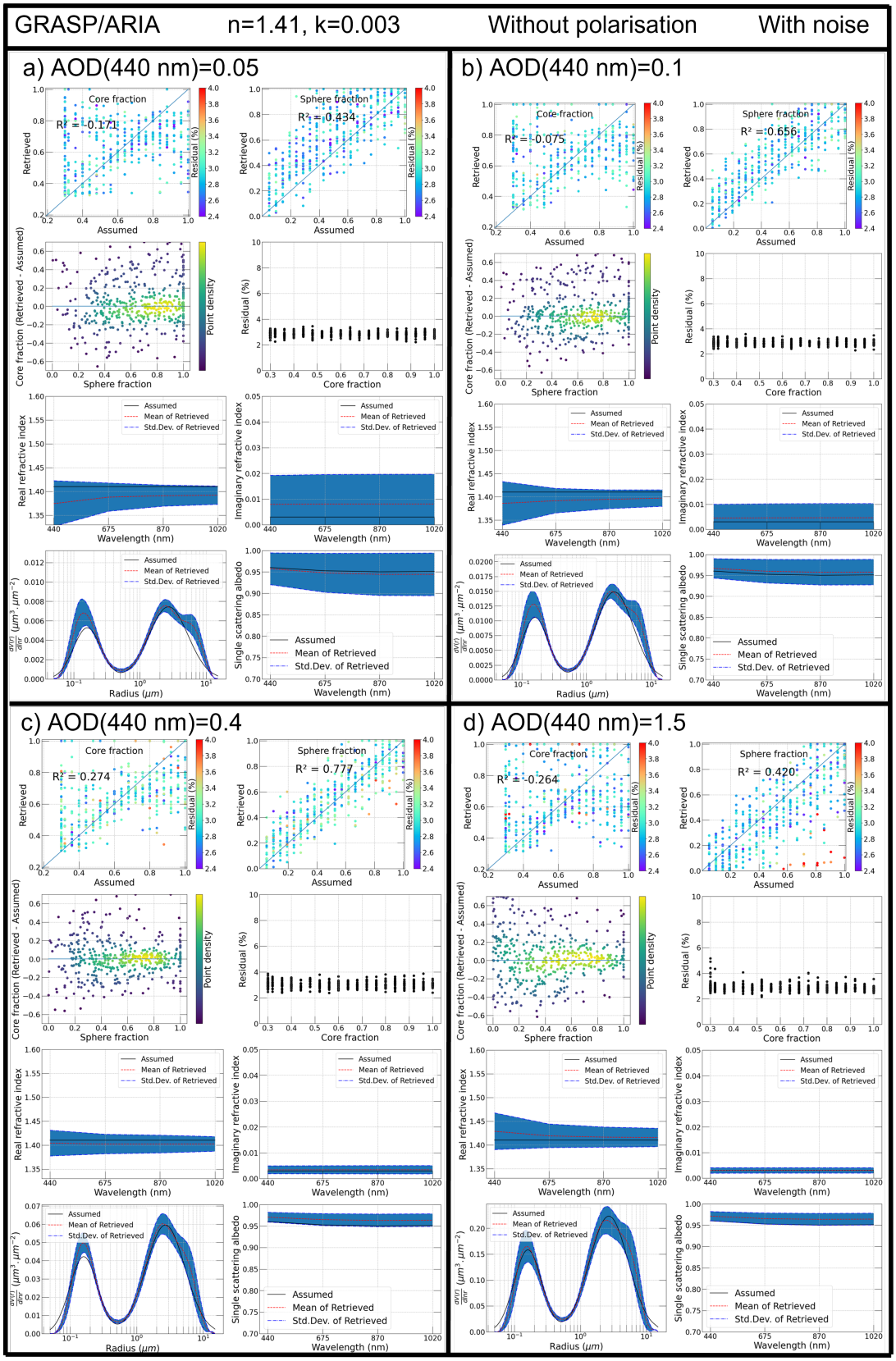

Figure A.56: Collection of plots of aerosol optical and microphysical characteristics derived by inversion of synthetic AERONET measurements. The case of bimodal aerosol size distribution and of refractive index n=1.41 and k=0.003. The radiances, are generated and inverted using GRASP/ARIA (with inhomogeneous aerosol model), simulation of measurements polarisation is not included and noise is included. In panels, the AOD at 440 nm are a) 0.05, b) 0.1, c) 0.4, d) 1.5.

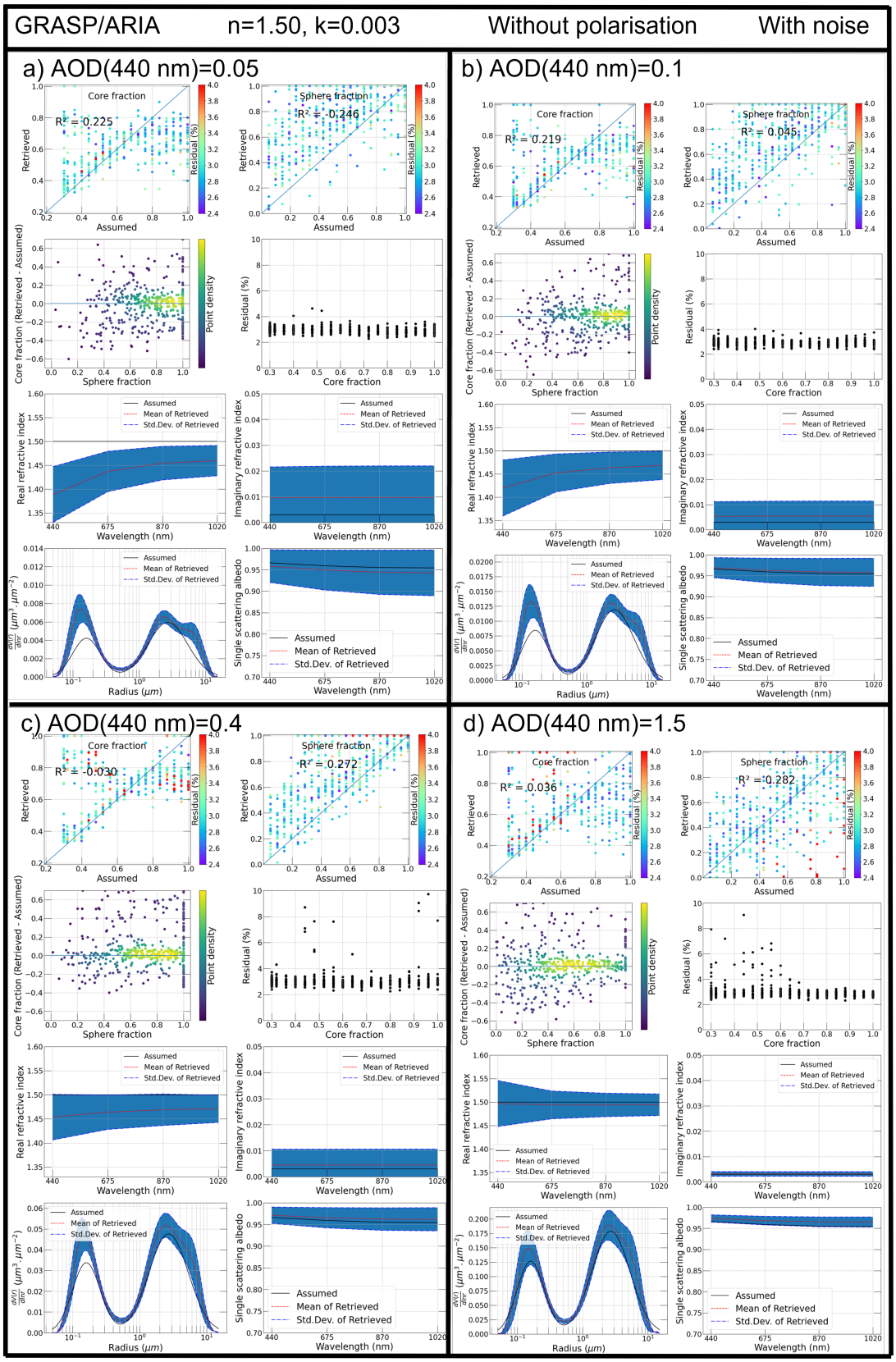

Figure A.57: Collection of plots of aerosol optical and microphysical characteristics derived by inversion of synthetic AERONET measurements. The case of bimodal aerosol size distribution and of refractive index n=1.50 and k=0.003. The radiances, are generated and inverted using GRASP/ARIA (with inhomogeneous aerosol model), simulation of measurements polarisation is not included and noise is included. In panels, the AOD at 440 nm are a) 0.05, b) 0.1, c) 0.4, d) 1.5.

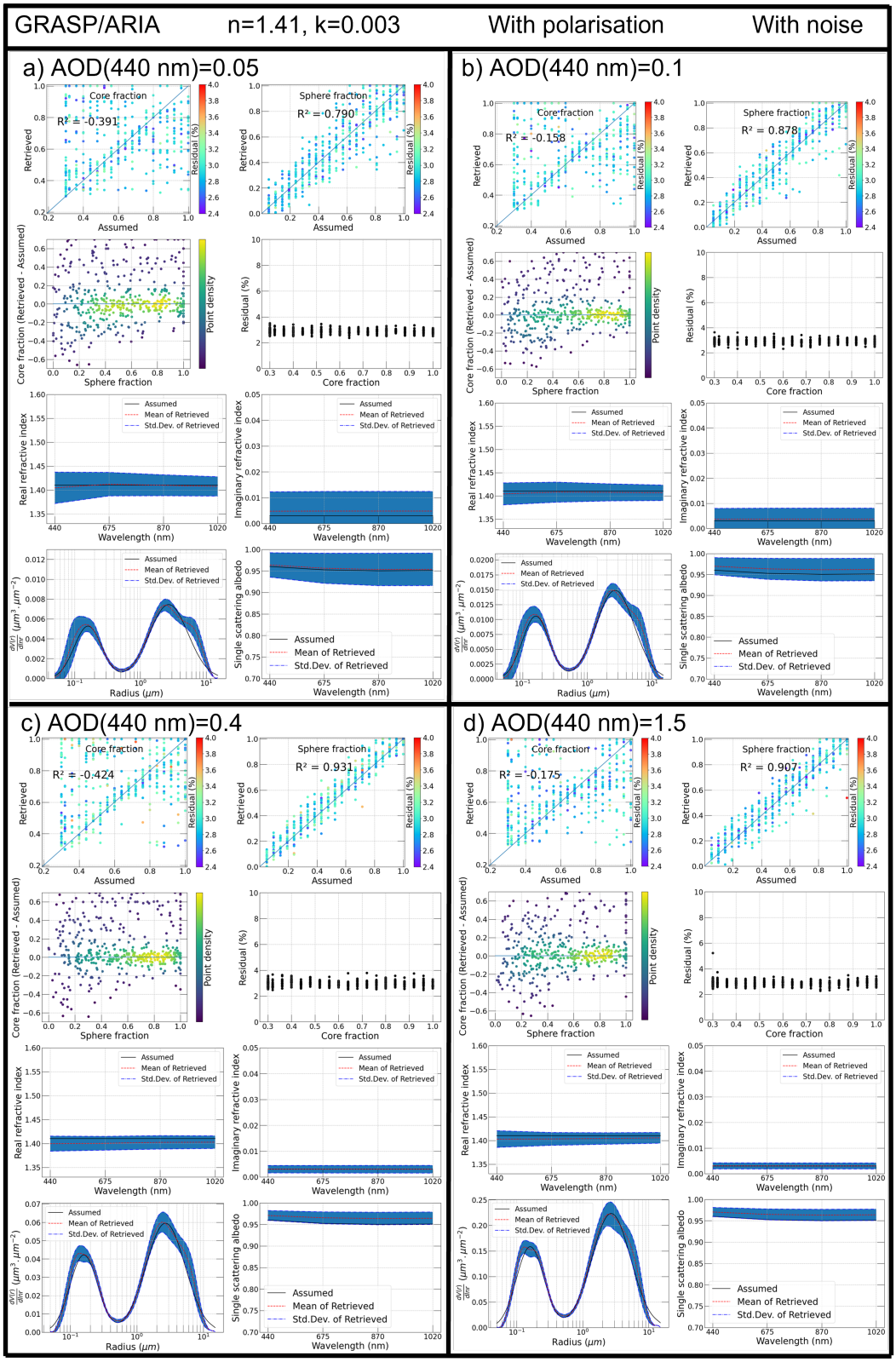

Figure A.58: Collection of plots of aerosol optical and microphysical characteristics derived by inversion of synthetic AERONET measurements. The case of bimodal aerosol size distribution and of refractive index n=1.41 and k=0.003. The radiances, are generated and inverted using GRASP/ARIA (with inhomogeneous aerosol model), simulation of measurements noise and polarisation are included. In panels, the AOD at 440 nm are a) 0.05, b) 0.1, c) 0.4, d) 1.5.

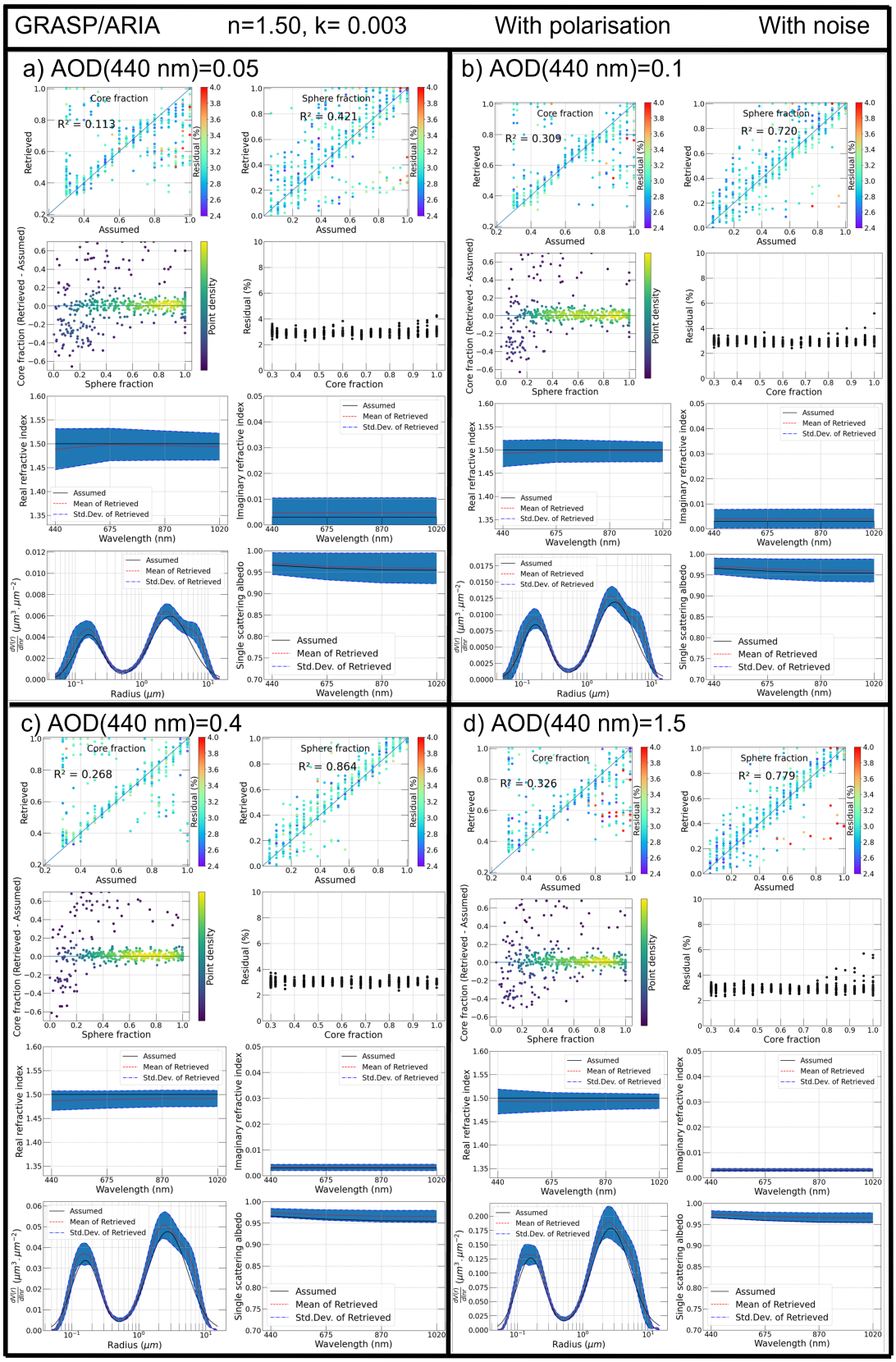

Figure A.59: Collection of plots of aerosol optical and microphysical characteristics derived by inversion of synthetic AERONET measurements. The case of bimodal aerosol size distribution and of refractive index n=1.50 and k=0.003. The radiances, are generated and inverted using GRASP/ARIA (with inhomogeneous aerosol model), simulation of measurements noise and polarisation are included. In panels, the AOD at 440 nm are a) 0.05, b) 0.1, c) 0.4, d) 1.5.

A.4 GRASP/ARIA application to real AERONET measurements

A.4.1 Relative humidities

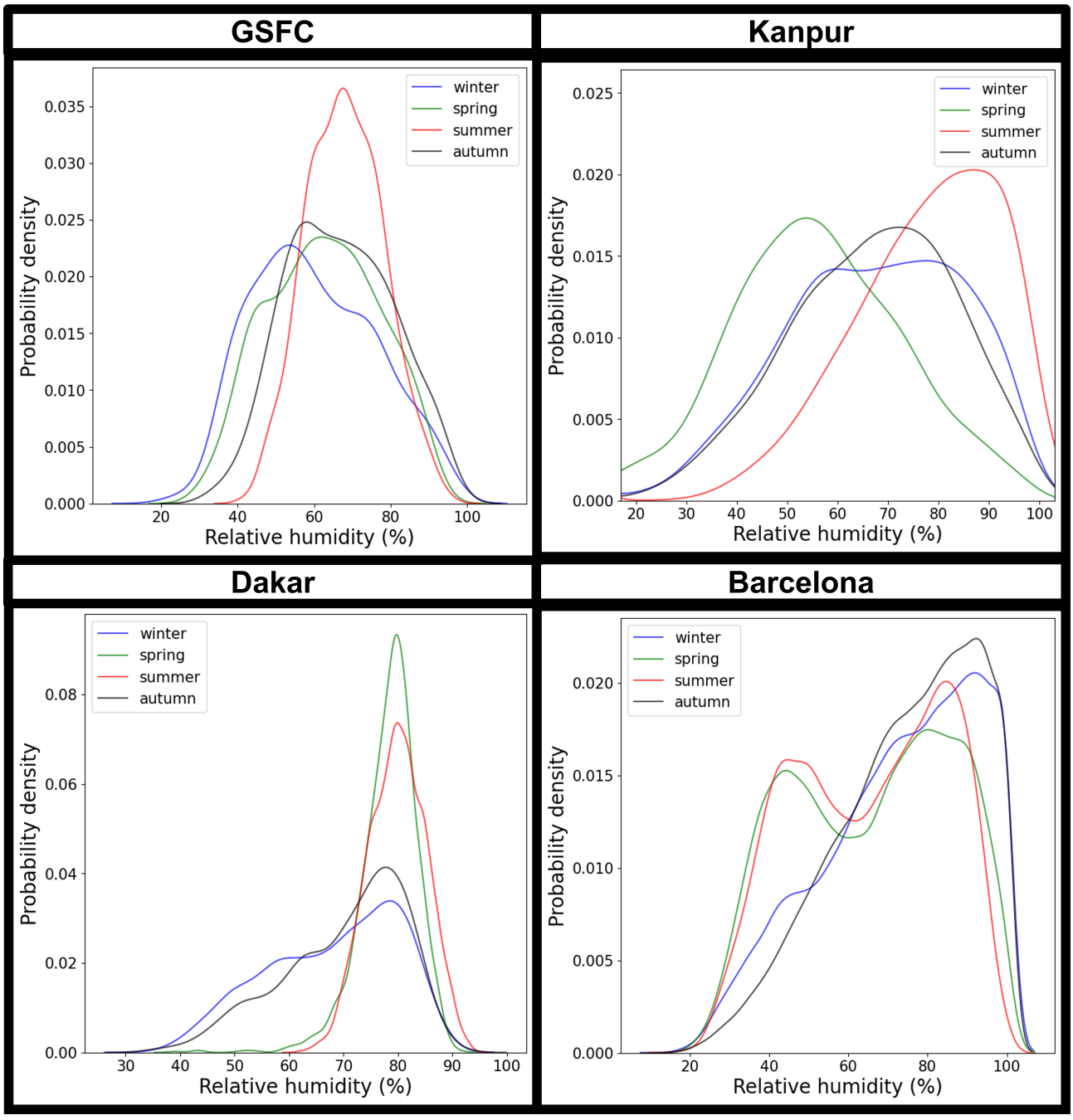

Figure A.60: Probability density of seasonal relative humidity for the AERONET sites of GSFC, Kanpur, Dakar and Barcelona.

A.4.2 Complementary figures

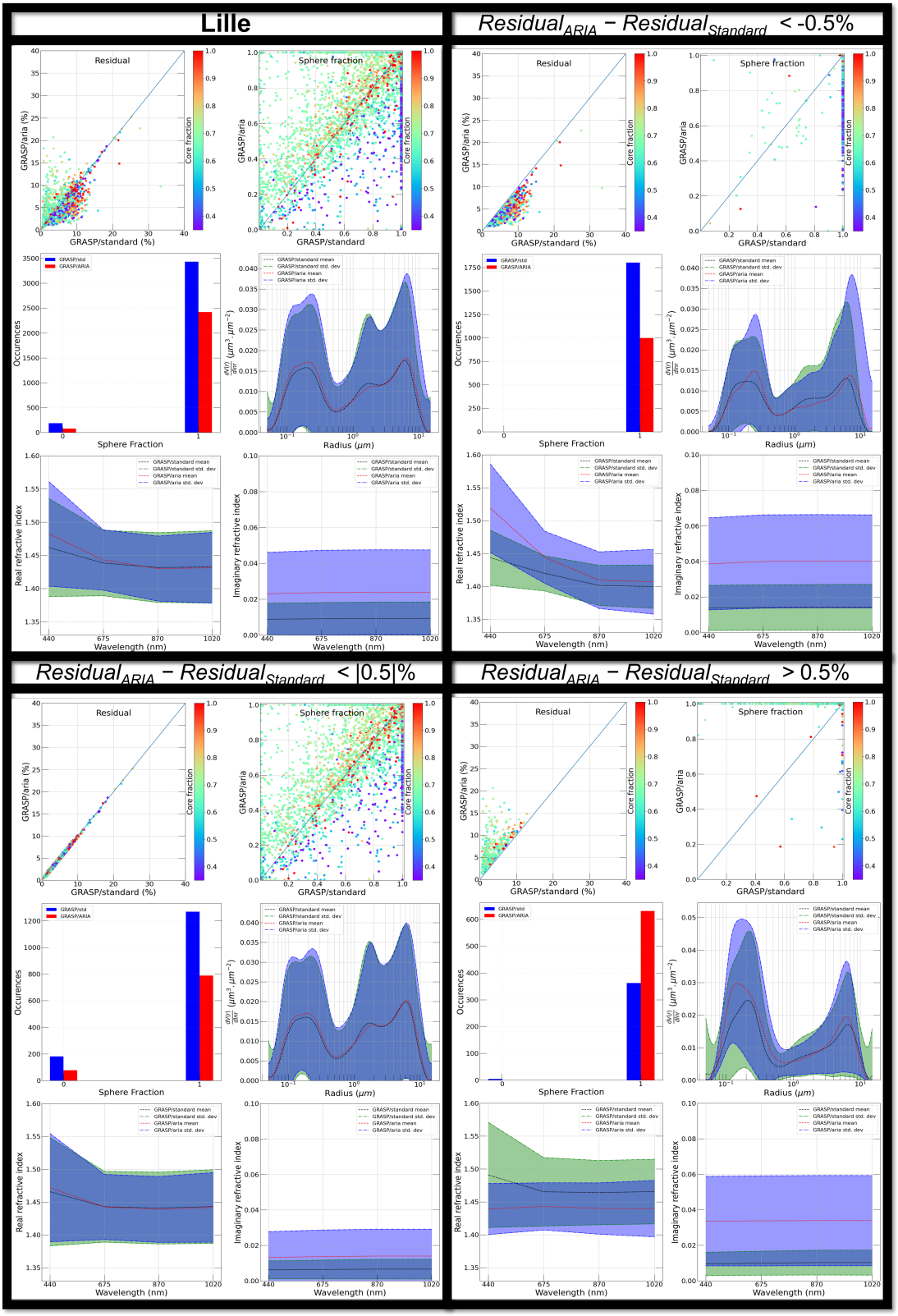

Figure A.61: Collection of plots of aerosol optical and microphysical characteristics derived by inversion of measurements from the AERONET site of Lille. The comparison is made between the retrievals from two models - GRASP/ARIA (with inhomogeneity) and GRASP/Standard (only homogeneous). Panel with the site name uses all measurements, the other panels are filtered by the quality of radiance retrieval of GRASP/ARIA relative to GRASP/Standard. In optical and microphysical characteristic plots, red is for GRASP/ARIA (StDev - shaded in blue), black is for GRASP/Standard (StDev - shaded in green).

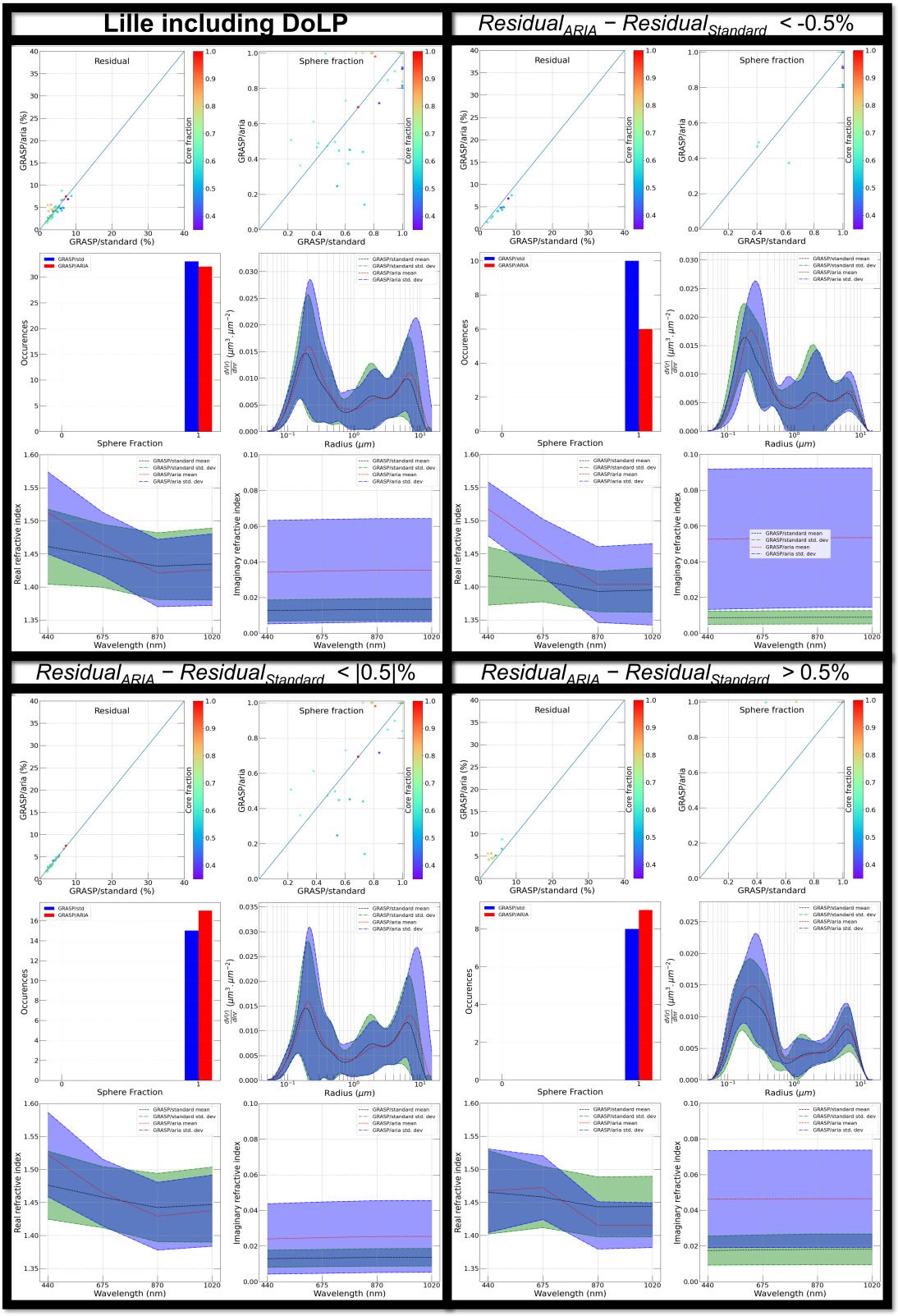

Figure A.62: Collection of plots of aerosol optical and microphysical characteristics derived by inversion of measurements from the AERONET site of Lille including information on light polarisation. The comparison is made between the retrievals from two models - GRASP/ARIA (with inhomogeneity) and GRASP/Standard (only homogeneous). Panel with the site name uses all measurements, the other panels are filtered by the quality of radiance retrieval of GRASP/ARIA relative to GRASP/Standard. In optical and microphysical characteristic plots, red is for GRASP/ARIA (StDev - shaded in blue), black is for GRASP/Standard (StDev - shaded in green).

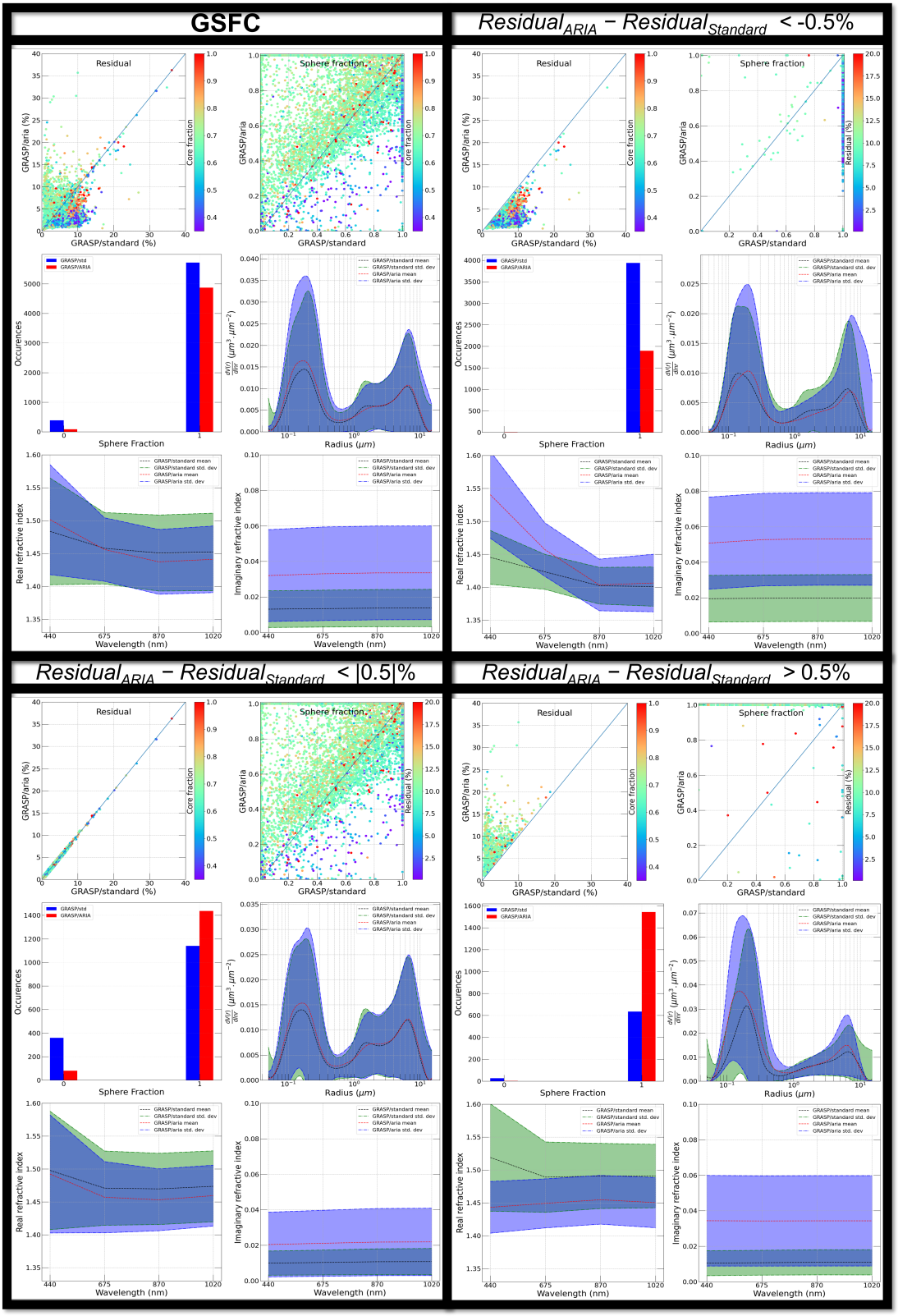

Figure A.63: Collection of plots of aerosol optical and microphysical characteristics derived by inversion of measurements from the AERONET site of GSFC. The comparison is made between the retrievals from two models - GRASP/ARIA (with inhomogeneity) and GRASP/Standard (only homogeneous). Panel with the site name uses all measurements, the other panels are filtered by the quality of radiance retrieval of GRASP/ARIA relative to GRASP/Standard. In optical and microphysical characteristic plots, red is for GRASP/ARIA (StDev - shaded in blue), black is for GRASP/Standard (StDev - shaded in green).

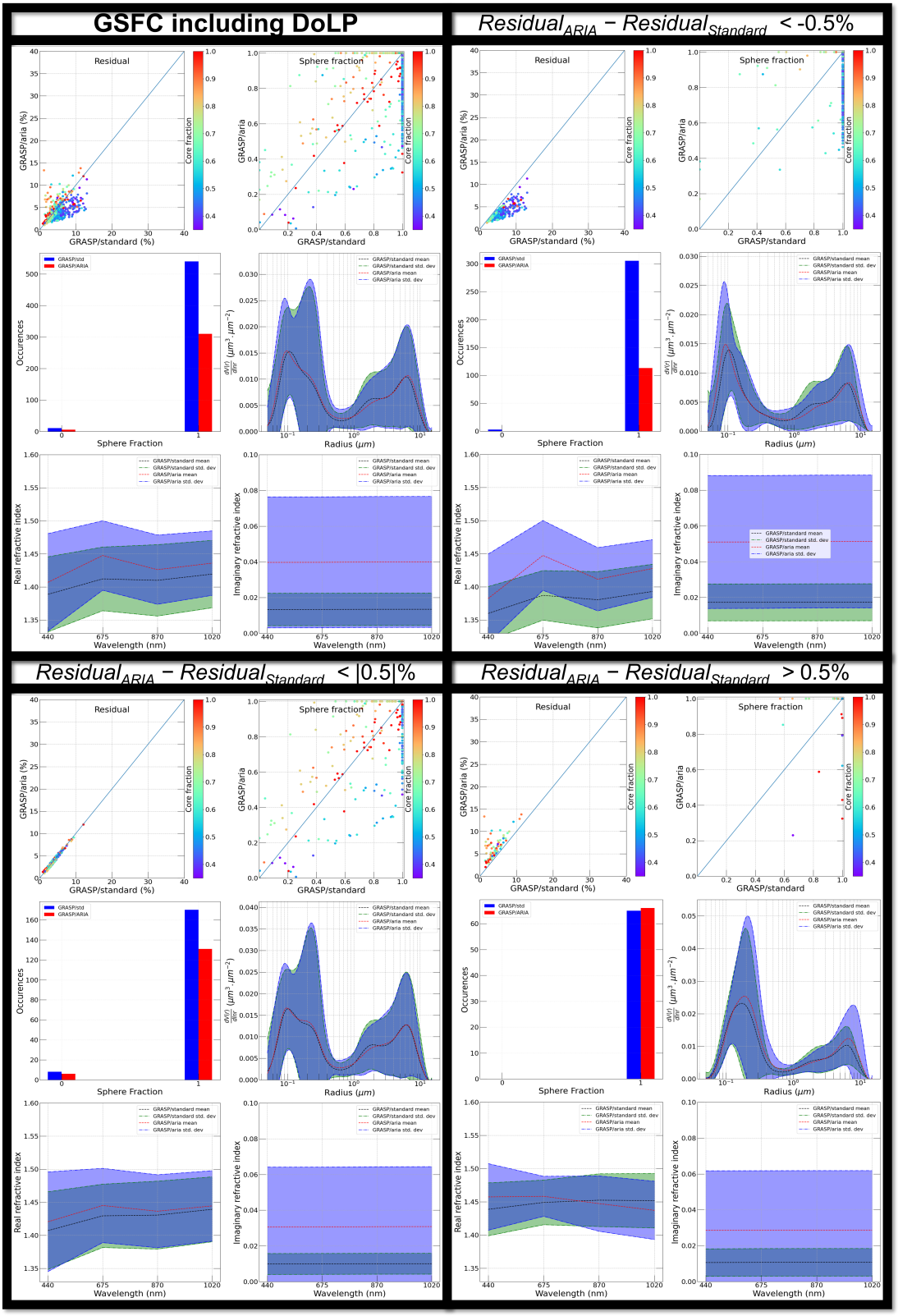

Figure A.64: Collection of plots of aerosol optical and microphysical characteristics derived by inversion of measurements from the AERONET site of GSFC including information on light polarisation. The comparison is made between the retrievals from two models - GRASP/ARIA (with inhomogeneity) and GRASP/Standard (only homogeneous). Panel with the site name uses all measurements, the other panels are filtered by the quality of radiance retrieval of GRASP/ARIA relative to GRASP/Standard. In optical and microphysical characteristic plots, red is for GRASP/ARIA (StDev - shaded in blue), black is for GRASP/Standard (StDev - shaded in green).

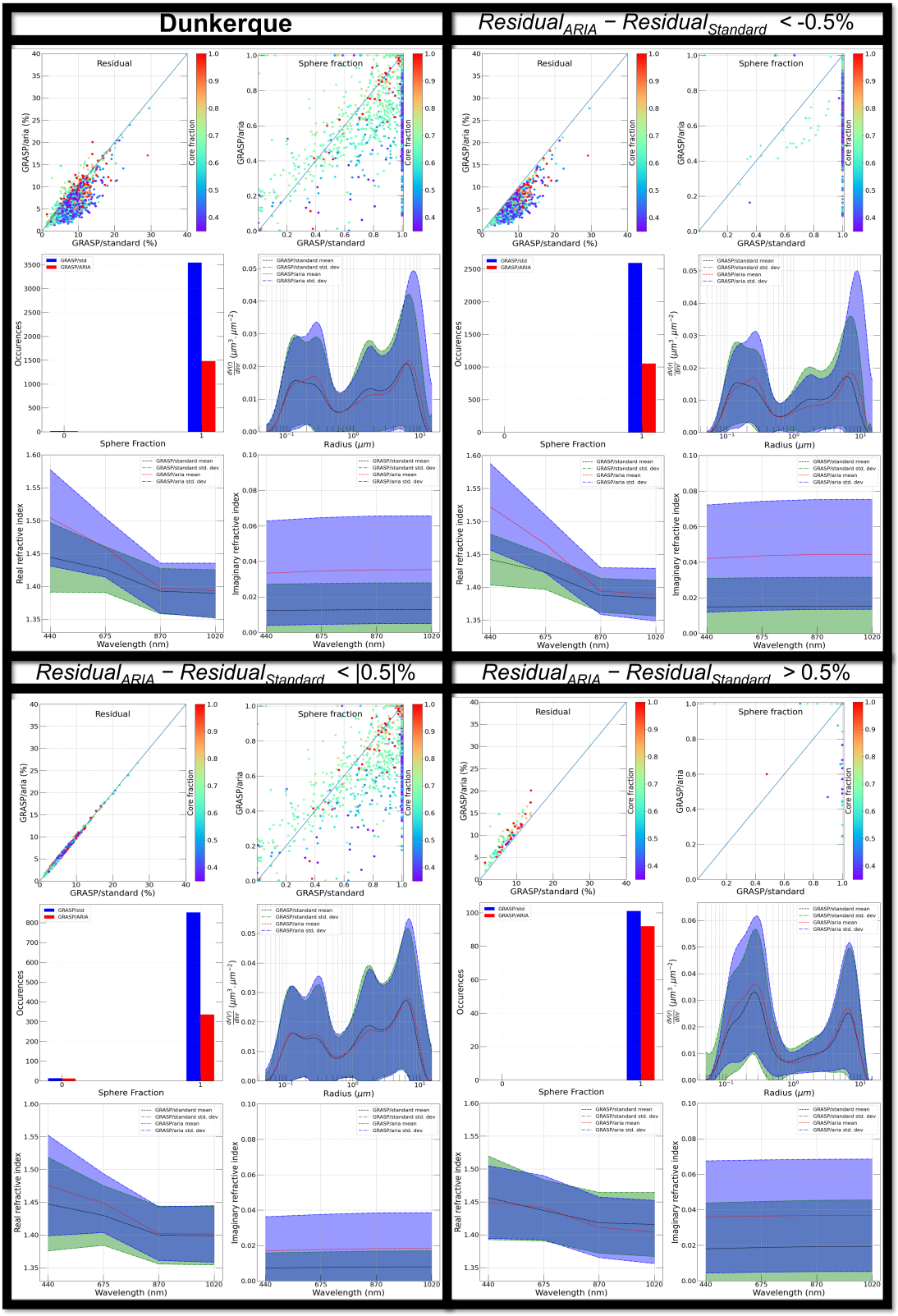

Figure A.65: Collection of plots of aerosol optical and microphysical characteristics derived by inversion of measurements from the AERONET site of Dunkerque. The comparison is made between the retrievals from two models - GRASP/ARIA (with inhomogeneity) and GRASP/Standard (only homogeneous). Panel with the site name uses all measurements, the other panels are filtered by the quality of radiance retrieval of GRASP/ARIA relative to GRASP/Standard. In optical and microphysical characteristic plots, red is for GRASP/ARIA (StDev - shaded in blue), black is for GRASP/Standard (StDev - shaded in green).

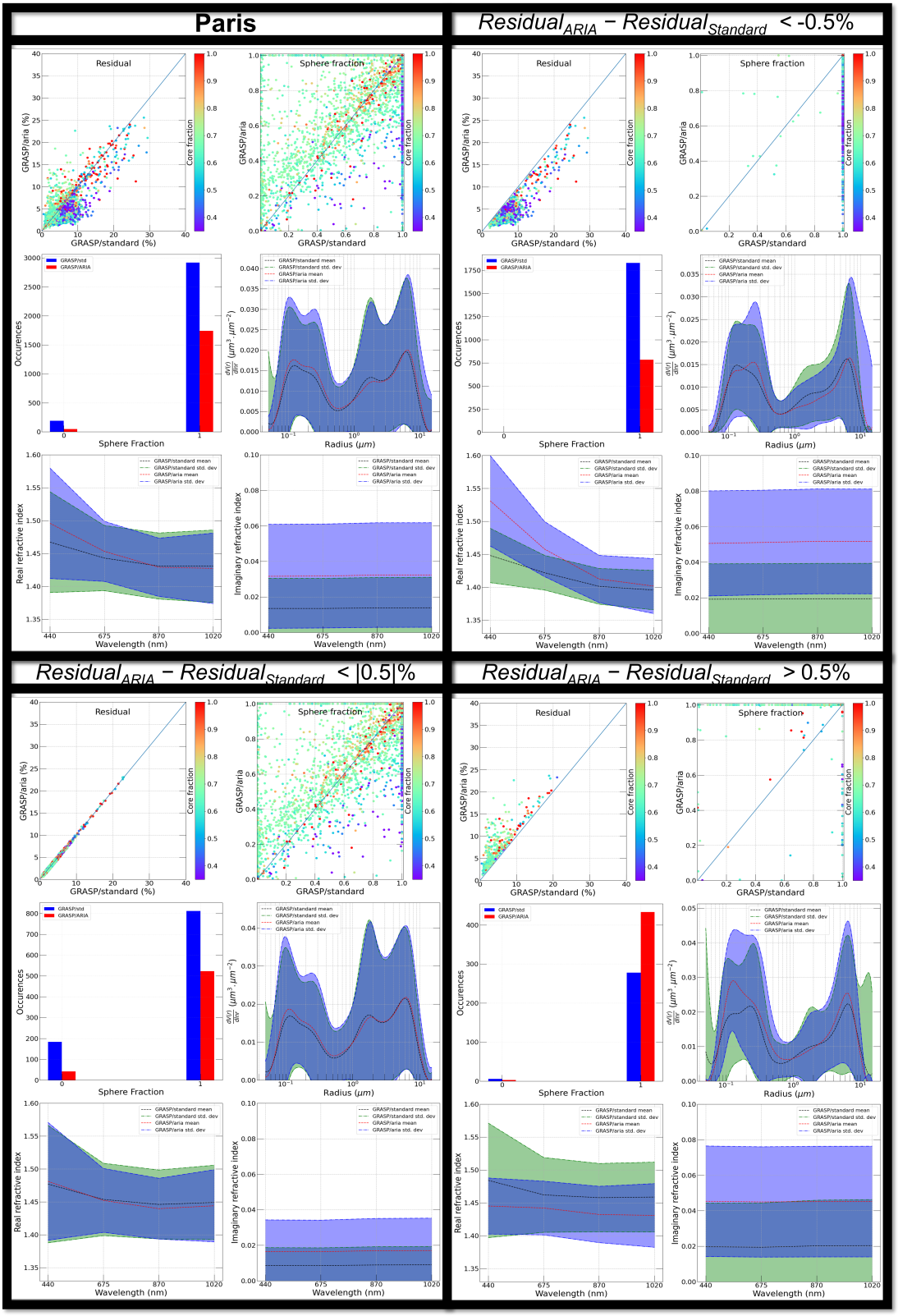

Figure A.66: Collection of plots of aerosol optical and microphysical characteristics derived by inversion of measurements from the AERONET site of Paris. The comparison is made between the retrievals from two models - GRASP/ARIA (with inhomogeneity) and GRASP/Standard (only homogeneous). Panel with the site name uses all measurements, the other panels are filtered by the quality of radiance retrieval of GRASP/ARIA relative to GRASP/Standard. In optical and microphysical characteristic plots, red is for GRASP/ARIA (StDev - shaded in blue), black is for GRASP/Standard (StDev - shaded in green).

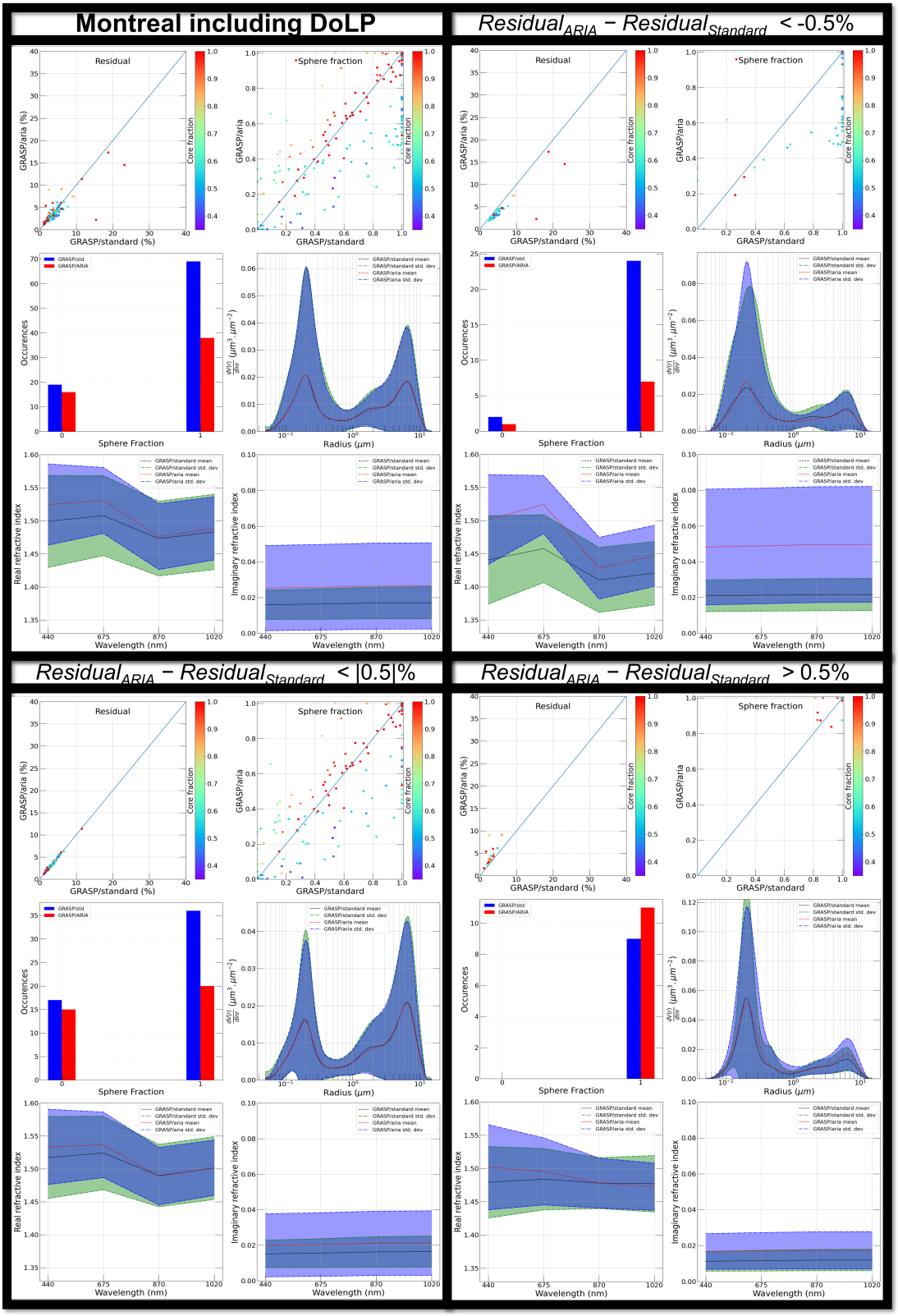

Figure A.67: Collection of plots of aerosol optical and microphysical characteristics derived by inversion of measurements from the AERONET site of Montreal including information on light polarisation. The comparison is made between the retrievals from two models - GRASP/ARIA (with inhomogeneity) and GRASP/Standard (only homogeneous). Panel with the site name uses all measurements, the other panels are filtered by the quality of radiance retrieval of GRASP/ARIA relative to GRASP/Standard. In optical and microphysical characteristic plots, red is for GRASP/ARIA (StDev - shaded in blue), black is for GRASP/Standard (StDev - shaded in green).

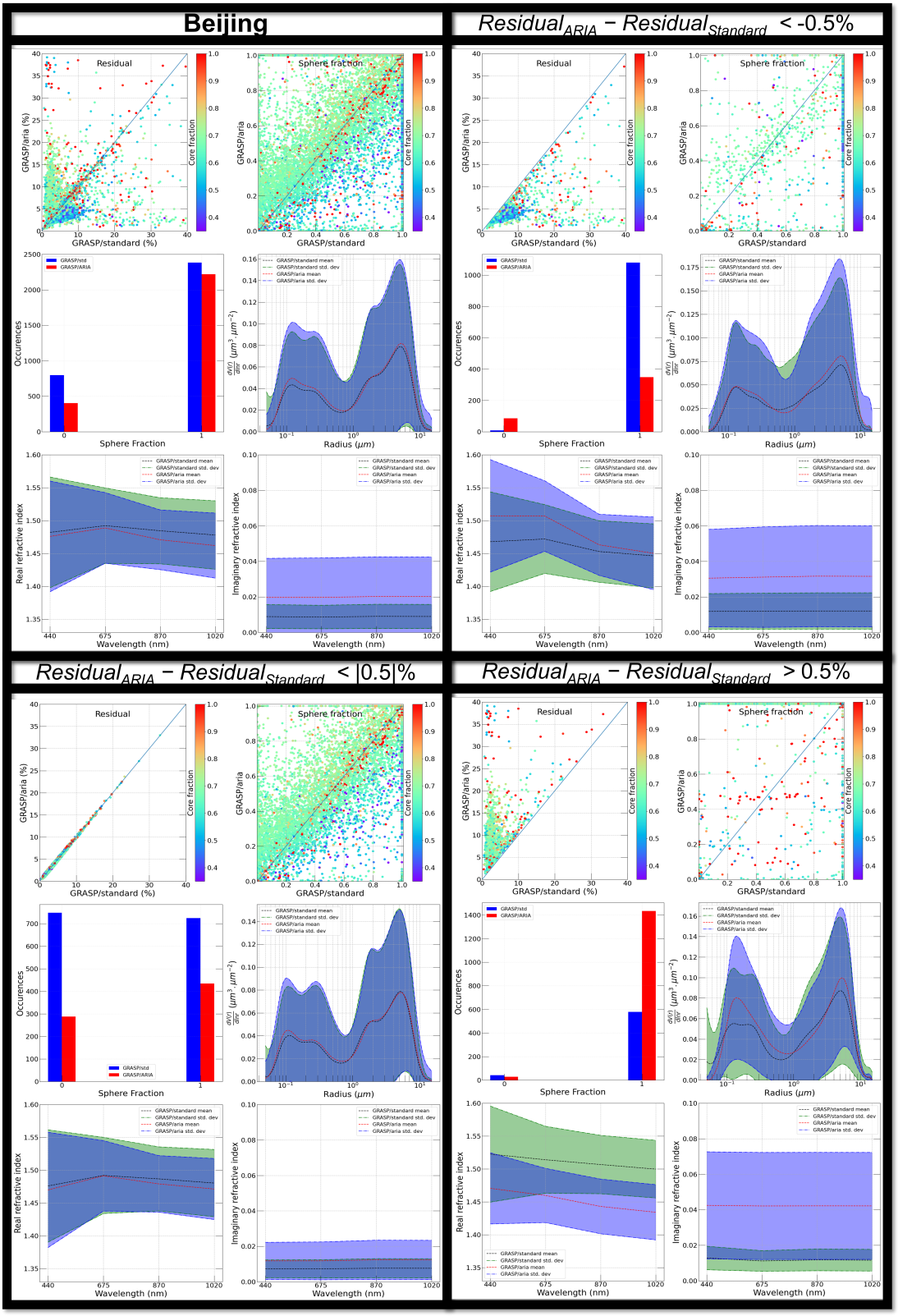

Figure A.68: Collection of plots of aerosol optical and microphysical characteristics derived by inversion of measurements from the AERONET site of Beijing. The comparison is made between the retrievals from two models - GRASP/ARIA (with inhomogeneity) and GRASP/Standard (only homogeneous). Panel with the site name uses all measurements, the other panels are filtered by the quality of radiance retrieval of GRASP/ARIA relative to GRASP/Standard. In optical and microphysical characteristic plots, red is for GRASP/ARIA (StDev - shaded in blue), black is for GRASP/Standard (StDev - shaded in green).

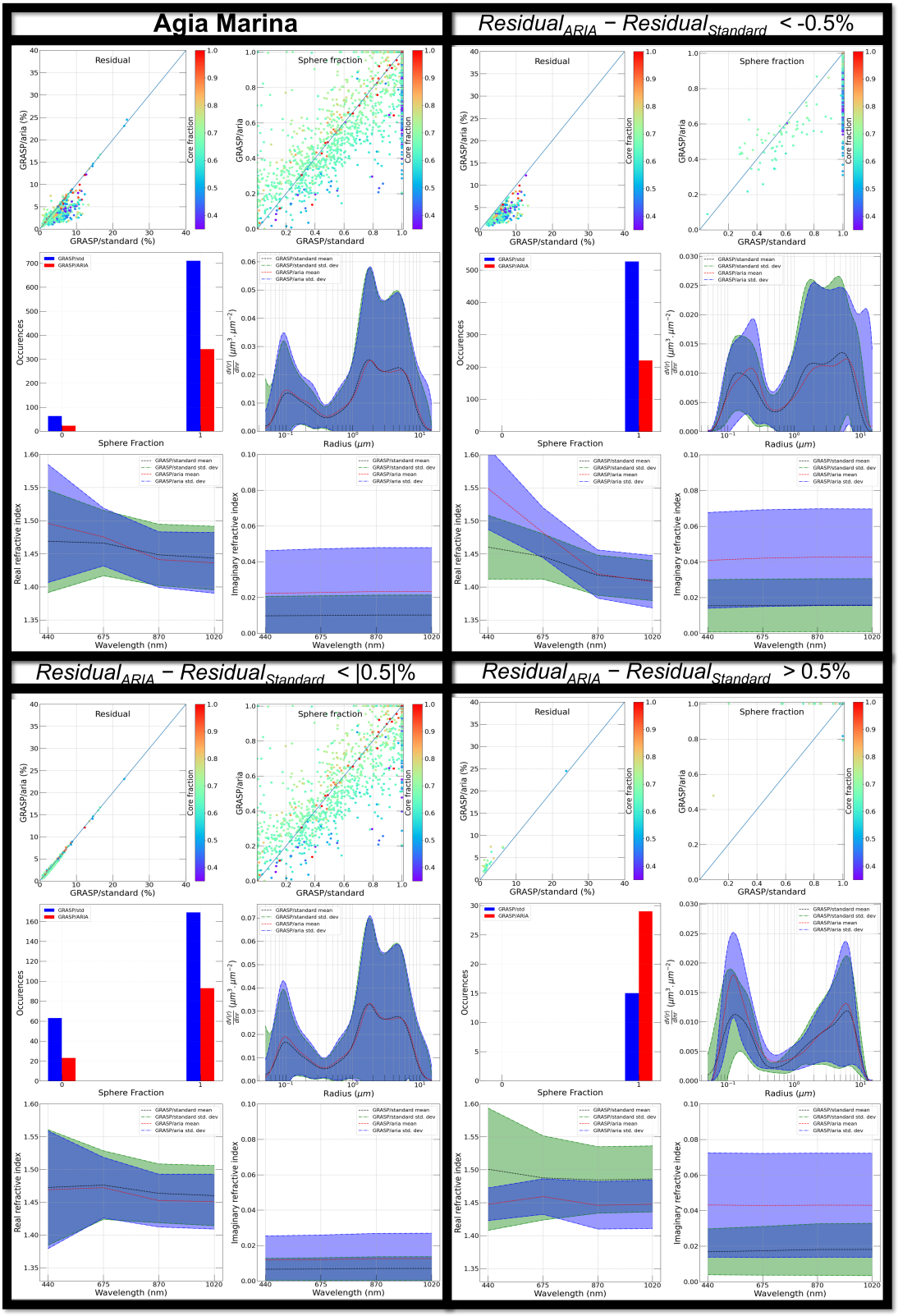

Figure A.69: Collection of plots of aerosol optical and microphysical characteristics derived by inversion of measurements from the AERONET site of Agia Marina. The comparison is made between the retrievals from two models - GRASP/ARIA (with inhomogeneity) and GRASP/Standard (only homogeneous). Panel with the site name uses all measurements, the other panels are filtered by the quality of radiance retrieval of GRASP/ARIA relative to GRASP/Standard. In optical and microphysical characteristic plots, red is for GRASP/ARIA (StDev - shaded in blue), black is for GRASP/Standard (StDev - shaded in green).

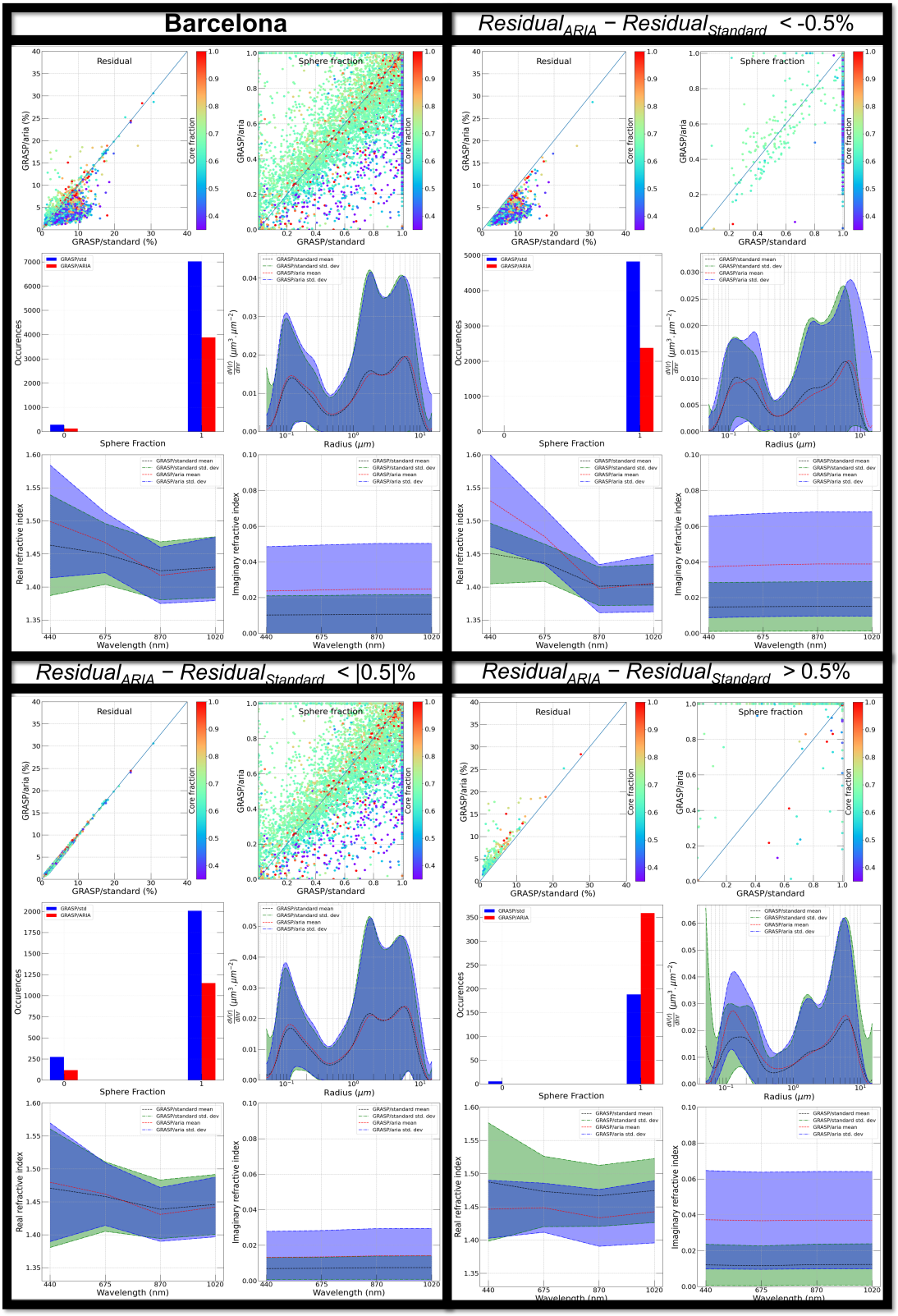

Figure A.70: Collection of plots of aerosol optical and microphysical characteristics derived by inversion of measurements from the AERONET site of Barcelona. The comparison is made between the retrievals from two models - GRASP/ARIA (with inhomogeneity) and GRASP/Standard (only homogeneous). Panel with the site name uses all measurements, the other panels are filtered by the quality of radiance retrieval of GRASP/ARIA relative to GRASP/Standard. In optical and microphysical characteristic plots, red is for GRASP/ARIA (StDev - shaded in blue), black is for GRASP/Standard (StDev - shaded in green).

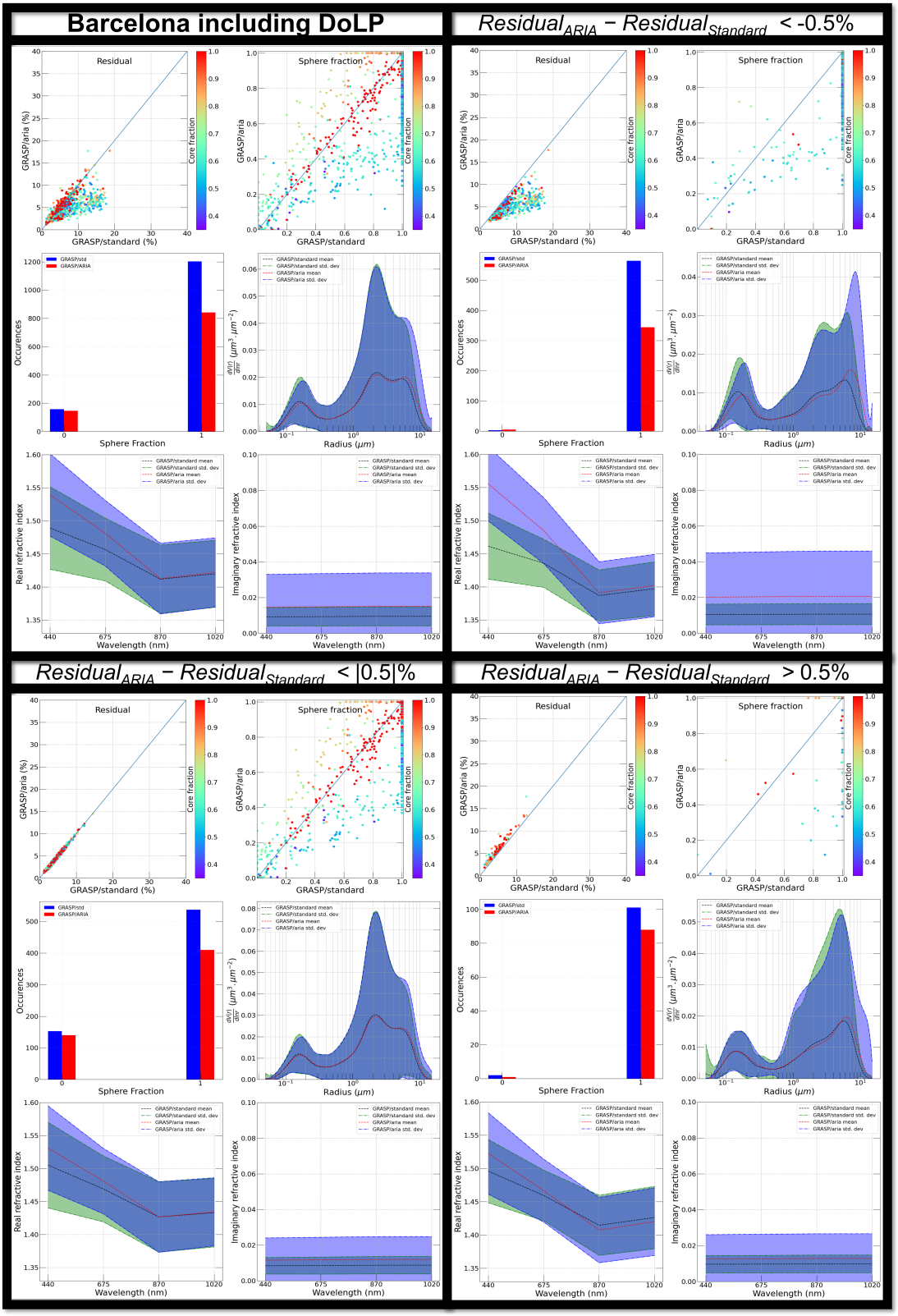

Figure A.71: Collection of plots of aerosol optical and microphysical characteristics derived by inversion of measurements from the AERONET site of Barcelona including information on light polarisation. The comparison is made between the retrievals from two models - GRASP/ARIA (with inhomogeneity) and GRASP/Standard (only homogeneous). Panel with the site name uses all measurements, the other panels are filtered by the quality of radiance retrieval of GRASP/ARIA relative to GRASP/Standard. In optical and microphysical characteristic plots, red is for GRASP/ARIA (StDev - shaded in blue), black is for GRASP/Standard (StDev - shaded in green).

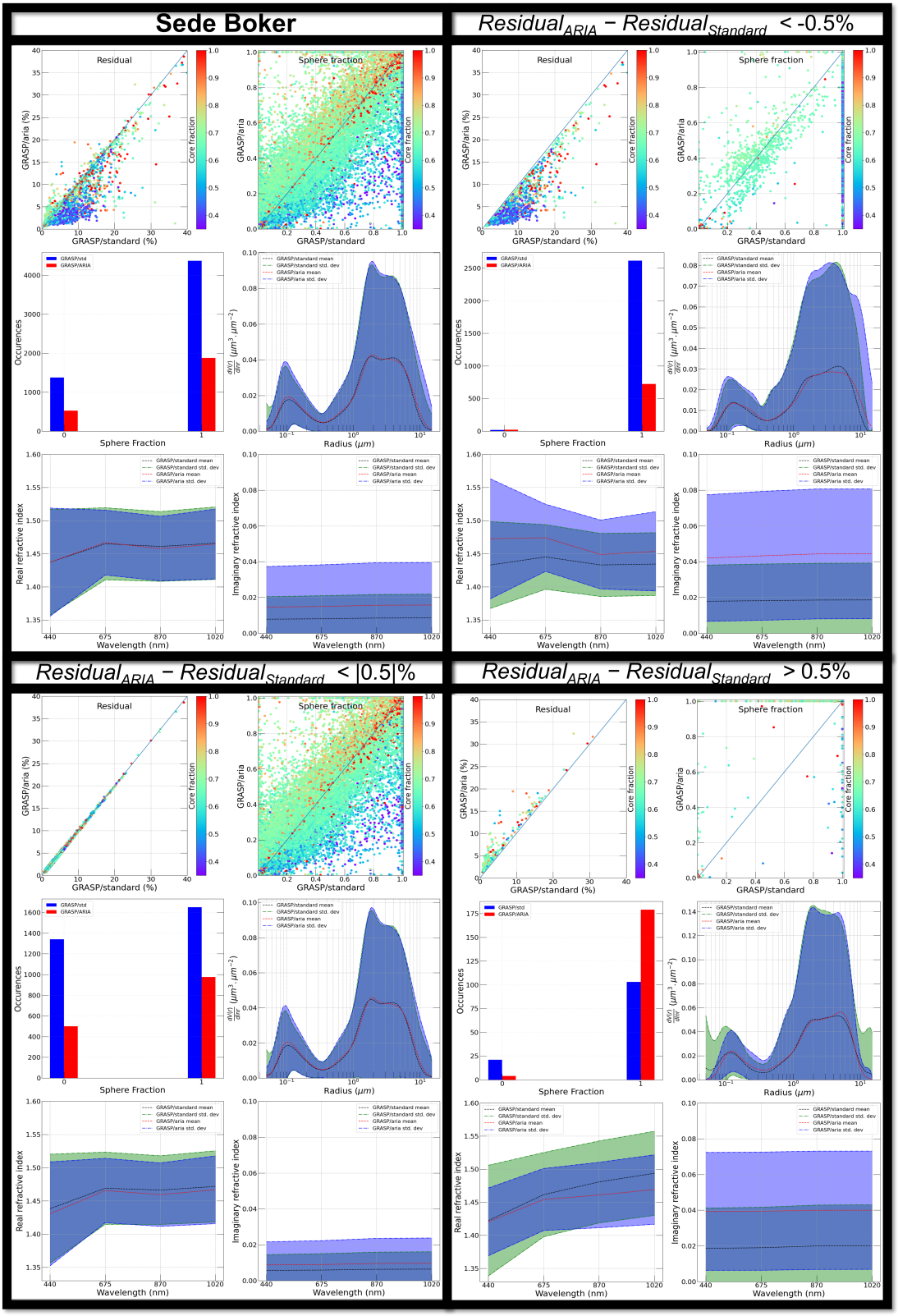

Figure A.72: Collection of plots of aerosol optical and microphysical characteristics derived by inversion of measurements from the AERONET site of Sede Boker. The comparison is made between the retrievals from two models - GRASP/ARIA (with inhomogeneity) and GRASP/Standard (only homogeneous). Panel with the site name uses all measurements, the other panels are filtered by the quality of radiance retrieval of GRASP/ARIA relative to GRASP/Standard. In optical and microphysical characteristic plots, red is for GRASP/ARIA (StDev - shaded in blue), black is for GRASP/Standard (StDev - shaded in green).

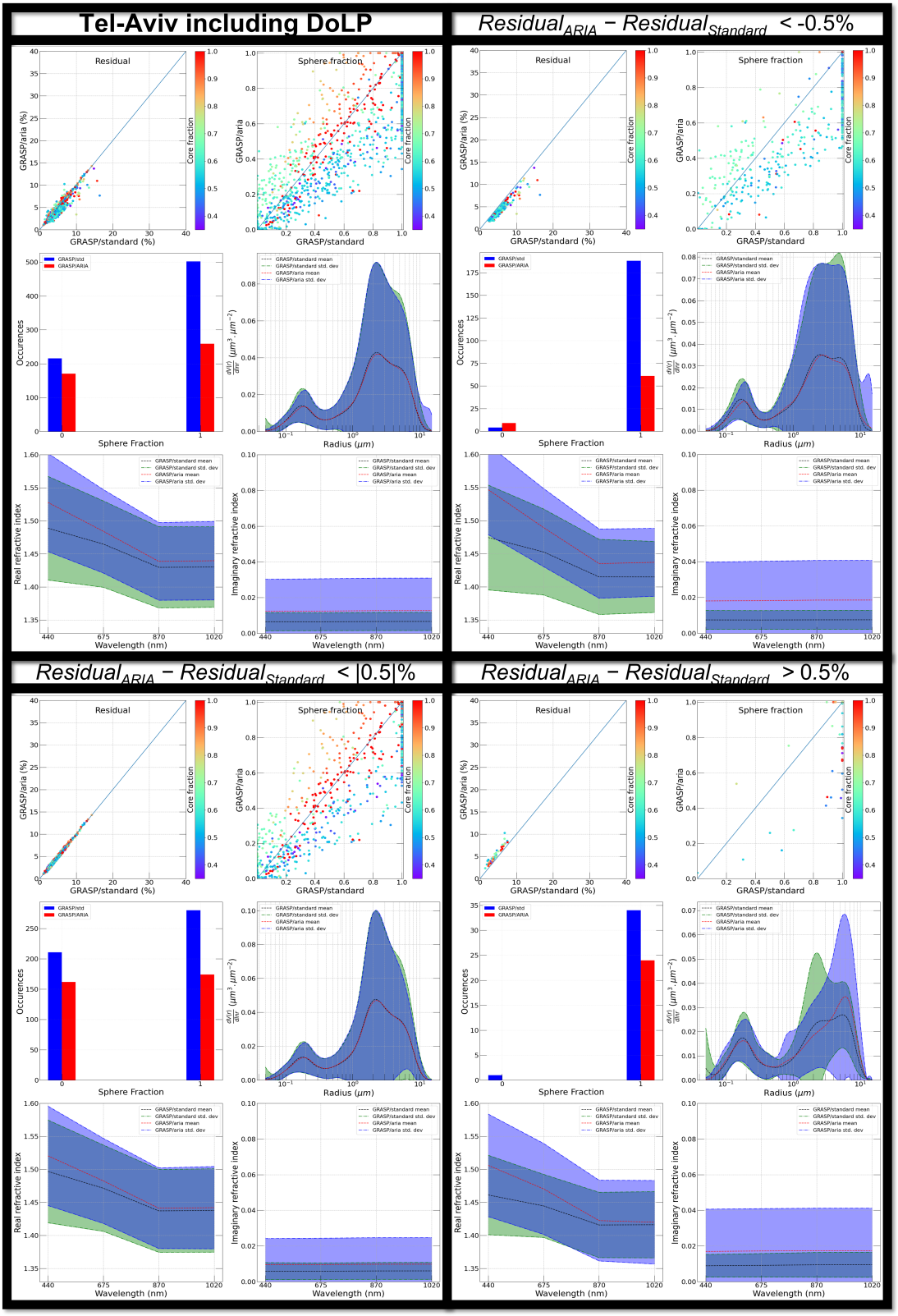

Figure A.73: Collection of plots of aerosol optical and microphysical characteristics derived by inversion of measurements from the AERONET site of Tel-Aviv University including information on light polarisation. The comparison is made between the retrievals from two models - GRASP/ARIA (with inhomogeneity) and GRASP/Standard (only homogeneous). Panel with the site name uses all measurements, the other panels are filtered by the quality of radiance retrieval of GRASP/ARIA relative to GRASP/Standard. In optical and microphysical characteristic plots, red is for GRASP/ARIA (StDev - shaded in blue), black is for GRASP/Standard (StDev - shaded in green).

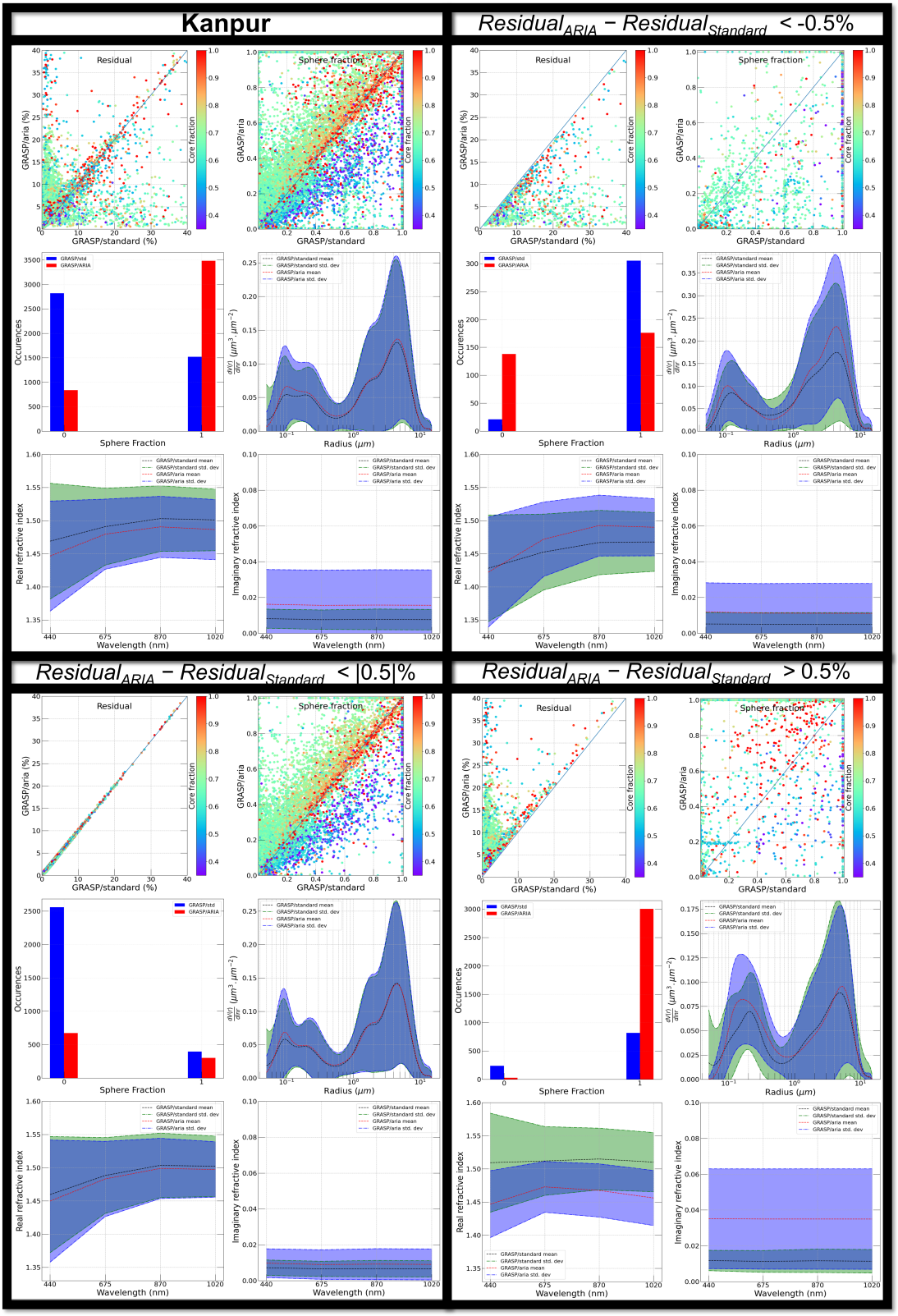

Figure A.74: Collection of plots of aerosol optical and microphysical characteristics derived by inversion of measurements from the AERONET site of Kanpur. The comparison is made between the retrievals from two models - GRASP/ARIA (with inhomogeneity) and GRASP/Standard (only homogeneous). Panel with the site name uses all measurements, the other panels are filtered by the quality of radiance retrieval of GRASP/ARIA relative to GRASP/Standard. In optical and microphysical characteristic plots, red is for GRASP/ARIA (StDev - shaded in blue), black is for GRASP/Standard (StDev - shaded in green).

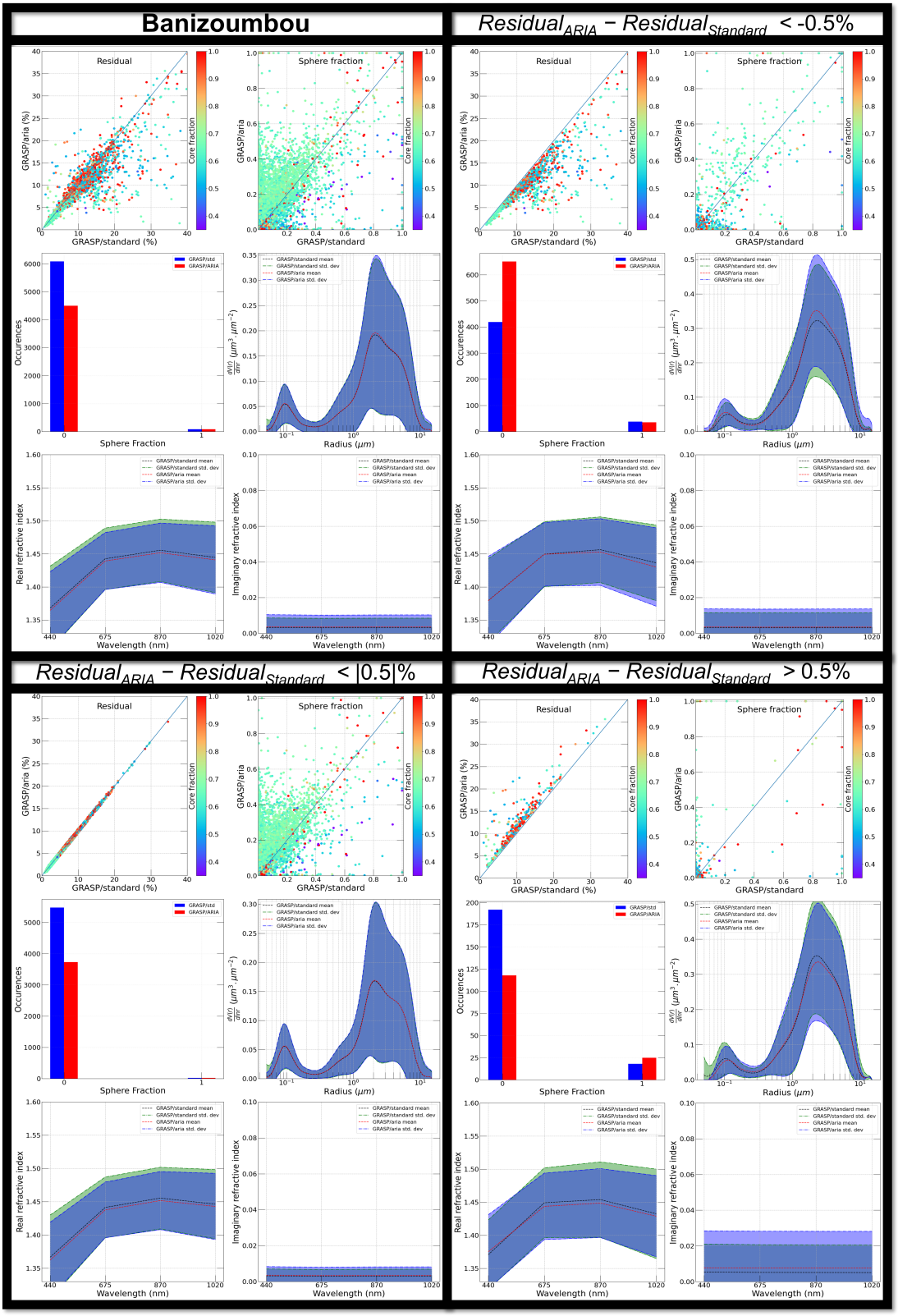

Figure A.75: Collection of plots of aerosol optical and microphysical characteristics derived by inversion of measurements from the AERONET site of Banizoumbou. The comparison is made between the retrievals from two models - GRASP/ARIA (with inhomogeneity) and GRASP/Standard (only homogeneous). Panel with the site name uses all measurements, the other panels are filtered by the quality of radiance retrieval of GRASP/ARIA relative to GRASP/Standard. In optical and microphysical characteristic plots, red is for GRASP/ARIA (StDev - shaded in blue), black is for GRASP/Standard (StDev - shaded in green).

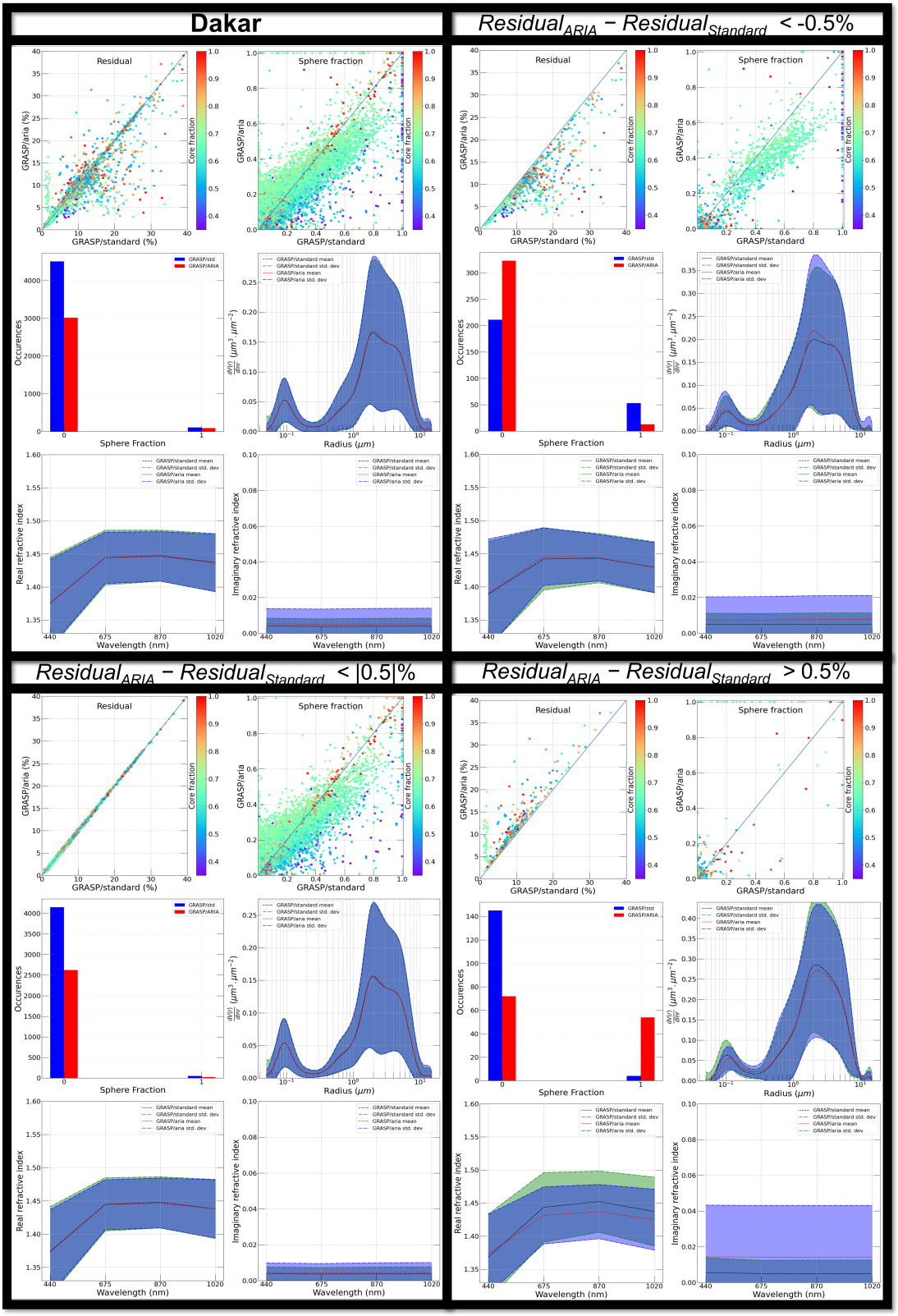

Figure A.76: Collection of plots of aerosol optical and microphysical characteristics derived by inversion of measurements from the AERONET site of Dakar. The comparison is made between the retrievals from two models - GRASP/ARIA (with inhomogeneity) and GRASP/Standard (only homogeneous). Panel with the site name uses all measurements, the other panels are filtered by the quality of radiance retrieval of GRASP/ARIA relative to GRASP/Standard. In optical and microphysical characteristic plots, red is for GRASP/ARIA (StDev - shaded in blue), black is for GRASP/Standard (StDev - shaded in green).

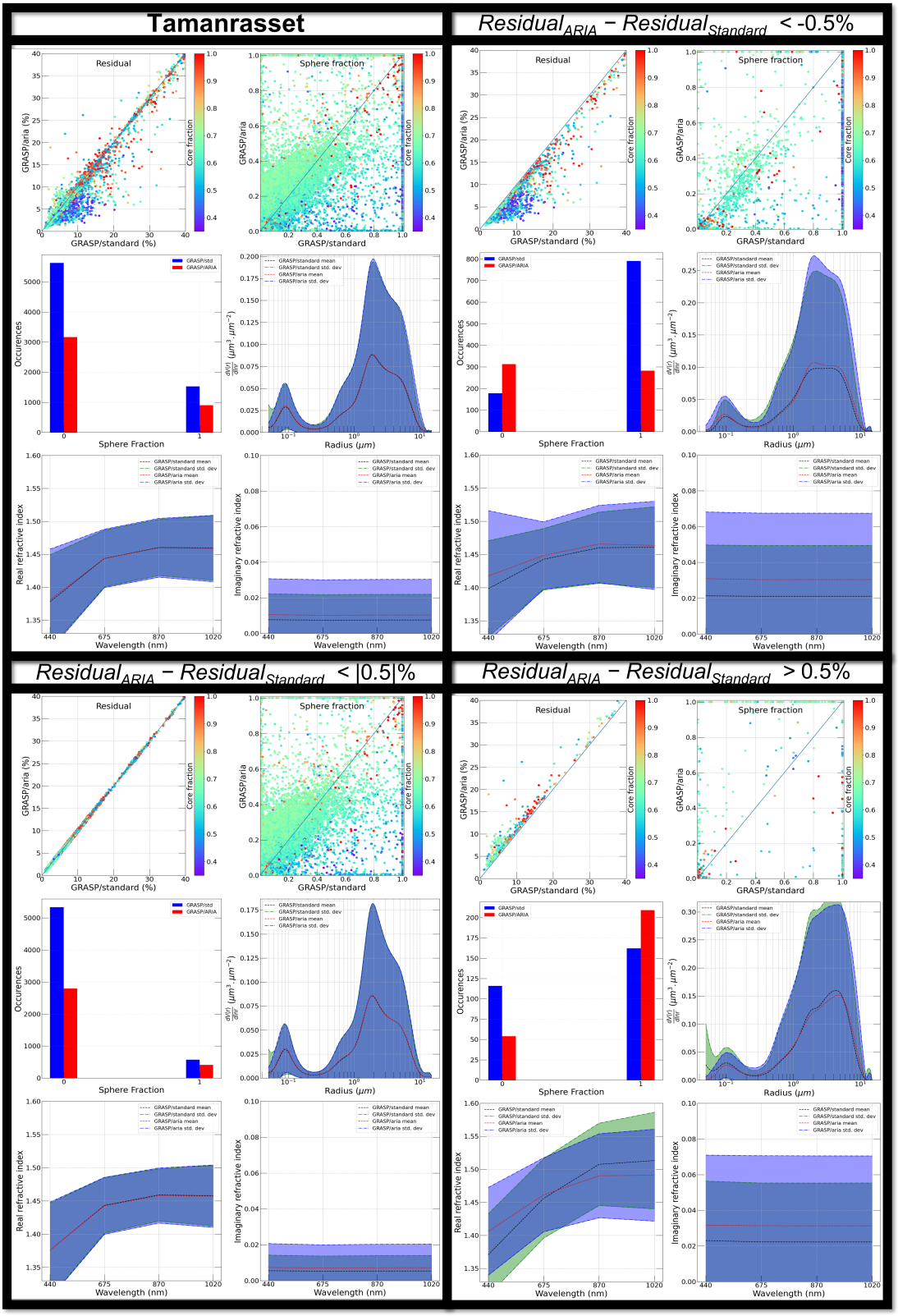

Figure A.77: Collection of plots of aerosol optical and microphysical characteristics derived by inversion of measurements from the AERONET site of Tamanrasset. The comparison is made between the retrievals from two models - GRASP/ARIA (with inhomogeneity) and GRASP/Standard (only homogeneous). Panel with the site name uses all measurements, the other panels are filtered by the quality of radiance retrieval of GRASP/ARIA relative to GRASP/Standard. In optical and microphysical characteristic plots, red is for GRASP/ARIA (StDev - shaded in blue), black is for GRASP/Standard (StDev - shaded in green).

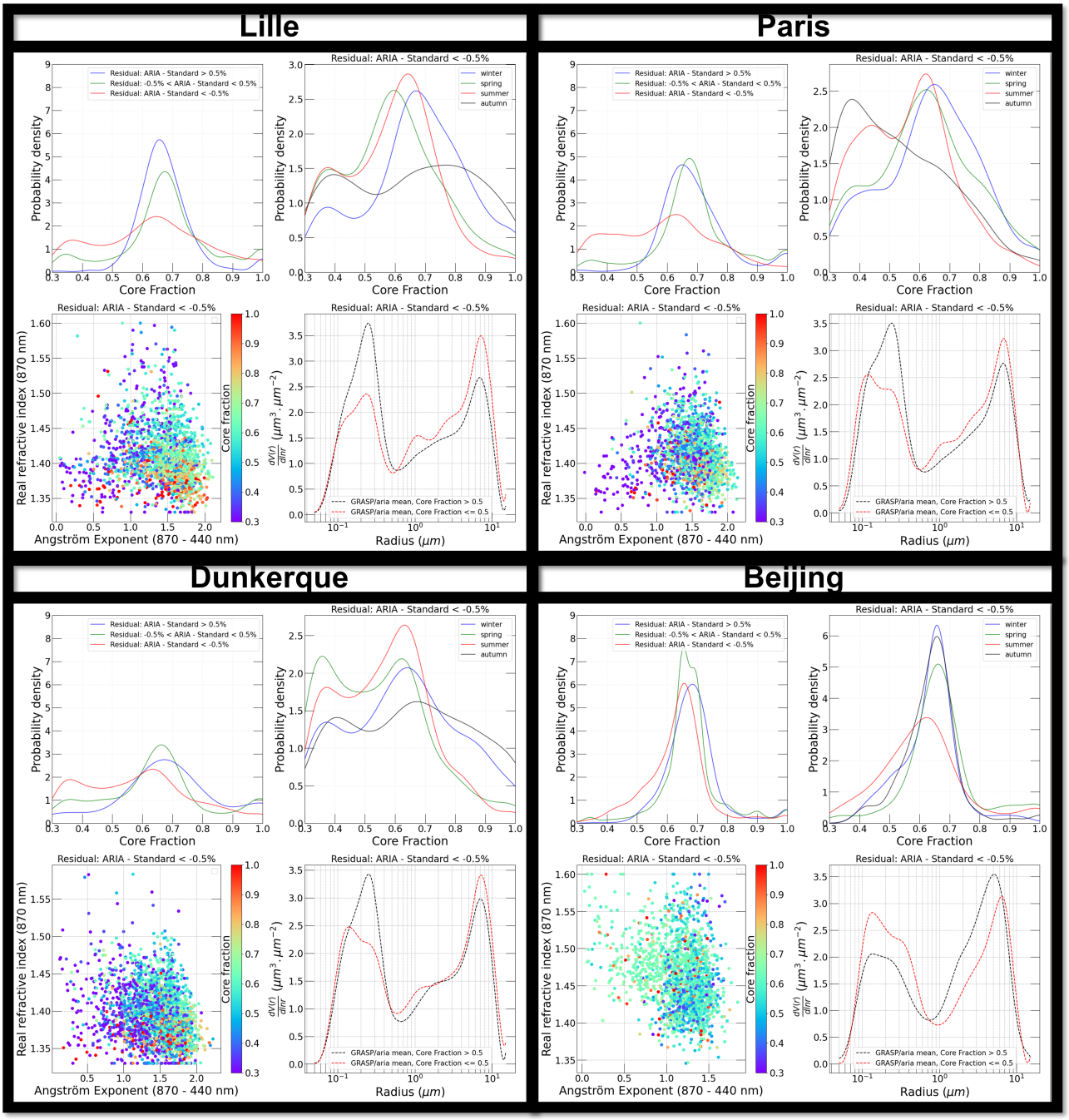

Figure A.78: Collection of plots illustrating the interpretation of core fraction retrievals in the context of residual improvement, seasonality, dominant particle size (represented by the Ångström exponent), composition (represented by the real refractive index), and shifts in the particle size distribution. The plots show results of GRASP/ARIA retrievals for real AERONET measurements from the period 2008 to 2025, which do not include information on light polarisation. The data are filtered by quality of radiance fit. The AERONET sites Lille, Paris, Dunkerque and Beijing represent urban aerosol types.

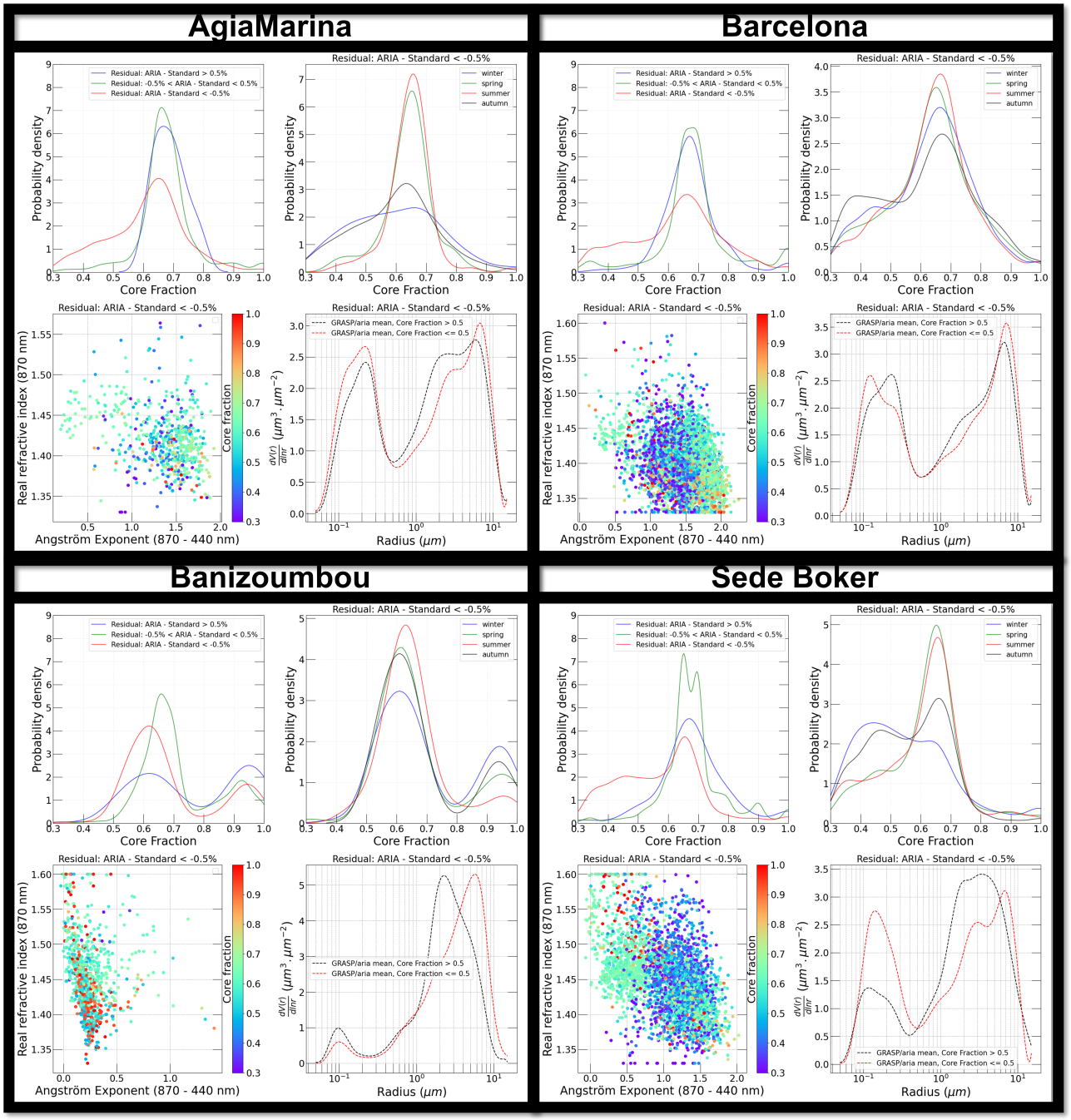

Figure A.79: Collection of plots illustrating the interpretation of core fraction retrievals in the context of residual improvement, seasonality, dominant particle size (represented by the Ångström exponent), composition (represented by the real refractive index), and shifts in the particle size distribution. The plots show results of GRASP/ARIA retrievals for real AERONET measurements from the period 2008 to 2025, which do not include information on light polarisation. The data are filtered by quality of radiance fit. The AERONET sites Agia Marina, Barcelona, Bonizoumbou and Sede Boker represent mixed aerosol types.

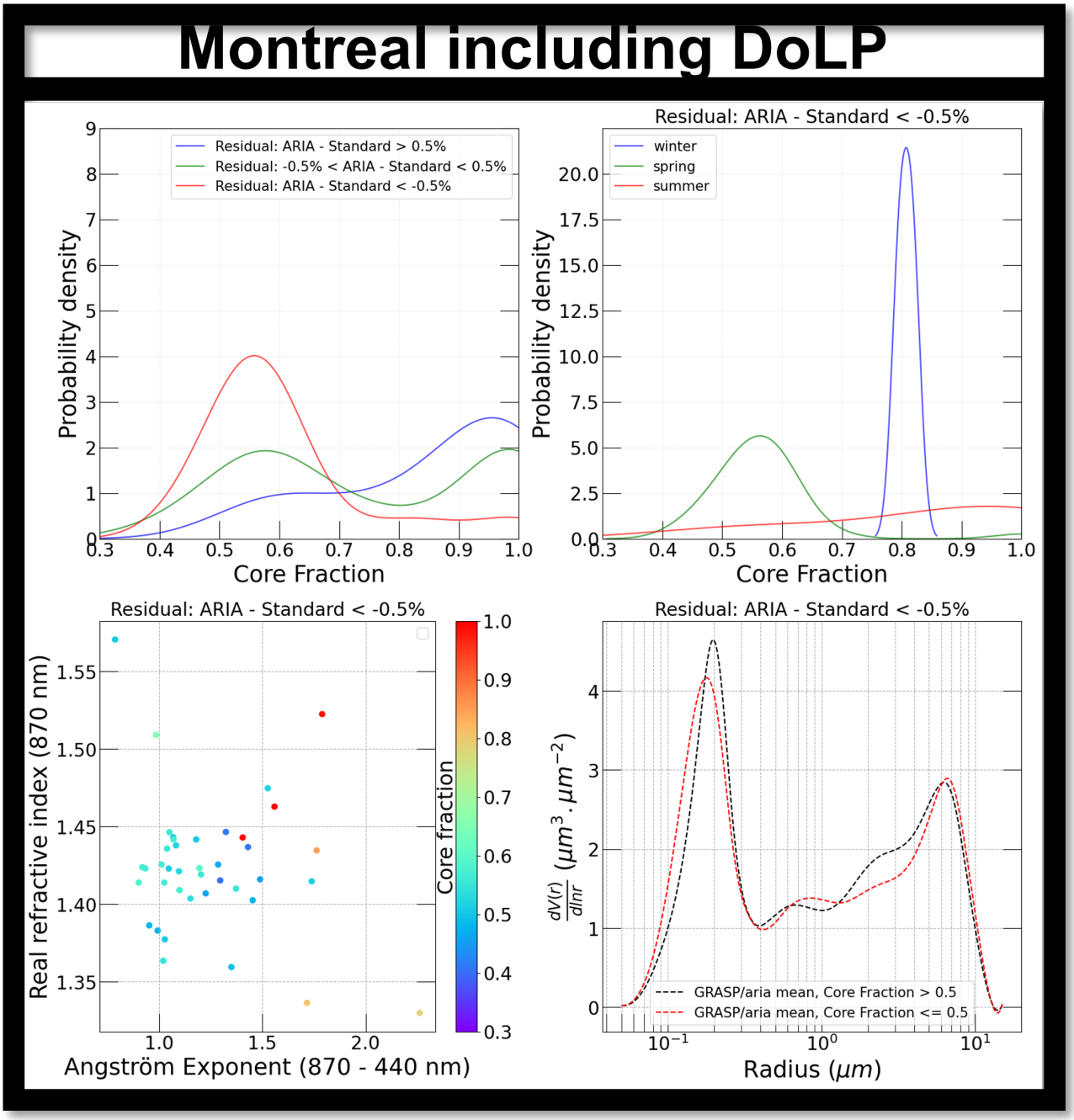

Figure A.80: Collection of plots illustrating the interpretation of core fraction retrievals in the context of residual improvement, seasonality, dominant particle size (represented by the Ångström exponent), composition (represented by the real refractive index), and shifts in the particle size distribution. The plots show results of GRASP/ARIA retrievals for real AERONET measurements of the Montreal site, which includes information on light polarisation. The data are filtered by quality of radiance fit.

A.4.3 Grouped by AOD

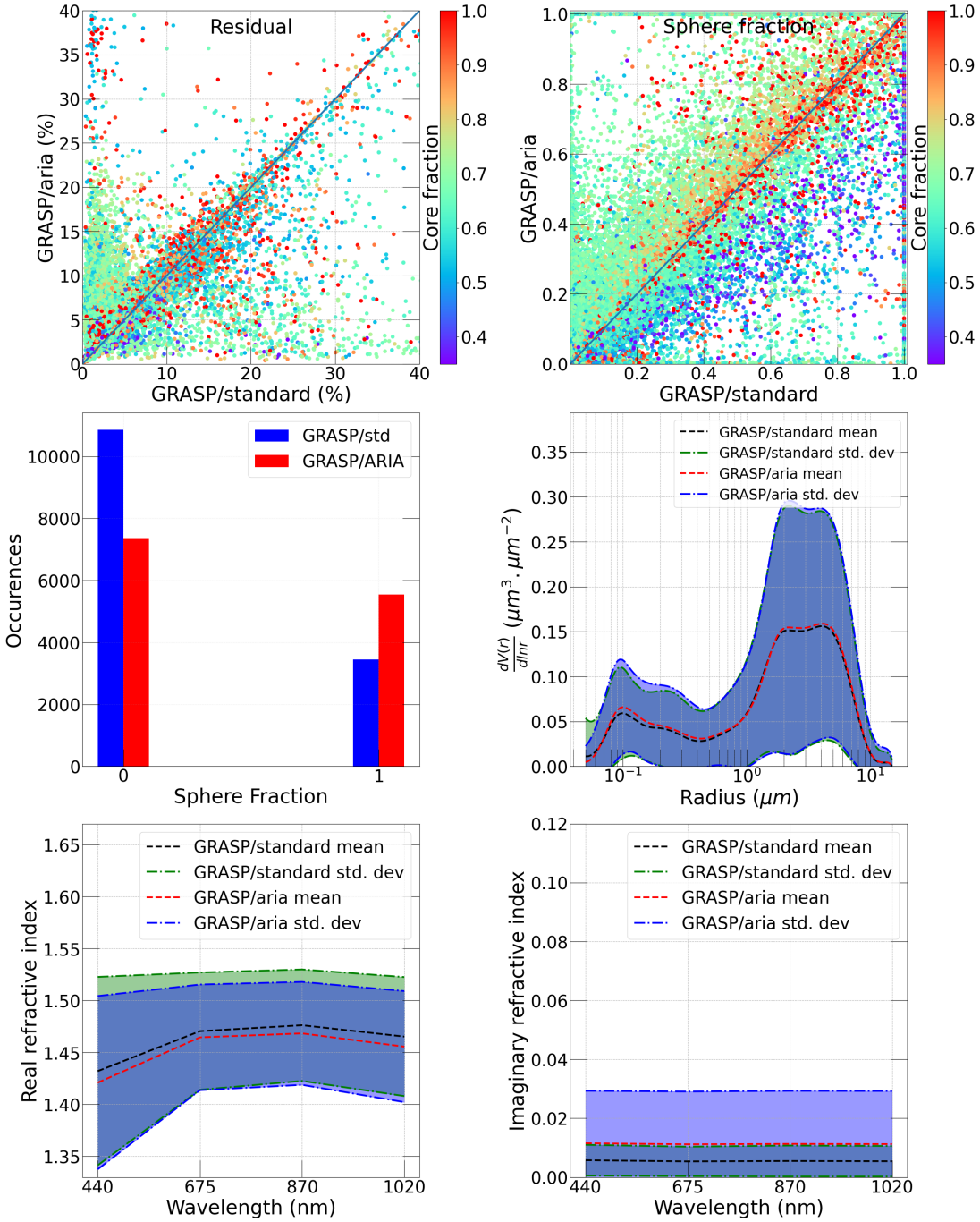

Figure A.81: Collection of plots of aerosol optical and microphysical characteristics derived by inversion of measurements from all AERONET sites. The comparison is made between the retrievals from two models - GRASP/ARIA (with inhomogeneity) and GRASP/Standard (only homogeneous) for AOD(440 nm) > 0.4.

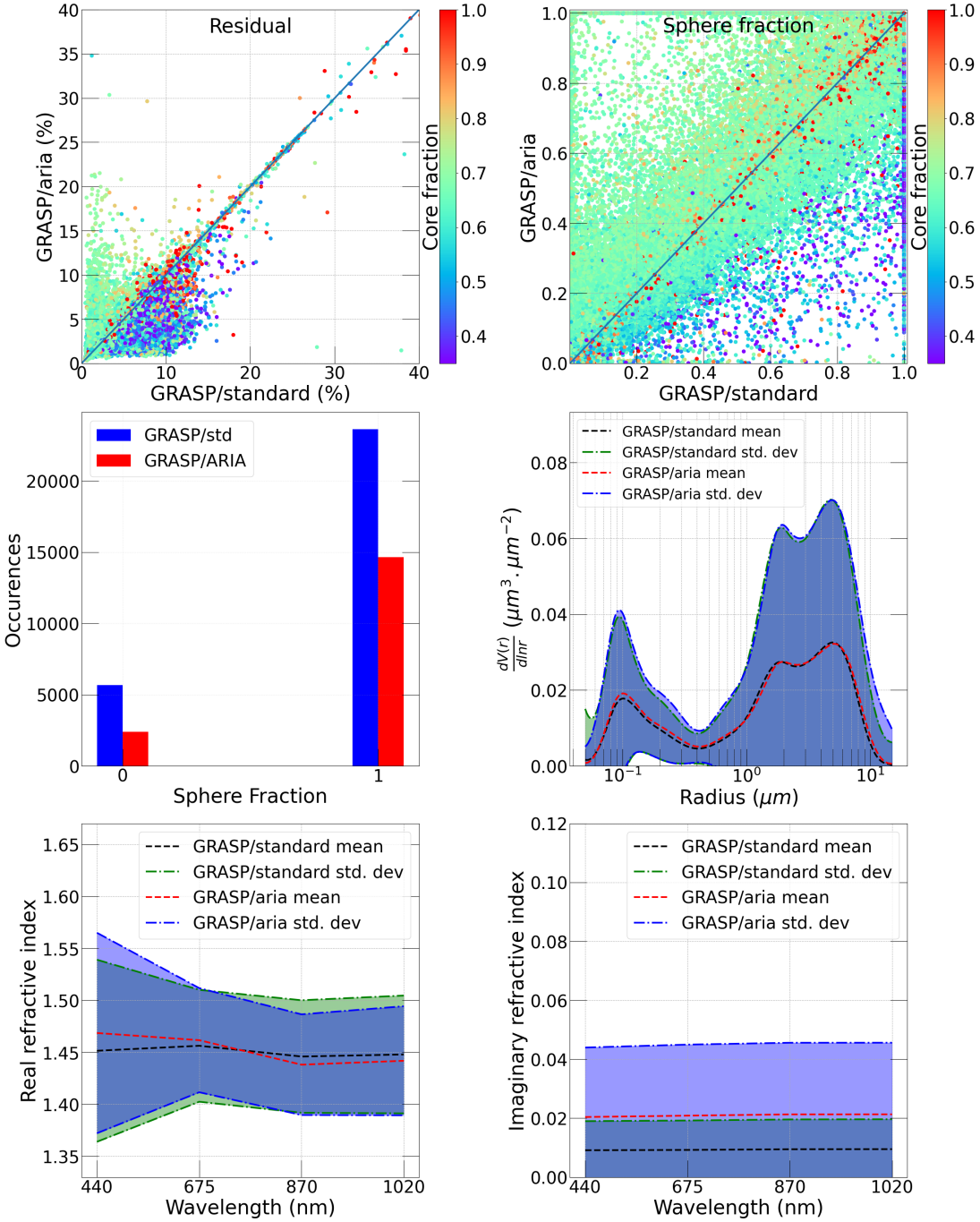

Figure A.82: Collection of plots of aerosol optical and microphysical characteristics derived by inversion of measurements from all AERONET sites. The comparison is made between the retrievals from two models - GRASP/ARIA (with inhomogeneity) and GRASP/Standard (only homogeneous) for AOD(440 nm) < 0.4.

A.5 TACO database ER diagramm

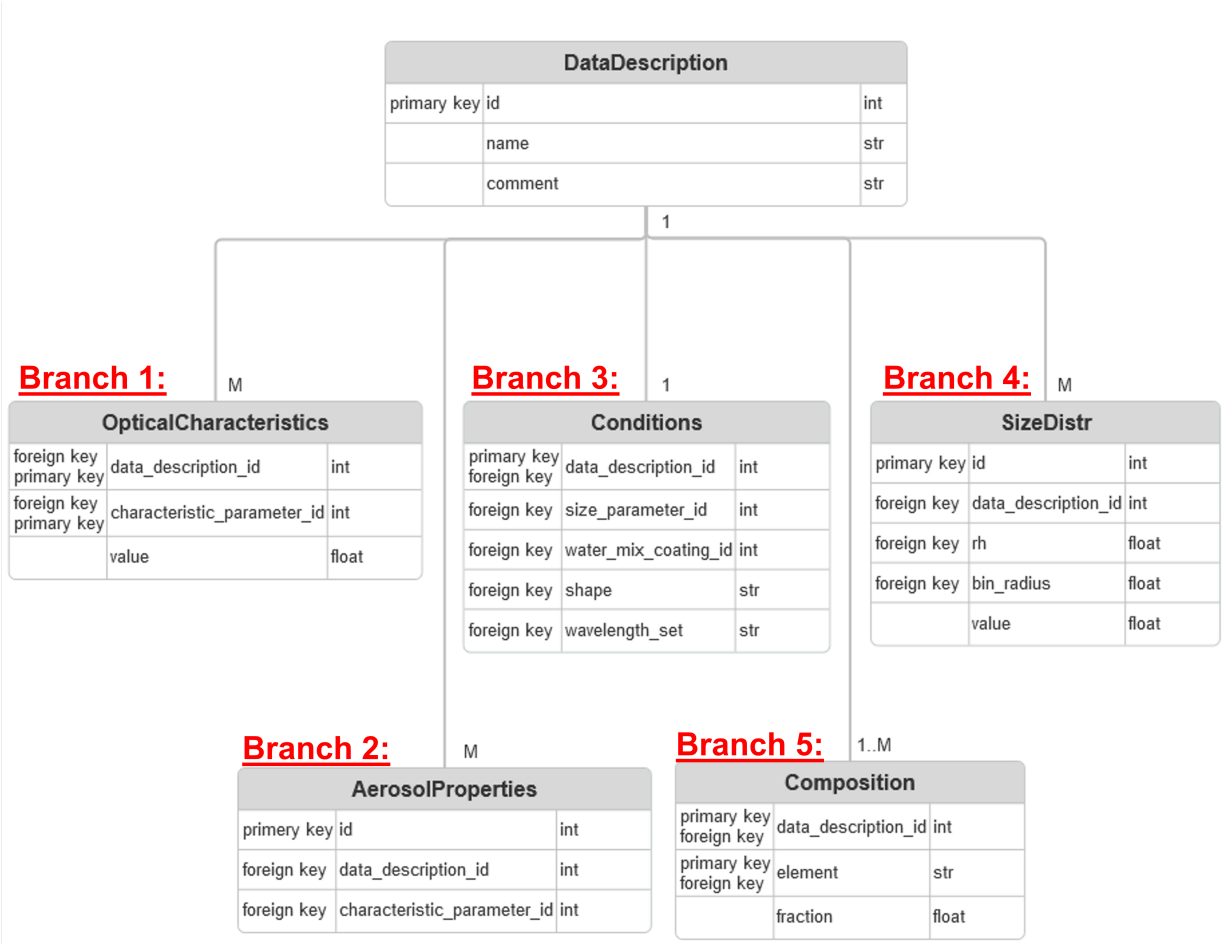

Figure A.83: ER diagram of the base structure of the database, dividing into 5 branches.

The Figure A.83 represents the main structure of the database with the first table "DataDescription" storing the meta-data of the input, all other tables are directly or indirectly linked to this one to be able to trace the origins of each value.

"OpticalCharacteristics" and "AerosolProperties", respectively branch 1 and 2, gather values dependent on relative humidity and wavelength. Their name is self-explanatory, the first holds values bound to the optical effects of the aerosols and the second on properties of the aerosols them-selves. They are detailed in Figure A.84.

"Conditions" and "Composition", respectively branch 3 and 5 gather the initial conditions of the calculation or climatology. "Composition" is only used for aerosols types (e.g., urban, biomass burning) to describe and quantify the different components. They are detailed in Figure A.85. Finally, "SizeDistr" (branch 4) gathers the information on the size distribution of the

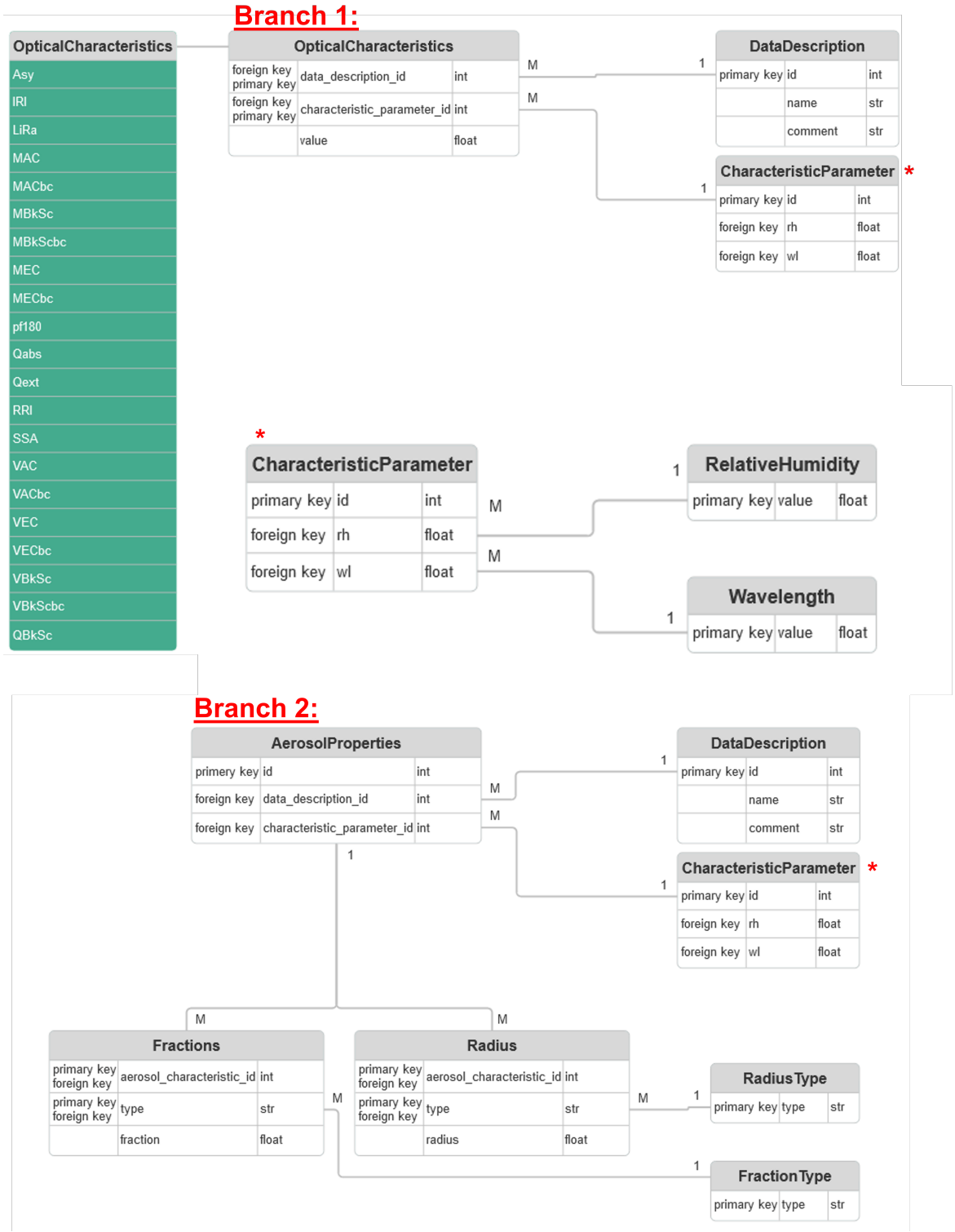

Figure A.84: ER diagram of the structure of the branches 1 and 2 of the database.

aerosols for the different relative humidity values (detailed in Figure A.86).

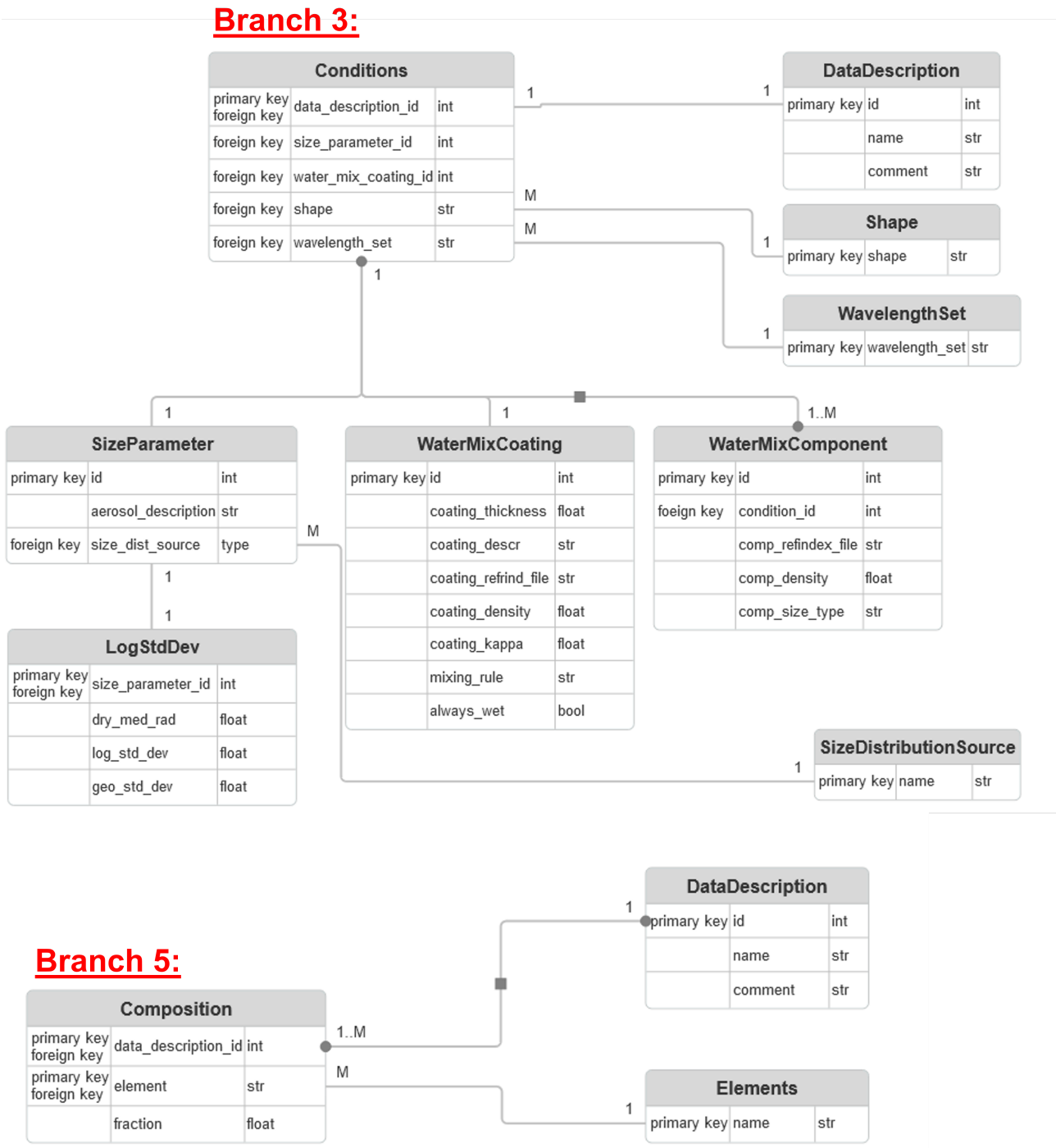

Figure A.85: ER diagram of the structure of the branches 3 and 5 of the database.

The database was implemented and constructed with tests files in order to communicate about it in several conferences like EGU, AGU, Aerocom/Aerosat and others. The project

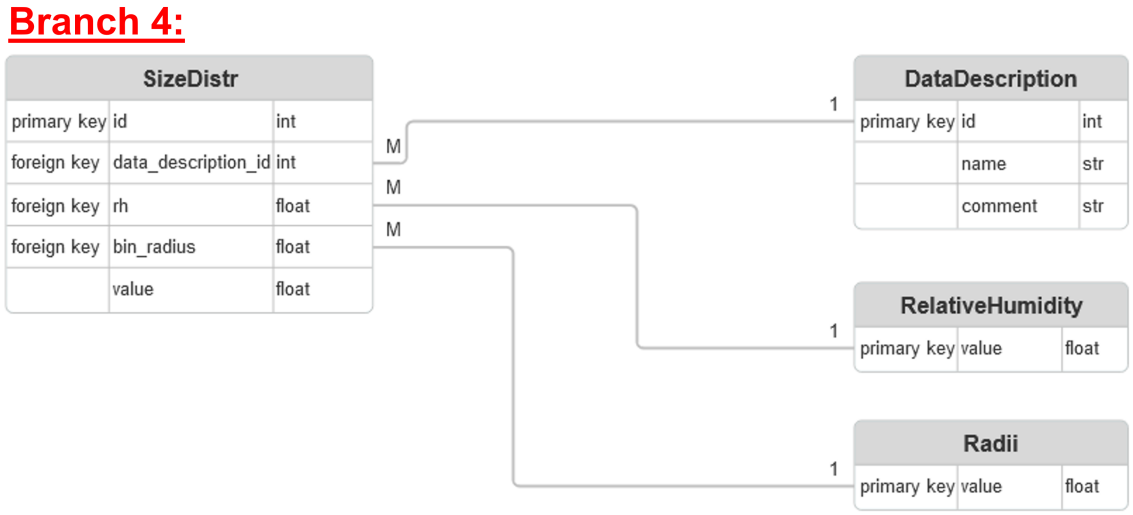

Figure A.86: ER diagram of the structure of the branches 4 of the database.

was submitted to ICARE, a database and service provider of the University of Lille, with the already implemented architecture to host the database and build an API and a website. It was accepted, and the database was transferred to ICARE in March 2025.

Résumé : Les aérosols atmosphériques sont des particules microscopiques en suspension dans l'air qui influencent le bilan radiatif de la Terre et affectent la formation des nuages, la qualité de l'air ainsi que la visibilité. Ils exercent ainsi un impact important sur le climat, l'environnement et les processus socio-économiques. La télédétection des propriétés physico-chimiques des aérosols permet d'obtenir des informations particulièrement précieuses à grande échelle spatiale et en quasi temps réel. Dans ce contexte, ce travail de thèse porte sur la problématique du suivi des situations dans lesquelles les aérosols sont enrobés par un matériau liquide. Ce travail est consacré au développement d'une nouvelle version d'un algorithme de télédétection (GRASP), applicable aux observations photométriques solaires au sol du réseau mondial AERONET. Les aspects théoriques de la diffusion de la lumière solaire par des particules enrobées ont été étudiés à l'aide de simulations numériques. L'approche ainsi développée a ensuite été implémentée et évaluée à partir d'observations issues de plusieurs régions géographiques représentatives d'aérosols urbains, désertiques et mixtes.

Keywords: Aérosol, adsorption d'eau par aérosol, inhomogénéité des aérosols, télédétection, photométrie solaire, réseau AERONET

Abstract: Atmospheric aerosols are microscopic particles suspended in the air that influence the Earth's radiative budget, affect cloud formation, air quality, and visibility. Aerosols thus have an important impact on climate, environment, and socio-economic processes. Remote sensing of aerosol physicochemical properties can provide highly valuable information over wide spatial scales and in near real time. For this reason, this thesis work focuses on the problem of monitoring cases in which aerosols are coated by a liquid material. The work is dedicated to the development of a new version of a remote sensing algorithm (GRASP) that can be applied to the AERONET global network of ground-based sun-photometric observations. The theoretical aspects of sunlight scattering by coated particles were studied using numerical simulations. The newly developed approach was then implemented and evaluated using observations from several geographical regions representing urban, desert, and mixed aerosol types.

Keywords: Aerosol, aerosol water uptake, aerosol inhomogeneity, remote sensing, photometer, AERONET network